

**Carderock Division**  
**Naval Surface Warfare Center**

Bethesda, Maryland 20084-5000

---

NSWCCD-SIG-96/072-7030 July 1996  
Signatures Directorate  
Research and Development Report

**Phenomena of Aliasing and Pass and Stop  
Bands in the Drive in Lieu of Ribs on  
Cylindrical Shells**

by

G. Maidanik  
K.J. Becker

DTIC QUALITY INSPECTED 2



---

Approved for public release; Distribution is unlimited.

---

19961015 015

UNCLASSIFIED

SECURITY CLASSIFICATION OF THIS PAGE

## REPORT DOCUMENTATION PAGE

Form Approved  
OMB No. 0704-0188

1a. REPORT SECURITY CLASSIFICATION Unclassified			1b. RESTRICTIVE MARKINGS None		
2a. SECURITY CLASSIFICATION AUTHORITY			3. DISTRIBUTION / AVAILABILITY OF REPORT Approved for public release. Distribution is unlimited.		
2b. DECLASSIFICATION/DOWNGRADING SCHEDULE					
4. PERFORMING ORGANIZATION REPORT NUMBER(S) NSWCCD-SIG-96/072-7030			5. MONITORING ORGANIZATION REPORT NUMBER(S)		
6a. NAME OF PERFORMING ORGANIZATION NSWC, Carderock Division		6b. OFFICE SYMBOL (If applicable) Code 7030		7a. NAME OF MONITORING ORGANIZATION	
6c. ADDRESS (City, State, and ZIP Code) Bethesda, MD 20084-5000		7b. ADDRESS (City, State, and ZIP Code)			
8a. NAME OF FUNDING/SPONSORING ORGANIZATION		8b. OFFICE SYMBOL (If applicable)		9. PROCUREMENT INSTRUMENT IDENTIFICATION NUMBER	
8c. ADDRESS (City, State, and ZIP Code)		10. SOURCE OF FUNDING NUMBERS			
		PROGRAM ELEMENT NO.	PROJECT NO.	TASK NO.	WORK UNIT ACCESSION NO.
11. TITLE (Include Security Classification) Phenomena of Aliasing and Pass and Stop Bands in the Drive in Lieu of Ribs on Cylindrical Shells					
12. PERSONAL AUTHOR(S) G. Maidanik and K.J. Becker					
13a. TYPE OF REPORT Research & Development		13b. TIME COVERED FROM 960101 TO 960731		14. DATE OF REPORT (Year, Month, Day) 1996 July 31	
				15. PAGE COUNT 196	
16. SUPPLEMENTARY NOTATION					
17. COSATI CODES			18. SUBJECT TERMS (Continue on reverse if necessary and identify by block number)		
FIELD	GROUP	SUB-GROUP	Structural Acoustics      Fourier Transform      Double-Sum		
			Wave Propagations		
19. ABSTRACT (Continue on reverse if necessary and identify by block number) This report constitutes an introduction to the investigation of the response of geometrically simple structural shells. The simplicity stems not only with respect to the mechanical description of the shell but also with respect to the inclusion of fluid loading. The report further deals with the influence of attaching ribs to the shells. The attachments are also confined to specific geometries; namely, those in which the ribs are set parallel and in conformity with the geometrical scheme of the shell. Again, this is devised to keep the formalism simple. Moreover, the formalism is largely developed on the basis that the ribs are identical and are regularly attached. Although this assumption is restrictive, the formalism developed harbors a number of characteristics and phenomena that are often encountered in practice and, therefore, the restrictions do not demerit the formalism, but rather, help decipher a number of significant footprints in field-data. Thus, the formalism reveals that in the drive in lieu of the ribs characteristics of aliasing and the phenomenon of pass and stop bands is present. Moreover, the phenomenon of pass and stop bands is					
20. DISTRIBUTION / AVAILABILITY OF ABSTRACT <input checked="" type="checkbox"/> UNCLASSIFIED/UNLIMITED <input type="checkbox"/> SAME AS RPT. <input type="checkbox"/> DTIC USERS			21. ABSTRACT SECURITY CLASSIFICATION Unclassified		
22a. NAME OF RESPONSIBLE INDIVIDUAL Maidanik, G.			22b. TELEPHONE (Include Area Code) (301) 227-1292		22c. OFFICE SYMBOL NSWCCD 7030

**REPORT DOCUMENTATION PAGE (Continuation Sheet)**

## 19. ABSTRACT (continued)

complementally exhibited in both the spectral and the spatial domains. This dual format is found to benefit the understanding and the interpretation of this phenomenon.

Moreover, this report, apart from its intrinsic value, serves as an introduction to a thesis presented by one of the authors. The thesis carries the investigation in this report a step further by attempting to answer the question: Since the strict aliasing in the drive in lieu of the ribs is spoiled in the response, does the high quality of the phenomenon of pass and stop bands in this drive also deteriorate in the response?

The formalism in this report is cast in terms of the impulse response function so that the external drive needs not be specified a priori; the furnishing of a compatible external drive is an independent task. Simple partial and circumference modal components in the external drive are used in this report as test external drives; a compatible external drive can then be composed of appropriately weighted components of this type. The casting of the formalism in terms of the impulse response function suitably serves also as an introduction to the investigation of scattering of incident sound fields from regularly ribbed shells. The external drives generated by the incident sound fields need merely be expressed in terms of components that are compatible with the impulse response functions developed and investigated in the report. These external drives are commensurate with the drives generated on the shell when the shell is blocked. [The response of the ribbed shell to this type of an external drive yields the scattered field due to this response. The other portion of the scattered field, in this instance, is given by the blocked scattered field.]

# CONTENTS

	<u>Page</u>
ABSTRACT .....	1
I. PROLOGUE.....	2
II. INTRODUCTION.....	7
III. AN IMPULSE RESPONSE FUNCTION OF A SHELL .....	13
IV. A SHELL WITH A FINITE NUMBER OF RIBS.....	35
V. AN EXTERNAL DRIVE .....	43
VI. MECHANICAL SURFACE IMPEDANCES OF SHELLS .....	47
VII. FLUID SURFACE IMPEDANCE ON SHELLS .....	64
VIII. FLUID LOADED SURFACE IMPEDANCE OF SHELLS .....	73
IX. ANALYTICAL DEFINITION OF THE RIBS .....	88
X. ALIASING IN THE DRIVE $P_{sn}(k, \omega)$ IN LIEU OF THE RIBS .....	103
XI. PASS AND STOP BANDS IN THE DRIVE $P_{sn}(k, \omega)$ IN LIEU OF THE RIBS .....	138
XII. PASS AND STOP BANDS IN THE DRIVE $\tilde{P}_{sn}(x, \omega)$ IN LIEU OF THE RIBS .....	153
XIII. COMPLEMENTAL DISPLAYS OF THE DRIVE IN LIEU OF THE RIBS .....	176
APPENDIX A: THE EQUIVALENCE OF AN EIGENOPERATOR AND A STATIONARY IMPULSE RESPONSE FUNCTION .....	183
APPENDIX B: COMPUTATIONAL DISPLAYS .....	186
REFERENCES .....	189



## ABSTRACT

This report constitutes an introduction to the investigation of the response of geometrically simple structural shells. The simplicity stems not only with respect to the mechanical description of the shell but also with respect to the inclusion of fluid loading. The report further deals with the influence of attaching ribs to the shells. The attachments are also confined to specific geometries; namely, those in which the ribs are set parallel and in conformity with the geometrical scheme of the shell. Again, this is devised to keep the formalism simple. Moreover, the formalism is largely developed on the basis that the ribs are identical and are regularly attached. Although this assumption is restrictive, the formalism developed harbors a number of characteristics and phenomena that are often encountered in practice and, therefore, the restrictions do not demerit the formalism, but rather, help decipher a number of significant footprints in field-data. Thus, the formalism reveals that in the drive in lieu of the ribs characteristics of aliasing and the phenomenon of pass and stop bands is present. Moreover, the phenomenon of pass and stop bands is complementally exhibited in both the spectral and the spatial domains. This dual format is found to benefit the understanding and the interpretation of this phenomenon.

Moreover, this report, apart from its intrinsic value, serves as an introduction to a thesis presented by one of the authors. The thesis carries the investigation in this report a step further by attempting to answer the question: Since the strict aliasing in the drive in lieu of the ribs is impaired in the response, does the high quality of the phenomenon of pass and stop bands in this drive also deteriorate in the response?

The formalism in this report is cast in terms of the impulse response function so that the external drive needs not be specified a priori; the furnishing of a compatible external drive is an independent task. Simple partial and circumference modal components in the external drive are used in this report as test external drives; a compatible external drive can then be composed of appropriately weighted components of this type. The casting of the formalism in terms of the impulse response function suitably serves also as an introduction to the investigation of scattering of incident sound fields from regularly ribbed shells. The external drives generated by the incident sound fields need merely be expressed in terms of components that are compatible with the impulse response functions developed and investigated in the report. These external drives are commensurate with the drives generated on the shell when the shell is blocked. [The response of the ribbed shell to this type of an external drive yields the scattered field due to this response. The other portion of the scattered field, in this instance, is given by the blocked scattered field.]

## I. PROLOGUE

The intention of this investigation is to increase understanding of structural acoustics by focusing on the vibrational and to a lesser extent on the radiative characteristics of shell structures (shells) that are subjected to external drives. In particular, interest is focused on the acoustic behavior of ribbed thin elastic panels and cylinders. For these types of shells (shell structures), the interactions of supporting ribs are often the controlling mechanism of the vibrational and radiative responses; not only are the interactions of the ribs with the shell significant, but also significant are the interactions among the various ribs via the shell. To emphasize the latter kind of interactions, largely two models are investigated. One is a proper model in which the natural interactions among the ribs are preserved. In the other model, which is artificially contrived, the interactions among the ribs are discounted. Comparison between results issued by the models exposes the role that is played by these interactions. However, the study transcends just those particular comparisons. Specifically, the goal is to examine the influence of ribs (localized stiffeners) and fluid loading on the acoustic behavior of shells. The unribbed shells involved in the analysis herein performed are plane and cylindrical; namely, panels and cylinders, respectively. A panel is a uniform plane shell structure and a cylinder is a uniform cylindrical shell structure. The axial-direction in the cylinder and a corresponding direction in the panel is uniform in this investigation and is assigned the  $x$ -direction. In the corresponding normal direction to this common uniformity, the panel is uniform but the cylinder is repetitively finite or circumferentially uniform. A component in the normal direction, assigned the  $y$ -direction, in the panel is designated "partial" and is one component in a continuous set. A component in the normal direction, assigned the  $y$ -direction, in the cylinder is designated

"circumferential mode" or "ring mode" and is one component in a discrete set. The investigations in this report are, therefore, based largely on a continuous and a circumferential modal analysis as manifested in the vibration and radiation responses when unribbed and ribbed panels and cylinders are driven by an external partial line and modal ring drive, respectively. ("Partial" is a continuous modal designation.) The external partial line and modal ring drives are devised to excite a partial and a single circumferential mode in the panel and the cylinder, respectively. The influences of parameters that define the mechanical surface impedance of a panel and a cylinder, the partial line and modal ring impedance of the ribs, and the fluid loading are examined. The influence of these quantities on wave phenomena associated with aliasing and pass and stop bands are of particular concern. The emphasis is on understanding and explaining the fundamental characteristics on a mode by mode basis so that the simultaneous presence of other modes will not make interpretation more difficult. Indeed, this is the universal purpose for using modal distributions. Again, the modal reference here is the partial line designation for the panel and the circumferential mode for the cylinder. The vibrational and radiative properties of the panel and cylinder, when externally driven by a more compounded external drive, are derived by an appropriately weighted integration of the partial contributions and by an appropriately weighted summation of the modal contributions, respectively; the validity of partial and modal superposition is then assumed. The weights are a constant with respect to both, the partial designation and the modal designation, when the external drive is a point drive.

The approach begins with an examination of the vibrational behavior of a regularly ribbed idealized uniform shell (a panel or a cylinder). The commonality of shells that are panel-like and those that are cylinder-like are discussed and

formulated. The formalisms of shells that are panel-like and those that are cylinder-like are laid side by side so that the commonality and disparity between these two classes of shells can be readily deciphered. In the first class, the models are described by continuous eigenfunctions (partial designations) and in the second, by discrete eigenfunctions (circumferential modes); both eigenfunctions fall into sets of functions that are complete and orthogonal. The environmental loading; e.g., fluid loading, is considered to be uniform and is lumped into the mechanical surface impedance of the uniform shell. In both chosen shells; the panel and the cylinder, the lumping of fluid loading into the mechanical surface impedance is straightforward. Indeed, in large part this straightforwardness is responsible for the usual modeling of structures in terms of these shells. The influence of attached ribs is described by a set of drives; the presence of the ribs is accounted for by a drive composed of a set of drives that are located at the positions occupied by the ribs. This set of drives constitutes the **drive in lieu of the ribs**, the presence of the ribs is completely accounted for by this drive. The response of the **ribbed shell** is then determined by applying this drive in lieu of the ribs, in addition to the external drive, to the **uniform shell**.

The regularity of the attached ribs simplify the formalism and is, therefore, imposed on the models of the ribbed shell structures considered in this work. The simplification so attained renders the commonality and disparity between the formalisms for the vibrational behavior of the panel-like and the cylinder-like structures easy to decipher and understand. Further, this simplicity is used to advantage in introducing the format by which computations are displayed and in illustrating the kind of results that can be expected as the more rigorous and extensive investigation proceeds in subsequent works. Of course, the simplification just discussed is not derived without penalties. For example, having

imposed regularity on the ribs, the influence of varying the spacing between adjacent ribs and the line and ring impedance identities among the ribs is not available under this simplification. Thus, the investigation may so begin but by no means may it so end. Many extensions to the analysis presented herein await attention in subsequent investigations. The elements of such extensions lie, however, outside the immediate interest of this report. These extensions are issued under separate covers in subsequent reports.

With respect to the vibrational response of a shell, only a hybrid and a natural cylinder, unribbed and ribbed, are treated in detail. [A hybrid cylinder is one from which certain parts of the mechanical surface impedance are artificially removed; namely, those describing the longitudinal and shear responses and those pertaining to curvature effects. Structural acoustics of a hybrid cylinder relates closely to the acoustics of a panel and the differences are readily deciphered. Thus the hybrid cylinder bridges the relationship between the structural acoustics of panels and natural cylinders.] The influence of ribs is investigated by computations that are displayed in manners that tend to accentuate features of general interest and significance. For the most part the computations are displayed in a waterfall format. The waterfall lies in the frequency domain. Such displays can dispense, at a glance, a large volume of information. The intended purpose of using displays in this format is to present this large volume of information in order to accentuate a phenomenon of concern by a visual scan of a few such displays. Changes in a phenomenon due to parametric variations can then be revealed by merely comparing displays. Extra details can be revealed by zooming in on special regions. In this report, however, these regions are chosen to be large so that in comparing displays only gross features that are commensurate with the intended purpose of the report are

significantly investigated. Also, to accentuate significant and insignificant differences in specific displays, one may isolate and contrast one or two curves in one display with another. In these kinds of displays trees are compared with trees rather than forests with forests. These trees-to-trees comparisons can be readily and quickly implemented and yet be compatible with the major aims to be achieved in this report.

Both, the spectral domain and the spatial domain with respect to the  $x$ -direction, are examined in this report. The spectral domain is the  $k$ -domain and the spatial domain is the  $x$ -domain; these two domains are related Fourier conjugate domains -- Fourier pair. For certain purposes one domain may be the more suitable to either exhibit a phenomenon or interpret data. In certain situations, however, the complementarity of the two domains advantageously assist in the recognition and interpretation of a phenomenon. Thus, in this report the phenomenon of pass and stop bands is extensively investigated in both domains to exemplify the advantages of complementarity in the investigation of the drive in lieu of the ribs and whence in the determination of the response behavior of ribbed shells.

## II. INTRODUCTION

Often the response of a shell structure (a shell) and the consequent response of the fluid in which the shell is immersed are treated analytically in a manner that is highly dependent on the geometrical form of the shell. Initially an attempt is made to try and divorce the explicit geometrical form of the shell from the formalism. In this way some of the salient assumptions that are made with respect to the geometrical form of the shell can be more generally made and assessed. An observation is made that the analytical procedures used in deriving the formalism fall primarily into two categories; one relating to an infinitely extended shell in both the spatial coordinates that describe the shell, and the other relating to a finitely extended shell in one of the coordinates. The first category is exemplified by an infinite plane shell -- a panel -- and the second category by an axially infinite cylindrical shell -- a cylinder. In the next section the two procedures are cast side by side in order to emphasize and decipher their commonalities and idiosyncrasies. Indeed, in many cases one procedure can be derived from the other by a simple manipulation of the notations.

For the most part the development of the formalism, cast herein, engaged the impulse response methodology. There are several advantages to this methodology. Firstly, the propriety of the impulse response operator function is a cornerstone that can be used to advantage; i.e., the impulse response function is specified by quantities and parameters that describe the structure and the fluid only; it is independent of the response and the external drive. Secondly, although the external drive must be rendered compatible with the impulse response operator, the character of the external drive does not need a prior

specification except for the fact that it needs to be external; namely, it needs to be independent of the response that it may generate.

In this development, the ribs are attached along a single coordinate and are assumed to be simple in the sense that they cannot exert higher moments than the zeroth. The introduction of moments can be handled by extending the formalism to accommodate a more compounded description for the ribs and for the mechanical surface impedance of the shell. For example; if a first moment is allowed in the rib motion, then the mechanical surface impedance of the shell needs to diminish at high wavenumbers at least to the inverse fourth power in these wavenumbers so that convergence can be ensured. Moreover, when the first moment is introduced, the number of equations in the formalism doubles [1-4]. This kind of extension to the formalism is considered to be, however, outside the scope of this investigation.

In Section III the response of a general shell to a general, but compatible, external drive is considered and is formulated in dual forms. One form is applicable to an infinite and the other to a finite general shell. The response of the unribbed shell is derived and is then assumed to be known. In this derivation fluid loading on the shell is taken into account [1-9]. A regular set of ribs is then attached to the shell along one of the orthogonal coordinates on the surface of the shell. The modifications to the response of the shell due to the attachment of the ribs is then considered. This modification is derived as a separate term which vanishes when the ribs are removed [1-4, 10-16].

In Section IV a finite set of ribs, instead of a regular set, is attached to the shell, again, along one of the orthogonal coordinates on the surface of the shell.



Again, the modifications to the response of the shell due to the attachment of this set of ribs is considered [10, 17]. The analogies and differences in this response and that of a regularly ribbed shell are briefly discussed.

In Section V the external point and line drives are cast in a compatible manner that fits the formalism developed in Section III. These external drives are test drives from which many more compounded external mechanical drives can be constructed by superposition [1-3, 10].

In Section VI the mechanical surface impedances of shells, specifically those of a panel and a cylinder, are stated and cast in a form that is suitable for the purposes of the investigations in this report [1-3, 8, 13]. Although in the literature many forms for the surface impedances are proposed, especially those pertaining to a cylinder, the exact expression to be used in this report is selected. In this selection a hybrid cylinder is defined and its commonality with a panel is established. The nature of the selected surface impedances in the spectral domain are depicted by waterfall displays [15]. The displays effectively span the normalized frequency domain from about one octave above the ring frequency to about sixteen times the ring frequency which is about half an octave below the critical frequency; this is the range of frequency in which investigations are carried out in this report. A specific model of a cylindrical shell is chosen for exemplifying the formalism developed in this report; in this model the ring frequency is more than an order of magnitude below the critical frequency. This range of frequency avoids consideration of curvature free waves at the lower frequency range and consideration of supersonic flexural free waves at the higher frequency range; a safe and convenient frequency range indeed! The displays effectively span the normalized wavenumber domain from zero to seventy-five,

the normalization factor being the radius of the cylinder. The meaning of standard parametric values to generate the displays are also defined in this section. The flexural free waves dominate the patterns in a panel and in its analog, the hybrid cylinder. Although the flexural free waves are dominant in the patterns of a natural cylinder, the membrane free waves are also present in the patterns. The nature of the membrane free waves is investigated in these displays. The dependence of these free waves on the mode index  $n$  is investigated. The absence of the shear free waves when this index is zero is of particular interest.

In Section VII the explicit form for the fluid loading is defined for both the panel and the cylinder. The nature of the surface fluid impedance is illustrated in this section. For the panel, the surface fluid impedance is found to be real (resistance controlled) for supersonic components and imaginary (mass controlled) for subsonic components [1-3, 8, 9]. For the cylinder the surface fluid impedance is real (resistance controlled) for supersonic components and is imaginary (mass controlled) for all components [1-3, 8, 9]. A sonic ridge in the surface impedance of the fluid is observed and the fluid loading parameter and the fluid wavenumber at the critical frequency are defined. The critical frequency is the frequency at which the speed of the flexural free waves is equal to the speed of sound in the fluid.

In Section VIII the fluid loaded surface impedance of the panel and cylinder are derived using the material in Sections VI and VII. The difference between the fluid loading on a panel and on a hybrid cylinder is highlighted. The use of a hybrid cylinder as an investigative companion to a natural cylinder is thus justified and its use is explained.

In Section IX the analytical description of the ribs is presented. This description comprises a line impedance and provisions are made to allow for a resonance. This resonance is defined in terms of a resonance frequency and a loss factor. In this report only a minimal use is made of this versatility in the ribs leaving the more thorough investigations for subsequent work. Nonetheless, a provision for such an extended research work is made herein and the deployment of this provision is exemplified.

In Section X the phenomenon of aliasing is investigated and displayed. In a regularly ribbed shell the aliasing is shown to reside in the drive in lieu of the ribs. The aliasing patterns in this drive are displayed and investigated. A first and a proper order model are discussed and contrasted.

In Section XI the aliasing phenomenon is related to the pass and stop bands in the drive in lieu of the ribs. The relationship between the dispersive loci and false dispersive loci is discussed. The cancellations at the spectral regions where false dispersive loci cross (intersect) and the manifestation of stop bands are established.

In Section XII the spatial domain is introduced and is used to investigate the phenomenon of pass and stop bands in the drive in lieu of the ribs. The usefulness of the complementarity of the spectral and spatial domains is made clearer in this section. The drive in lieu of the ribs in the domain is derived from that in the domain by a novel computational technique designed to perform a Fourier transformation [16, 18]. The phenomenon of pass and stop bands in this drive is given some quantitative manifestation in the displays of this phenomenon in the spatial domain.

In the final section; i.e., Section XIII, Sections X and XI and Section XII are complemented and the enhancement that results from this procedure, to the understanding of the phenomenon of pass and stop bands, is discussed and highlighted.

### III. AN IMPULSE RESPONSE FUNCTION OF A SHELL

Consider a general shell (e.g., a panel or a cylinder) such as shown in Fig. 3-1; having a surface defined by two spatial coordinates; namely, the surface is defined by the spatial vector variable  $\{x, y\}$ . The surface is in contact with a surrounding acoustic fluid defined by the density ( $\rho$ ) and the speed of sound ( $c$ ) which comprise the characteristic impedance ( $\rho c$ ) of the fluid. In the interior of the shell a vacuum prevails. The surface of the shell is driven by an external drive  $p_e(x, y, \omega)$ , where ( $\omega$ ) is the Fourier conjugate of the temporal variable ( $t$ ) as expressed below

$$p_e(x, y, \omega) = (2\pi)^{-1/2} \int dt \tilde{p}_e(x, y, t) \exp(-i\omega t) , \quad (3-1a)$$

$$\tilde{p}_e(x, y, t) = (2\pi)^{-1/2} \int d\omega p_e(x, y, \omega) \exp(i\omega t) . \quad (3-1b)$$

The response of the shell in the absence of the fluid; namely, when  $(\rho c) = 0$ , is governed by the equation of motion

$$z_t(x, y, \omega) v(x, y, \omega) = p_e(x, y, \omega) , \quad (3-2)$$

where  $z_t(x, y, \omega)$  is the mechanical surface impedance operator of the shell and  $v(x, y, \omega)$  is the response, in terms of the normal velocity, of the shell in the absence of fluid. In Eq. (3-2) a fundamental assumption is made that the structural system is stationary in time so that the equation with respect to the frequency variable ( $\omega$ ) is algebraic. [cf. Appendix A.]

"Fluid loading" is a term used to describe the drive generated by the shell reacting to the presence of the fluid on its surface. Here this fluid loading is designated by the pressure  $-p_f(x, y, \omega)$ . Introducing this pressure in the equation of motion modifies Eq. (3-2) in the linearly superposed form

$$z_t(x, y, \omega) v(x, y, \omega) = p_e(x, y, \omega) - p_f(x, y, \omega) . \quad (3-3)$$

The general shell is now restricted to geometries in which the fluid loading can be expressed in the separable form

$$p_f(x, y, \omega) = z_f(x, y, \omega) v(x, y, \omega) , \quad (3-4)$$

where  $z_f(x, y, \omega)$  is a uniform surface impedance. That surface impedance is the fluid surface impedance on the shell boundaries that are in contact with the fluid. Geometries in which the separability stated in Eq. (3-4) is valid are exemplified by a uniform panel and a uniform cylindrical shell. Shells of these descriptions and the appropriate coordinate systems are sketched in Figs. 3-2 and 3, respectively. From Eqs. (3-3) and (3-4) one obtains

$$z_{tf}(x, y, \omega) v(x, y, \omega) = p_e(x, y, \omega) , \quad (3-5)$$

where

$$z_{tf}(x, y, \omega) = z_t(x, y, \omega) + z_f(x, y, \omega) . \quad (3-6)$$

Thus, the linear superposition in pressures, stated in Eq. (3-3), is elevated to the linear superposition in the surface impedances in Eq. (3-5), a major step indeed.

Situations occur which are conducive to separating the mechanical surface impedance  $z_t(x, y, \omega)$  of the shell into two terms. The first, designated  $z_p(x, y, \omega)$ , describes the mechanical surface impedance of a uniform shell, uniform in the  $\{x, y\}$ -domain. The second, designated  $z_s(x, y, \omega)$ , accounts for the nonuniformities in the surface impedance of the shell. Thus

$$z_t(x, y, \omega) = z_p(x, y, \omega) + z_s(x, y, \omega) , \quad (3-7)$$

and from Eqs. (3-5), (3-6) and (3-7) one derives

$$z_\infty(x, y, \omega) v(x, y, \omega) = p_e(x, y, \omega) - p_s(x, y, \omega) , \quad (3-8)$$

where

$$p_s(x, y, \omega) = z_s(x, y, \omega) v(x, y, \omega) , \quad (3-9)$$

and

$$z_\infty(x, y, \omega) = z_p(x, y, \omega) + z_f(x, y, \omega) . \quad (3-10)$$

The surface impedance  $z_\infty(x, y, \omega)$  is, by definition, uniform in the  $x$ - and  $y$ -domains. The nonuniformities that are defined in  $z_s(x, y, \omega)$  are assumed in this investigation to be confined to the  $x$ -domain only so that  $z_s(x, y, \omega)$  is uniform with respect to the  $y$ -domain as is, of course,  $z_\infty(x, y, \omega)$ . The choice of the spatial coordinates and their orientation depends on the disposition of the geometrical form of the shell. The uniformity of the surface impedances  $z_\infty(x, y, \omega)$  and  $z_s(x, y, \omega)$  in the  $y$ -domain makes it convenient to transform

Eq. (3-8) into the continuous (partial)  $k_y$ -domain or the discrete (modal)  $n$ -domain. The continuous  $k_y$ -domain is the Fourier conjugate domain of the  $y$ -domain. The Fourier transformation is appropriate when the uniformity in this domain is extended infinitely. The discrete (modal)  $n$ -domain is appropriately employed when the uniformity in this domain is extended finitely. Subsequently the two transformations are presented side by side. This presentation helps exhibit the commonality and the disparity in the two transformations. Moreover, comparisons of this kind often facilitate understanding of either and both. The response  $v(x, y, \omega)$  in terms of these two transformations is

$$v(x, y, \omega) = (2\pi)^{-1/2} \int dk_y V(x, \underline{\omega}_2) \exp(-iyk_y) \\ \underline{\omega}_2 = \{k_y, \omega\} , \quad (3-11a)$$

$$v(x, y, \omega) = \sum_n \tilde{V}_n(x, \omega) \psi_n(y) . \quad (3-11b)$$

Similarly, for the external drive  $p_e(x, y, \omega)$  the corresponding transformations are

$$p_e(x, y, \omega) = (2\pi)^{-1/2} \int dk \tilde{P}_e(x, \underline{\omega}_2) \exp(-iyk_y) , \quad (3-12a)$$

$$p_e(x, y, \omega) = \sum_n \tilde{P}_{en}(x, \omega) \psi_n(y) . \quad (3-12b)$$



In Eqs. (3-11) and (3-12),  $(2\pi)^{-1/2} \exp(-iyk_y)$  and  $\psi_n(y)$  are chosen to be the eigenfunctions in the  $y$ -domain with respect to the surface impedance eigenoperator  $z_\infty(x, y, \omega)$ . This choice is expressed

$$\{z_\infty(x, y, \omega) = \tilde{Z}_\infty(x, \omega_2)\} (2\pi)^{-1/2} \exp(-iyk_y) , \quad (3-13a)$$

$$\{z_\infty(x, y, \omega) = \tilde{Z}_{\infty n}(x, \omega)\} \psi_n(y) , \quad (3-13b)$$

and each of these eigenfunction sets are assumed to form a complete and orthogonal set. Completeness is expressed

$$(2\pi)^{-1} \int dk \exp[-i(y-y')k_y] = \delta(y-y') , \quad (3-14a)$$

$$\sum_n \psi_n(y) \psi_n^*(y') = \delta(y-y') , \quad (3-14b)$$

and orthogonality is expressed

$$(2\pi)^{-1} \int dy \exp[-iy(k_y - k'_y)] = \delta(k_y - k'_y) , \quad (3-15a)$$

$$\int dy \psi_n(y) \psi_n^*(y) = \delta_{nm} . \quad (3-15b)$$

The quantities  $\tilde{Z}_\infty(x, \omega_2)$  and  $\tilde{Z}_{\infty n}(x, \omega)$ , defined in Eq. (3-13), are the eigenvalues of the  $(k_y)$ th and  $(n)$ th eigenfunctions in the  $y$ -domain, respectively. Utilization of these transformations and conditions, as expressed in Eqs. (3-11)

through (3-15), yields, for the partial and modal designations of Eqs. (3-8) and (3-9), the forms

$$\bar{Z}_\infty(x, \omega_2) \bar{V}(x, \omega_2) = \bar{P}_e(x, \omega_2) - \bar{P}_s(x, \omega_2) , \quad (3-16a)$$

$$\tilde{Z}_{\infty n}(x, \omega) \tilde{V}_n(x, \omega) = \tilde{P}_{en}(x, \omega) - \tilde{P}_{sn}(x, \omega) , \quad (3-16b)$$

respectively, where

$$\bar{P}_s(x, \omega_2) = \tilde{Z}_s(x, \omega_2) \bar{V}(x, \omega_2) , \quad (3-17a)$$

$$\tilde{P}_{sn}(x, \omega) = \tilde{Z}_{sn}(x, \omega) \tilde{V}_n(x, \omega) . \quad (3-17b)$$

The drive (pressure) components  $\bar{P}_s(x, \omega_2)$  and  $\tilde{P}_{sn}(x, \omega)$  are of particular interest; they are associated with the nonuniformities described by the portion  $z_s(x, y, \omega)$  in the mechanical surface impedance  $z_t(x, y, \omega)$  stated in Eq. (3-7). The fluid loading pressure  $-p_f(x, y, \omega)$  is conveniently expressed in terms of a uniform surface impedance  $z_f(x, y, \omega)$  so that it can be transferred from the right to the left side of the equation and incorporated with the uniform component described by the portion  $z_p(x, y, \omega)$  in the mechanical surface impedance  $z_t(x, y, \omega)$  of the shell. Fluid loading is indeed a spatially extended phenomenon and, therefore, the uniformity of  $z_f(x, y, \omega)$  can be partially justified. This incorporation results in the definition of the uniform surface impedance  $z_\infty(x, y, \omega)$ . The nonuniformities in  $z_t(x, y, \omega)$ , on the other hand, are induced by spatially localized impedances and, therefore, it is natural to remove  $z_s(x, y, \omega)$  from the left to the right side of the equation and treat the influence of these nonuniformities in the surface impedance of the shell in terms of the drives

(pressures) that they generate. This is why  $z_f(x, y, \omega)$  and  $z_s(x, y, \omega)$  find themselves on opposite sides of the equation, having exchanged their original places. This manipulation advantageously leaves the surface impedance operator  $z_\infty(x, y, \omega)$  on the left side of the equation uniform in  $(x)$ ; this operator can thus potentially be rendered algebraic by a Fourier transformation with respect to  $(x)$ . Indeed, this potential procedure has been implicitly employed in the Fourier transformation from the  $t$ -domain into the  $\omega$ -domain. In this investigation the  $t$ -domain is uniform and is assumed to be infinitely extended. [cf. Appendix A.]

Formally, Eq. (3-16) can be expressed in terms of the surface impulse response functions  $\tilde{G}_\infty(x|x', \omega_2)$  and  $\tilde{G}_{\infty n}(x|x', \omega)$ ; which are simply the inverse surface impedance operator of  $\tilde{Z}_\infty(x, \omega_2)$  and  $\tilde{Z}_{\infty n}(x, \omega)$ , respectively. In the format of the impulse response function, Eq. (3-16) becomes

$$\tilde{V}(x, \omega_2) = \int \tilde{G}_\infty(x|x', \omega_2) dx' [\tilde{P}_e(x', \omega_2) - \tilde{P}_s(x', \omega_2)], \quad (3-18a)$$

$$\tilde{V}_n(x, \omega) = \int \tilde{G}_{\infty n}(x|x', \omega) dx' [\tilde{P}_{en}(x', \omega) - \tilde{P}_{sn}(x', \omega)]. \quad (3-18b)$$

Ostensibly, Eq. (3-18) is an acceptable description for the partial and modal response of the shell to an external drive. Whether this description is useful and proper remains to be substantiated. If the nonuniformities are removed; i.e., when  $\tilde{P}_s$  and  $\tilde{P}_{sn}$  are set equal to zero, one obtains and defines

$$\tilde{V}_\infty(x, \omega_2) = \int \tilde{G}_\infty(x|x', \omega_2) dx' \tilde{P}_e(x', \omega_2) , \quad (3-19a)$$

$$\tilde{V}_{\infty n}(x, \omega) = \int \tilde{G}_{\infty n}(x|x', \omega) dx' \tilde{P}_{en}(x', \omega) . \quad (3-19b)$$

The impulse response functions  $\tilde{G}_\infty$  and  $\tilde{G}_{\infty n}$  are proper in the sense that they are dependent only on quantities and parameters that describe the uniform shell; they are independent of the response  $\tilde{V}_\infty$  and  $\tilde{V}_{\infty n}$ , and the external drive  $\tilde{P}_e$  and  $\tilde{P}_{en}$ , to which the shells may be subjected, respectively. Equation (3-19) is then, by definition, proper. On the other hand, except in the limits in which Eq. (3-18) becomes Eq. (3-19), the former equation is improper. The impropriety of Eq. (3-18) arises in the sense that the desired surface response (velocity) is implicitly present on the right side of the equation through the dependence expressed in Eq. (3-17). In order to remedy this impropriety certain assumptions and restrictions need to be imposed. One needs to do this without jeopardizing the description of the phenomena of interest in this investigation. The solution being sought can be expressed formally as

$$\tilde{V}(x, \omega_2) = \int \tilde{G}(x|x', \omega_2) dx' \tilde{P}_e(x', \omega_2) , \quad (3-20a)$$

$$\tilde{V}_n(x, \omega) = \int \tilde{G}_n(x|x', \omega) dx' \tilde{P}_{en}(x', \omega) , \quad (3-20b)$$

and  $\tilde{G}$  and  $\tilde{G}_n$  in Eq. (3-20) are required to be functions only of the properties of the structure and the fluid and to be independent of the response  $\tilde{V}(x, \omega_2)$  and  $\tilde{V}_n(x, \omega)$  and the external drive  $\tilde{P}_e(x, \omega_2)$  and  $\tilde{P}_{en}(x, \omega_2)$ , respectively. Thus the goals of the assumptions and restrictions must be compatible with these

requirements. The derivation of  $\tilde{G}$  and  $\tilde{G}_n$  that satisfy these requirements renders Eq. (3-20) proper.

There are a number of methodologies by which one may convert Eqs. (3-18) toward Eq. (3-20), notably various iteration techniques. Examples would include the Born and other similar approximation schemes, variational approximations, and finite element techniques and their offspring. Here, however, a specific methodology is employed in which the structure is idealized in a manner that permits an easy conversion from Eq. (3-18) toward Eq. (3-20), notwithstanding that less restrictive conversions than the one here described can be analogously performed with reasonable payment in complications. However, pursuit of such extensions are deemed to be beyond the scope of the present investigation and are not, therefore, discussed herein.

Returning to Eq. (3-18) and remembering that  $\tilde{Z}_\infty(x, \omega_2)$  and  $\tilde{Z}_{\infty n}(x, \omega)$  are by definition uniform in the  $x$ -domain, it follows that

$$\tilde{G}_\infty(x|x', \omega_2) \rightarrow (2\pi)^{-1/2} G_\infty(x-x', \omega_2) , \quad (3-21a)$$

$$\tilde{G}_{\infty n}(x|x', \omega) \rightarrow (2\pi)^{-1/2} G_{\infty n}(x-x', \omega) , \quad (3-21b)$$

and hence by Fourier transformations with respect to  $(x)$  and  $(x')$  one obtains

$$G_\infty(k|k', \omega_2) \rightarrow G_\infty(k, \omega_2) \delta(k-k') , \quad (3-22a)$$

$$G_{\infty n}(k|k', \omega) \rightarrow G_{\infty n}(k, \omega) \delta(k-k') . \quad (3-22b)$$

[cf. Appendix A in which the analogous Fourier transformation from the  $t$ -domain to the  $\omega$ -domain is discussed.] The uniformity of the shell in the  $x$ -domain renders  $\tilde{Z}_\infty(x, \underline{\omega}_2)$  and  $\tilde{Z}_{\infty n}(x, \omega)$  eigenoperators with respect to the Fourier eigenfunction  $(2\pi)^{-1/2} \exp(-ixk)$  in that domain; namely

$$\{\tilde{Z}_\infty(x, \underline{\omega}_2) = Z_\infty(k, \underline{\omega}_2)\} (2\pi)^{-1/2} \exp(-ixk) , \quad (3-23a)$$

$$\{\tilde{Z}_{\infty n}(x, \omega) = Z_{\infty n}(k, \omega)\} (2\pi)^{-1/2} \exp(-ixk) . \quad (3-23b)$$

[cf. Eq. (3-13a).] From Eqs. (3-16), (3-18), (3-22) and (3-23) one may identify

$$G_\infty(k, \underline{\omega}_2) = [Z_\infty(k, \underline{\omega}_2)]^{-1} , \quad (3-24a)$$

$$G_{\infty n}(k, \omega) = [Z_{\infty n}(k, \omega)]^{-1} . \quad (3-24b)$$

Using Eqs. (3-21) and (3-23) and performing a Fourier transformation of Eq. (3-18) with respect to the  $x$ -domain yields

$$V(k, \underline{\omega}_2) = G_\infty(k, \underline{\omega}_2) [P_e(k, \underline{\omega}_2) - P_s(k, \underline{\omega}_2)] , \quad (3-25a)$$

$$V_n(k, \omega) = G_{\infty n}(k, \omega) [P_{en}(k, \omega) - P_{sn}(k, \omega)] , \quad (3-25b)$$

where typically the conversion of Eq. (3-18) to Eq. (3-25) involves the Fourier transformation convention

$$\tilde{V}(x, \omega_2) = (2\pi)^{-1/2} \int dk V(k, \omega_2) \exp(-ikx);$$

$$\begin{aligned} \tilde{G}_\infty(x|x', \omega_2) = \\ (2\pi)^{-1} \iint dk dk' G_\infty(k|k', \omega_2) \exp[-i(xk - x'k')] , \end{aligned} \quad (3-26a)$$

$$\tilde{V}_n(x, \omega) = (2\pi)^{-1/2} \int dk V_n(k, \omega) \exp(-ikx) ;$$

$$\begin{aligned} \tilde{G}_{\infty n}(x|x', \omega) = \\ (2\pi)^{-1} \int dk dk' G_{\infty n}(k|k', \omega) \exp[-i(xk - x'k')] . \end{aligned} \quad (3-26b)$$

To proceed further it is necessary to define more explicitly the drives  $P_s(k, \omega_2)$  and  $P_{sn}(k, \omega)$  in lieu of the nonuniformities. To this end one assumes that the ribs can be described by nonuniformities in the surface impedance of the shell that are highly localized in the  $x$ -domain. This assumption is expressed in the form

$$\tilde{Z}_s(x, \omega_2) = \sum_j Z_{sj}(\omega_2) \delta(x - x_j) , \quad (3-27a)$$

$$\tilde{Z}_{sn}(x, \omega) = \sum_j Z_{snj}(\omega) \delta(x - x_j) , \quad (3-27b)$$

where  $(x_j)$  is the position, in the  $x$ -domain, of the  $(j)$ th rib and it is assumed that a nonuniformity represents a simple line and ring impedance to the shell,

respectively. A physical entity that befits such a localized nonuniformity is an attached rib. The rib exerts a line and a ring drive on the shell in reaction to the motion of the shell. Such loading of the shell by the ribs is stated in terms of a simple drive; remembering, of course, that in this investigation a priori no higher moments in the drive are to be allowed. A gross simplification is attained by assuming the ribs to be identical, infinite in number, and regularly spaced; namely and respectively

$$Z_{sj}(\omega_2) = Z_s(\omega_2) , \quad (3-28a)$$

$$Z_{snj}(\omega) = Z_{sn}(\omega) , \quad (3-28b)$$

and

$$-\infty < j < \infty ; \quad |x_{j+1} - x_j| = b_j ; \quad b_j = b , \quad (3-29)$$

where ( $b$ ) is the separation distance between adjacent ribs. In this report only regularly ribbed shells, defined by Eqs. (3-28) and (3-29), are investigated. Although this restriction severely limits phenomena that can be investigated, many of interest remain. This report is directed toward investigations relating to these remaining phenomena. Substituting Eqs. (3-27) and (3-28) in Eq. (3-17) yields

$$\tilde{P}_s(x, \omega_2) = Z_s(\omega_2) \sum_j \tilde{V}(x_j, \omega_2) \delta(x - x_j) , \quad (3-30a)$$

$$\tilde{P}_{sn}(x, \omega) = Z_{sn}(\omega) \sum_j \tilde{V}_n(x_j, \omega) \delta(x - x_j) . \quad (3-30b)$$



Casting the responses  $\tilde{V}(x_j, \omega_2)$  and  $\tilde{V}_n(x_j, \omega)$  in terms of their Fourier transforms  $V(k, \omega_2)$  and  $V_n(k, \omega)$ , respectively, and simultaneously transforming Eq. (3-30) into the  $k$ -domain, one obtains

$$P_s(k, \omega_2) = Z(\omega_2) \int dk' V(k', \omega_2) (\kappa_1)^{-1} \sum_j \exp[-x_j(k - k')] , \quad (3-31a)$$

$$P_{sn}(k, \omega) = Z_n(\omega) \int dk' V_n(k', \omega) (\kappa_1)^{-1} \sum_j \exp[-ix_j(k - k')] , \quad (3-31b)$$

where  $(\kappa_1)$  is the wavenumber associated with the separation between adjacent ribs

$$\kappa_1 = (2\pi / b) , \quad (3-32a)$$

and  $(x_j)$  is stated in the form

$$x_j = jb ; \quad x_o = 0 . \quad (3-32b)$$

The imposition that  $(x_o)$  is zero is universally assumed in this report. In Eq. (3-31) the quantities  $Z(\omega_2)$  and  $Z_n(\omega)$  are defined as

$$Z(\omega_2) = Z_s(\omega_2) / b , \quad (3-33a)$$

$$Z_n(\omega) = Z_{sn}(\omega) / b . \quad (3-33b)$$

[cf. Eqs. (3-28) and (3-30).] These quantities are the equivalent mechanical surface impedances of a rib; i.e., the line impedances,  $Z_s(\omega_2)$  and  $Z_{sn}(\omega)$ , respectively, of a rib divided by the separation ( $b$ ) between adjacent ribs. Making use of Poisson's summation formula; namely

$$\sum_j \exp[ix_j(k-k')] = \kappa_1 \sum_j \delta(k+\kappa_j-k') , \quad (3-34)$$

Eq. (3-31) yields

$$P_s(k, \omega_2) = Z(\omega_2) \int dk' V(k', \omega_2) \sum_j \delta(k+\kappa_j-k') , \quad (3-35a)$$

$$P_{sn}(k, \omega) = Z_n(\omega) \int dk' V_n(k', \omega) \sum_j \delta(k+\kappa_j-k') . \quad (3-35b)$$

Assuming that the convergence of Eq. (3-35) is unconditional, the summation and integration may be interchanged to yield

$$P_s(k, \omega_2) = [Z(\omega_2)] S_b(k) V(k, \omega_2) , \quad (3-36a)$$

$$P_{sn}(k, \omega) = [Z_n(\omega)] S_b(k) V_n(k, \omega) , \quad (3-36b)$$

where  $S_b(k)$  is the "separation wavenumber operator" defined by

$$S_b(k) [N(k)] = \sum_j N(k + \kappa_j); \quad \kappa_j = j \kappa_1 ;$$

$$S_b(k) [M(k) N(k)] = \sum_j \{M(k + \kappa_j) N(k + \kappa_j)\}. \quad (3-37a)$$

The separation wavenumber operator  $S_b(k)$  is a "self-aliased" operator in the sense that

$$S_b(k) [M(k) S_b(k) [N(k)]] = S_b(k) [N(k)] S_b(k) [M(k)];$$

$$= \sum_j \{N(k + \kappa_j)\} \sum_r \{M(k + \kappa_r)\}, \quad (3-37b)$$

where  $(r)$  and  $(j)$  are integers, and  $M(k)$  and  $N(k)$  are well behaved functions of  $(k)$ . The desired derivation of  $\tilde{G}(x|x', \omega_2)$  and  $\tilde{G}_n(x|x', \omega)$  as stated in Eq. (3-20) is approaching. However, it may be convenient to first transform this equation from the  $x$ -domain into the  $k$ -domain, now that the procedures of such a transformation are defined and, indeed, the equations to be used are already so transformed.

Performing a Fourier transformation of Eq. (3-20) yields

$$V(k, \omega_2) = \int G(k|k', \omega_2) dk' P_e(k, \omega_2) , \quad (3-38a)$$

$$V_n(k, \omega) = \int G_n(k|k', \omega) dk' P_{en}(k', \omega) . \quad (3-38b)$$

Here the desired derivation of  $\tilde{G}(x|x', \omega_2)$  and  $\tilde{G}_n(x|x', \omega)$  in Eq. (3-20) is understood to be equivalent, in every respect, to the derivation of  $G(k|k', \omega_2)$  and  $G_n(k|k', \omega)$  in Eq. (3-38) and vice versa. In particular, the requirements that  $\tilde{G}$  and  $\tilde{G}_n$  need to satisfy with regard to propriety are equivalently imposed on  $G$  and  $G_n$ , respectively.

Two models are considered. In the first the interactions among the ribs, via the uniform shell, are artificially removed. This model may be dubbed a first order model of a ribbed shell. The formalism of this first order model is introduced briefly, herein, merely to contrast it with the second model in which the ribs are allowed to naturally interact. This second model is dubbed a proper model. In the investigation of the influence on the response of the shell of the interactions of a rib with its neighbors, via the shell, this contrast is a valuable analytical tool. Using Eqs. (3-18) and (3-30), substituting Eq. (3-35) in Eq. (3-25) and multiplying the resulting equations by  $Z_s(\omega_2) G_\infty(k, \omega_2)$  and  $Z_{sn}(\omega) G_{\infty n}(k, \omega)$ , respectively, and performing straightforward algebraic manipulations, one obtains

$$G(k|k', \omega_2) =$$

$$G_{\infty}(k, \omega_2) \left\{ 1 - \left\{ \frac{T(\omega_2)}{I_b(k, \omega_2)} \right\} S_b(k) [Q_{\infty}(k, \omega_2)] \right\} \delta(k - k'), \quad \begin{matrix} (3-39a) \\ (3-40a) \end{matrix}$$

$$G_n(k|k', \omega) =$$

$$G_{\infty n}(k, \omega) \left\{ 1 - \left\{ \frac{T_n(\omega)}{I_{bn}(k, \omega)} \right\} S_b(k) [Q_{\infty n}(k, \omega)] \right\} \delta(k - k'), \quad \begin{matrix} (3-39b) \\ (3-40b) \end{matrix}$$

where

$$\begin{aligned} T(\omega_2) &= \{1 + Z_s(\omega_2) \tilde{G}_{\infty}(x|x, \omega_2)\}^{-1} ; \\ I_b(k, \omega_2) &= \{1 + S_b(k) [Q_{\infty}(k, \omega_2)]\}^{-1} , \end{aligned} \quad (3-41a)$$

$$\begin{aligned} T_n(\omega) &= \{1 + Z_{sn}(\omega) \tilde{G}_{\infty n}(x|x, \omega)\}^{-1} ; \\ I_{bn}(k, \omega) &= \{1 + S_b(k) [Q_{\infty n}(k, \omega)]\}^{-1} . \end{aligned} \quad (3-41b)$$

and the incomplete square brackets preceded by the wavenumber operator  $S_b(k)$  merely indicates that the operation to be performed by  $S_b(k)$  is yet to be completed. The quantities  $Q_{\infty}(k, \omega_2)$  and  $Q_{\infty n}(k, \omega)$  are the ratios of the equivalent mechanical surface impedances  $Z(\omega_2)$  and  $Z_n(\omega)$  of the ribs, stated in Eq. (3-33), and the surface impedances  $Z_{\infty}(k, \omega_2)$  and  $Z_{\infty n}(k, \omega)$  of the

uniform shell, stated in Eq. (3-24), respectively; namely

$$Q_{\infty}(k, \underline{\omega}_2) = Z(\underline{\omega}_2) G_{\infty}(k, \underline{\omega}_2) , \quad (3-42a)$$

$$Q_{\infty n}(k, \omega) = Z_n(\omega) G_{\infty n}(k, \omega) . \quad (3-42b)$$

[cf. Eq. (3-24).] The quantities  $T(\underline{\omega}_2)$  and  $T_n(\omega)$  are the transmission coefficients of free waves across a single rib on the shell in the absence of the other ribs. Again, the first order model which is based on noninteracting ribs, is contrived, notwithstanding that real situations exist in which ribs negligibly interact with each other; e.g., when the uniform shell is highly damped and the distance between adjacent ribs is large. The simplicity of Eqs. (3-39) and (3-40) is striking. Moreover,  $G(k|k', \underline{\omega}_2)$  and  $G_n(k|k', \omega)$  in this equation are proper in the sense that they are neither dependent on  $V(k, \underline{\omega}_2)$  and  $V_n(k, \omega)$  nor on  $P_e(k, \underline{\omega}_2)$  and  $P_{en}(k, \omega)$ , respectively. Indeed, these impulse response functions (operators if strictly worded) are merely functional of the quantities and parameters that describe and specify the uniform shell, the fluid, and the ribs. Consequently, the impulse response functions  $\tilde{G}(x|x', \underline{\omega}_2)$  and  $\tilde{G}_n(x|x', \omega)$  as expressed in Eq. (3-20) are also correspondingly proper if derived by an appropriate Fourier transformation with respect to  $(k)$  and  $(k')$  of  $G(k|k', \underline{\omega}_2)$  and  $G_n(k|k', \omega)$ , as expressed in Eq. (3-26).

In order to establish an interpretive baseline for comparison purposes, the responses of the shell in the absence of nonuniformities are sometimes established as basic quantities. Often these quantities are stored as such in a computer and

are assumed known. These quantities are readily specified in the  $k$ -domain in the form

$$V_{\infty}(k, \underline{\omega}_2) = G_{\infty}(k, \underline{\omega}_2) P_e(k, \underline{\omega}_2) , \quad (3-43a)$$

$$V_{\infty n}(k, \omega) = G_{\infty n}(k, \omega) P_{en}(k, \omega) , \quad (3-43b)$$

as can be verified by setting identically zero the drives  $P_s(k, \underline{\omega}_2)$  and  $P_{sn}(k, \omega)$  in lieu of the nonuniformities in Eq. (3-25). [cf. Eq. (3-19).] The utilization of these responses as basic quantities can be illustrated by substituting Eqs. (3-25) and (3-43) in Eqs. (3-39) and (3-40) to yield

$$V(k, \underline{\omega}_2) = V_{\infty}(k, \underline{\omega}_2) - V_s(k, \underline{\omega}_2) ;$$

$$V_s(k, \underline{\omega}_2) = G_{\infty}(k, \underline{\omega}_2) P_s(k, \underline{\omega}_2) ;$$

$$V(k, \underline{\omega}_2) = G_{\infty}(k, \underline{\omega}_2) [P_e(k, \underline{\omega}_2) - P_s(k, \underline{\omega}_2)] , \quad (3-44a)$$

$$P_s(k, \underline{\omega}_2) = \left\{ \begin{array}{c} T(\underline{\omega}_2) \\ I_b(k, \underline{\omega}_2) \end{array} \right\} P_{os}(k, \underline{\omega}_2) , \quad \begin{array}{l} (3-45a) \\ (3-46a) \end{array}$$

where

$$P_{os}(k, \omega_2) = S_b(k) [Q_\infty(k, \omega_2) P_e(k, \omega_2)] , \quad (3-47a)$$

$$V_n(k, \omega) = V_{\infty n}(k, \omega) - V_{sn}(k, \omega) ;$$

$$V_{sn}(k, \omega) = G_{\infty n}(k, \omega) P_{sn}(k, \omega) ;$$

$$V_n(k, \omega) = G_{\infty n}(k, \omega) [P_{en}(k, \omega) - P_{sn}(k, \omega)] , \quad (3-44b)$$

$$P_{sn}(k, \omega) = \begin{Bmatrix} T_n(\omega) \\ I_{bn}(k, \omega) \end{Bmatrix} P_{osn}(k, \omega) , \quad \begin{matrix} (3-45b) \\ (3-46b) \end{matrix}$$

where

$$P_{osn}(k, \omega) = S_b(k) [Q_{\infty n}(k, \omega) P_{en}(k, \omega)] . \quad (3-47b)$$

Since  $T(\omega_2)$  and  $T_n(\omega)$  are independent of  $(k)$ , and  $I_b(k, \omega_2)$  and  $I_{bn}(k, \omega)$  are aliased in the  $k$ -domain with respect to the separation wavenumber  $(\kappa_1)$ , it follows that  $P_s(k, \omega_2)$  and  $P_{sn}(k, \omega)$ , respectively, are aliased quantities in that domain; both in the first and proper order models; namely

$$P_s(k, \omega_2) = P_s(k + \kappa_j, \omega_2) , \quad (3-48a)$$

$$P_{sn}(k, \omega) = P_{sn}(k + \kappa_j, \omega) . \quad (3-48b)$$



The "phenomenon of aliasing" in the response of a regularly ribbed shell is directly related to the aliasing in  $P_s(k, \omega_2)$  and  $P_{sn}(k, \omega)$ . However, before the phenomenon of aliasing can be deciphered in these quantities, or for that matter, in the response  $V(k, \omega_2)$  and  $V_n(k, \omega)$  of the shell, it is necessary to define more explicitly the external drive  $P_e(k, \omega_2)$  and  $P_{en}(k, \omega)$ , the mechanical surface impedance  $Z_p(k, \omega_2)$  and  $Z_{pn}(k, \omega)$  of the uniform shell, the fluid surface impedance  $Z_f(k, \omega_2)$  and  $Z_{fn}(k, \omega)$  [or  $Z_n^f(k, \omega)$ ], and hence the surface impedance  $Z_\infty(k, \omega_2)$  and  $Z_{\infty n}(k, \omega)$  of the fluid loaded uniform shell, and finally the line and ring impedance  $Z(\omega_2)$  and  $Z_n(\omega)$  of the ribs. Then one can derive the explicit form of the drive  $P_s(k, \omega_2)$  and  $P_{sn}(k, \omega)$  in lieu of the ribs, as expressed in Eqs. (3-45) and (3-46), and hence the response  $V(k, \omega_2)$  and  $V_n(k, \omega)$  as expressed in Eq. (3-44).

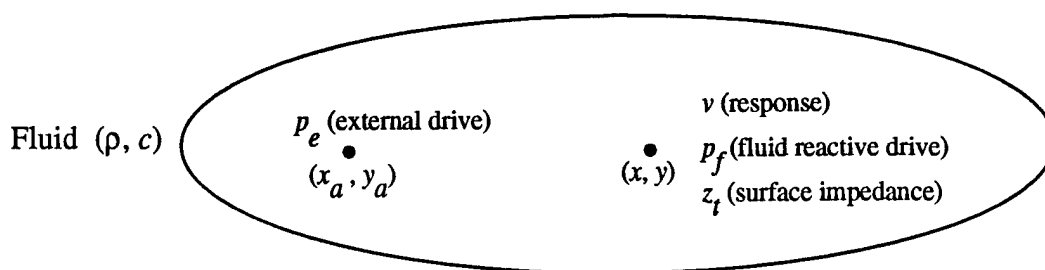


Fig. 3-1. Sketch of a Generalized Shell and some of the quantities involved in its equation of motion.

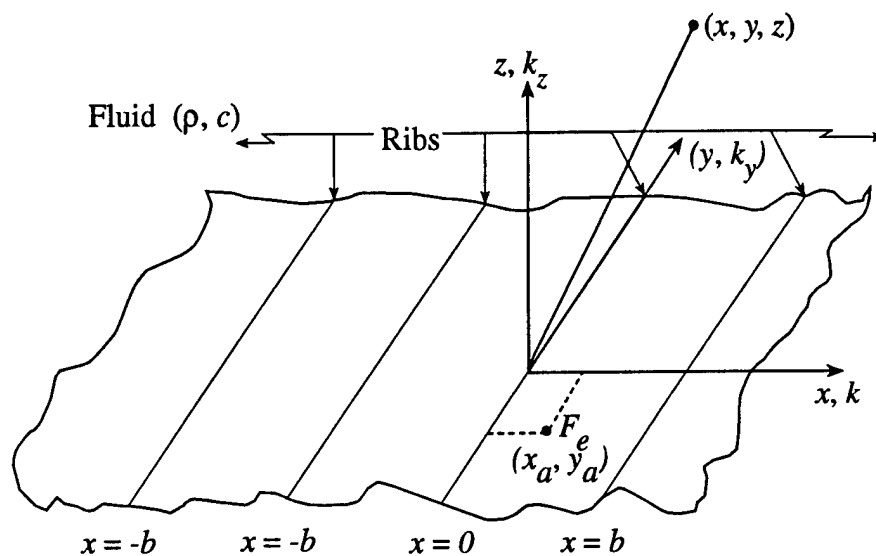


Fig. 3-2. Sketch of a ribbed panel and coordinate system.

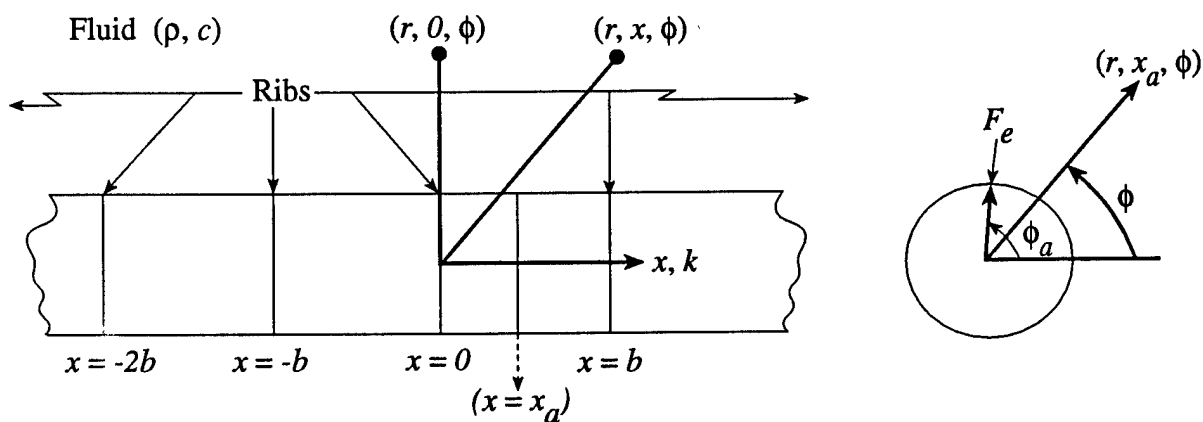


Fig. 3-3. Sketch of a ribbed cylinder and coordinate system.

#### IV. A SHELL WITH A FINITE NUMBER OF RIBS

Situations arise in which the assumption of regularly ribbed shells may be too drastic an assumption. Moreover, the assumption of regularity may deprive the formalism of some of its versatility. For example, if the shell is regularly ribbed, the influence of changing the regularity of the spacings between adjacent ribs and/or the identity of the line impedances of the ribs can no longer be examined. Such examination may, however, be desirable. Also, it may be desirable to investigate the influence of bulkheads on the behavior of the response. In this situation the bulkheads are ribs of line impedances that are substantially different from those of the "ordinary" ribs and the distances between adjacent bulkheads may not only be different from those between ordinary ribs but may be different for different pairs of adjacent bulkheads. Many other variations on those themes are possible in which the regularity of the ribs is not befitting. Again, the a priori imposition that the shell is regularly ribbed scuttles the possibility of accounting for these and similar kinds of variations. Under certain conditions a formalism for a finite number of ribs with regular or non-regular spacings can be made. In this formalism the line impedance and the position of each rib is individually accounted for. The finiteness is a prerequisite, otherwise the formalism becomes unwieldy and cumbersome. Although in this report only the regularly ribbed shell is computationally considered, for the sake of completeness and for future reference, the formalism for a finite number of ribs, in which each rib is individually accounted for, is briefly stated below.

The formalism in this section relies on steps developed in the preceding section up to the imposition of regularity in Eqs. (3-28) and (3-29). In the absence of regularity instead of Eq. (3-30) one derives

$$\tilde{P}_s(x, \omega_2) = \sum_j Z_{sj}(\omega_2) \tilde{V}(x_j, \omega_2) \delta(x - x_j) , \quad (4-1a)$$

$$\tilde{P}_{sn}(x, \omega) = \sum_j Z_{snj}(\omega) \tilde{V}_n(x_j, \omega) \delta(x - x_j) , \quad (4-1b)$$

for the drive in lieu of the ribs. Substituting Eq. (4-1) in Eq. (3-18) and making use of Eq. (3-19) one derives

$$\begin{aligned} \tilde{V}(x, \omega_2) = \\ \tilde{V}_\infty(x, \omega_2) - \sum_j \tilde{G}_\infty(x | x_j, \omega_2) Z_{sj}(\omega_2) \tilde{V}(x_j, \omega_2) , \end{aligned} \quad (4-2a)$$

$$\begin{aligned} \tilde{V}_n(x, \omega) = \\ \tilde{V}_{\infty n}(x, \omega) - \sum_j \tilde{G}_{\infty n}(x | x_j, \omega) Z_{snj}(\omega) \tilde{V}_n(x_j, \omega) . \end{aligned} \quad (4-2b)$$

The dependence of Eqs. (4-2a) and (4-2b) on the spectral variables  $(\omega_2)$  and  $(\omega)$  respectively, is obvious and, therefore, without loss in meaning they can be suppressed for convenience; namely, Eqs. (4-2a) and (4-2b) can be abbreviated in the form

$$\tilde{V}(x) = \tilde{V}_\infty(x) - \sum_j \tilde{G}_\infty(x | x_j) Z_{sj} \tilde{V}(x_j) , \quad (4-2c)$$

$$\tilde{V}_n(x) = \tilde{V}_{\infty n}(x) - \sum_j \tilde{G}_{\infty n}(x | x_j) Z_{snj} \tilde{V}_n(x_j) . \quad (4-2d)$$

From Eqs. (4-2c) and (4-2d) one may construct the following matrix equation:

$$\begin{aligned} \underline{B}(\underline{T})^{-1} \underline{\tilde{V}} &= \underline{\tilde{V}}_{\infty} ; & \underline{\tilde{V}} &= \{\tilde{V}(x_j)\} ; & \underline{\tilde{V}}_{\infty} &= \{\tilde{V}_{\infty}(x_j)\} ; \\ \underline{B} &= (\delta_{ji} + \tilde{G}_{\infty}(x_j | x_i) Z_{si} T_i (1 - \delta_{ji})) ; & \underline{T} &= (T_j \delta_{ji}) ; \\ T_j &= [1 + \tilde{G}_{\infty}(x_j | x_j) Z_{sj}]^{-1} , \end{aligned} \quad (4-3a)$$

$$\begin{aligned} \underline{B}_n(\underline{T}_n)^{-1} \underline{\tilde{V}}_n &= \underline{\tilde{V}}_{\infty n} ; & \underline{\tilde{V}}_n &= \{\tilde{V}_n(x_j)\} ; & \underline{\tilde{V}}_{\infty n} &= \{\tilde{V}_{\infty n}(x_j)\} ; \\ \underline{B}_n &= (\delta_{ji} + \tilde{G}_{\infty n}(x_j | x_i) Z_{sni} T_{ni} (1 - \delta_{ji})) ; & \underline{T}_n &= (T_{nj} \delta_{ji}) ; \\ T_{nj} &= [1 + \tilde{G}_{\infty n}(x_j | x_j) Z_{snj}]^{-1} . \end{aligned} \quad (4-3b)$$

Inverting the first expression in Eqs. (4-3a) and (4-3b) one derives

$$\underline{\tilde{V}} = \underline{T} \underline{C} \underline{\tilde{V}}_{\infty} , \quad (4-4a)$$

$$\underline{\tilde{V}}_n = \underline{T}_n \underline{C}_n \underline{\tilde{V}}_{\infty n} , \quad (4-4b)$$

where the matrices  $\underline{C}$  and  $\underline{C}_n$  are defined

$$\underline{C} = (C_{ji}) = (\underline{B})^{-1} ; \quad \underline{C}_n = (C_{nji}) = (\underline{B}_n)^{-1} . \quad (4-5)$$

From Eqs. (4-2) and (4-4) one obtains

$$\tilde{V}(x) = \tilde{V}_\infty(x) - \sum_j \sum_i G_\infty(x | x_j) Z_{sj} T_j C_{ji} \tilde{V}_\infty(x_i), \quad (4-6a)$$

$$\tilde{V}_n(x) = \tilde{V}_{\infty n}(x) - \sum_j \sum_i \tilde{G}_{\infty n}(x | x_j) Z_{snj} T_{nj} C_{nji} \tilde{V}_{\infty n}(x_i). \quad (4-6b)$$

From Eq. (4-6), and using Eq. (3-19), one obtains by inspection

$$\begin{aligned} \tilde{G}(x | x') &= \tilde{G}_\infty(x | x') - \\ &\sum_j \sum_i \tilde{G}_\infty(x | x_j) Z_{sj} T_j C_{ji} \tilde{G}_\infty(x_i | x'), \end{aligned} \quad (4-7a)$$

$$\begin{aligned} \tilde{G}_n(x | x') &= \tilde{G}_{\infty n}(x | x') - \\ &\sum_j \sum_i \tilde{G}_{\infty n}(x | x_j) Z_{snj} T_{nj} C_{nji} \tilde{G}_{\infty n}(x_i | x'). \end{aligned} \quad (4-7b)$$

In the non-abbreviated form, Eq. (4-7) assumes the form

$$\begin{aligned} \tilde{G}(x | x', \underline{\omega}_2) &= \tilde{G}_\infty(x | x', \underline{\omega}_2) - \\ &\sum_j \sum_i \tilde{G}_\infty(x | x_j, \underline{\omega}_2) Z_{sj}(\underline{\omega}_2) T_j(\underline{\omega}_2) C_{ji}(\underline{\omega}_2) \tilde{G}_\infty(x_i | x', \underline{\omega}_2), \end{aligned} \quad (4-7c)$$

$$\begin{aligned} \tilde{G}_n(x | x', \omega) &= \tilde{G}_{\infty n}(x | x', \omega) - \\ &\sum_j \sum_i \tilde{G}_{\infty n}(x | x_j, \omega) Z_{snj}(\omega) T_{nj}(\omega) C_{nji}(\omega) \tilde{G}_{\infty n}(x_i | x', \omega), \end{aligned} \quad (4-7d)$$

and by definition

$$\tilde{V}(x, \underline{\omega}_2) = \int \tilde{G}(x|x', \underline{\omega}_2) dx' \tilde{P}_e(x', \underline{\omega}_2) , \quad (4-8a)$$

$$\tilde{V}_n(x, \omega) = \int \tilde{G}_n(x|x', \omega) dx' \tilde{P}_{en}(x', \omega) . \quad (4-8b)$$

[cf. Eq. (3-20).] Making use of Eq. (3-26), and casting Eq. (4-8) in the format of Eq. (3-31), one finds that

$$P_s(k, \underline{\omega}_2) = \sum_j \sum_i (\kappa_1)^{-1} T_j(\underline{\omega}_2) C_{ji}(\underline{\omega}_2) \exp(ix_j k) \int dk' Q_{\infty j}(k', \underline{\omega}_2) \exp(-ix_i k') P_e(k', \underline{\omega}_2) , \quad (4-9a)$$

$$P_{sn}(k, \omega) = \sum_j \sum_i (\kappa_1)^{-1} T_{nj}(\omega) C_{nji}(\omega) \exp(ix_j k) \int dk' Q_{\infty j}(k', \omega) \exp(-ix_i k') P_{en}(k', \omega) , \quad (4-9b)$$

where

$$Q_{\infty j}(k', \underline{\omega}_2) = [Z_{sj}(\underline{\omega}_2)/b] G_{\infty}(k, \underline{\omega}_2) , \quad (4-10a)$$

$$Q_{\infty nj}(k', \omega) = [Z_{snj}(\omega)/b] G_{\infty n}(k, \omega) . \quad (4-10b)$$

[cf. Eqs. (3-44) - (3-47) and (3-42).] Clearly, if the ribs are regularly spaced so that  $x_j = jb$ , the drive  $P_s(k, \underline{\omega}_2)$  and  $P_{sn}(k, \omega)$  is "aliased in  $(k)$  with respect to  $(\kappa_1)$ ," as defined in Eq. (3-48). Thus, the aliasing of the drive in lieu of the ribs is not predicated on the equality of the line impedances and/or the number of the

attached ribs. It is merely and solely dependent on the regularity of the spacing between the ribs. On the other hand, to reconcile Eq. (4-9) with Eq. (3-46) it must follow that

$$\begin{aligned} \sum_j \sum_i (\kappa_1)^{-1} T_j(\omega_2) C_{ji}(\omega_2) \exp[i(x_j k - x_i k')] \Big|_{-\infty}^{+\infty} \\ \rightarrow I_b(k, \omega_2) S_b(k) [\delta(k - k') , \end{aligned} \quad (4-11a)$$

$$\begin{aligned} \sum_j \sum_i (\kappa_1)^{-1} T_{nj}(\omega) C_{nji}(\omega) \exp[i(x_j k - x_i k')] \Big|_{-\infty}^{+\infty} \\ \rightarrow I_{bn}(k, \omega) S_b(k) [\delta(k - k') , \end{aligned} \quad (4-11b)$$

where the infinities indicate that the shell is regularly ribbed as specified in Eqs. (3-28) and (3-29). Equations (4-9) and (4-11) enable one to define an artificial, but a useful, first order model in which the interactions among the ribs via the shell are suppressed. In this case the left side of Eq. (4-11) can be readily evaluated since the coupling matrix between ribs is rendered the unit matrix. Substituting the equalities

$$C_{ji}(\omega_2) = \delta_{ji} ; \quad C_{nji}(\omega_2) = \delta_{ji} , \quad (4-12)$$



in Eq. (4-11) one obtains

$$\begin{aligned} \sum_j (\kappa_1)^{-1} T(\underline{\omega}_2) \exp[ix_j(k-k')] \Big|_{-\infty}^{+\infty} \\ \rightarrow T(\underline{\omega}_2) S_b(k) \delta(k-k') \text{ if } T_j(\underline{\omega}_2) = T(\underline{\omega}_2) , \end{aligned} \quad (4-13a)$$

$$\begin{aligned} \sum_j (\kappa_1)^{-1} T_n(\omega) \exp[ix_j(k-k')] \Big|_{-\infty}^{+\infty} \\ \rightarrow T_n(\omega) S_b(k) [\delta(k-k')] \text{ if } T_{nj}(\omega) = T_n(\omega) . \end{aligned} \quad (4-13b)$$

Equations (4-12) and (4-13) define the first order model. Substitution of these equations in Eq. (4-9) derives  $P_s(k, \underline{\omega}_2)$  and  $P_{sn}(k, \omega)$  that are commensurate with those of the first order model, as specified in Eq. (3-45).

An observation is made: Whereas evaluations for the proper regularly ribbed shell require the functional form of the surface admittance  $G_\infty(k, \underline{\omega}_2)$  and  $G_{\infty n}(k, \omega)$ , similar evaluations for the finite and the first order model require, in addition, the determination of  $\{C_{ji}(\underline{\omega}_2), T_j(\underline{\omega}_2)\}$  and  $\{C_{nji}(\omega), T_{nj}(\omega)\}$ . In this latter determination the functional form of  $\tilde{G}_\infty(x|x', \omega)$  and  $\tilde{G}_{\infty n}(x|x', \omega)$  is needed. The inclusion of fluid loading in  $G_\infty(k, \underline{\omega}_2)$  and  $G_{\infty n}(k, \omega)$  is straightforward; however, in  $\tilde{G}_\infty(x|x', \omega)$  and  $\tilde{G}_{\infty n}(x|x', \omega)$  it is not. Therefore, often in the formalism of Eqs. (4-7) and (4-13), the fluid loading is neglected, at least initially. This neglect may contribute to subsequent interpretive difficulties unless the influence of these initial assumptions are understood in subsequent manipulations of the formalism. Another observation of note is that the summations involved in Eq. (4-7) are over ribs (and bulkheads) whereas in Eq. (3-34) or those involving the operator  $S_b(k)$ , the summations are over

harmonics of the separation wavenumber ( $\kappa_1$ ). The latter are infinite summations while the former, if the number of ribs is finite, are finite summations and the summations are over the ribs.

## V. AN EXTERNAL DRIVE

To investigate the response  $\tilde{V}(x, \omega_2)$  and  $\tilde{V}_n(x, \omega)$  or equivalently  $V(k, \omega_2)$  and  $V_n(k, \omega)$ , and for that matter to investigate the drives in lieu of the ribs  $\tilde{P}_s(x, \omega_2)$  and  $\tilde{P}_{sn}(x, \omega)$  or equivalently  $P_s(k, \omega_2)$  and  $P_{sn}(k, \omega)$ , it becomes necessary to specify the external drive  $p_e(x, y, \omega)$  and  $p_e(x, \phi, \omega)$  either in terms of  $P_e(x, \omega_2)$  and  $\tilde{P}_{en}(x, \omega)$  or, equivalently,  $P_e(k, \omega_2)$  and  $P_{en}(k, \omega)$ , respectively. This specification needs to be compatible with the form of the impulse response function just formulated. In this investigation the external drive is specified to be a point mechanical drive. For the panel this drive may be defined

$$p_e(x, y, \omega) = F_e(\omega) \delta(x - x_a) \delta(y - y_a); \quad \underline{x}_a = \{x_a, y_a\}, \quad (5-1a)$$

$$P_e(k, \omega_2) = F_e(\omega) (2\pi)^{-1} \exp(i \underline{x}_a \underline{k}); \quad \underline{k} = \{k_x, k_y\}, \quad (5-2a)$$

and for the cylinder this drive may be defined

$$p_e(x, \phi, \omega) = F_e(\omega) \delta(x - x_a) \delta[(a(\phi - \phi_a))]; \quad 0 \leq \phi < (2\pi), \quad (5-1b)$$

$$P_e(k, \phi, \omega) = [F_e(\omega)/(2\pi a)] (2\pi)^{-1/2} \exp(ix_a k) \sum_n \exp[-in(\phi - \phi_a)], \quad (5-2b)$$

where  $\underline{x}_a = \{x_a, y_a\}$  and  $\{x_a, (a\phi_a)\}$  are the position vector of application on the panel and the cylinder, respectively, and  $F_e(\omega)$  is the point force strength. In

deriving Eqs. (5-1b) and (5-2b) use is made of Poisson's summation formula; namely

$$\delta(\phi - \phi_a) = (2\pi)^{-1} \sum_n \exp(-in(\phi - \phi_a)) ; \quad 0 \leq \phi < 2\pi . \quad (5-3)$$

[cf. Eq. (3-34).] Situations arise in which it is convenient to cast the external drive on a panel in terms of a line drive. The point drive can be expanded in terms of line drives in the form

$$p_e(x, y, \omega) = (2\pi)^{-1/2} \int dk_y \tilde{P}_e(x, \omega_2) \exp(-iyk_y) . \quad (5-4)$$

To relate the point and line drives one may identify

$$\begin{aligned} \tilde{P}_e(x, \omega_2) &= P_{ea}(\omega_2) \delta(x - x_a) ; \\ P_{ea}(\omega_2) &= F_e(\omega) (2\pi)^{-1/2} \exp(iy_a k_y) , \end{aligned} \quad (5-5)$$

so that

$$P_e(k, \omega_2) = P_{ea}(\omega_2) (2\pi)^{-1/2} \exp(ix_a k) , \quad (5-6)$$

where  $P_{ea}(\omega_2)$  is a partial external line drive that lies in the  $y$ -domain and is applied at the position  $(x_a)$  in the  $x$ -domain. [cf. Fig. 3-2.] When the influence of ribs is of concern, the external partial line drives are useful in the sense that they are more compatible with the drives that are generated by the ribs; these drives constitute the loading of the panel by the ribs. This compatibility is of

considerable analytical significance. With respect to the cylindrical shell, identifying the modal function as a Fourier series function

$$\psi_n(y) = (2\pi)^{-1/2} \exp(-in\phi) \text{ and replacing } \int dy \text{ by } \sum_n, \quad (5-7)$$

one may then cast the external drive on a cylinder in the modal ring form

$$P_e(k, \phi, \omega) = \sum_n P_{en}(k, \omega) [(2\pi)^{-1/2} \exp(-in\phi)] ;$$

$$P_{en}(k, \omega) = [F_e(\omega)/(2\pi a)] \exp[i(x_a k + n\phi_a)] . \quad (5-8)$$

In summary then, the partial and modal external mechanical drives on a panel and on a cylinder are defined in the form

$$P_e(k, \omega_2) = P_{ea}(\omega_2) (2\pi)^{-1/2} \exp(ix_a k) , \quad (5-9a)$$

$$P_{en}(k, \omega) = P_{ean}(\omega) (2\pi)^{-1/2} \exp(ix_a k) , \quad (5-9b)$$

respectively, where

$$P_{ea}(k, \omega) = [F_e(\omega) (2\pi)^{-1/2}] \exp(iy_a k_y) , \quad (5-10a)$$

$$P_{ean}(k, \omega) = [(F_e(\omega)/a) (2\pi)^{-1/2}] \exp(in\phi_a) . \quad (5-10b)$$

The external mechanical drives stated in Eq. (5-9) are compatible with the forms of the impulse response function  $G(k|k', \omega_2)$  and  $G_n(k|k', \omega)$  and the drive in

lieu of the ribs  $P_s(k, \omega_2)$  and  $P_{sn}(k, \omega)$  as stated in Eqs. (3-39), (3-40) and (3-44) through (3-47), respectively.

## VI. MECHANICAL SURFACE IMPEDANCES OF SHELLS

A large number of publications exist to reflect the many attempts made to derive the expressions for the mechanical surface impedance  $z_p(x,y,\omega)$  of shells, where  $\{x,y\}$  defines a generalized two-dimensional spatial vector and  $(\omega)$  is the frequency variable. The mechanical surface impedance of the shell is basic to the determination of its response. These attempts cover not only the analytical description of the mechanical surface impedance of plane shells, but also cylindrical, spherical, spheroidal, and shells involving others types of curved surfaces. Naturally many of the derived expressions for each type of a shell exhibit, on the one hand, strong commonalities and, on the other, many and varied differences. The commonalities and differences must be judged with respect to their influence on phenomena of interest; commonality in one phenomenon may turn into a difference in another. For example, in the absence of ribs two derived expressions for the mechanical surface impedance may predict the same far-field radiation from a shell. The commonality in the expressions stems, in this case, from the fact that in the range of large scale spatial components the two expressions yield the same response. The large scale spatial components in the response are those that contribute directly to the far-field radiation. When ribs are attached, the prediction of the far-field radiation by the use of the two expressions for the surface impedance of the shell may be substantially different. In the presence of ribs, conversions of small scale spatial components in the response, into large scale spatial components, take place. Thus, if the description in the range of small scale spatial components in the response does not match in the two expressions, different far-field radiation may result and the commonality of the two expressions no longer holds. Another major problem that arises in the derivation of the expressions for the mechanical surface impedance of shells is that often the

expressions are deficient in the description of the various types of propagating (free) waves that a shell may support. With each wave type is identified free waves; the flexural wave type is identified by the flexural free waves. Of particular concern in connection with the presence of several wave types on the surface of a shell is the coupling among these types and the manner by which they are externally driven. For example, in panels it is usual to describe the flexural wave type only and to ignore other wave types; e.g., longitudinal and shear wave types. Situations may arise in which such a neglect may prevent a proper accounting of several important phenomena. One only needs to remember that longitudinal and shear free waves are supersonic even below the critical frequency, whereas in that frequency range, the flexural free waves are subsonic. Thus, in the frequency range below the critical frequency the longitudinal and shear free waves are superior radiation components compared with the flexural free waves. Attempts to be more comprehensive, in the description of the mechanical surface impedance of a panel, are needed, so that longitudinal and shear effects can be included. Indeed, failure to do so has, at times, caused mishaps and led to wrong phenomenological conclusions. In the case of the cylinder it has been recognized that the expression for the mechanical surface impedance is invariably compounded in the sense that in addition to the flexural wave type it naturally involves terms and factors that describe membrane wave types. The membrane wave types comprise the longitudinal and shear wave types as well as the curvature wave type. The curvature wave type and the associated curvature free waves are found in the low frequency range only and they are associated with the speeding of flexural free waves by the curvature (flexural Bloch waves). Curvature free waves commence as the frequency decreases from an octave or so above the ring frequency. Interestingly, the largely accepted expression for the mechanical surface impedance of a cylinder



accommodates the flexural wave type as a term. A second term accounts, in unison, for the longitudinal and shear wave types and for the curvature (flexural Bloch) wave type. The scope of the investigation in this report does not include the goal of seeking and providing an ultimate expression for the mechanical surface admittance of a panel and a cylinder as such. Therefore, the most accepted expressions are readily adopted. At best, they are modified in form to suite more readily the purposes and goals of this report.

The normalized mechanical surface impedance  $\bar{Z}_p(k, \omega_2)$  of a panel that is plate like is expressed in spectral space as

$$\bar{Z}_p(k, \omega_2) = [Z_p(k, \omega_2)/(i\omega m)] = \{1 - [(k/k_{px})^2 + (k_y/k_{py})^2]^2\}, \quad (6-1a)$$

and further, if the plate is isotropic

$$\bar{Z}_p(k, \omega_2) = [Z_p(k, \omega_2)/(i\omega m)] = \{1 - (|\underline{k}|/k_p)^4\};$$

$$\bar{G}_p(k, \omega_2) = [\bar{Z}_p(k, \omega_2)]^{-1}; \quad \underline{k} = \{k, k_y\}, \quad (6-1b)$$

where the free wavenumbers  $(k_{px})$  and  $(k_{py})$  are defined as

$$k_{px} = k_{pxo}(1 - i\eta_{px}); \quad k_{py} = k_{pyo}(1 - i\eta_{py});$$

$$k_{pxo}^2 = (\omega \omega_{cx} / c^2); \quad k_{pyo}^2 = (\omega \omega_{cy} / c^2), \quad (6-2)$$

and isotropy of the panel is defined in the form

$$\begin{aligned} \omega_c &= \omega_{cx} = \omega_{cy} ; \quad k_{po} = k_{pxo} = k_{pyo} ; \quad k_{po} = \omega / c_p ; \\ c_p &= c(\omega / \omega_c)^{1/2} ; \quad \eta_p = \eta_{px} = \eta_{py} , \end{aligned} \quad (6-3)$$

where the parameter ( $m$ ) is the surface mass of the thin plate, ( $\omega_{cx}$ ) and ( $\omega_{cy}$ ) are, respectively, the critical frequencies, with respect to a wavespeed ( $c$ ), for propagations in the ( $x$ ) and ( $y$ ) principal axes and ( $\eta_{px}$ ) and ( $\eta_{py}$ ) are, respectively, the loss factors associated with these propagations. [cf. Fig. 3-3.] In this report only isotropic panels are considered. The critical frequency, as Eqs. (6-2) and (6-3) state, is the frequency at which the wavespeed ( $c$ ) is equal to the speed ( $c_p$ ) of the free waves in the panel. The response of a panel in flexure is the only type of motion considered herein. Again, consideration of other types of response in a panel lie outside the scope of this investigation. The magnitude of the normalized mechanical surface admittance  $\overline{G}_p(k, \omega_2)$  is displayed in Fig. 6-1 as a function of ( $ak$ ) in a frequency waterfall format; this format is discussed in Appendix B. The standard parametric values are chosen to be

$$(a\omega_c / c) = (ak_c) = 97.35 , \quad \eta_p = 10^{-3} \quad \text{and} \quad (ak_y) = 0, \quad (6-4a)$$

where ( $a$ ) is a spatial scale factor and ( $k_c$ ) is the wavenumber with respect to the critical frequency ( $\omega_c$ ) and the wavespeed ( $c$ );  $k_c = (\omega_c / c)$ . Standard parametric values are defined so that in the captions of figures only the specific changes in these values need to be reported. In Fig. 6-1a the surface admittance  $\overline{G}_p(k, \omega_2)$  is displayed as a function of ( $ak$ ) under the standard parametric values stated in Eq. (6-4a). A standard spectral  $\{(ak), (\omega / \omega_c)\}$  range is conveniently

assigned to accommodate the standard parametric values within the investigative scope of the report. This standard spectral range is defined by

$$\{0, 10^{-2}\} \leq \{(ak), (\omega/\omega_c)\} < \{75, 0.6\} . \quad (6-4b)$$

In Figs. 6-1b-e the value of  $(ak_y)$  is changed from its standard value of zero to 1, 3, 9 and 21, respectively. The ridges and the associated dispersive peaks of the flexural free waves are clearly discernible; the peaks lie on the "dispersive locus" of the flexural free waves. The affects of changes in  $(ak_y)$  are as expected and they are noted: As the value of  $(ak_y)$  increases, the dispersive locus is swallowed at  $(ak) = 0$  at the lower frequency range, where  $(\omega/\omega_c) < (k_y/k_c)^2$ , and is thus suppressed. Otherwise, the dispersive locus is incrementally shifted to lower wavenumbers and the shift is less pronounced the more the inequality  $(\omega/\omega_c) > (k_y/k_c)^2$  is. To accentuate the parametric dependences, a curve or two among the waterfall graphs are compared in isolation. In this type of comparison two curves out of each of Figs. 6-1a-e are collectively cast in Figs. 6-1e1 and 2. Only when  $(ak_y) \geq 9$ , does a significant difference exist between these curves and the difference is most significant in the lower frequency range. Figure 6-1a is repeated in Figs. 6-2a and b except that the value of the loss factor  $(\eta_p)$  is increased from its standard value of  $10^{-3}$  to  $5 \times 10^{-3}$  and  $2.5 \times 10^{-2}$ , respectively. Compared with Fig. 6-1 the ridges are widened and the peaks are subdued by these changes. One curve out of each of Figs. 6-1a, 2a and 2b are collectively cast in Fig. 6-2b1. Figures 6-1e1 and 2 and 6-2b1 show that selecting a few trees for comparison, rather than a few forests, may be advantageous when details are sought. For the purpose of this report it suffices to indicate that such computational and graphical capabilities are available; these capabilities, however, are not extensively used herein.

The normalized mechanical surface impedance  $\bar{Z}_{pn}(k, \omega)$  of a cylinder is also expressed in spectral space. It comprises a flexural term  $\bar{Z}_n^p(k, \omega)$  and a membrane term  $\bar{Z}_n^m(k, \omega)$  and is expressed in the form

$$\bar{Z}_{pn}(k, \omega) = (i\omega m)^{-1} Z_{pn}(k, \omega) = \bar{Z}_n^p(k, \omega) + \bar{Z}_n^m(k, \omega), \quad (6-5)$$

$$\bar{Z}_n^p(k, \omega) = (i\omega m)^{-1} Z_n^p(k, \omega) = \bar{Z}_p(k, (n/a), \omega), \quad (6-6a)$$

$$\begin{aligned} \bar{Z}_n^m(k, \omega) &= (i\omega m)^{-1} Z_n^m(k, \omega) \\ &= \{[(1-\nu/2)^2 (nak)^2 (1+i\eta_s) (1+i\eta_{bn}) - R_s R_{bn}] [(ak_l)^2 R_{ln} R_{sn}]^{-1}\}, \quad (6-6b) \end{aligned}$$

where

$$\begin{aligned} R_{ln} &= (ak_l)^2 - [(ak)^2 + n^2] (1+i\eta_{ln}); \\ R_{sn} &= (ak_l)^2 - [(1-\nu)/2] \{(ak)^2 + n^2\} (1+i\eta_{sn}); \\ R_s &= (ak_l)^2 - [(1-\nu)/2] (ak)^2 (1+i\eta_s); \\ R_{bn} &= (ak_l)^2 - [(1-\nu^2) (ak)^2 + \{(1-\nu)/2\} n^2] (1+i\eta_{bn}), \quad (6-7a) \end{aligned}$$

and

$$\begin{aligned} (ak_l)^2 &= (\omega/\omega_r)^2; \quad \omega_r = (c_l/a); \\ c_l^2 &= Yh [m(1-\nu^2)]^{-1}; \quad c_s^2/c_l^2 = \{(1-\nu)/2\}. \quad (6-7b) \end{aligned}$$

The loss factors ( $\eta_\gamma$ );  $\eta_\gamma = \eta_{ln}, \eta_{sn}, \eta_s$  and  $\eta_{bn}$ , in Eq. (6-7a) are artificially introduced in the stiffness controlled terms; ( $Y$ ), ( $\nu$ ), and ( $m$ ) are, respectively, Young's modulus, Poisson's ratio, and surface mass of the plating of the cylinder while ( $c_l$ ) and ( $c_s$ ) are the speeds of the free waves of the longitudinal and shear response, respectively. From Eqs. (6-7b) it is noted that  $c_l > c_s$  if  $0 < \nu < 1$ . Also, from Eqs. (6-6b) and (6-7b) one finds that these speeds are functional of the Poisson's ratio ( $\nu$ ) of the plating of the shell. When dealing with a cylinder, ( $a$ ) is defined to be the radius and ( $ak$ ) and ( $n$ ) are the normalized axial wavenumber and the circumferential mode index, respectively. The term  $\bar{Z}_n^p$ , in Eqs. (6-5a) and (6-6a), accounts for the normalized mechanical impedance that is flexural in nature. The term  $\bar{Z}_n^m$ , in Eqs. (6-5a) and (6-6b), accounts, in this vein, for the natures of the membrane wave types in the response. Were one to remove the membrane term in Eq. (6-5a) and use the identity expressed in Eq. (6-6a), one finds that

$$\bar{G}_n^p(k, \omega) = [\bar{Z}_n^p(k, \omega)]^{-1} = [\bar{G}_p(k, \{n/a\}, \omega)] . \quad (6-8a)$$

It follows from Eqs. (6-1b) and (6-8a) that Figs. 6-1a-d and 6-2a and b directly depict the absolute values of  $\bar{G}_n^p(k, \omega)$  as a function of ( $ak$ ) in a waterfall format; again, the spatial scale factor ( $a$ ) being now identified with the radius of the cylinder. A cylinder from which the membrane response is removed, by setting  $\bar{Z}_n^m(k, \omega)$  identically to zero, is dubbed a hybrid cylinder. Clearly, this kind of a cylinder is mechanically akin to a panel. As such, the hybrid cylinder plays a major role in this report. Casting Eq. (6-5) in the format of Eq. (6-8a), one obtains

for the normalized mechanical surface admittance  $\bar{G}_{pn}(k, \omega)$  of a cylinder in spectral space

$$\bar{G}_{pn}(k, \omega) = [\bar{Z}_{pn}(k, \omega)]^{-1} = [\bar{Z}_n^p(k, \omega) + \bar{Z}_n^m(k, \omega)]^{-1} . \quad (6-8b)$$

In Fig. 6-3 the magnitude of the normalized mechanical surface admittance  $\bar{G}_{pn}(k, \omega)$ , as stated in Eq. (6-8b), is displayed as a function of  $(ak)$  in a waterfall format. In Fig. 6-3a the standard parametric values are used. The standard parametric values stated in Eq. (6-4a) are appropriately augmented by

$$\begin{aligned} n &= 0 ; & \eta_\gamma &= 10^{-3} ; & \nu &= (1/3) ; & (c_l / c) &= 3.5 ; \\ (\omega_r / \omega_c) &= 3.6 \times 10^{-2} ; & c_l &= 5338 \text{ m/sec} . \end{aligned} \quad (6-4c)$$

Comparing Fig. 6-3a with Fig. 6-1a reveals that a longitudinal type of free waves are present in the former figure; this "longitudinal dispersive locus" is directly associated with the presence of the surface impedance  $Z_n^m(k, \omega)$  in the mechanical impedance  $Z_{pn}(k, \omega)$  of the cylinder. In Figs. 6-3b-e, the standard mode index of zero is changed to 1, 3, 9 and 21, respectively. Except when the mode index is zero, the "shear dispersive locus" accompanies the longitudinal dispersive locus. It is observed that both, the longitudinal and shear free waves, are accompanied by "anti-dispersive loci" which lie closely adjacent and on the outside of each. These anti-dispersive loci are associated with the low values (the singularities, in the absence of damping) of  $R_{ln}$  and  $R_{sn}$  in  $\bar{Z}_n^m(k, \omega)$ , as stated in Eq. (6-6b). Figure 6-3a illustrates that for a mode index of zero, longitudinal free waves originate in the vicinity of the ring frequency  $(\omega / \omega_r) \approx 1$ , and that the accompanied "anti-dispersive locus" (a locus of nadirs) extends without interruptions to the lower frequency range. Otherwise, as already stated, this

anti-dispersive locus is adjacent and on the outside of the dispersive locus. Simultaneously, as the frequency decreases from an octave or so above the ring frequency  $(\omega/\omega_r) \simeq 2$ , the flexural free waves become curvature free waves (flexural Bloch waves). The "curvature dispersive locus" possess speeds well in excess of the flexural dispersive locus that it replaces. [cf. Figs. 6-1a and 6-3a.] Figure 6-3b illustrates that for a mode index of unity, in addition to the longitudinal and the curvature free waves, shear free waves join in. These shear free waves originate in the vicinity of an octave below the ring frequency  $(\omega/\omega_r) \simeq (1/2)$ ; below this frequency there are no shear free waves. The shear dispersive locus is also accompanied by an anti-dispersive locus that, as already stated, is adjacent and on the outside of the dispersive locus. With increase in the mode index, as illustrated in Figs. 6-3a-e, the longitudinal, shear and curvature free waves are swallowed at  $(ak) = 0$  and are thus suppressed in the lower frequency range, where  $(\omega/\omega_c) < (n\omega_r/\omega)$ ,  $(n\omega_r/\omega_c) (c_s/c_l)$  and  $(n/ak_c)^2$ , respectively. Otherwise, at the higher frequency range, the dispersive loci are incrementally shifted to lower wavenumbers and the shifts are less pronounced the more the inequalities  $(\omega/\omega_c) > (n\omega_r/\omega_c)$ ,  $(n\omega_r/\omega_c) (c_s/c_l)$  and  $(n/ak_c)^2$ , respectively, are. These shifts cause the longitudinal and shear speeds to be frequency dependent at the lower wavenumber ranges; this frequency dependence is clearly discernible in Figs. 6-3c and d. Also, once  $(n/ak_c)^2 \lesssim (2\omega_r/\omega_c)$ , the curvature free waves are substantially absent; at these higher mode indices the curvature no longer influences the flexural free waves. Considerations of curvature free waves and the origins from which the membrane (the longitudinal and shear) free wave emerge at  $(ak) = 0$ , are not conducted in this report; the frequency range below  $(\omega/\omega_r) \simeq 2$  is to be considered under separate cover. In this sense, although

the displays are assigned the standard range stated in Eq. (6-4b), considerations in this report are focused on the more restricted range defined by

$$\{0, (2\omega_r / \omega_c)\} \leq \{(ak), (\omega / \omega_c)\} < \{75, 0.6\} . \quad (6-4d)$$

To emphasize some of the previous statements two curves out of each of Fig. 6-3a-e are collectively cast in Fig. 6-3e1 and 2. Figure 6-3b is repeated in Fig. 6-4a except that the loss factor ( $\eta_p$ ) is changed from its standard value of  $10^{-3}$  to  $10^{-2}$ . Observe that the membrane loci remain substantially unchanged; only the flexural locus is substantially subdued. Similarly, Fig. 6-3b is repeated in Figs. 6-4b and c except that the loss factors ( $\eta_{ln}$ ) and ( $\eta_{bn}$ ) and then the loss factors ( $\eta_{sn}$ ) and ( $\eta_s$ ) are changed from the standard value of  $10^{-3}$  to  $10^{-2}$ , respectively. Again, observe that in Fig. 6-4b only the longitudinal locus is subdued and in Fig. 6-4c only the shear locus is subdued. It follows that the flexural, the longitudinal, and the shear free waves maintain substantially independent existences and, therefore, they can be individually subdued by damping each individually. This can be analytically used to advantage. One curve out of each of Figs. 6-3b and 6-4a-c are collectively displayed in Fig. 6-4c1. Again, Figs. 6-3e1 and 2 and 6-4c1 are shown merely to indicate the availability of such figures; again, however, in this report only the potential usage of such figures is demonstrated.



Finally it may be usefully recognized, from Eq. (6-7a), that one may define

$$\begin{aligned}\bar{Z}_{ln}(k, \omega) &= (ak_l)^{-2} R_{ln} \\ &= [1 - (ak_l)^{-2} \{(ak)^2 + n^2\} (1 + i\eta_{ln})] ,\end{aligned}\quad (6-9a)$$

$$\begin{aligned}\bar{Z}_{sn}(k, \omega) &= (ak_l)^{-2} R_{sn} \\ &= [1 - (ak_l)^{-2} \{(1 - \nu/2) \{(ak)^2 + n^2\} (1 + i\eta_{sn})\}] .\end{aligned}\quad (6-9b)$$

The quantities  $\bar{Z}_{ln}(k, \omega)$  and  $\bar{Z}_{sn}(k, \omega)$  can be identified as the normalized longitudinal and shear mechanical surface impedances, respectively. The relationship between these two impedances is established in that the speeds of the free waves bear the same ratio that is specified in Eq. (6-7b). Such surface impedances may be assigned, for example, to a panel, giving the panel more compounded mechanical properties. Again, an assignment of this kind lies, however, outside the scope of this report.

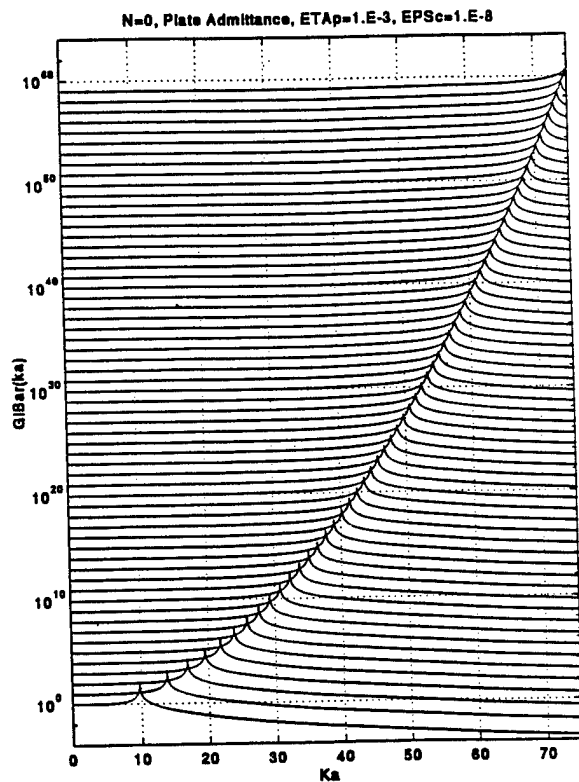


Fig. 6-1a

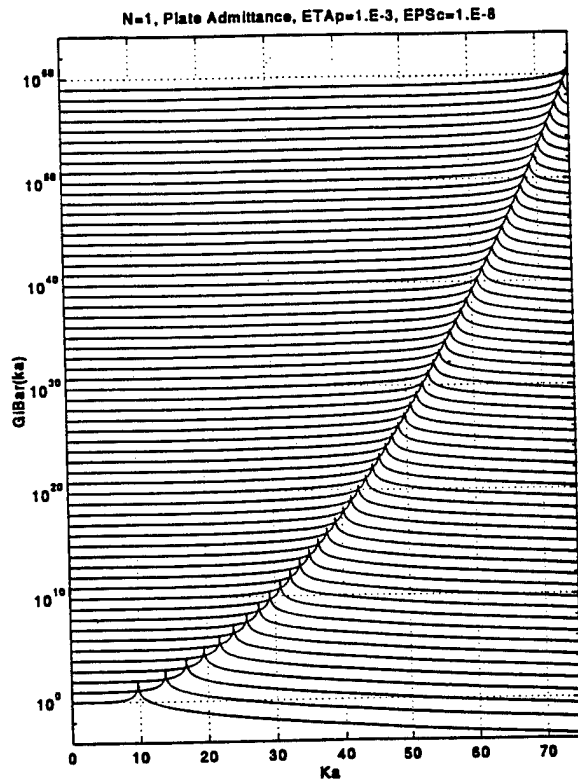


Fig. 6-1b

Fig. 6-1. Magnitude of the normalized mechanical surface admittance  $\bar{G}_p(k, \omega_2)$  of a panel (or equivalently a hybrid cylinder) as a function of  $(ka)$  in a  $(\omega/\omega_c)$  – waterfall format. [A fluid loading parameter  $(\varepsilon_c)$  of  $10^{-8}$  is here considered to represent a negligible fluid loading.]

- a. Standard parametric values  $[(ak_y) = 0]$ ;
- b.  $(ak_y) = 1$ ;
- c.  $(ak_y) = 3$ ;
- d.  $(ak_y) = 9$ ;
- e.  $(ak_y) = 21$ .

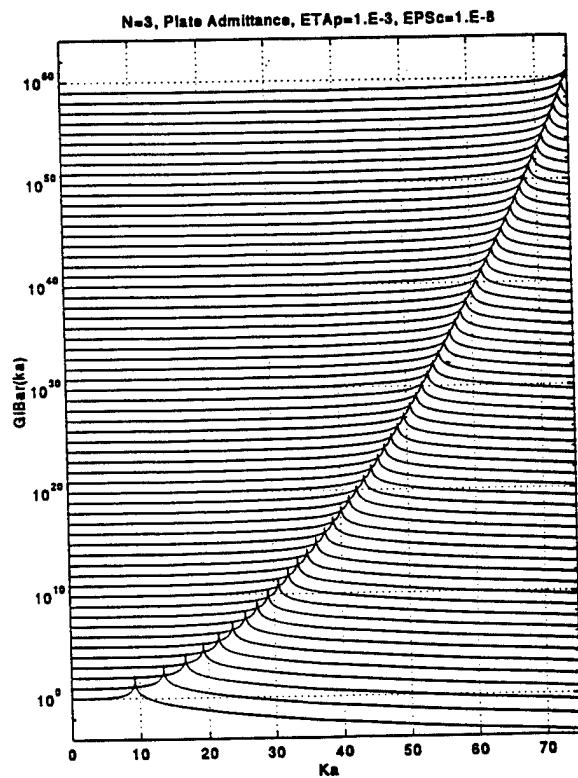


Fig. 6-1c

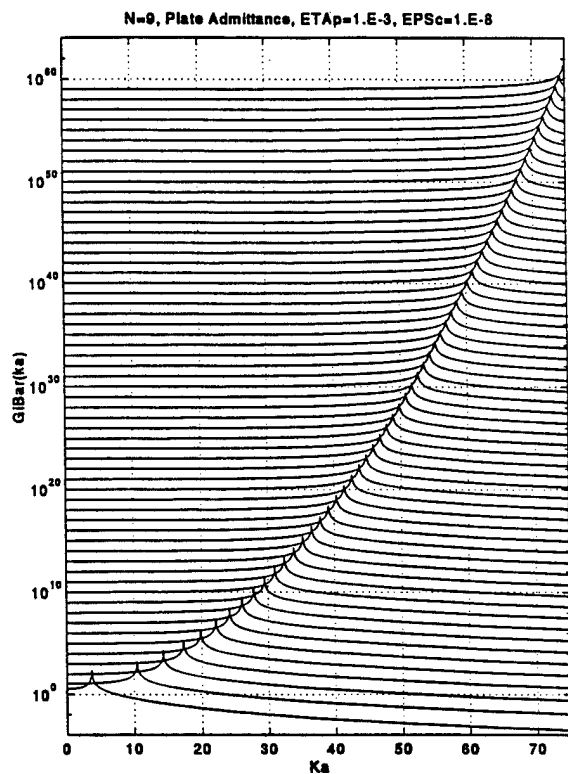


Fig. 6-1d

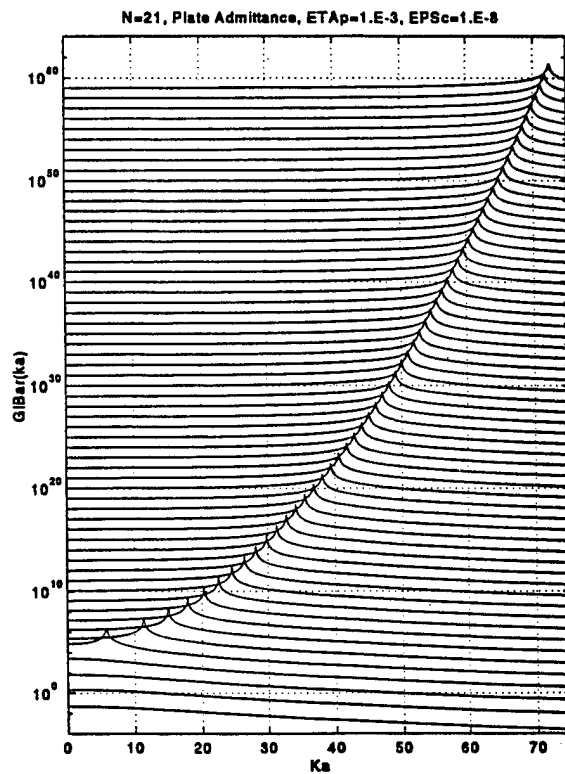


Fig. 6-1e

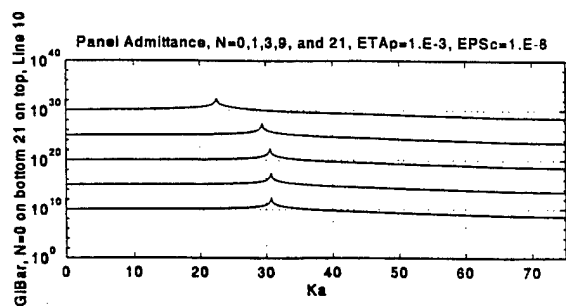


Fig. 6-1e1. Single curve from 6-1a-e  
all with  $(\omega/\omega_c) = 0.10$ .

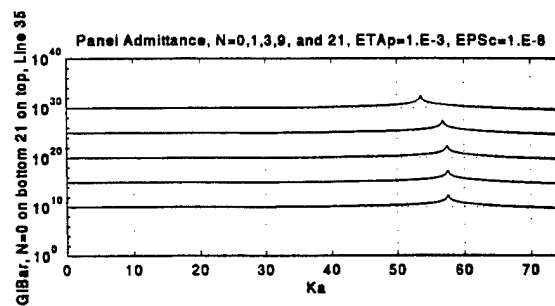


Fig. 6-1e2. Single curve from 6-1a-e  
all with  $(\omega/\omega_c) = 0.35$ .

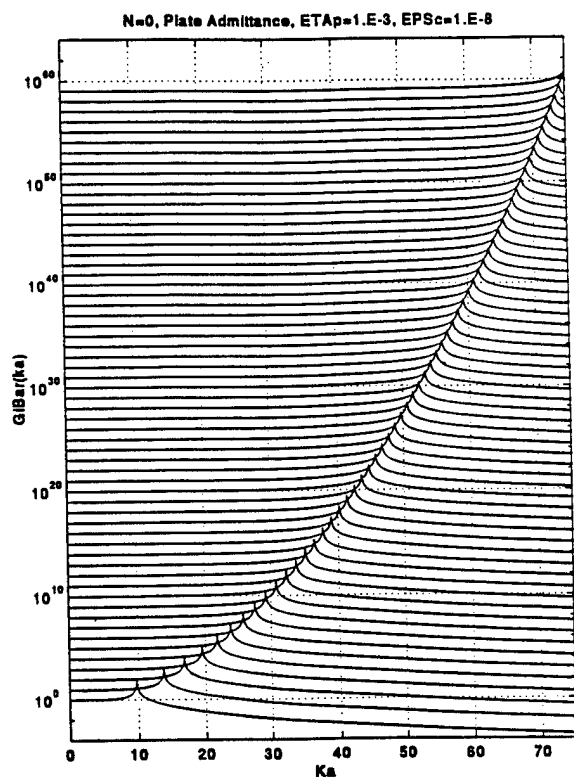


Fig. 6-1a (Repeated)

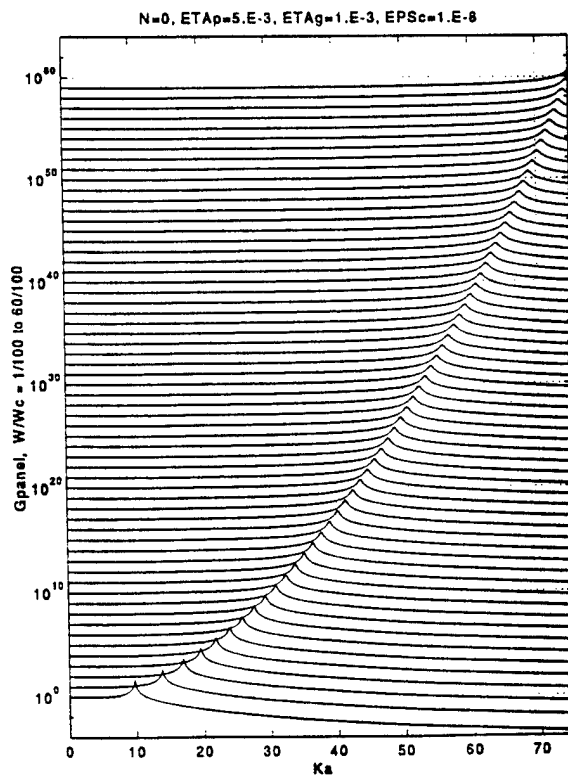


Fig. 6-2a

Fig. 6-2. As in Fig. 6-1a except for a change in the loss factor ( $\eta_p$ ) from the standard value of  $10^{-3}$  to:

- $5 \times 10^{-3}$ .
- $2.5 \times 10^{-2}$ .

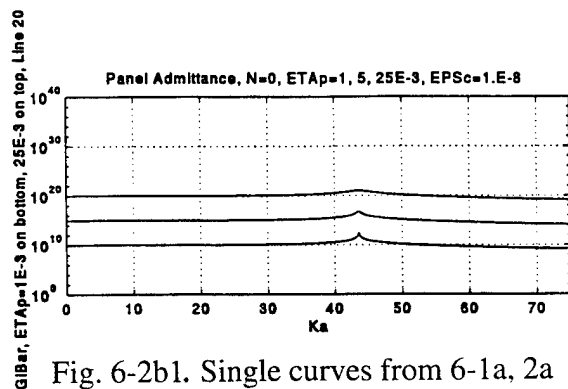


Fig. 6-2b1. Single curves from 6-1a, 2a and b all with  $(\omega/\omega_c) = 0.20$ .

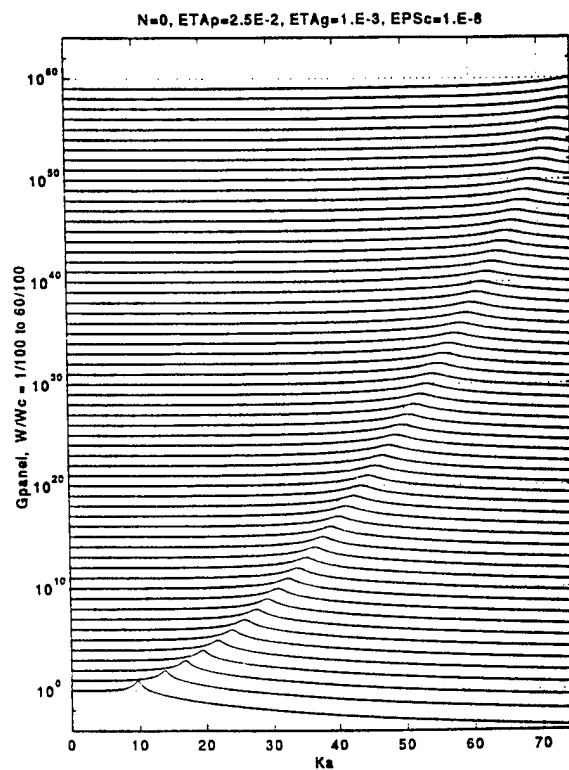


Fig. 6-2b

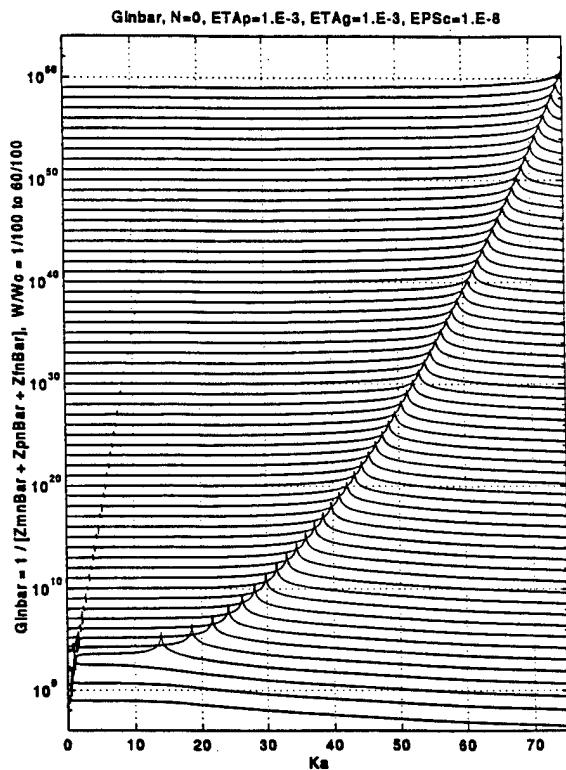


Fig. 6-3a

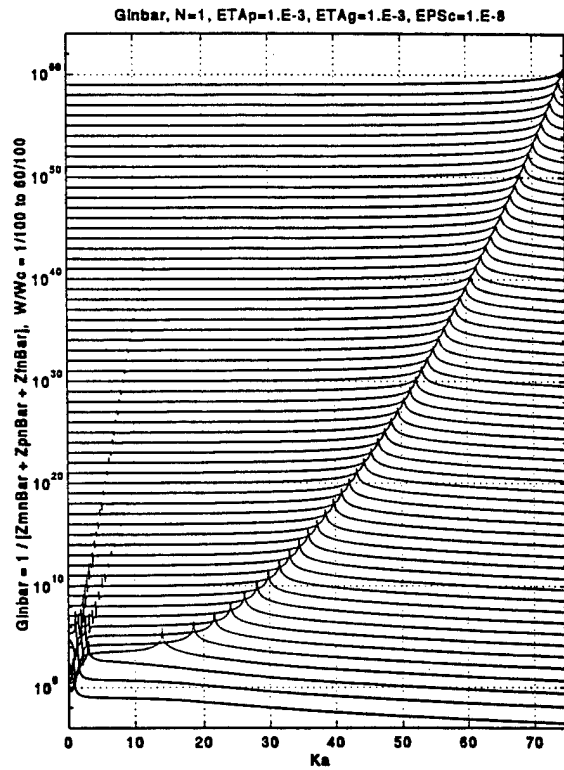


Fig. 6-3b

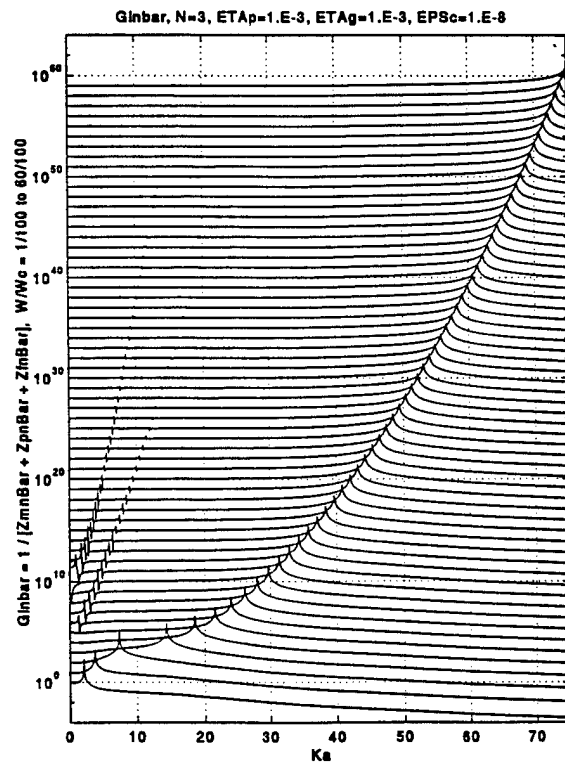
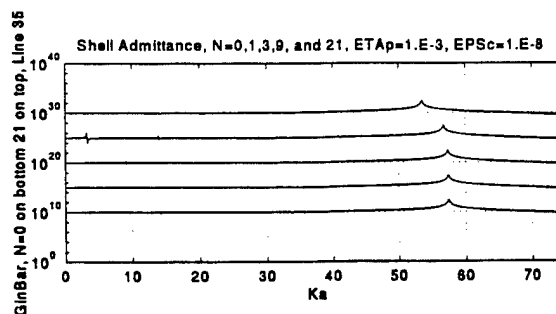
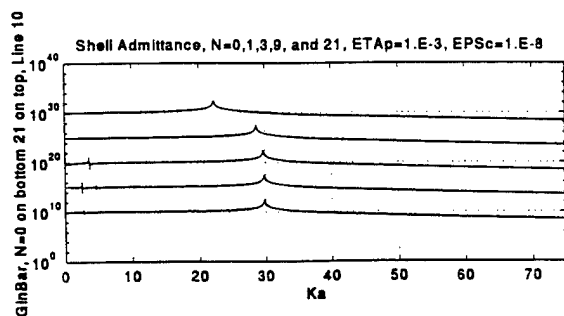
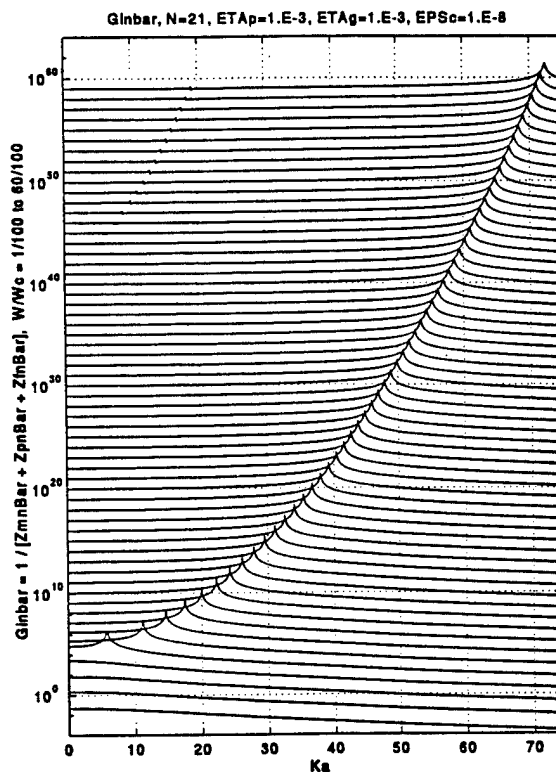
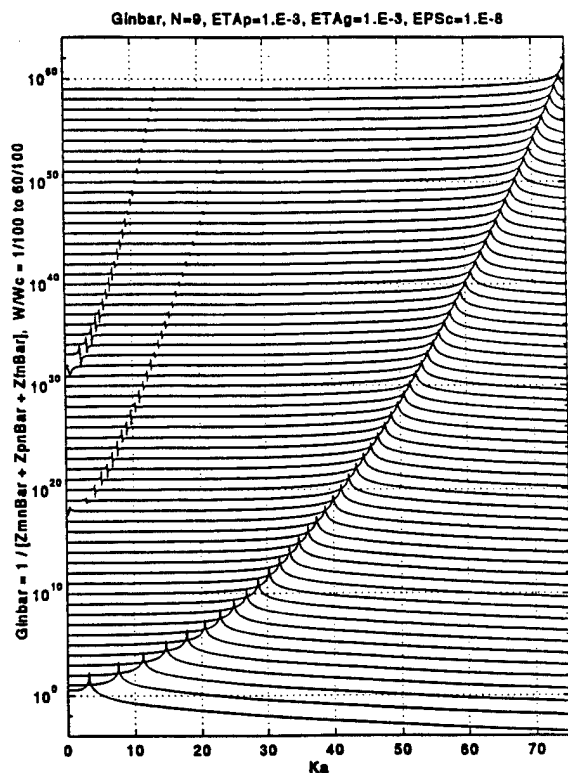


Fig. 6-3c

Fig. 6-3. Magnitude of a normalized modal mechanical surface admittance  $G_p(k, \omega_2)$  of a natural cylinder as a function of  $(ak)$  in a  $(\omega/\omega_c)$  – waterfall format.

- a. Standard parametric values [ $n = 0$ ];
- b.  $n = 1$
- c.  $n = 3$ ;
- d.  $n = 9$ ;
- e.  $n = 21$ .



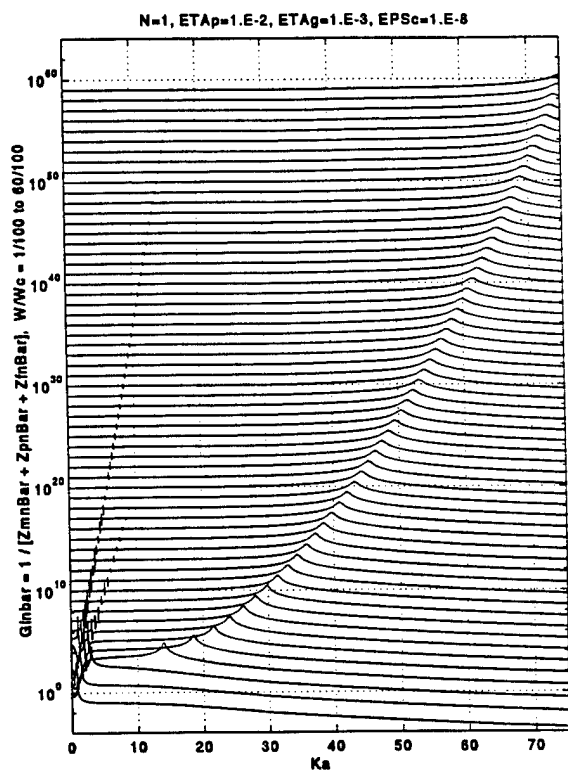


Fig. 6-4a

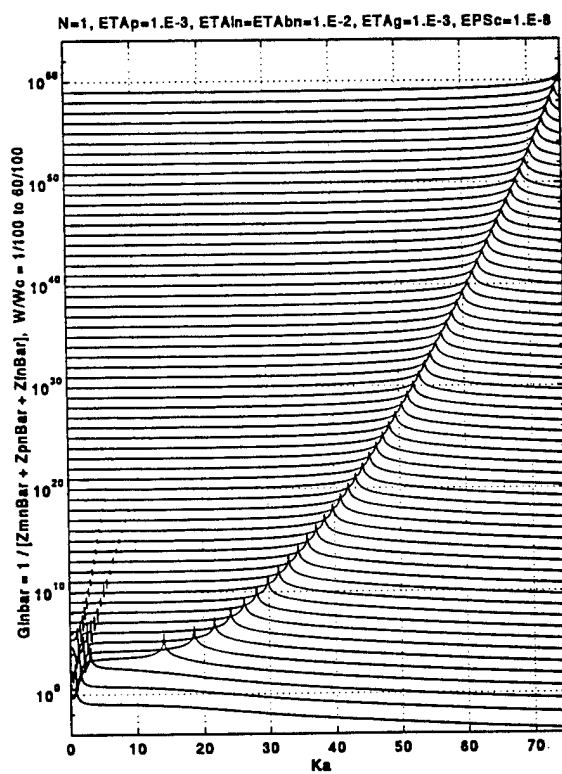


Fig. 6-4b

Fig. 6-4. As in Fig. 6-3a except for a change in the loss factors ( $\eta_p$ ), ( $\eta_{sn}, \eta_s$ ), ( $\eta_{ln}, \eta_{bn}$ ), respectively, from the standard value of  $10^{-3}$  to:

- $\eta_p = 10^{-2}$ ;
- $\eta_{ln} = \eta_{bn} = 10^{-2}$ ;
- $\eta_{sn} = \eta_s = 10^{-2}$ .

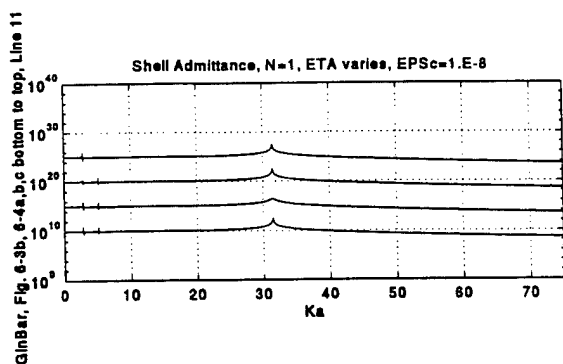


Fig. 6-4c1. Single curves from 3b and 4a-c all with  $(\omega/\omega_c) = 0.11$ .

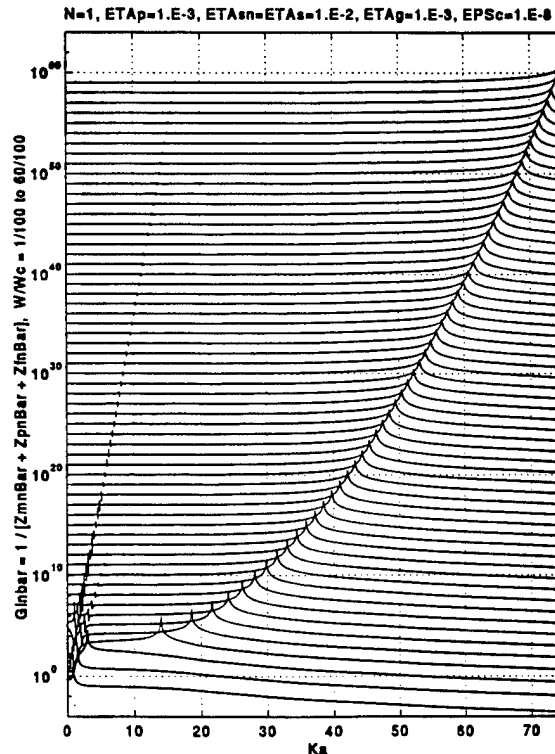


Fig. 6-4c

## VII. FLUID SURFACE IMPEDANCE ON SHELLS

The compatibility of the geometry of a panel and a cylindrical shell with the surface impedance of the fluid on the boundary of each, renders the inclusion of fluid loading in the surface impedance simple in these two geometrical cases.

The fluid surface impedance on the plane of the panel is expressed in the form

$$\begin{aligned}\bar{Z}_f(k, \omega) &= [Z_f(k, \omega)] (i\omega m)^{-1} \\ &= (\rho\omega / k_3) (i\omega m)^{-1} = (\epsilon_c a k_c) (i a k_3)^{-1},\end{aligned}\quad (7-1a)$$

where the wavenumber  $k_3$  is given by

$$k_3(k, \omega) = (\omega / c) \left\{ \begin{array}{ll} [1 - (|k|c / \omega)^2]^{1/2} & U[1 - (|k|c / \omega)^2] \\ -i[(|k|c / \omega)^2 - 1]^{1/2} & U[(|k|c / \omega)^2 - 1] \end{array} \right\}, \quad (7-2)$$

the function  $U$  is the unit step function, the fluid loading parameter ( $\epsilon_c$ ) and the critical acoustic wavenumber ( $k_c$ ) are defined

$$\epsilon_c = (\rho c / \omega_c m); \quad k_c = (\omega_c / c), \quad (7-3)$$

respectively, the panel is assumed to be an isotropic thin-plate, ( $a$ ), in Eq. (7-1a), is merely a linear spatial scale factor, but ( $c$ ) is now identified to be the speed of sound in the fluid atop the panel. The fluid loading parameter ( $\epsilon_c$ ) is the absolute value of the ratio of the fluid characteristic impedance ( $\rho c$ ) and the



surface mass impedance ( $i \omega_c m$ ) of that plate at the critical frequency. The wavenumber ( $k_3$ ) is the wavenumber ( $k_z$ ) evaluated so that  $k_z^2 \rightarrow k_3^2 = (\omega/c)^2 - |k|^2$ . [cf. Fig. 3-2.] The expression for ( $k_3$ ) is, therefore, a statement of the wave equation in the fluid, whereas ( $k_z$ ) is merely the Fourier conjugate variable of  $z$ . [cf. Fig. 3-2.] Equations (7-1a) and (7-2) follow from consideration of the conservation of momentum across the interface between the panel and the fluid atop. In Figs. 7-1a and b the real and imaginary parts of the normalized surface fluid impedance  $\bar{Z}_f(k, \omega_2)$  are displayed, respectively, as a function of ( $ak$ ) in a waterfall format. The real and imaginary parts of  $\bar{Z}_f(k, \omega_2)$  are defined

$$\bar{Z}_f(k, \omega_2) = \text{Re} \{ \bar{Z}_f(k, \omega_2) \} + i \text{Im} \{ \bar{Z}_f(k, \omega_2) \} . \quad (7-1b)$$

The term  $\text{Re} \{ \bar{Z}_f(k, \omega_2) \}$  is found to be positive and non-zero only in the subsonic range, where  $(a|k|) > (a\omega/c)$ , indicating that the fluid loading contributes only surface mass to the panel in this range of spectral space, as shown in Fig. 7-1a. The standard fluid loading is designated by  $\epsilon_c = 10^{-2}$ . Appropriately, as the sonic locus is approached, this quantity increases and becomes infinite at this locus. The quantity  $\text{Im} \{ \bar{Z}_f(k, \omega_2) \}$  is also found to be positive indicating that the fluid loading causes loss of energy from the panel to the fluid by radiation to the far-field. The quantity  $\text{Im} \{ \bar{Z}_f(k, \omega_2) \}$  is, however, non-zero only in the supersonic range, where  $(a|k|) < (a\omega/c)$ , as shown in Fig. 7-1b. Thus, only supersonic components in the response of the panel radiate to the far-field resulting in energy transport from the panel to the fluid. Figures 7-1a and b and Fig. 7-1c, the latter depicting the absolute values of  $\bar{Z}_f(k, \omega_2)$ , and the interpretations of these figures are fundamental in acoustics and are commonplace. For the record, Figs. 7-1d-f repeat Fig. 7-1c, except that

the value of  $(ak_y)$  is changed from the standard value of zero to 1, 3 and 9, respectively. Again, as the value of  $(ak_y)$  increases, the sonic locus, constituted by the peaks in these figures, is swallowed at  $(ak) = 0$  in the lower frequency range, where  $(\omega / \omega_c) < (k_y / k_c)$ , and is thus suppressed. Otherwise, the sonic locus is incrementally shifted to lower wavenumbers and the shift is less pronounced the more the inequality  $(\omega / \omega_c) > (k_y / k_c)$  is. The expected spectral shifts accompanying increases in  $(ak_y)$  are seen in these figures; Figs. 7-1d-f.

The surface impedance for the fluid in which a cylinder is externally immersed is dependent on the circumferential mode. This surface impedance is expressed in the form

$$\bar{Z}_n^f(k, \omega) = Z_n^f(k, \omega) / (i\omega m) = -\epsilon_c(ak_c) D_n^{(2)}(ak_3), \quad (7-4a)$$

where

$$D_n^{(2)}(ak_3) = H_n^{(2)}(ak_3) / [(ak_3) H_n^{(2)'}(ak_3)], \quad (7-5a)$$

$$k_3(\underline{k}, \omega) = (\omega / c) \begin{Bmatrix} [1 - (|\underline{k}|c / \omega)^2]^{1/2} & U[1 - (|\underline{k}|c / \omega)^2] \\ -i[ (|\underline{k}|c / \omega)^2 - 1]^{1/2} & U[(|\underline{k}|c / \omega)^2 - 1] \end{Bmatrix}, \quad (7-5b)$$

and in this equation  $\underline{k} = \{k, (n/a)\}$ ,  $H_n^{(2)}$  is the Hankel function of the second kind and the  $(n)$ th order and  $H_n^{(2)'}$  is the first derivative of  $H_n^{(2)}$  with respect to its argument. [cf. Eqs. (7-1) - (7-3).] In Figs. 7-2a and b the real and imaginary parts,

respectively, of the normalized fluid surface impedance  $\bar{Z}_n^f(k, \omega)$  are displayed as a function of  $(ak)$  in a waterfall format, where

$$\bar{Z}_n^f(k, \omega) = \text{Re}\{\bar{Z}_n^f(k, \omega)\} + i \text{Im}\{\bar{Z}_n^f(k, \omega)\} . \quad (7-4b)$$

The term  $\text{Re}\{\bar{Z}_n^f(k, \omega)\}$  is found to be positive throughout the spectral range indicating that the fluid loading contributes surface mass to the cylinder throughout the spectral range. Appropriately, the contribution is level in the supersonic range, increases as the sonic locus is approached, becomes large at the sonic locus, and falls off steadily as the subsonic range is further penetrated; these features are exhibited in Fig. 7-2a. [cf. Fig. 7-1a.] The quantity  $\text{Im}\{\bar{Z}_n^f(k, \omega)\}$  is also found to be positive indicating that the fluid loading causes loss of energy from the cylindrical shell to the fluid by radiation to the far-field.  $\text{Im}\{\bar{Z}_n^f(k, \omega)\}$  is, however, non-zero only in the supersonic range, where  $(ak) < (a\omega/c)$ , as shown in Fig. 7-2b. [cf. Fig. 7-1b.] Thus only supersonic components in the response of the cylinder radiate to the far-field; resulting in energy transport from the cylinder to the fluid. Figures 7-2a and b and Fig. 7-2c, the latter depicting the absolute values of  $\bar{Z}_n^f(k, \omega)$ , and the interpretations of these figures are fundamental in the acoustics of cylinders and are commonplace. The influence of changing the circumferential mode index  $(n)$  on the fluid impedance is briefly illustrated in Figs. 7-2d-f. These figures repeat Fig. 7-2c except that the mode index  $(n)$  is changed from the standard value of 0 to 1, 3 and 9, respectively. Again, as the value of  $(n)$  increases, the sonic locus, constituted by the peaks in these figures, is swallowed at  $(ak) = 0$  in the lower frequency range, where  $(\omega/\omega_c) < (n/ak_c)$ , and is thus suppressed. Otherwise, the sonic locus is incrementally shifted to lower wavenumbers and the shift is less pronounced the more the inequality  $(\omega/\omega_c) > (n/ak_c)$  is. The expected spectral shifts

accompanying increases in the mode index ( $n$ ) are seen in these figures; Figs. 7-2d-f.

Comparing Figs. 7-1 and 7-2 reveals that the fluid loading on panels and on cylinders do bear qualitative resemblance even if they differ quantitatively. A major difference is that the fluid loading on a cylinder possesses a mass term in the supersonic range, where  $(ak) < (a\omega/c)$ . The fluid loading on a panel does not possess a reactive term in this spectral range. In addition, one finds that the fluid loading at and in the immediate vicinity of the sonic locus tends to be more pronounced for a panel than a cylinder. This difference becomes more pronounced as the normalized wavenumber  $(ak_y)$  and the mode index ( $n$ ) are correspondingly increased. [cf. Figs. 7-1c-f and Figs. 7-2c-f, respectively.]

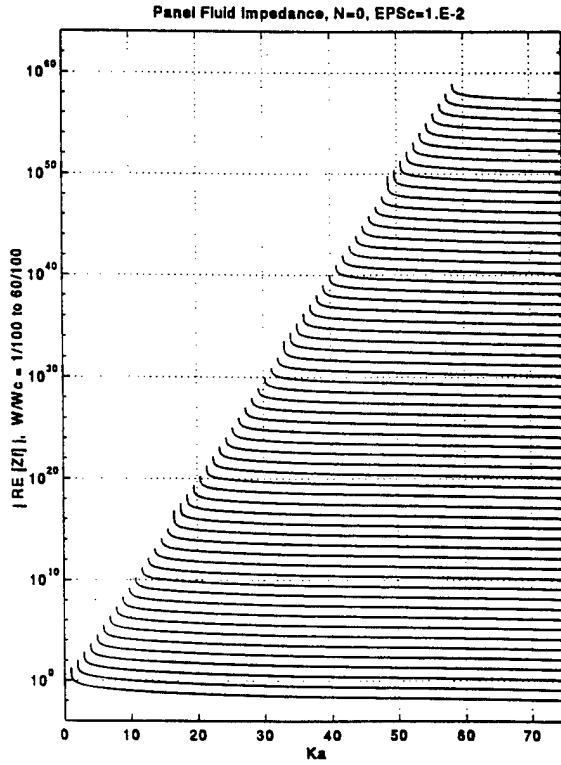


Fig. 7-1a

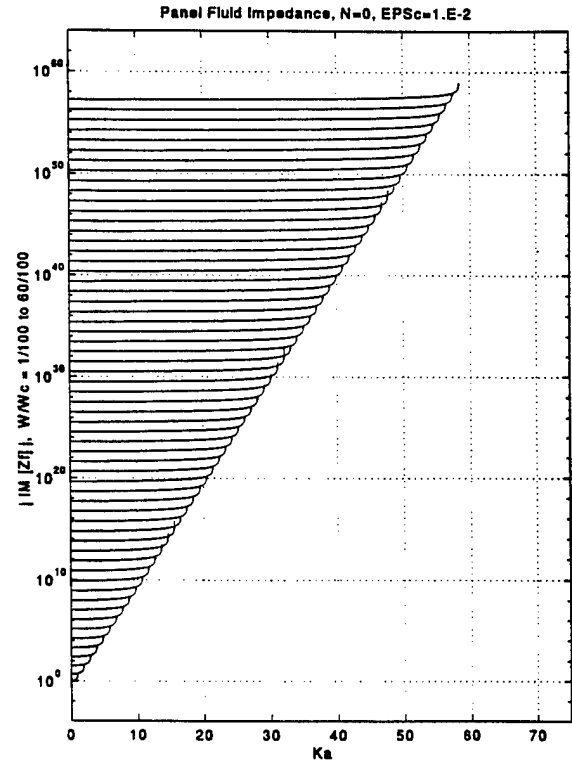


Fig. 7-1b

Fig. 7-1. Normalized fluid surface impedance  $\bar{Z}_f(k, \omega_2)$  on a panel as a function of  $(ak)$  in a  $(\omega/\omega_c)$  – waterfall format.

- a. Real part.
- b. Imaginary part.
- c. Magnitude.
- d. Magnitude with  $(ak_y) = 1$ .
- e. Magnitude with  $(ak_y) = 3$ .
- f. Magnitude with  $(ak_y) = 9$ .

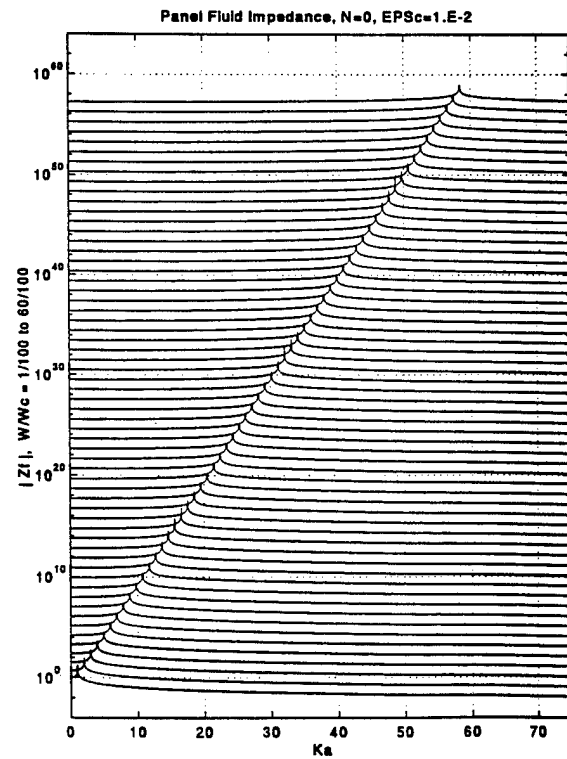


Fig. 7-1c

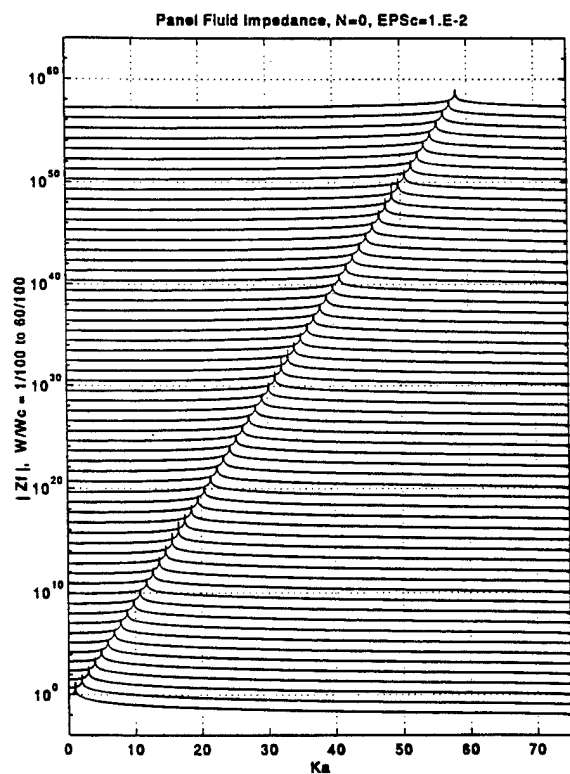


Fig. 7-1c (Repeated)

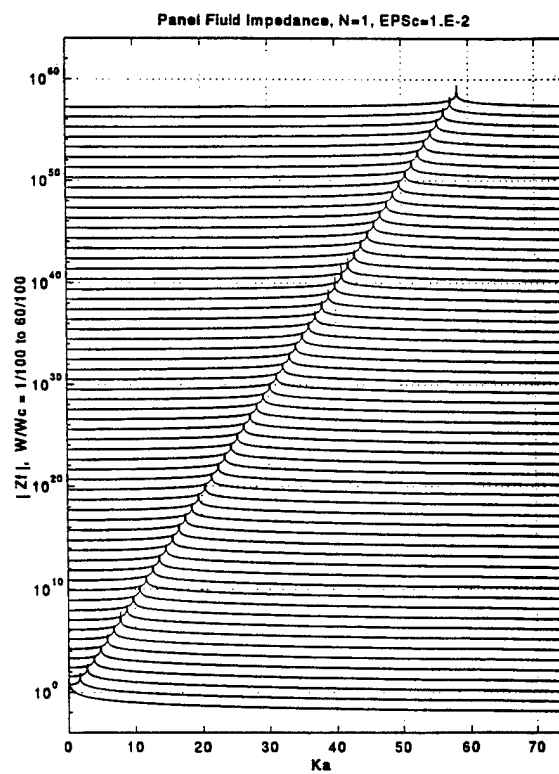


Fig. 7-1d

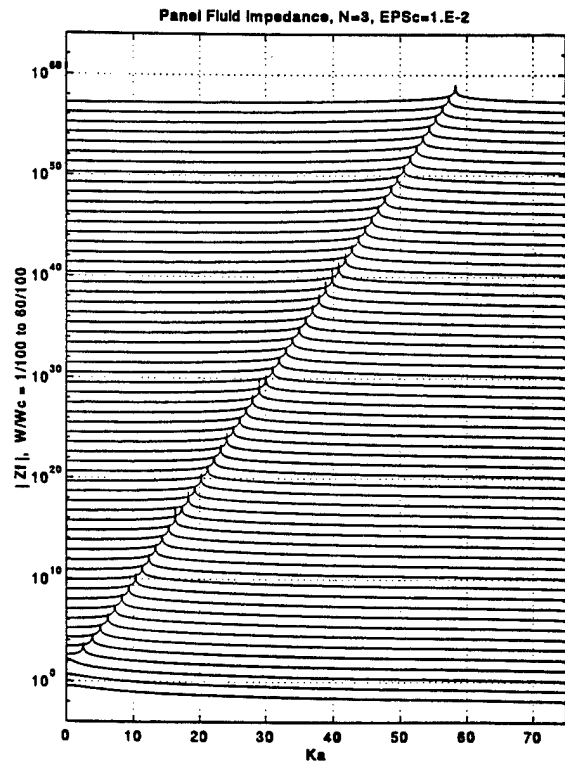


Fig. 7-1e

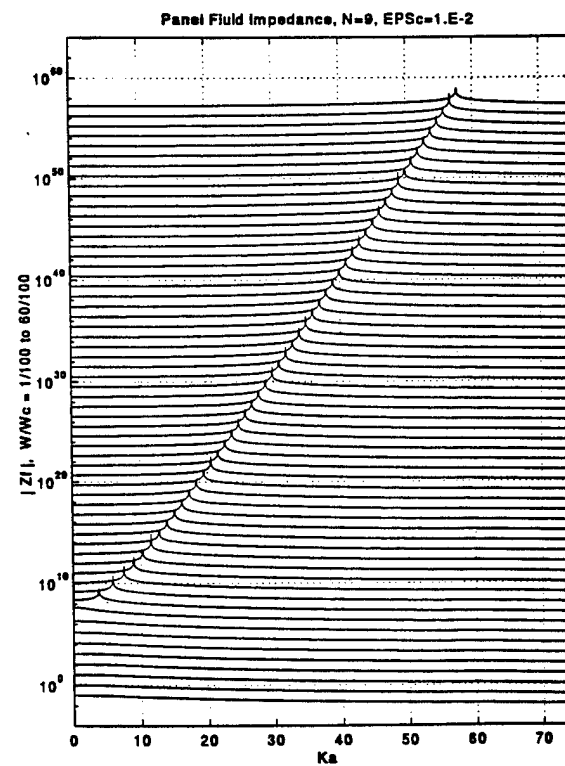


Fig. 7-1f

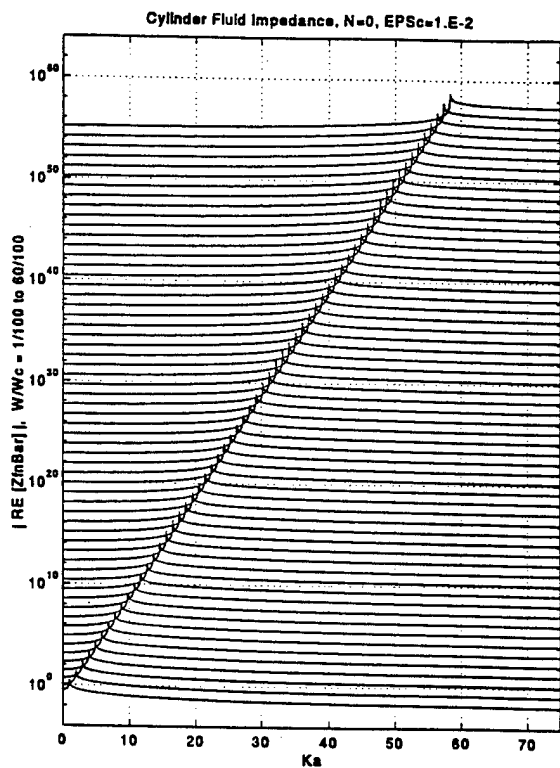


Fig. 7-2a

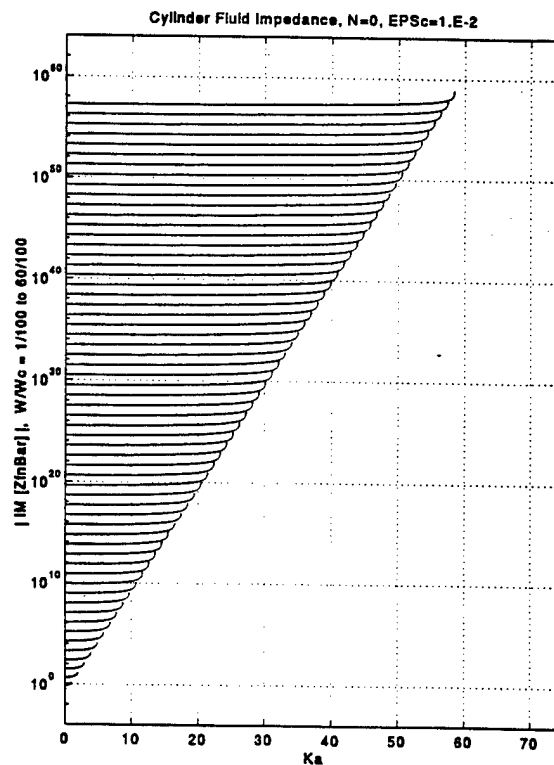


Fig. 7-2b

Fig. 7-2. Normalized modal fluid surface impedance  $\bar{Z}_n^f(k, \omega)$  on a cylindrical surface as a function of  $(ak)$  in a  $(\omega/\omega_c)$ -waterfall format.

- a. Real part.
- b. Imaginary part.
- c. Magnitude.
- d. Magnitude with  $n = 1$ .
- e. Magnitude with  $n = 3$ .
- f. Magnitude with  $n = 9$ .

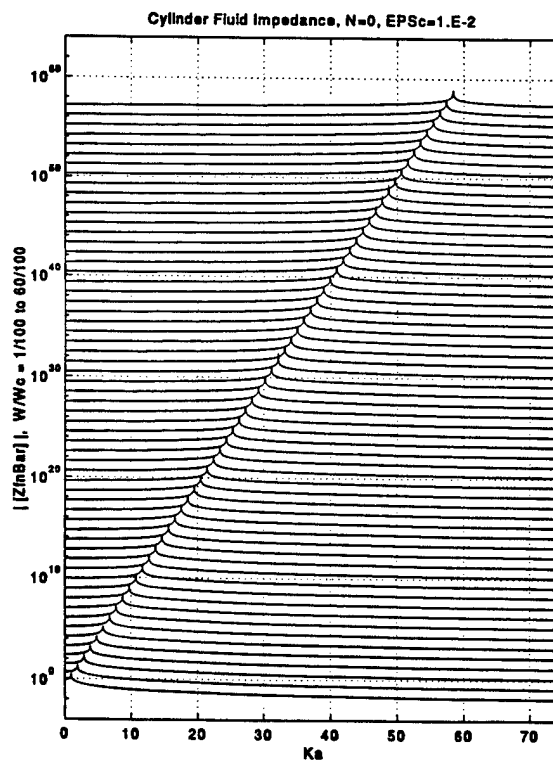


Fig. 7-2c

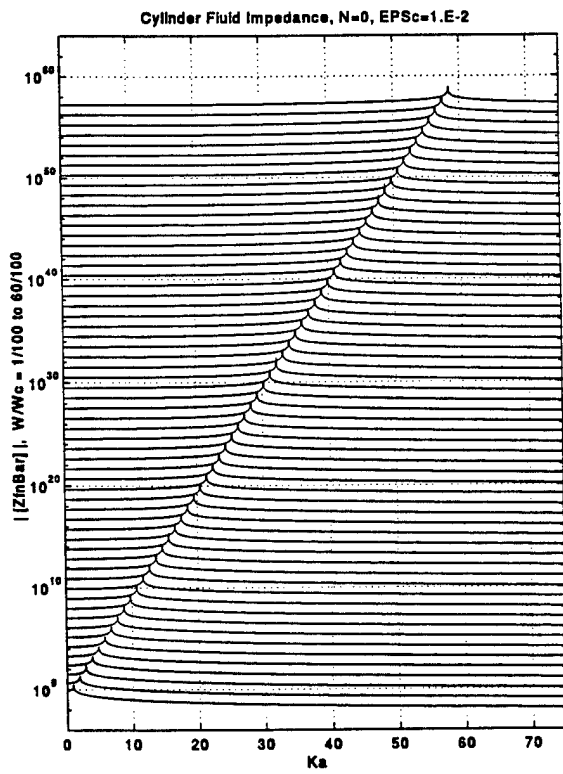


Fig. 7-2c (Repeated)

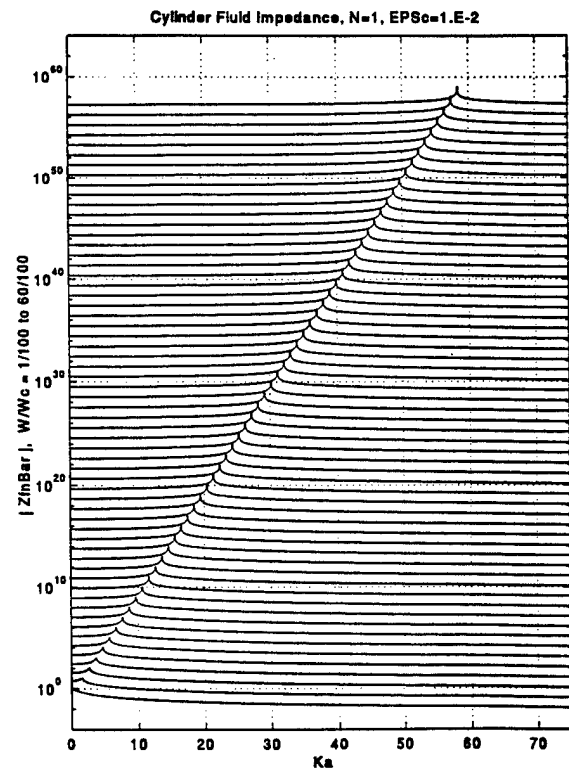


Fig. 7-2d

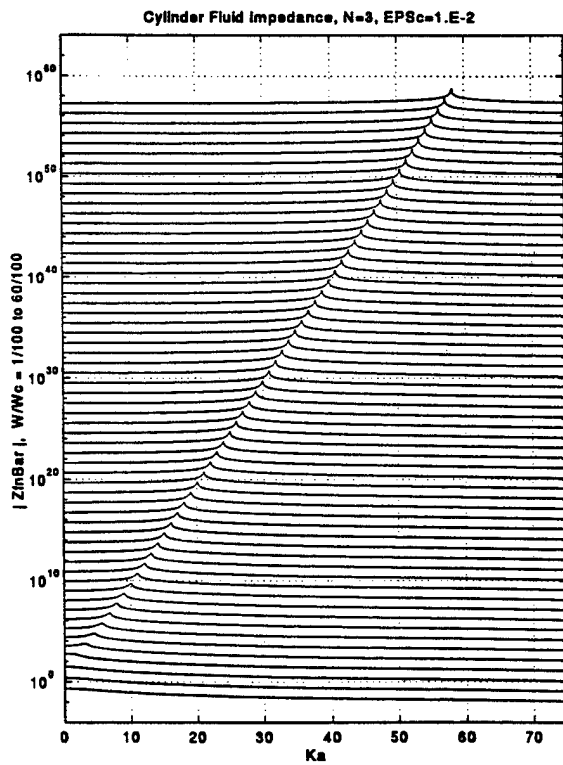


Fig. 7-2e

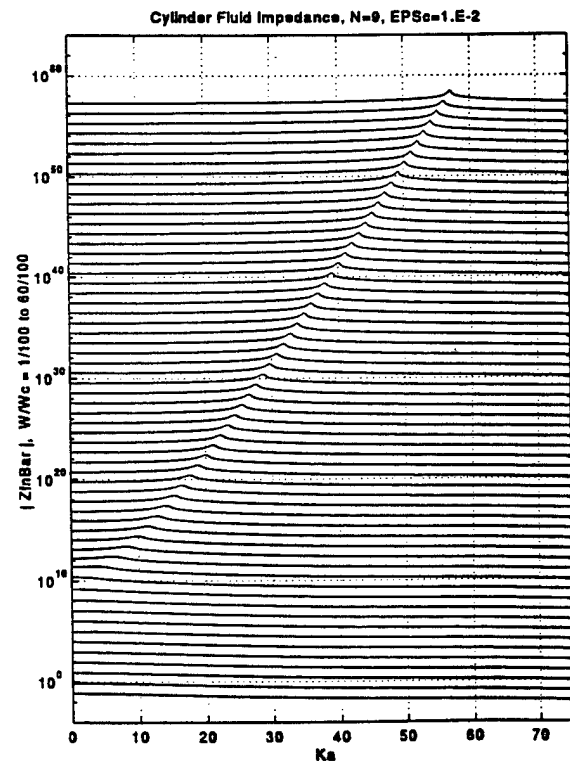


Fig. 7-2f



## VIII. FLUID LOADED SURFACE IMPEDANCE OF SHELLS

Sections VI and VII can now be combined to yield the surface impedance of a uniform panel and a uniform cylinder including fluid loading.

From Eqs. (3-10), (3-13a), (3-23a), (3-24a), (6-1) and (7-1) one obtains for the normalized partial surface admittance  $\bar{G}_\infty(k, \omega_2)$  of a uniform panel

$$\begin{aligned} G_\infty(k, \omega_2) &= [Z_p(k, \omega_2) + (\rho\omega / k_3)]^{-1}; \\ \bar{G}_\infty(k, \omega_2) &= [(i\omega m) G_\infty(k, \omega_2)] \\ &= [1 - (|k|/k_p)^4 - i(\epsilon_c a k_c) (a k_3)^{-1}]^{-1}, \end{aligned} \quad (8-1)$$

where, again, the panel is assumed to be an isotropic thin plate. The magnitude of the normalized fluid loaded surface admittance  $\bar{G}_\infty(k, \omega_2)$  is displayed under the standard parametric values in Fig. 8-1a. At the sonic locus the fluid loaded surface admittance  $\bar{G}_\infty(k, \omega_2)$  vanishes by virtue of the infinite peak values that the normalized fluid surface impedance assumes at these sonic locations. In the normalized fluid loaded surface admittance  $\bar{G}_\infty(k, \omega_2)$ , the "sonic dispersive locus" of the fluid is characterized, therefore, by valleys and associated nadirs. [Strictly, the sonic dispersive locus is more commensurate with an anti-dispersive locus. Nonetheless, a sonic dispersive locus is assigned to this fluid loading feature.] Figure 8-1a is repeated in Figs. 8-1b-d except that  $(a k_y)$  is changed from the standard value of zero to 1, 3, and 9, respectively. The effects of these changes are as expected and they are noted. [cf. Sections VI and VII.] The obvious difference, between Figs. 8-1a-d and the fluid free Figs. 6-1a-d, is the presence of the fluid dispersive locus -- the sonic locus -- in the former set and the

absence of this locus in the latter set. The presence of the sonic locus in these kinds of displays requires, however, at least a moderate fluid loading. The standard fluid loading parameter ( $\epsilon_c$ ) represents a moderate fluid loading. Figure 8-1a is repeated in Fig. 8-2a except that ( $\epsilon_c$ ) is changed from the standard value of  $10^{-2}$  to  $10^{-4}$ ; a fluid loading characterized by  $\epsilon_c = 10^{-4}$  is light. Indeed, in Fig. 8-2a the sonic locus is hardly discernible; Fig. 8-2a substantially overlays with Fig. 6-1a in which fluid loading is absent. On the other hand, Fig. 8-1a, is repeated in Fig. 8-2b except that ( $\epsilon_c$ ) is changed from the standard value of  $10^{-2}$  to  $10^{-1}$ ; a fluid loading characterized by  $\epsilon_c = 10^{-1}$  is heavy. Clearly, the sonic locus is more pronounced in this new figure than in Fig. 8-1a. However, not only is the sonic locus more pronounced in Fig. 8-2b than in Figs. 8-1a and 2a, but the flexural dispersive locus is shifted to higher wavenumber regions signifying lower speeds for the flexural free waves. This is commensurate with the "added surface mass" influence of the fluid loading on a panel in the subsonic range of the spectral domain in which the flexural free waves reside. There is a shift of this kind also between Fig. 8-2a and Fig. 8-1a, however, this shift is slight compared with that between Fig. 8-1a and Fig. 8-2b, respectively. These shifts are made clearer in Fig. 8-2b1 in which one curve from each of Figs. 8-1a, 2a and b are collectively displayed. The three curves in Fig. 8-2b1 are in reference to the same normalized frequency. Note that in the spectral range covered in the displays represented in this report, the flexural dispersive locus is subsonic.

From Eqs. (3-10), (3-13b), (3-23b), (3-24b), (6-5), and (7-4) one obtains for the normalized modal surface admittance  $\bar{G}_{\infty n}(k, \omega)$  of a uniform cylinder

$$\bar{G}_{\infty n}(k, \omega) = [(i\omega m) G_{\infty n}(k, \omega)] = [\bar{Z}_{pn}(k, \omega) + \bar{Z}_n^f(k, \omega)]^{-1} ;$$

$$\bar{G}_{\infty n}(k, \omega) = \{\bar{Z}_n^p(k, \omega) + \bar{Z}_n^m(k, \omega) - (\epsilon_c a k_c) D_n^{(2)}(ak_3)\}^{-1} , \quad (8-2)$$

where  $(\epsilon_c)$  and  $(k_c)$  are defined in Eqs. (7-3) and  $D_n^{(2)}(ak_3)$  is defined in Eq. (7-5a). The magnitude of the normalized fluid loaded modal surface admittance  $\bar{G}_{\infty n}(k, \omega)$  is displayed under standard parametric values in Fig. 8-3a. Again, there are valleys and associated nadirs at the sonic locus. The influence of changing the circumferential mode index ( $n$ ) from the standard value of zero to 1, 3 and 9 is presented in Figs. 8-3b-d, respectively. The affects of these changes are as expected and they are noted. [cf. Sections VI and VII and Figs. 8-1b-d.] Figure 8-3a is repeated in Figs. 8-4a and b and Fig. 8-3b is repeated in Figs. 8-5a and b, except that the fluid loading parameter  $(\epsilon_c)$  in the first figure of each set is changed from the standard value of  $10^{-2}$  to  $10^{-4}$  and in the second to  $10^{-1}$ . Again, there is hardly a difference between Figs. 8-3a and b and Figs. 8-4a and 5a, respectively. However, in contrast, in Figs. 8-4b and 5b, the sonic locus is more pronounced and there is a shift in the dispersive loci to higher wavenumber regions; this shift is by far more pronounced for the flexural dispersive locus than for the membrane loci. The shift is illustrated in a more pronounced manner in Figs. 8-4b1 and 5b1 in which one curve out of Figs. 8-3a, 4a, and 4b and 8-3b, 5a, and 5b, respectively, are collectively displayed. [Note the amplification used in Fig. 8-5b1 as compared with Fig. 8-4b1. This amplification advantageously accentuates details in Fig. 8-5b1.] Moreover, one can discern in Figs. 8-4b and 5b a suppression in the membrane loci when compared with those in

Figs. 8-4a and 5a. Since the mechanical damping remains unchanged, this suppression is likened to radiation damping of the membrane free waves. One remembers that, whereas the flexural dispersive locus lies in the subsonic region, the membrane dispersive loci lie in the supersonic region in the spectral range displayed. In this spectral range the influence of fluid loading on the subsonic flexural free waves is different from that on the supersonic membrane free waves. The influence on the first free waves is that of added surface mass. On the second free waves the influence is largely that of radiation damping.

A fluid loaded hybrid cylinder is defined by a fluid loaded surface admittance  $G_{\infty n}^P(k, \omega)$  which is normalized in the form

$$\overline{G}_{\infty n}(k, \omega) \equiv \overline{G}_{\infty n}^P(k, \omega) \equiv [(i\omega m) G_{\infty n}^P(k, \omega)] . \quad (8-3)$$

This surface admittance is derived from Eq. (8-2) by setting  $\overline{Z}_n^m(k, \omega)$  identically equal to zero. The surface admittance so derived is expressed in the form

$$\overline{G}_{\infty n}(k, \omega) \equiv \overline{G}_{\infty n}^P(k, \omega) = \{ \overline{Z}_n^P(k, \omega) - (\epsilon_c a k_c) D_n^{(2)}(a k_3) \}^{-1} . \quad (8-4)$$

[cf. Eqs. (8-1) and (8-2).] Thus, the  $(n)$ th circumferential mode in the hybrid cylindrical shell is described by a panel-like mechanical surface admittance, with  $(a k_y) = n$ , and a cylinder-like fluid loading again with  $n = (a k_y)$ . The hybrid structure emphasizes more and more that the investigation performed in this report is meant to be generic and phenomenological rather than dealing with a specific structure under one-to-one correspondence. The salient features of the admittance  $\overline{G}_{\infty n}^P(k, \omega)$  of the hybrid cylinder are displayed in Figs. 8-6 and 7.

[cf. Figs. 6-1-5.] By definition the longitudinal and shear (and the curvature) free waves are absent in these figures; the kinship of the hybrid cylinder and the panel stems from this absence. In Fig. 8-6a the standard parametric values are used. Figure 8-6a is repeated in Figs. 8-6b-d except that the standard circumferential mode index ( $n$ ) is changed from the standard value of zero to 1, 3 and 9, respectively. Except for the milder fluid loading at the appropriate sonic loci, Figs. 8-6a-d are hardly distinguishable from Figs. 8-1a-d, again emphasizing the close relationship between the mechanical behavior of the hybrid cylinder and the panel. Figures 8-7a and b repeat Fig. 8-6a except that the standard value of  $10^{-2}$  of the parameter ( $\epsilon_c$ ) of fluid loading is changed to  $10^{-4}$  and  $10^{-1}$ , respectively. Again, except for a milder fluid loading on the sonic locus, Figs. 8-7a and b are hardly distinguished from Figs. 8-2a and b, indeed, even under heavy fluid loading, as is the case with respect to Figs. 8-7b and 8-2b. Thus, little is sacrificed with respect to understanding the response behavior of a panel if the hybrid cylinder is used to simulate it. On the other hand, the hybrid cylinder, by definition, does not support membrane response. The investigation of the hybrid cylinder can, by contrasting the hybrid and the natural cylinder response behavior, be indirectly useful in the investigation of the role played by the membrane response in the natural cylinder. In this light, hereafter the reference to a panel as such is dropped and the hybrid cylinder is substituted for it. On the one hand, the preceding material should enable one to make inferences with respect to a panel through the investigation of the response behavior of the corresponding hybrid cylinder. On the other hand, by contrast, the hybrid cylinder can be useful in the investigation of the response behavior of a corresponding natural cylinder. Again, the hybrid cylinder formalism is derived by simply neglecting the membrane mechanical surface impedance  $Z_n^m(k, \omega)$  in the formalism for the cylindrical shell. Accepting, in subsequent consideration,

the inferential analysis between a panel and a hybrid cylinder to be adequate, the dual equations scheme representing the panel and the cylinder, respectively, becomes superfluous. The need for the dual equations is, thereby and hereafter, rescinded. Finally, and in this connection, the terms "a natural cylinder" and "a cylinder" are to be considered synonymous, the deviant is the hybrid cylinder.

Fig. 8-1. Normalized partial fluid loaded surface admittance  $\bar{G}_{\infty}(k, \omega_2)$  of a panel as a function of  $(ak)$  in a frequency waterfall format.

- a. Under standard parametric values  $[(ak_y) = 0]$ .
- b.  $(ak_y) = 1$ .
- c.  $(ak_y) = 3$ .
- d.  $(ak_y) = 9$ .

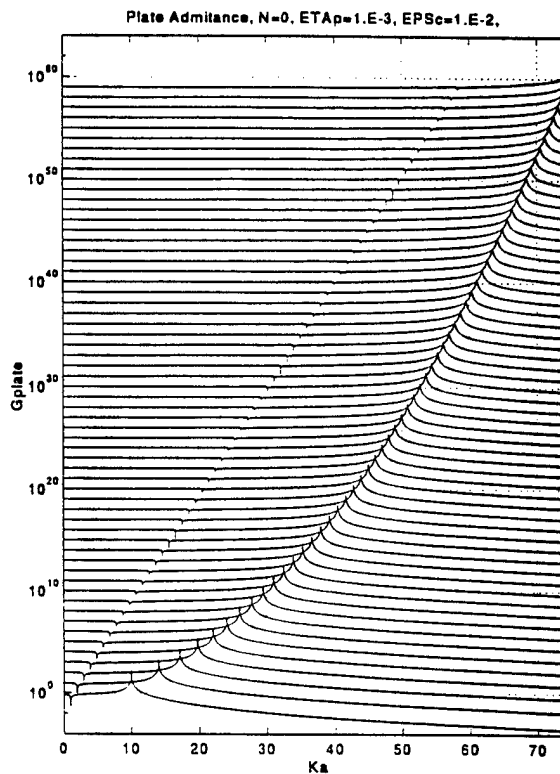


Fig. 8-1a

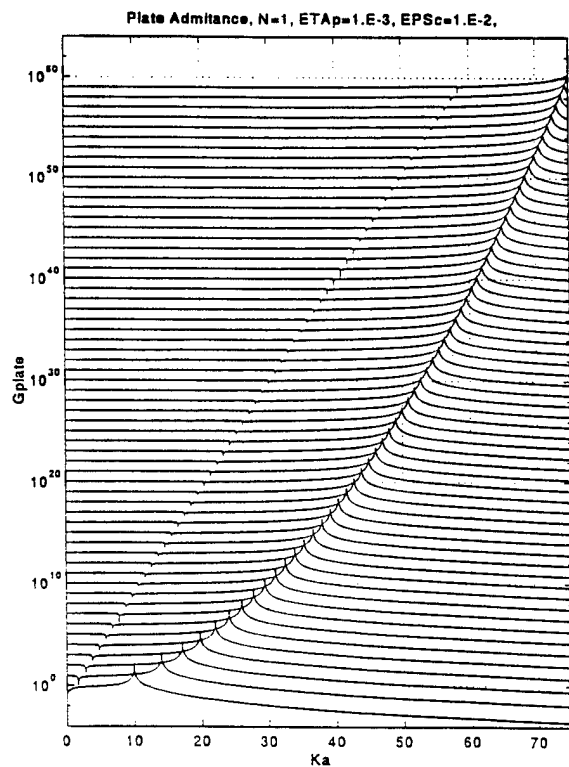


Fig. 8-1b

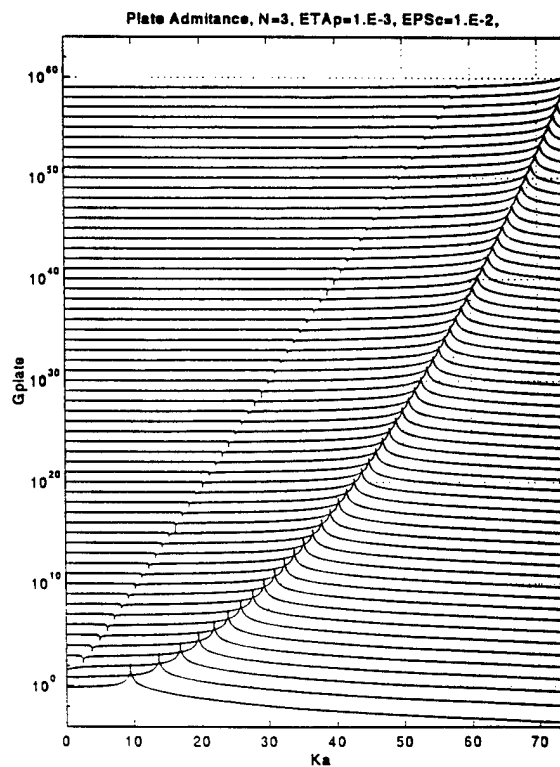


Fig. 8-1c

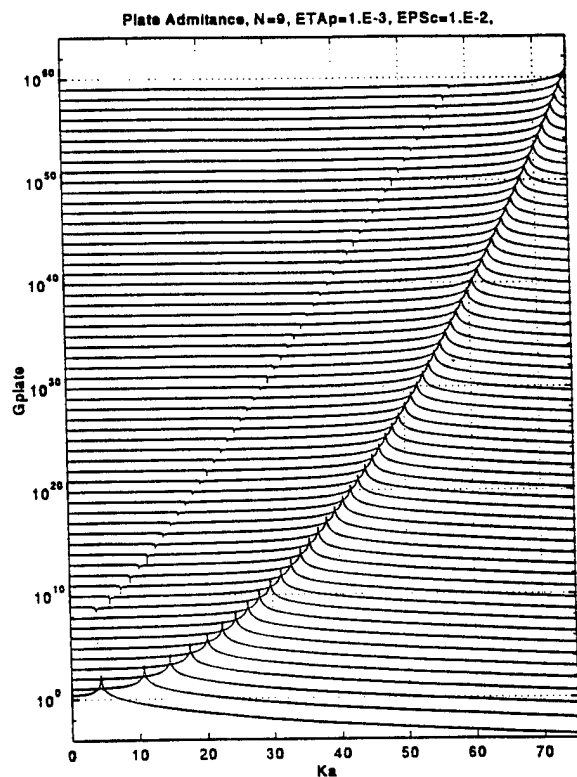


Fig. 8-1d

Fig. 8-2. As in Fig. 8-1a except that the fluid loading parameter is changed from the standard value of  $10^{-2}$  to:

a.  $\epsilon_c = 10^{-4}$ .

b.  $\epsilon_c = 10^{-1}$ .

b.1. Single curves from Figs. 8-1a, 2a and b.

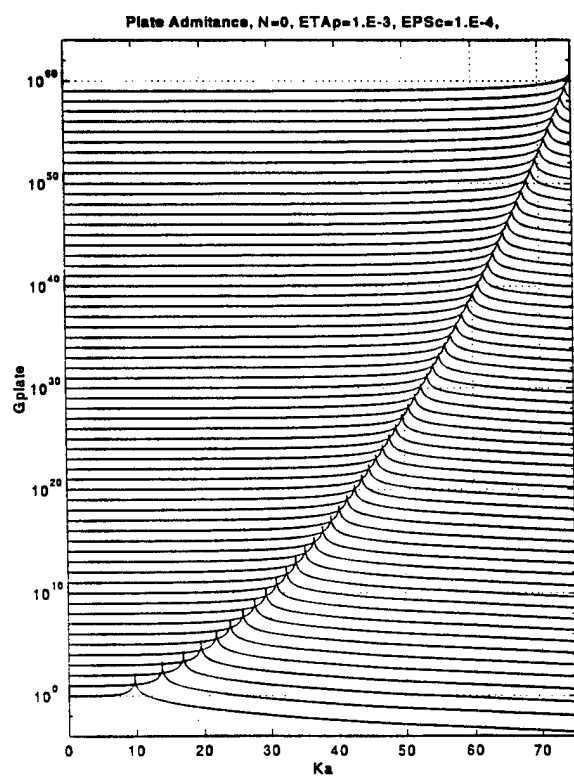


Fig. 8-2a

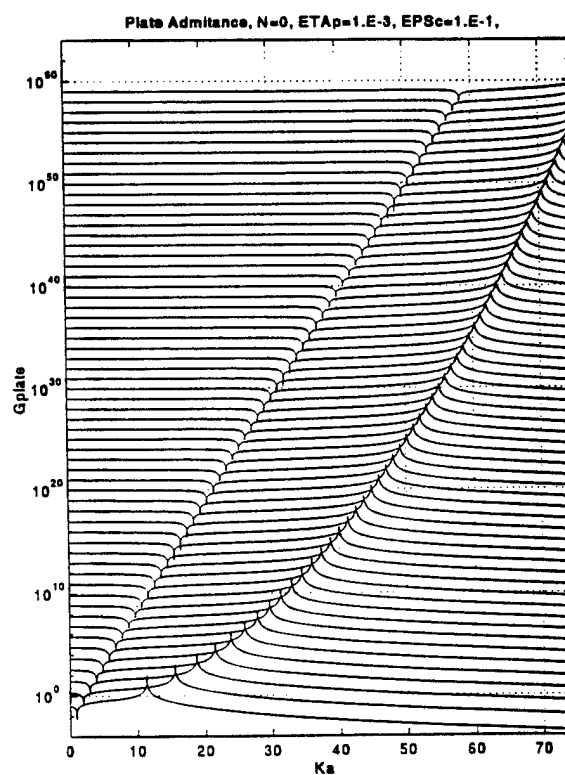


Fig. 8-2b



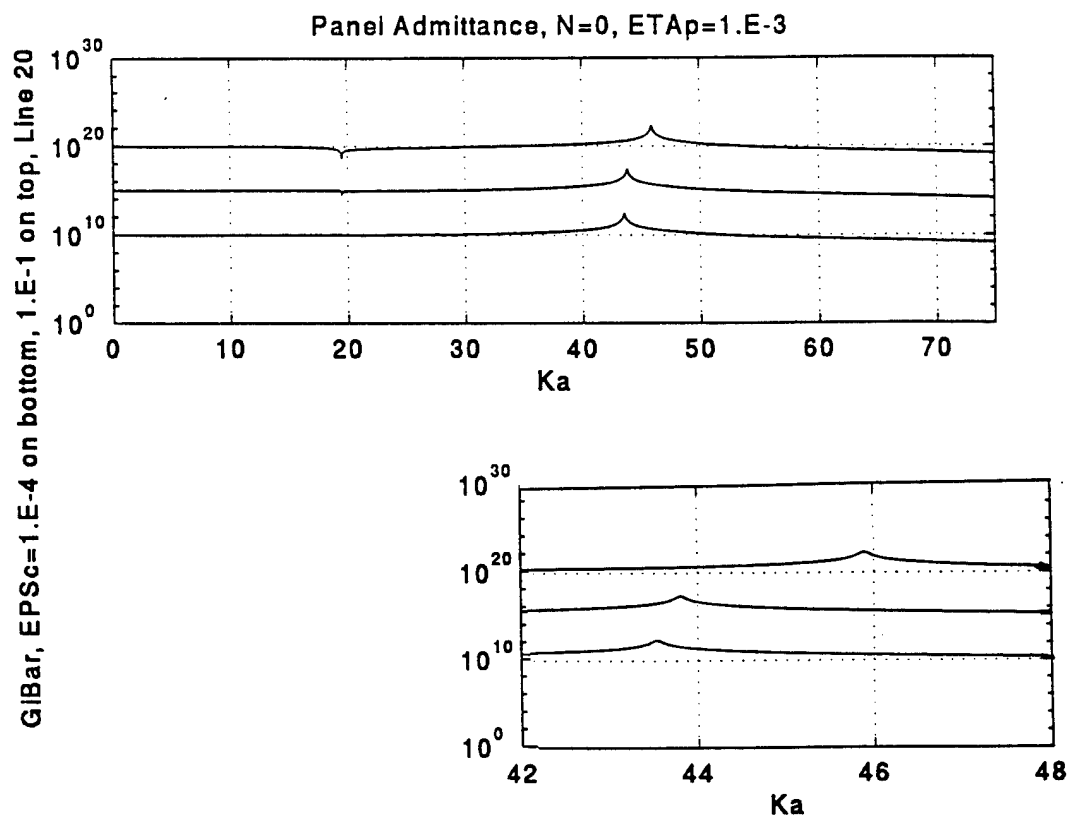


Fig. 8-2b1

Fig. 8-3. Normalized modal fluid loaded surface admittance  $\overline{G}_{\infty n}(k, \omega)$  of a natural cylinder as a function of  $(ak)$  in a frequency waterfall format.

- a. Under standard parametric values [ $n=0$ ].
- b.  $n=1$ .
- c.  $n=3$ .
- d.  $n=9$ .

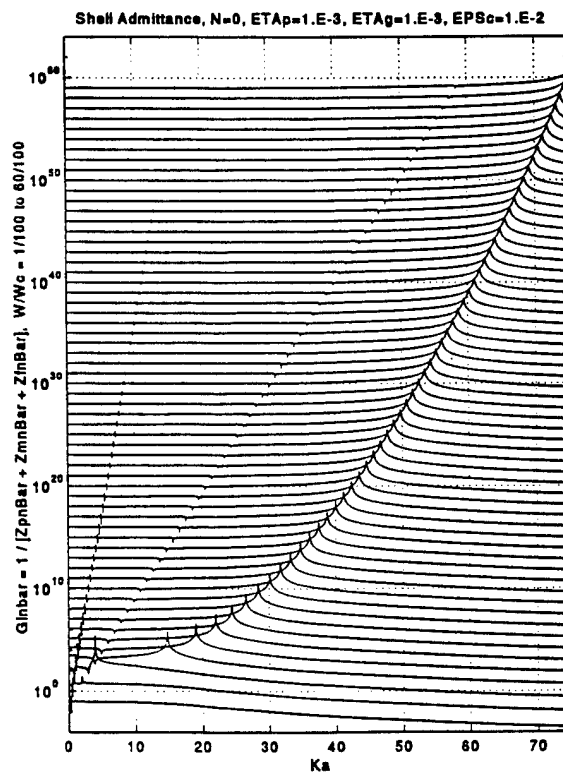


Fig. 8-3a

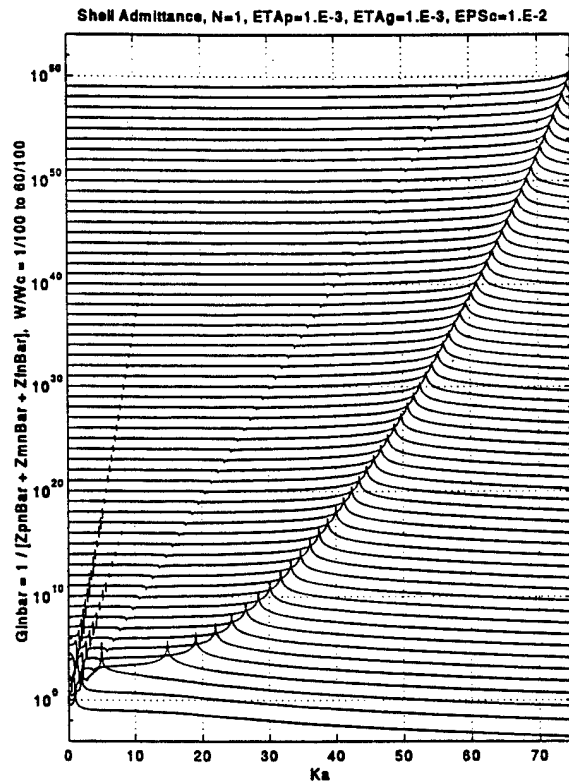


Fig. 8-3b

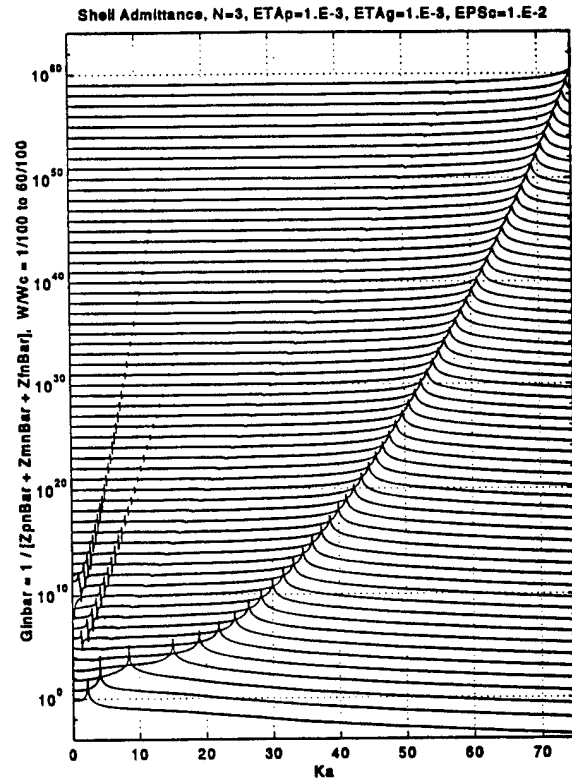


Fig. 8-3c

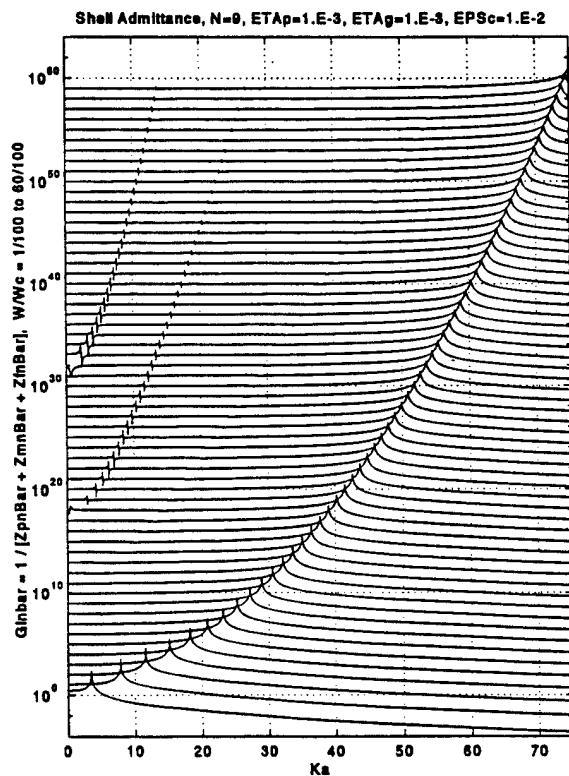


Fig. 8-3d

Fig. 8-4. As in Fig. 8-3a. except that the fluid loading parameter ( $\epsilon_c$ ) is changed from the standard value of  $10^{-2}$  to:

- a.  $\epsilon_c = 10^{-4}$ .
- b.  $\epsilon_c = 10^{-1}$ .
- b.1. Single curves from Figs. 8-3a, 4a and b.

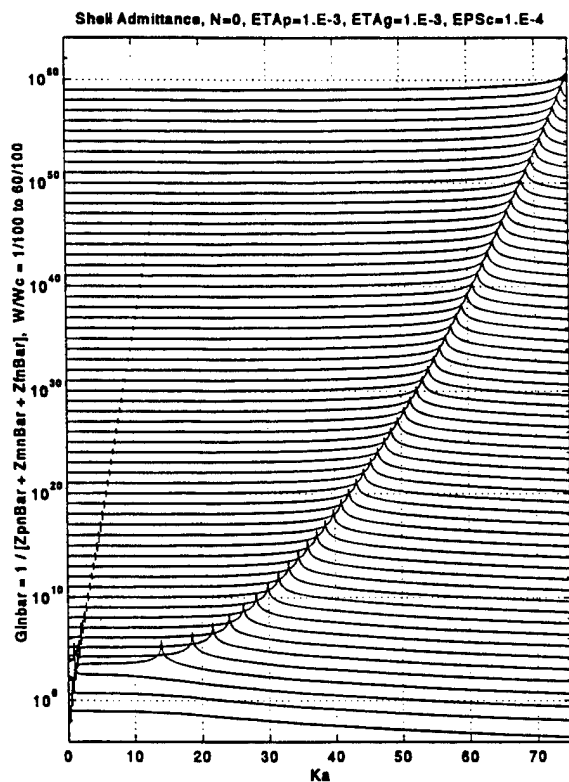


Fig. 8-4a

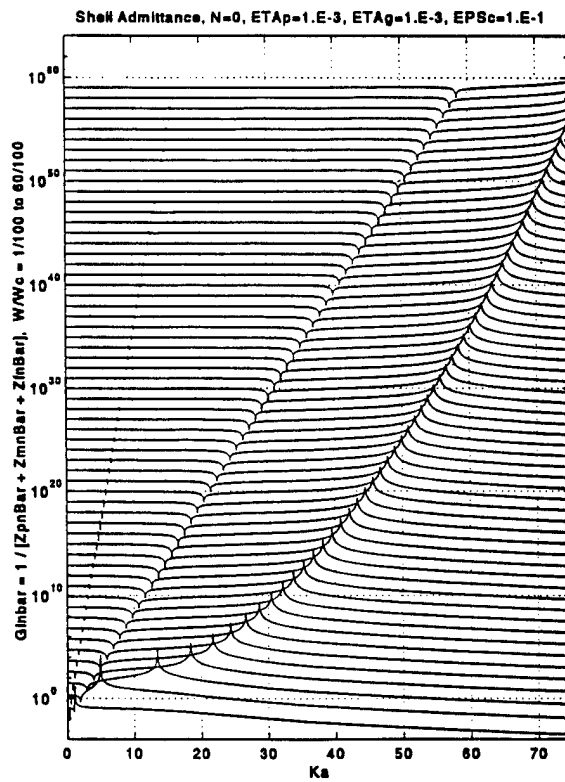


Fig. 8-4b

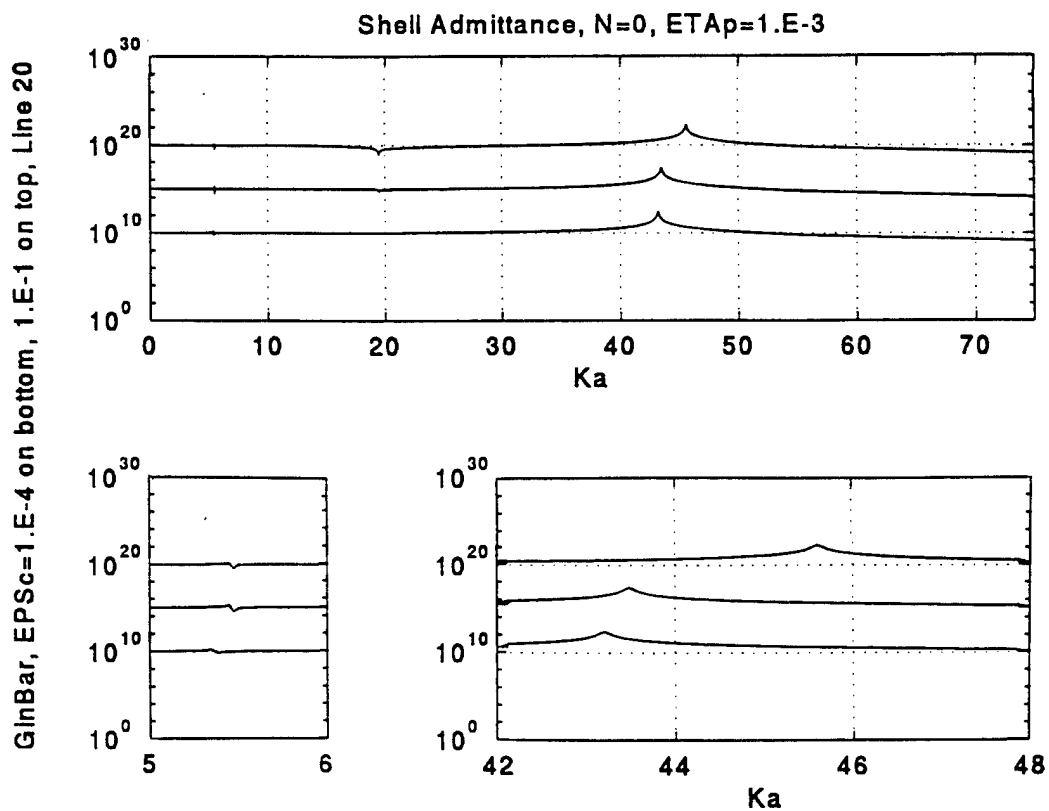


Fig. 8-4b1

Fig. 8-5. As in Fig. 8-3b except that the fluid loading parameter ( $\epsilon_c$ ) is changed from the standard value of  $10^{-2}$  to:

- a.  $\epsilon_c = 10^{-4}$ .
- b.  $\epsilon_c = 10^{-1}$ .
- b1. Single curves from Figs. 8-3b, 5a and b.

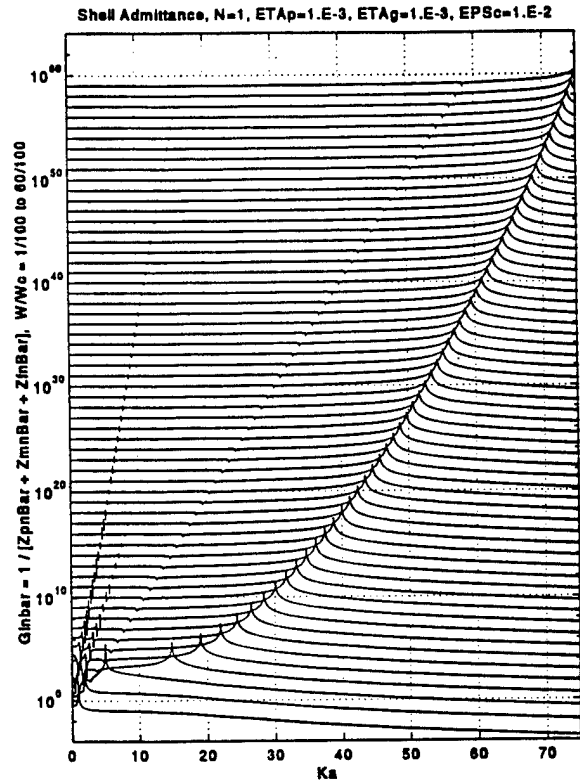


Fig. 8-3b (Repeated)

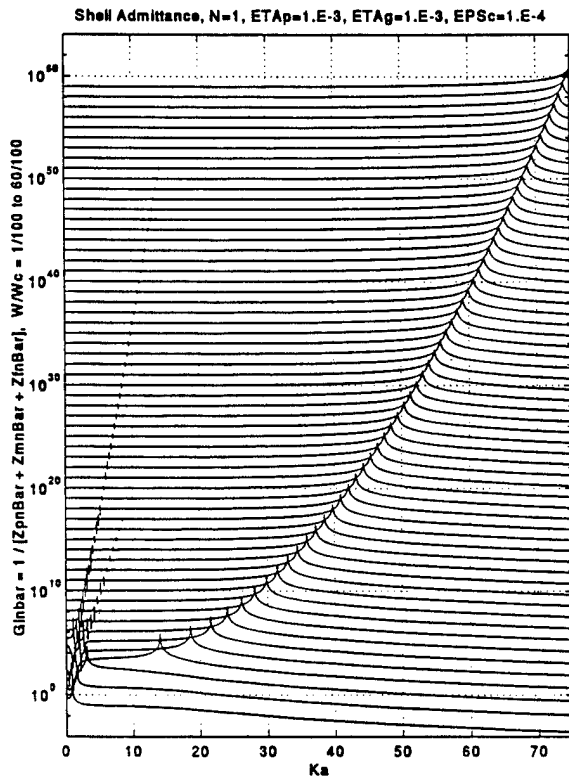


Fig. 8-5a

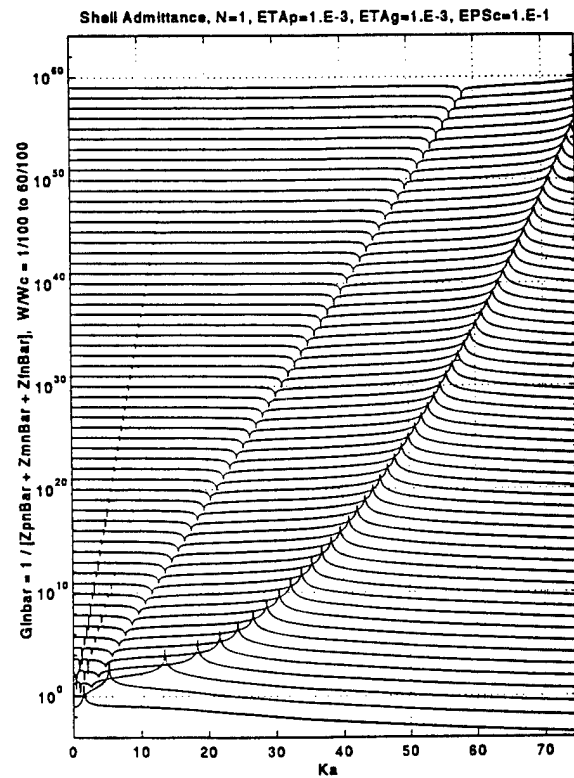


Fig. 8-5b

GlnBar, EPSc=1.E-4 on bottom, 1.E-1 on top, Line 20

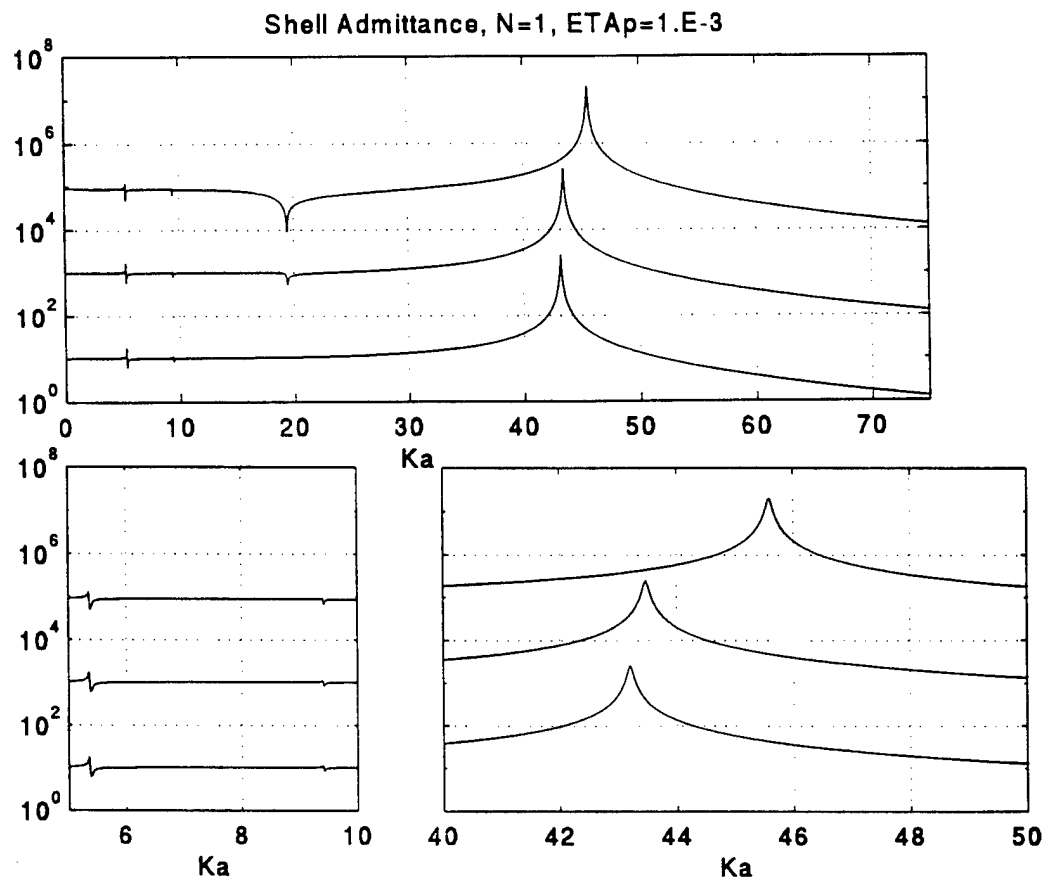


Fig. 8-5b1

Fig. 8-6. As in Fig. 8-3 except that the **natural** cylinder is replaced by a corresponding **hybrid** cylinder.

- a. Under standard parametric values [ $n = 0$ ].
- b.  $n = 1$ .
- c.  $n = 3$ .
- d.  $n = 9$ .

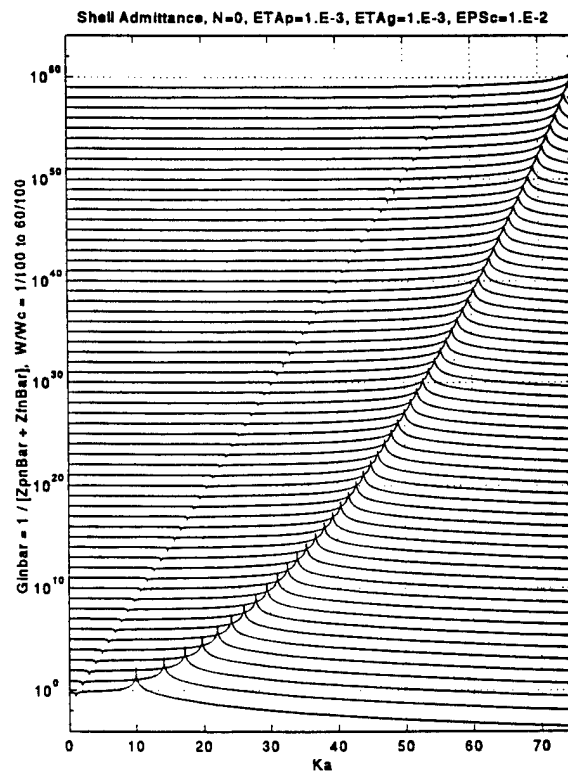


Fig. 8-6a

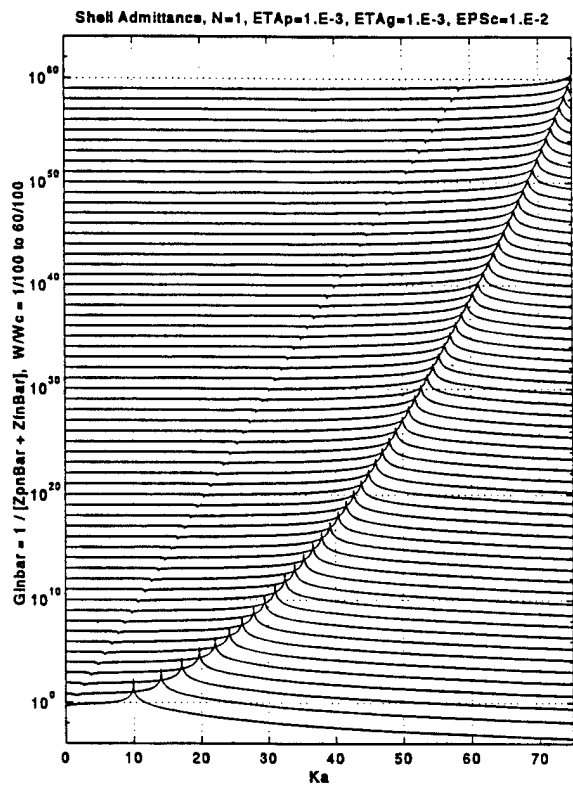


Fig. 8-6b

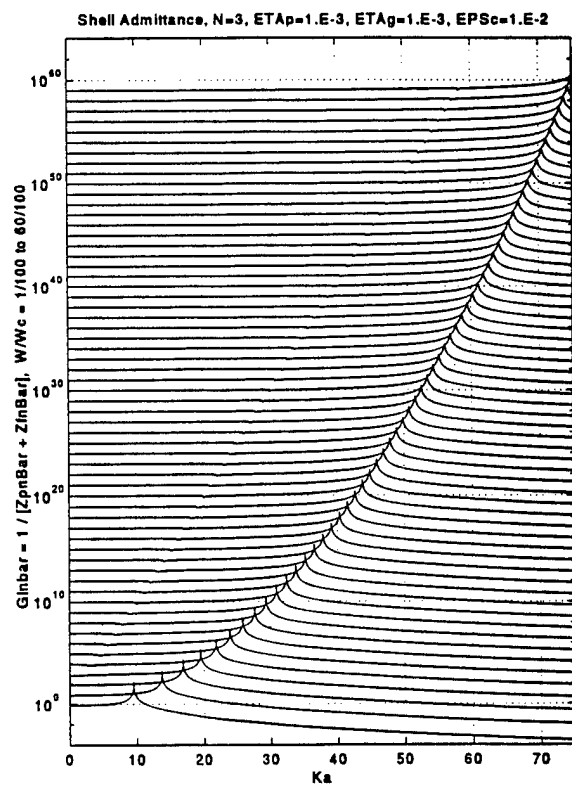


Fig. 8-6c

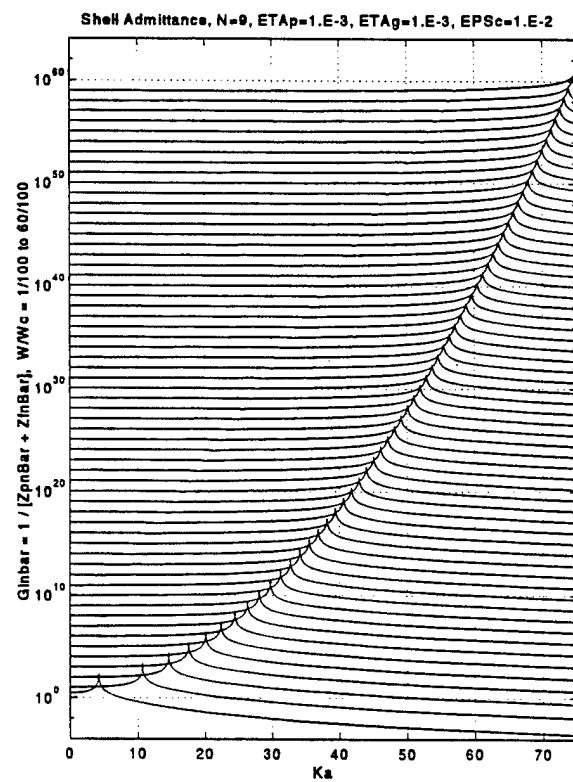


Fig. 8-6d

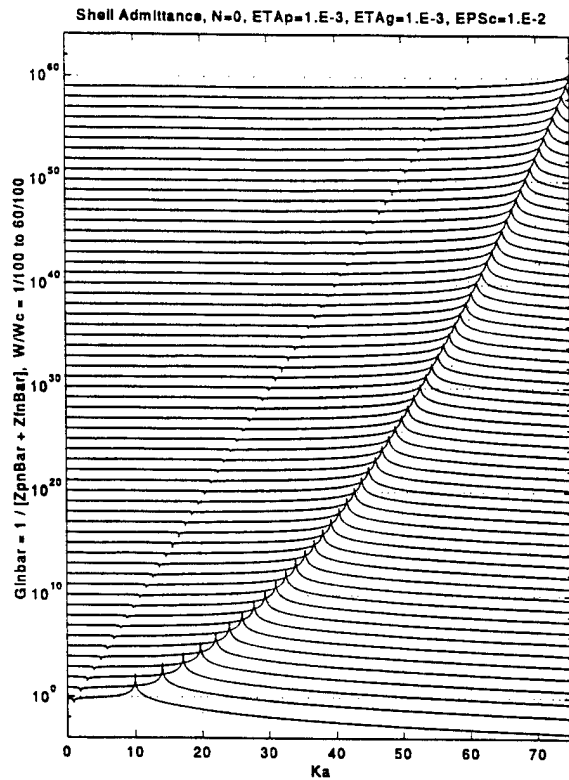


Fig. 8-6a (Repeated)

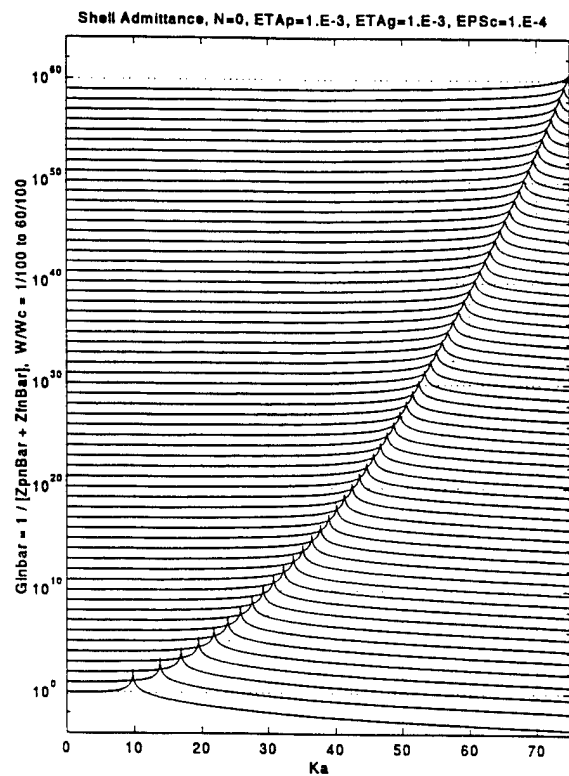


Fig. 8-7a

Fig. 8-7. As in Fig. 8-6a except that the fluid loading parameter ( $\epsilon_c$ ) is changed from the standard value of  $10^{-2}$  to:

- a.  $\epsilon_c = 10^{-4}$ .
- b.  $\epsilon_c = 10^{-1}$ .

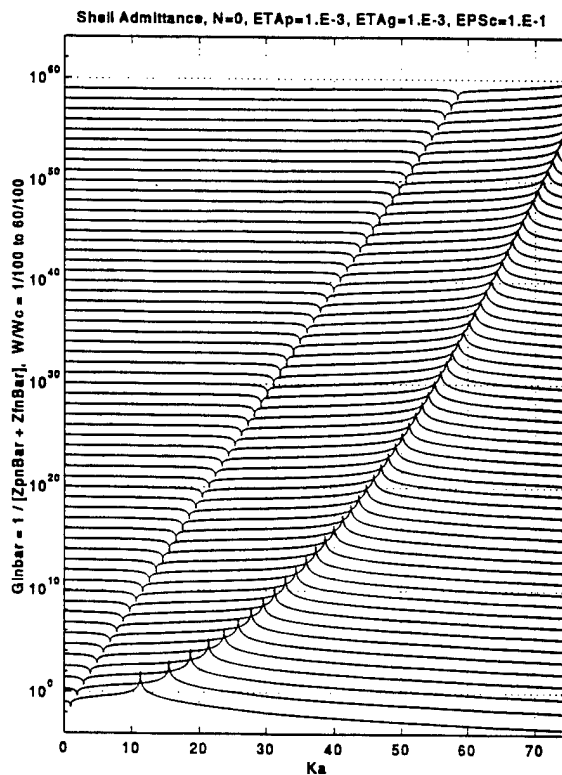


Fig. 8-7b

## IX. ANALYTICAL DEFINITION OF THE RIBS

In this investigation an attempt is made to employ ribs of such characteristics and structure that allow the mathematical description to be of a simple form. The purpose is to investigate phenomena without paying heed to one-to-one correspondence and without trying to address all possible phenomena. Often the presence of too many phenomena tend to obscure the interpretation of data. Understanding the kind of phenomena that may be present and the quantities and parameters that control each may be an essential tool to deciphering measured data. Here a phenomenological correspondence is addressed in the simplest of terms.

In this vein, the ring impedance  $Z_{sn}(\omega)$  of a rib on the cylinder is assumed to be point reacting so the Eqs. (3-28b) and (3-33b) may be stated in the "mode index independent" form

$$Z_{sn}(\omega) = Z_s(\omega) ; \quad [Z(\omega)] = [Z_s(\omega)/b] . \quad (9-1)$$

Since the investigations in this report are on a mode by mode basis, the assumption that  $Z_{sn}(\omega)$  is independent of modal distinction aids in the comparison between modal responses. However, phenomena that are associated with modal variations in the ring impedance of ribs are, thereby, suppressed. This suppression is introduced for the sake of simplicity and not because it is believed that phenomena associated with this modal dependence may not be significant in certain situations.



To infuse some collective variety in the ribs, however, the ring impedance  $Z_s(\omega)$  is assumed to be of the form

$$Z_s(\omega) = i\omega M A(\omega/\omega_o) ; \quad \omega_o = (K_o/M)^{1/2} , \quad (9-2)$$

where  $A(\omega/\omega_o)$  may exhibit a resonance phenomenon of the form

$$A(\omega/\omega_o) = (M_o/M) + \left[ e_o(\omega/\omega_o) + \alpha(\omega/\omega_o)^2 (1-i\eta_o) \right] \cdot \left[ e_o(\omega/\omega_o) - (\omega/\omega_o)^2 (1-i\eta_o) \right]^{-1} , \quad (9-3a)$$

$$e_o(\omega/\omega_o) = \exp[1-(\omega/\omega_o)^\gamma] ; \quad \alpha = [1+(\beta\omega/\omega_c)^2]^{-1} , \quad (9-3b)$$

the quantities  $M$  and  $M_o$  are line masses,  $K_o$  is a line stiffness,  $(\omega_o)$  is the resonance frequency and  $(\eta_o)$  is a loss factor of the rib and  $(\beta)$  and  $(\gamma)$  are adjustable constants; e.g.,  $\beta = 5$  and  $\gamma = 8$ . A physical realization of Eq. (9-3a) with  $\beta = 10^3$  and  $\gamma = 0$  is depicted in Fig. 9-1. The resonance characteristics of  $Z_s(\omega)$  in Eq. (9-3) may be made clearer by considering the asymptotic forms:

1. For  $(\omega/\omega_o) \ll 1$ ,

$$A(\omega/\omega_o) \rightarrow (M_o/M) + 1 , \quad (9-4a)$$

rendering  $Z_s(\omega)$  mass controlled.

2. For  $(\omega / \omega_o) \cong 1$ ,

$$A(\omega / \omega_o) \rightarrow (M_o / M) + [(1 + \alpha) \{(i\eta_o)^{-1} - \alpha(1 + \alpha)^{-1}\}] \quad (9-4b)$$

rendering  $Z_s(\omega)$  with a strong resistance controlled term and is substantially **resistance controlled** if  $|(M_o / M) - \alpha| \ll (\eta_o)^{-1} (1 + \alpha)$ .

3. For  $(\omega / \omega_o) \gg 1$ ,

$$A(\omega / \omega_o) \rightarrow (M_o / M) - \alpha, \quad (9-4c)$$

rendering  $Z_s(\omega)$  **stiffness controlled** if  $(M_o / M) \ll \alpha$ . The standard values of  $(M / mb)$ ,  $(\omega_o / \omega_c)$ ,  $\eta_o$ ,  $\beta$ , and  $\gamma$  are engaged by setting

$$\begin{aligned} (M / mb) &= 0.2 ; & (M_o / M) &= 0 ; & (\omega_o / \omega_c) &= 10 ; \\ \eta_o &= 3 \times 10^{-1} ; & \beta &= 5 ; \text{ and } & \gamma &= 8 . \end{aligned} \quad (9-5)$$

The factor  $A(\omega / \omega_o)$  is typically depicted in Figs. 9-2a-f as a function of  $(\omega / \omega_c)$ . In Figs. 9-2a-c, the factor  $A(\omega / \omega_o)$  is commensurate with the physical realization of the rib which is depicted in Fig. 9-1; in these figures  $(\omega_o / \omega_c) = 10, 10^{-2}$  and  $2.5 \times 10^{-1}$ , respectively. In Fig. 9-2d, the standard values prevail. In Figs. 9-2e and f,  $(\omega_o / \omega_c)$  is changed from the standard value of 10 to  $10^{-2}$  and  $2.5 \times 10^{-1}$ , respectively. Figure 9-2g repeats Fig. 9-2f except that the loss factor  $(\eta_o)$  is changed from the standard value of  $3 \times 10^{-1}$  to  $10^{-1}$ . The influence of this change is as expected. The asymptotic cases stated in Eq. (9-4) are readily discernible in all these figures. These asymptotic forms dictate the choice of the generic construction for the ribs. Again, the standard choice is

$\beta = 5, \gamma = 8$  and  $\eta_o = 0.3$ . These values facilitate the investigation of the influence that a particular ring impedance of the rib has on the response behavior of a ribbed cylinder. The facility is associated with the quicker transition with frequency from a mass controlled to stiffness controlled ring impedance, which is controlled by  $(\gamma)$ , and the avoidance of a sharp diminution of the ring impedance once it becomes stiffness controlled, which is controlled by  $(\beta)$ . These asymptotic forms may, in turn, answer questions regarding the worth of an effort to change this particular behavior by changing the construction of the ribs; e.g., is the introduction of resistance controlled line and ring impedance for the ribs advantageous in controlling the response behavior of panels and cylinders in the frequency band  $(\omega_o \eta_o)$  centered about  $(\omega / \omega_o) = 1$ ? In part, to answer such a question the influence of a resistance controlled line impedance in the ribs may be worth special diagnostic examination. For this purpose it may be useful to define  $A'(\omega / \omega_o)$  in the form

$$A'(\omega / \omega_o) = \text{Re}\{A(\omega / \omega_o)\} + (2)^{-1/2} \text{Im}\{A(\omega / \omega_o)\} \cdot \{U[(\omega_o / \omega_c) - (\omega / \omega_c)] - U[(\omega / \omega_c) - (\omega_o / \omega_c)]\} . \quad (9-6)$$

The substitution of  $A'(\omega / \omega_o)$  for  $A(\omega / \omega_o)$  maintains the magnitude of the line impedance of the rib but eliminates its resistance controlled character; this elimination is of significance at and in the vicinity of the resonance frequency when  $(\omega / \omega_o) \simeq 1$ . At frequencies outside of this narrow frequency band,  $A'(\omega / \omega_o)$  is substantially identical to  $A(\omega / \omega_o)$ . Figure 9-2f is repeated in Fig. 9-2h except that  $A'(\omega / \omega_o)$  is substituted for  $A(\omega / \omega_o)$ . The absence of damping in the rib is demonstrated by the imaginary part that is equal to zero; indeed,  $\text{Im}\{A'(\omega / \omega_o)\} = 0$  as can be verified from Eq. (9-6).

To condense the volume of information contained within figures cast in the waterfall format relative to the nature of the ribs,  $(\omega_o / \omega_c)$  is set equal largely to 10 and/or  $10^{-2}$ ; with  $(\omega_o / \omega_c)$  equal to 10,  $A(\omega / \omega_o) = 1$  and the ring impedance is mass controlled. On the other hand, with  $(\omega_o / \omega_c)$  equal to  $10^{-2}$ ,  $A(\omega / \omega_o) = -\alpha$  and the ring impedance is stiffness controlled. A few significant cases are, however, briefly depicted in which the resonance frequency falls inside the frequency range of consideration in this report; i.e.,  $(\omega_o / \omega_c)$  is selected equal to  $2.5 \times 10^{-1}$ . [cf. Fig. 9-2c.] A more elaborate investigation of the use of the ribs as effective damping agents awaits further investigation. In this report this investigation is merely initiated.

Using the form stated in Eq. (9-2) for the ring impedance of a rib, the quantity  $Q_{\infty n}(k, \omega)$ , defined in Eq. (3-42b) can be stated in the more explicit form

$$Q_{\infty n}(k, \omega) = Z_n(\omega_o) G_{\infty n}(k, \omega) = (M / mb) A(\omega / \omega_o) \bar{G}_{\infty n}(k, \omega), \quad (9-7)$$

where  $\bar{G}_{\infty n}(k, \omega)$  is the normalized fluid loaded surface admittance of the uniform cylinder, which is defined in Eqs. (8-2) and (8-4). The entrance of the functional form of the rib is completely accounted for in Eq. (9-7). Indeed, the function  $Q_{\infty n}(k, \omega)$  contains all the information that the formalism requires of the description of the rib in a regularly ribbed cylinder. In particular, Eq. (9-7) clarifies that  $Q_{\infty n}(k, \omega)$  duplicate the wavenumber ( $k$ ) dependence of  $\bar{G}_{\infty n}(k, \omega)$ ; it is modulated by the frequency dependent factor  $A(\omega / \omega_o)$ , and it admits to a scale factor  $(M / mb)$  that is independent of both the wavenumber ( $k$ ) and the frequency ( $\omega$ ). Thus, except for these frequency modulations, the patterns, in the waterfall representation of  $Q_{\infty n}(k, \omega)$ , are similar to those of  $\bar{G}_{\infty n}(k, \omega)$ , e.g., those

shown in Figs. 8-3 through 7. Figures 9-3 and 4 depict the absolute values of  $Q_{\infty n}(k, \omega)$ , as a function of  $(ak)$  in a waterfall format, for the hybrid and natural cylinders, respectively. The standard parametric values, stated in Eqs. (6-4) and (9-5), are used in Figs. 9-3a and 4a. Figure 9-5a duplicates Fig. 9-4a except that the standard value of zero for  $(n)$  is changed to unity. The emergence of the shear free waves is the only substantial difference between these two figures. [cf. Figs. 8-1 and 2.] In addition, in Figs. 9-3b and c, 9-4b and c and 9-5b and c the normalized resonance frequency  $(\omega_o / \omega_c)$  is changed from its standard value of 10 to  $10^{-2}$  and  $2.5 \times 10^{-1}$ , respectively. The influence of the resonance on the line impedance of the ribs is discernible in Figs. 9-3c, 4c and 5c. In particular, in the frequency range below the resonance; i.e., when  $(\omega / \omega_c) < 2.5 \times 10^{-1}$ , the patterns in these figures duplicate those in Figs. 9-3a, 4a and 5a and above the resonance; i.e., when  $(\omega / \omega_c) > 2.5 \times 10^{-1}$ , the patterns duplicate those in Figs. 9-3c, 4b and 5b, respectively. At resonance Figs. 9-3c, 4c and 5c neither duplicate Figs. 9-3a, 4a and 5a nor Figs. 9-3b, 4b and 5b; the line impedance at and in the vicinity of resonance is largely resistance controlled and its absolute value is high. Figure 9-5d repeats Fig. 9-5c, except that  $A(\omega / \omega_o)$  is replaced by a corresponding  $A'(\omega / \omega_o)$ ; where  $A'(\omega / \omega_o)$  is defined in Eq. (9-6). Figures 9-5c and d are substantially the same. Figure 9-5e repeats Fig. 9-5c except that the conditions depicted in Fig. 9-2c replace those depicted in Fig. 9-2f. Observe that the transition through resonance from mass to stiffness controlled is more gradual in Figs. 9-2c and 5e than in Figs. 9-2f and 5c. Again, it is emphasized that these curves differ only by modulation with respect to the frequency variable, and, of course, with respect to sign and quadrature. However, the differences with respect to sign and quadrature are not depicted in

Figs. 9-3, 4 and 5. The significance of the sign and quadrature of  $A(\omega / \omega_o)$  on the response of a regularly ribbed cylinder is yet to be deciphered.

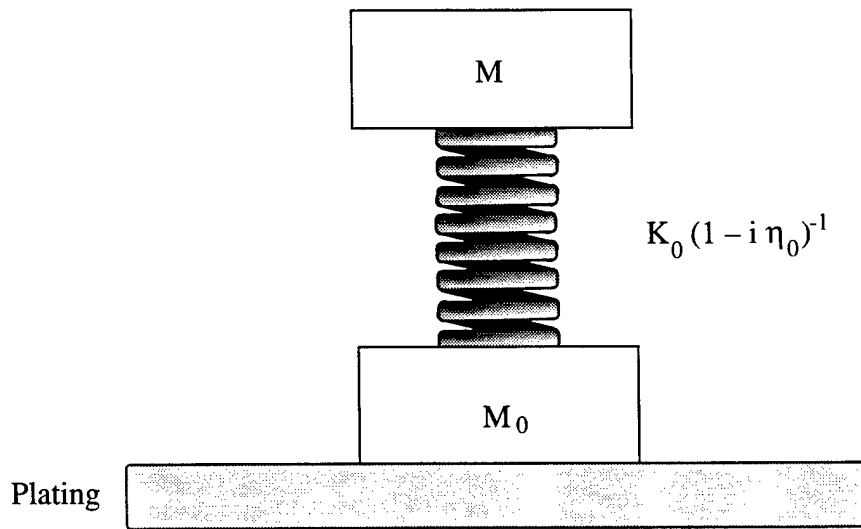


Fig. 9-1. A Simple Mass-Spring System Used to Provide Frequency Resonance in the Line or Ring Impedance of a Rib.

Fig. 9-2. Real and imaginary parts of the factor  $A(\omega / \omega_o)$  in the ring impedance of a rib as functions of the normalized frequency  $(\omega / \omega_c)$  and for  $(M_o / M) = 0$ . [cf. Eqs. (9-2) - (9-5).]

- a. Mass controlled rib  $[(\omega_o / \omega_c) = 10, \eta_o = 0.3], \beta = 10^3$  and  $\gamma = 0$ .
- b. Stiffness controlled rib  $[(\omega_o / \omega_c) = 10^{-2}, \eta_o = 0.3], \beta = 10^3$  and  $\gamma = 0$ .
- c. Resonating rib  $[(\omega_o / \omega_c) = 2.5 \times 10^{-1}, \eta_o = 0.3], \beta = 10^3$  and  $\gamma = 0$ .
- d. Standard mass controlled rib  $[(\omega_o / \omega_c) = 10, \beta = 5, \gamma = 8, \text{ and } \eta_o = 0.3]$ .
- e. Stiffness controlled rib  $[(\omega_o / \omega_c) = 10^{-2}]$ .
- f.  $(\omega_o / \omega_c) = 2.5 \times 10^{-1} [\eta_o = 0.3]$
- g.  $(\omega_o / \omega_c) = 2.5 \times 10^{-1} \quad \eta_o = 10^{-1}$
- h. As in f. except that the factor  $A(\omega / \omega_o)$  is replaced by the modified factor  $A'(\omega / \omega_o)$ . [cf. Eqs. (9-3 and 6).]

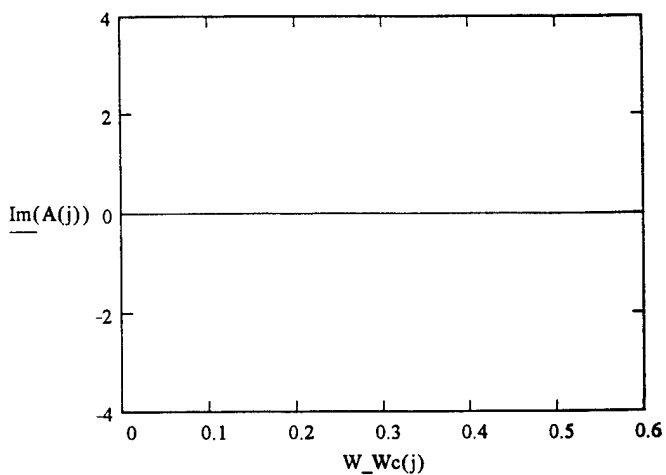
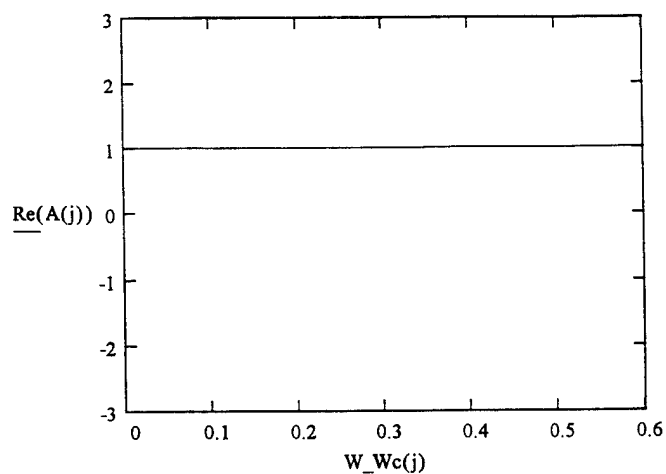


Fig. 9-2a

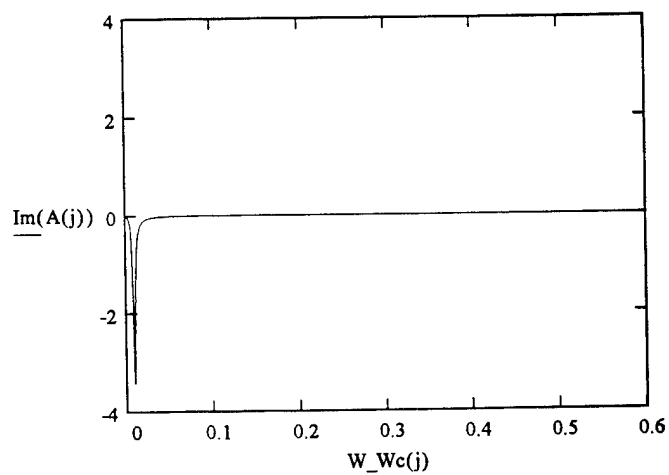
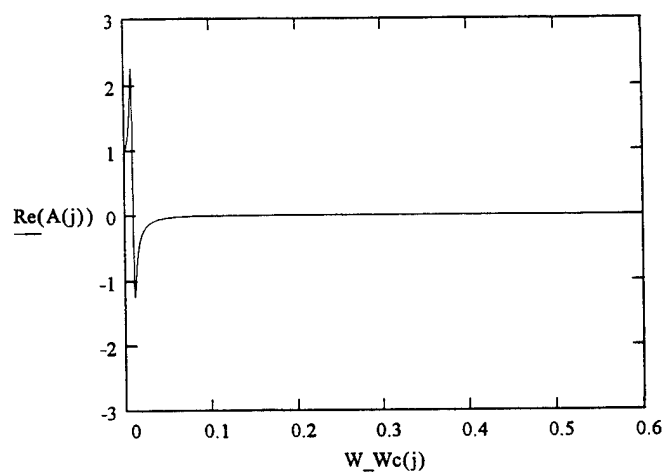


Fig. 9-2b

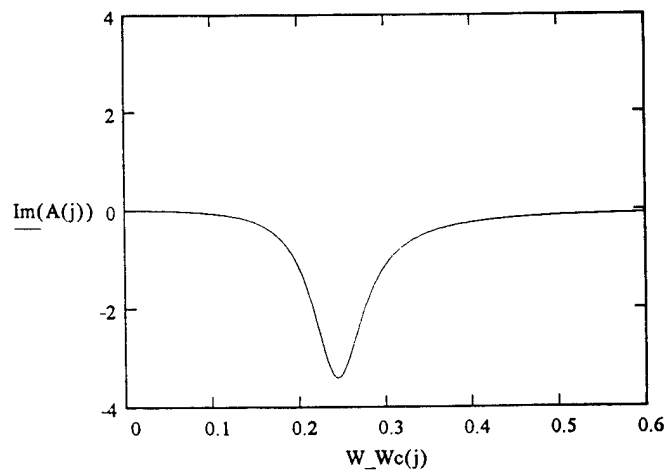
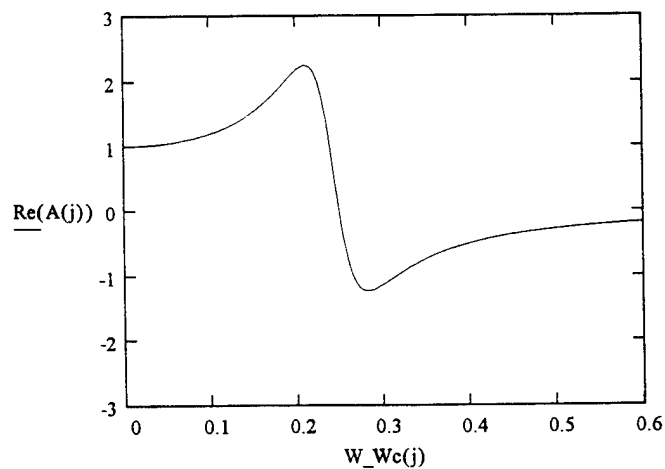


Fig. 9-2c



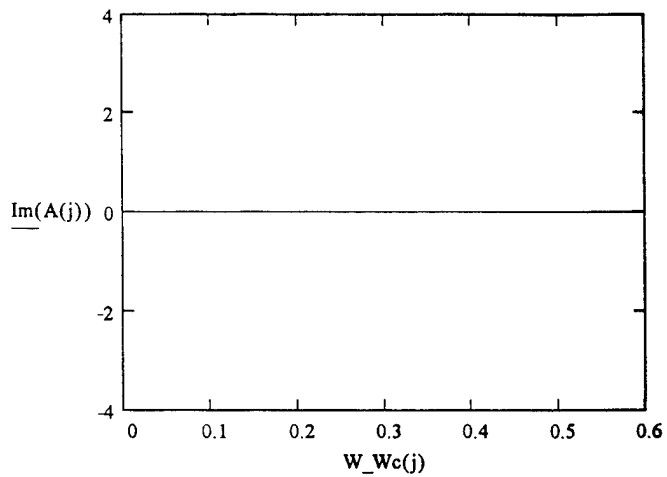
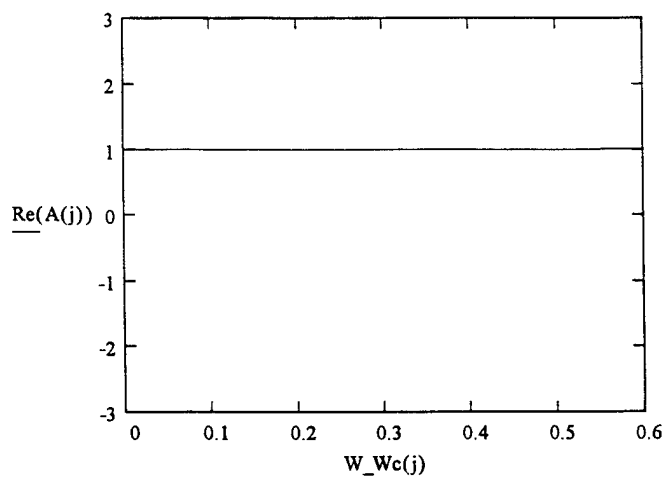


Fig. 9-2d

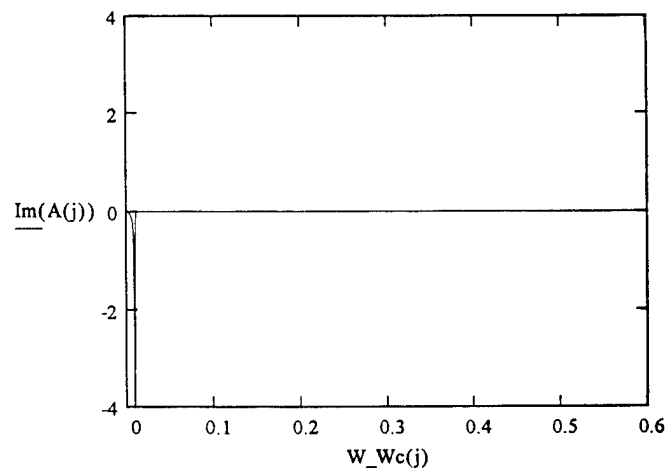
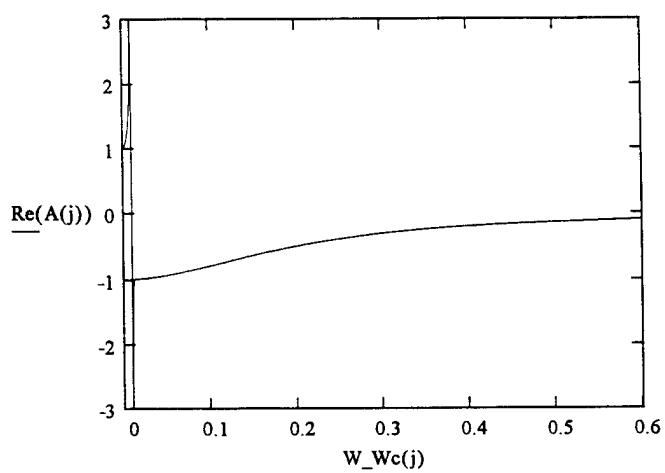


Fig. 9-2e

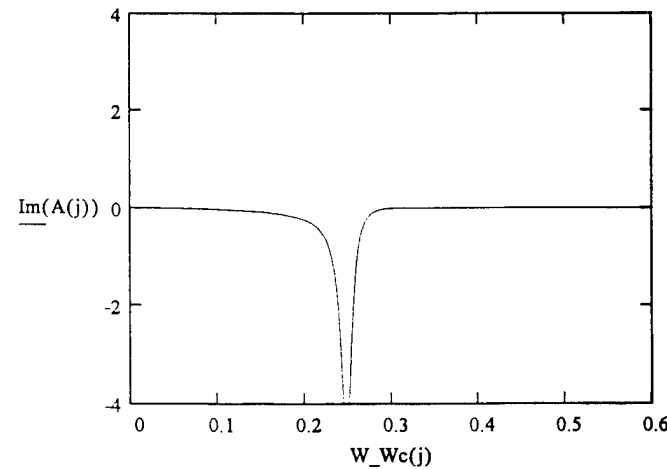
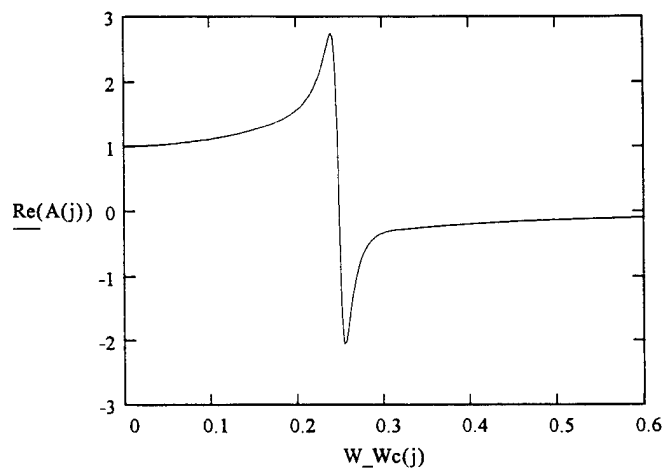


Fig. 9-2f

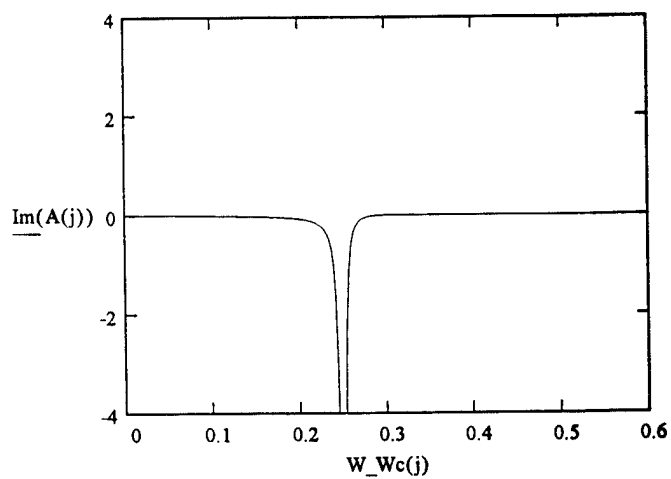
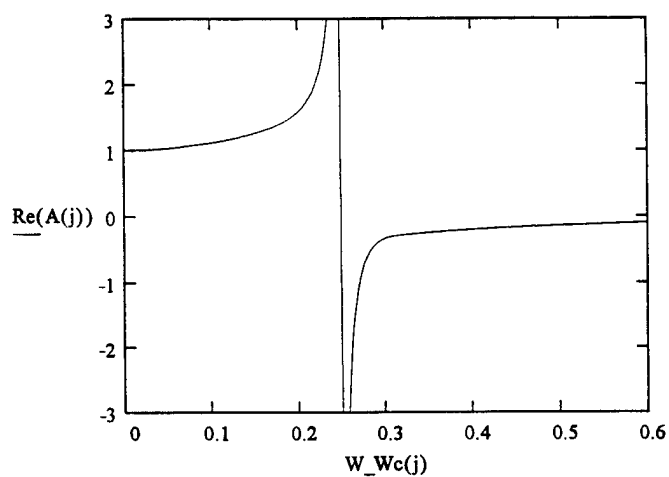


Fig. 9-2g

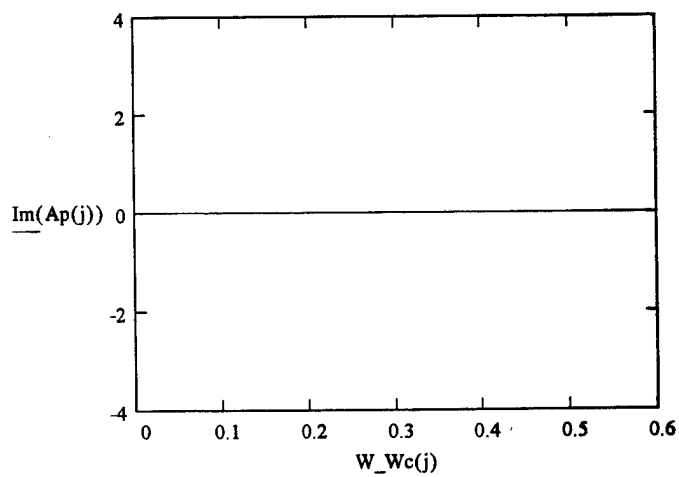
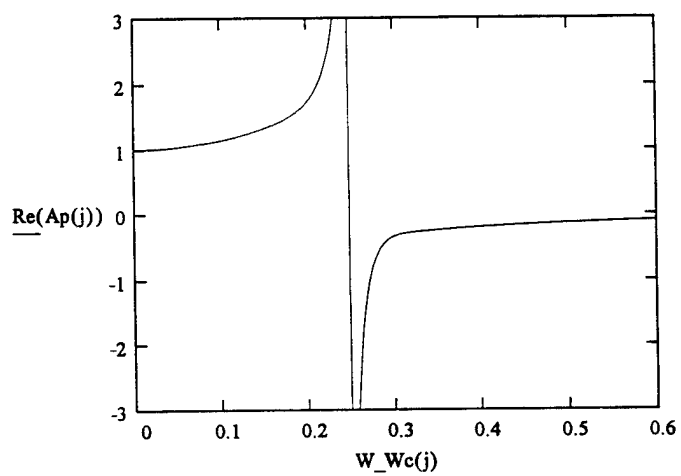


Fig. 9-2h

Fig. 9-3. Absolute value of the ratio  $Q_{\infty n}(k, \omega)$  for a hybrid cylinder as a function of  $(ka)$  displayed in a frequency waterfall format. [cf. Eq. (9-7).]

- a. Mass controlled rib  $[(\omega_o / \omega_c) = 10]$ .
- b. Stiffness controlled rib  $[(\omega_o / \omega_c) = 10^{-2}]$ .
- c.  $(\omega_o / \omega_c) = 2.5 \times 10^{-1}$ .

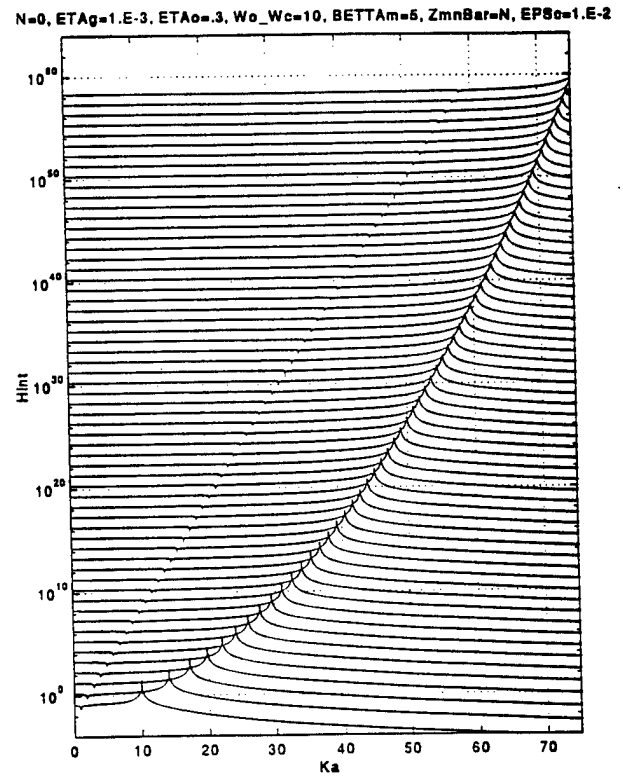


Fig. 9-3a

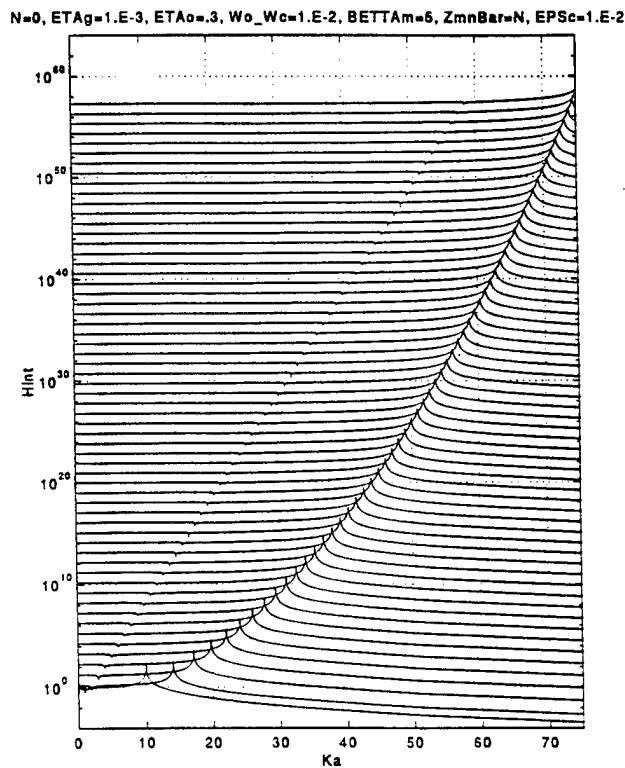


Fig. 9-3b

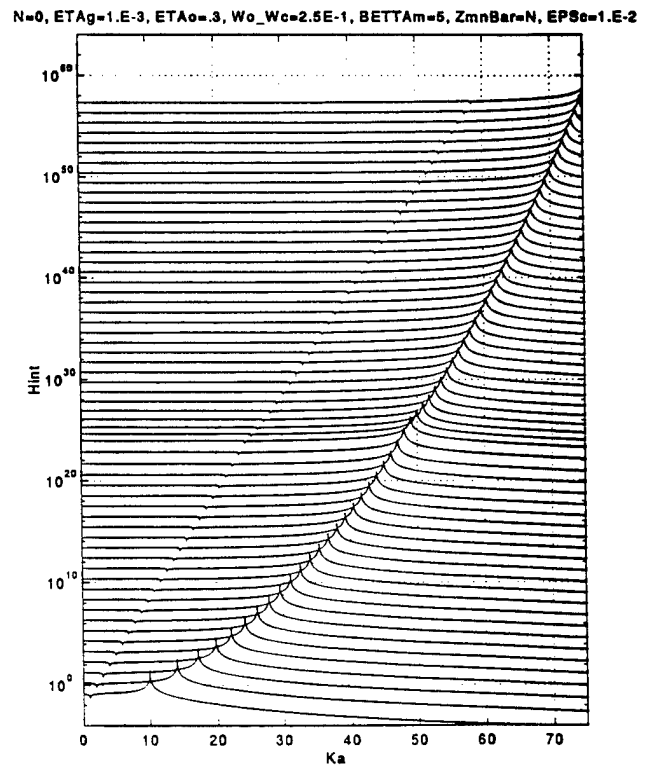


Fig. 9-3c

Fig. 9-4. As in Fig. 9-3 except that a **natural** cylinder is substituted.

- a. Mass controlled rib  $[(\omega_o / \omega_c) = 10]$ .
- b. Stiffness controlled rib  $[(\omega_o / \omega_c) = 10^{-2}]$ .
- c.  $(\omega_o / \omega_c) = 2.5 \times 10^{-1}$ .

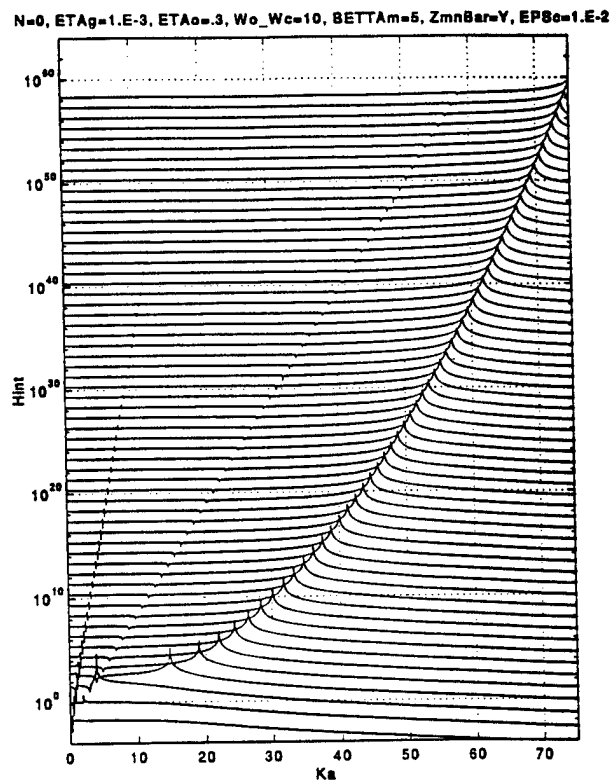


Fig. 9-4a

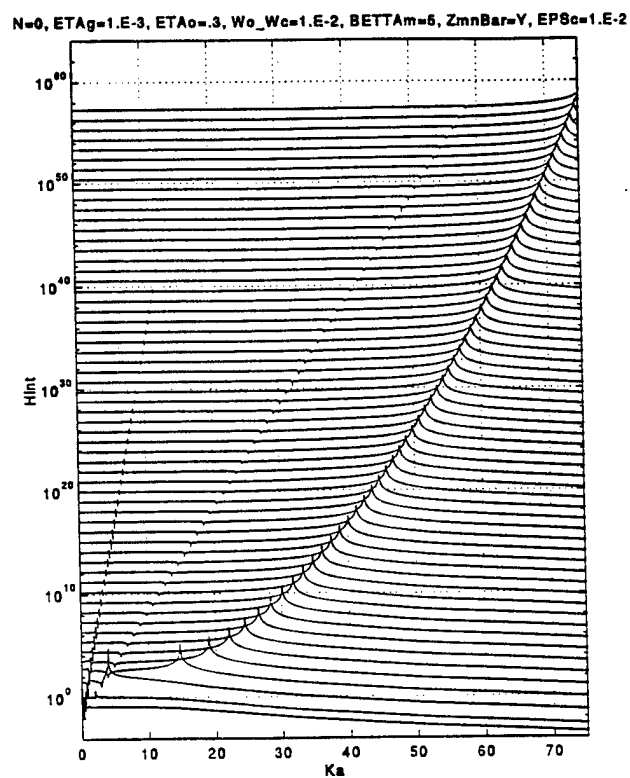


Fig. 9-4b

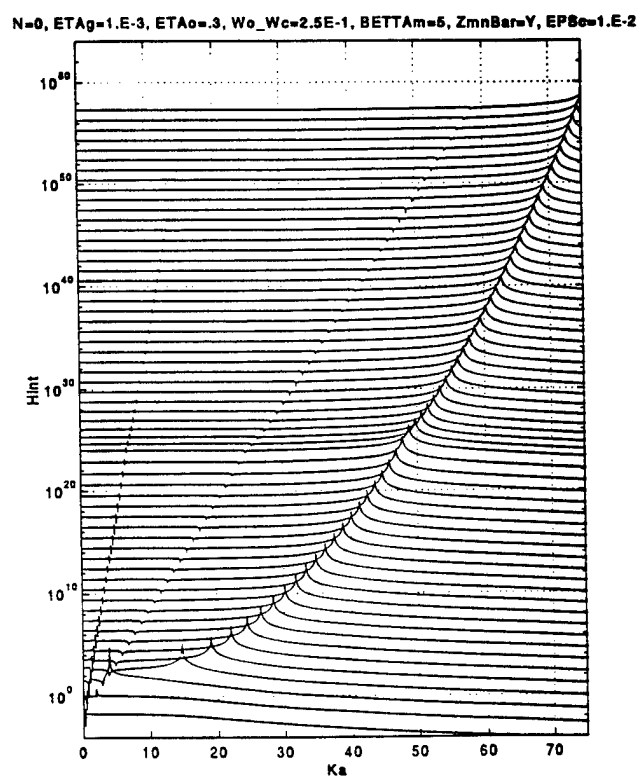


Fig. 9-4c

Fig. 9-5. As in Fig. 9-4 except that the mode index ( $n$ ) is changed from the standard value of zero to unity.

- Mass controlled rib  $[(\omega_o / \omega_c) = 10]$ .
- Stiffness controlled rib  $[(\omega_o / \omega_c) = 10^{-2}]$ .
- $(\omega_o / \omega_c) = 2.5 \times 10^{-1}$ .
- $(\omega_o / \omega_c) = 2.5 \times 10^{-1}$  and  $A(\omega / \omega_o)$  is replaced by  $A'(\omega / \omega_o)$  [cf. Eqs. (9-3 and 6).]
- $(\omega_o / \omega_c) = 2.5 \times 10^{-1}$ ,  $\beta = 10^3$  and  $\gamma = 0$  [cf. Fig.9-2c versus Fig. 9-2f.]

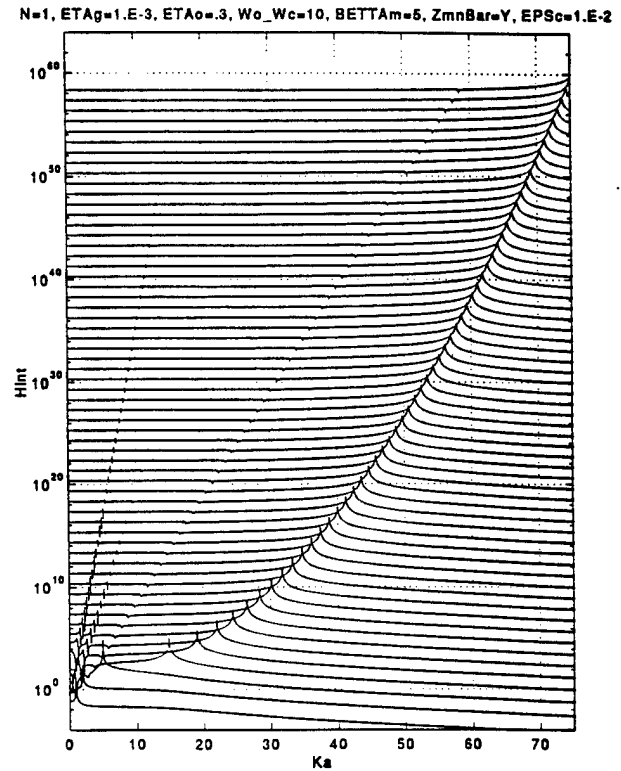


Fig. 9-5a

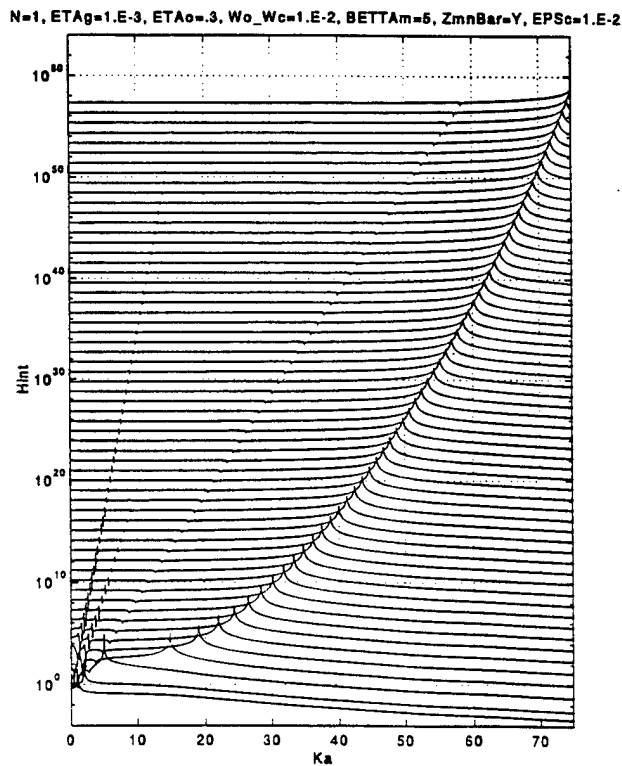


Fig. 9-5b

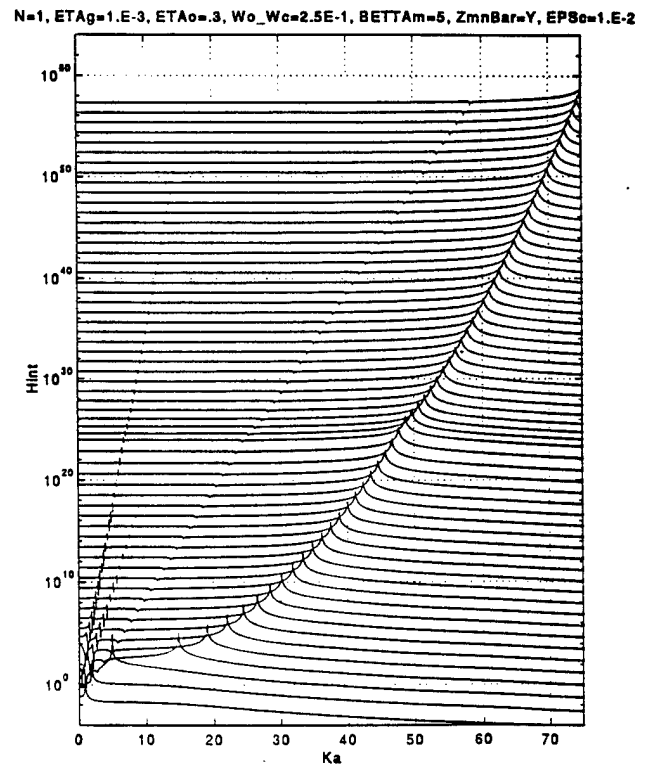


Fig. 9-5c

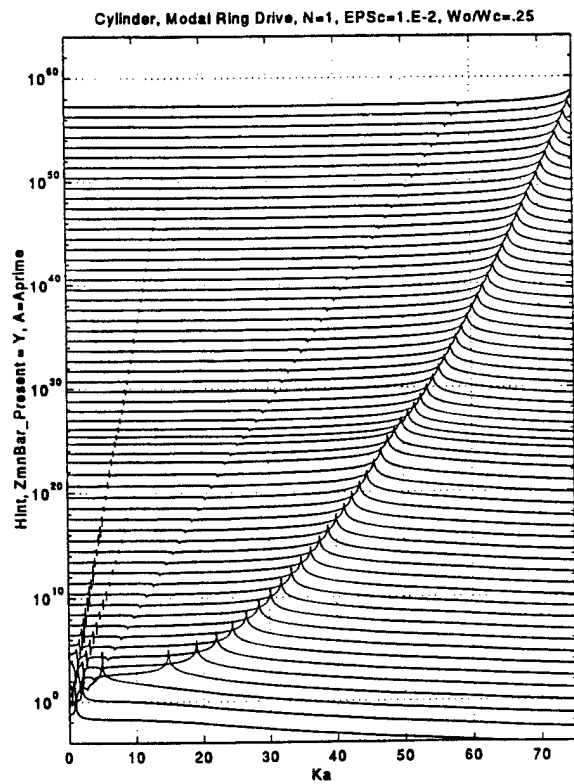


Fig. 9-5d

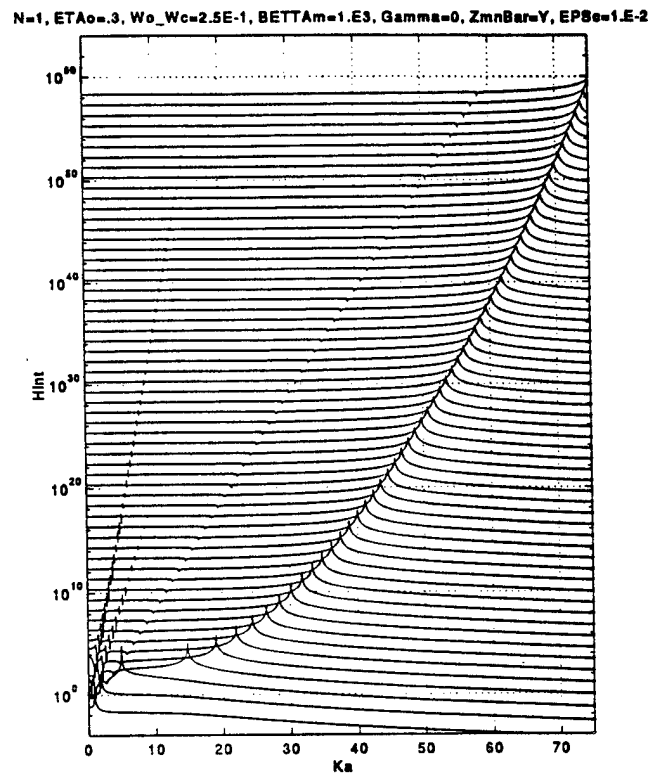


Fig. 9-5e

## X. ALIASING IN THE DRIVE $P_{sn}(k, \omega)$ IN LIEU OF THE RIBS

The requirements stated at the end of Section III are satisfied in Sections IV-IX and the phenomenon of aliasing stated in Eq. (3-48) can then be dealt with. Again it is emphasized that hereafter only the regularly ribbed hybrid cylinder and the regularly ribbed natural cylinder are considered so that the dual representations of the formalism can be condensed under a single mantle. One is reminded that the hybrid cylinder is a natural cylinder from which the membrane response is removed.

In this vein Eq. (3-48b) is repeated in this new format in the form

$$P_{sn}(k, \omega) = P_{sn}(k + \kappa_j, \omega) ; \quad \kappa_j = j \kappa_1 , \quad (10-1)$$

which states that the drive  $P_{sn}(k, \omega)$  is aliased in the wavenumber ( $k$ ) with respect to the separation wavenumber ( $\kappa_1$ ), where  $\kappa_1 = (2\pi / b)$  with ( $b$ ) the separation between adjacent ribs in the (axial)  $x$ -domain on a regularly ribbed cylindrical shell. This regularity is defined in Eqs. (3-28) and (3-29). From Eqs. (3-41b), (3-45b), (3-46b) and (5-9b) one obtains

$$\bar{\bar{P}}_{sn}(k, \omega) = P_{sn}(k, \omega) [T_n(\omega) P_{ean}(\omega)]^{-1} , \quad (10-2a)$$

$$\bar{P}_{sn}(k, \omega) = P_{sn}(k, \omega) [P_{ean}(\omega)]^{-1} , \quad (10-2b)$$

$$\bar{\bar{P}}_{sn}(k, \omega) = \bar{P}_{osn}(k, \omega) ;$$

$$\bar{P}_{osn}(k, \omega) = S_b(k) [Q_{\infty n}(k, \omega) (2\pi)^{-1/2} \exp(ix_a k)] , \quad (10-3a)$$

$$\begin{aligned} \bar{P}_{sn}(k, \omega) &= I_{bn}(k, \omega) \bar{P}_{osn}(k, \omega) ; \\ I_{bn}(k, \omega) &= \{1 + S_b(k) [Q_{\infty n}(k, \omega)]\} , \end{aligned} \quad (10-3b)$$

where  $\bar{P}_{osn}(k, \omega)$  relates directly to the first order case and  $\bar{P}_{sn}(k, \omega)$  is the normalized modal drive in lieu of the ribs when ribs are allowed to interact naturally via the shell. The self-aliased operator  $S_b(k)$  receives its name from the patterns that  $\bar{P}_{osn}(k, \omega)$  exhibits; these patterns are depicted in Figs. 10-1a-c, 2a-c and 3a-d. The patterns in  $[Q_{\infty n}(k, \omega) (2\pi)^{-1/2} \exp(ix_a k)]$  that are substantially depicted in Figs. 9-3a-c, 4a-c and 5a-d, are aliased in Figs. 10-1a-c, 2a-c and 3a-d, respectively; the working of  $S_b(k)$  is clearly deciphered in these figures. An aliased quantity obeys the rule that patterns in one segment in  $(k)$  that is  $(\kappa_1)$  wide; e.g.,  $0 \leq k < \kappa_1$ , is repetitively duplicated in every segment that is removed by  $(j\kappa_1)$ , where  $(j)$  may assume any positive or negative integer, including zero. [cf. Eq.(10-1).] Since the  $[Q_{\infty n}(k, \omega) (2\pi)^{-1/2} \exp(ix_a k)]$  are distinguished by the dispersive loci in  $G_{\infty n}(k, \omega)$ , the patterns in Figs. 10-1a-c, 2a-c and 3a-d are distinguished by the repetitive duplications of these loci and, at most, their possible modulation in the frequency domain by  $A(\omega/\omega_o)$ . Figures 10-2a-c and 3a-d show that not only the flexural and fluid loading dispersive loci are duplicated, but so are the membrane dispersive loci. Since the aliasing is due to scattering by the regularly spaced ribs, it is concluded that the simple rib structure can support phenomena that are associated with scattering not only of flexural free waves, but also of membrane free waves. It follows that it is not essential to upgrade the structure of the ribs on account of a few of the



phenomena that may be associated with the membrane free waves. At this initial stage, it is emphasized that aliasing is not to be confused with symmetry. Aliasing patterns can, but need not, be symmetric. Thus, since the standard position of the external ring drive is chosen at  $(x_a/b) = (0.5)$ , the patterns in Figs. 10-1a-c, 2a-c and 10-3a-d are not only aliased, but are also symmetric. Indeed, this symmetry requires that in spectral space the drive in lieu of the ribs vanish whenever  $(ak) = (a\kappa_1) [(1+2j)/2]$ , where  $(j)$  assumes any positive or negative integer, including zero. Figures 10-4a-c and 5a-c repeat Figs. 10-1a-c and 2a-c, respectively, except that the position  $(x_a/b)$  of the external drive is changed from the standard value of  $(0.5)$  to  $(0.3)$ . Not only is the drive in lieu of the ribs non-vanishing whenever  $(ak) = (a\kappa_1) [(1+2j)/2]$ , but the strict symmetry in the latter figures is no longer found in the former figures, notwithstanding that some of the asymmetry comes from the finiteness of the plotted points; i.e. as a result of graphical limitations. The influence of decreasing and increasing the value of the fluid loading parameter  $(\varepsilon_c)$  from the standard value of  $10^{-2}$  to  $10^{-4}$  and  $10^{-1}$ , respectively, are investigated in Figs. 10-6a and b and 10-7a and b, respectively. These two sets of figures repeat Figs. 10-4a and 5a, respectively, except for the specified change in the fluid loading parameter. There is a discernible influence, especially in the change to  $10^{-1}$ , but there are no surprises that transcend those already discussed with respect to Fig. 8. Again, Figs. 10-1 through 5 are derived by applying the aliasing operator directly to the corresponding figures in Sections VIII and IX. The direct application of the self-aliased operator to  $[Q_{\infty n}(k, \omega) (2\pi)^{-1/2} \exp(ikx_a)]$  yields results that are commensurate, by definition, with the first order model. A question may then arise: is the aliasing in the first order model, as illustrated in Figs. 10-1 through 7, preserved in the proper order model? The proper order model is the model in which a full account is made for the interactions among the ribs via the shell.

From Eq. (10-3) it is clear that this accounting is implemented by the factor  $I_{bn}(k, \omega)$ . This factor, it is recalled, is aliased in  $(k)$  with respect to  $(\kappa_1)$ , as is  $\bar{P}_{osn}(k, \omega)$ , and, therefore,  $\bar{P}_{sn}(k, \omega)$  is also aliased in  $(k)$  with respect to  $(\kappa_1)$ . Two aliased factors; if they are identically aliased, render the quantity aliased in the manner of each; if they are not identically aliased, the quantity is not aliased in the manner of either. [cf. Eq. (3-37).] However, the factor  $I_{bn}(k, \omega)$  is a function of both the wavenumber  $(k)$  and the frequency  $(\omega)$ , and, therefore, it may be influential enough to modify the dispersive patterns in Figs. 10-1 through 3 even if the aliased properties are to be preserved. The patterns in  $I_{bn}(k, \omega)$  are depicted, correspondingly to Figs. 10-1a-c, 2a-c, 3a-d, 4a and 5a, 6a and b and 7a and b in Figs. 10-8a-c, 9a-c, 10a-d, 8d and 9d, 11a and b and 12a and b, respectively. Comparison between these two sets of figures reveals, among others, four significant features. The first, and an obvious one, is that  $I_{bn}(k, \omega)$  is aliased in  $(k)$  with respect to  $(\kappa_1)$ , as is  $\bar{P}_{osn}(k, \omega)$ . The second, and again an obvious one, is that Figs. 10-8a and 9a are identical to Figs. 10-8d and 9d, respectively, since unlike  $\bar{P}_{osn}(k, \omega)$ ,  $I_{bn}(k, \omega)$  is independent of the position  $(x_a/b)$  of the external ring drive. Therefore, Figs. 10-8a and 9a are also designated Figs. 10-8d and 9d, respectively. The third indicates that at the dispersive loci in Fig. 10-1 through 7, anti-dispersive loci are correspondingly found in Figs. 10-8 through 12. Anti-dispersive loci are those pertaining to valleys and the associated nadirs. Since  $I_{bn}(k, \omega)$  is a companion factor to  $\bar{P}_{osn}(k, \omega)$  in  $\bar{P}_{sn}(k, \omega)$ , as stated in Eq. (10-3b),  $I_{bn}(k, \omega)$  is expected to suppress the prominent patterns in the factor  $\bar{P}_{osn}(k, \omega)$  so that  $\bar{P}_{sn}(k, \omega)$  tends not to exhibit these prominent patterns at the dispersive loci. In the absence of damping in the shell, the aliased dispersive loci are defined by the singularities (and zeros) in  $\{S_b(k) [Q_{\infty n}(k, \omega)]\}$ . These same singularities (but not the zeros), are to be found in  $\{1 + [S_b(k) Q_{\infty n}(k, \omega)]\}$ . The way that this factor features in  $I_{bn}(k, \omega)$ ,

explains how  $I_{bn}(k, \omega)$  abolishes the singularities in  $\{S_b(k) [Q_{\infty n}(k, \omega)]\}$  so that  $\bar{P}_{sn}(k, \omega)$  is devoid of prominent patterns at the dispersive loci. The zeros defined by the fluid dispersive locus remain intact and, therefore, the sonic locus in  $\bar{P}_{osn}(k, \omega)$  is preserved in  $\bar{P}_{sn}(k, \omega)$ . The fourth feature follows: The quantity  $I_{bn}(k, \omega)$  is singular whenever  $[S_b(k) Q_{\infty n}(k, \omega)] \approx -1$ . The singularities in  $I_{bn}(k, \omega)$  are shown in Figs. 10-8 through 12 as ridges and associated peaks. They lie closely adjacent to, but not on, the valleys and associated nadirs. The former dispersive loci in  $I_{bn}(k, \omega)$  are designated "false dispersive loci". The false dispersive loci lie just below the dispersive loci if  $A(\omega / \omega_o)$  is real and positive and just above if  $A(\omega / \omega_o)$  is real and negative. This feature is made clearer in Figs. 10-8a1, b1, and c1, 10-9a1, b1, and c1, and 10-10a1, b1, and c1; these figures are identical to Figs. 10-8 through 10, respectively, except that the waterfall is less densely populated. [cf. Appendix B.] When the ribs are endowed with a resonance, as in Figs. 10-8c, 9c and 10c, the false dispersive loci transit from those in Figs. 10-8a, 9a and 10a to those in Figs. 10-8b, 9b, and 10b, respectively, as  $(\omega / \omega_c)$  transit from being less than  $(\omega_o / \omega_c)$  to being more than  $(\omega_o / \omega_c)$ . The two regions, so defined, are smoothly bridged when a standard value for the loss factor  $(\eta_o)$  is introduced; see Figs. 10-8a-c, 9a-c and 10-10a-c. Again, since  $I_{bn}(k, \omega)$  is a companion factor to  $\bar{P}_{osn}(k, \omega)$  in  $\bar{P}_{sn}(k, \omega)$  and since  $\bar{P}_{osn}(k, \omega)$  does not exhibit valleys and associated nadirs at the false dispersive loci, these false dispersive loci become the prominent patterns in  $\bar{P}_{sn}(k, \omega)$ . The false dispersive loci yield patterns in the drive  $\bar{P}_{sn}(k, \omega)$  in lieu of the ribs that are exhibited in Figs. 10-13 through 20. These figures are reminiscent, but not quite overlapping with those shown in Figs. 10-1 through 7, for the first order model. In Figs. 10-13 through 20 the absolute value of  $\bar{P}_{sn}(k, \omega)$  are displayed as a function of  $(ak)$  in a waterfall format under those conditions and parametric values that are used in Figs. 10-1 through 7, respectively. As just argued, although the false dispersive

loci are in appearance similar to the corresponding dispersive loci, they are displaced by a small fraction of the normalized frequency from the latter; to a lower frequency if  $A(\omega / \omega_o)$  is real and positive (mass controlled) and to a higher frequency if  $A(\omega / \omega_o)$  is real and negative (stiffness controlled). Indeed, the displacements are such that the aliasing knots are displaced from those of the first order model. An aliasing knot is a spectral region on the  $\{(ak), (\omega / \omega_c)\}$ -domain where two aliasing orders converge, cross, and diverge. It follows that the displacement of a knot is to a lower frequency if the line impedance of the ribs is mass controlled; i.e., when  $A(\omega / \omega_o)$  is real and positive. This feature is illustrated in the comparison between Figs. 10-1a, 2a and 3a and Figs. 10-13a, 14a and 15a, respectively. The displacement of a knot is to a higher frequency if the line impedance of the ribs is stiffness controlled; i.e., when  $A(\omega / \omega_o)$  is real and negative. This feature is illustrated in the comparison between Figs. 10-1b, 2b and 3b and Figs. 10-13b, 14b and 15b, respectively. The transition between these two cases is depicted in Figs. 10-13c, 14c and 15c. Although obvious, it is noted, in Figs. 10-14a-c and 15a-c that knots of the longitudinal, the shear, and flexural free waves do not, in general, occupy the same regions on the  $\{(ak), (\omega / \omega_c)\}$ -domain. Furthermore, unlike the dispersive loci in the first order model, at an aliasing knot the false dispersive loci of the two crossing aliasing orders possess opposite signs, and a substantial cancellation occurs between them in the spectral region of overlap. The effective cancellation, at an aliasing knot, by the crossing of a pair of aliasing orders of opposite sign, is a significant feature in the phenomenon that manifests pass and stop bands. This phenomenon is dealt with in the next two sections.

Figures 10-16a-c, 10-17a-c, 10-18a-c, 10-19a-b and 10-20a-b are the proper order counterparts of the first order model computations depicted in Figs. 10-4a-c,

10-5a-c, 10-6a-c, 10-7a-b and 10-8a-b, respectively. As in the latter set, in the former set the vanishing of the drive in lieu of the ribs, whenever  $(ak) = (a\kappa_1) [(1+2j)/2]$ , and the strict symmetry in the aliasing are removed by the asymmetric position of the external drive. However, the manifestation of the influence of the interactions among the ribs via the shell sustain a difference between these two sets of figures that is substantially similar to that sustained between Figs. 10-13a-c, 10-14a-c and 10-15a-c and Figs. 10-1a-c, 10-2a-c and 10-3a-c, respectively. The explanation for this difference was just discussed.

Comparing Figs. 10-1c, 2c, 3c and d, 4c and 5c with Figs. 10-13c, 14c, 15c and d, 16c and 17c, respectively, indicates that in the vicinity of the resonance frequency at  $(\omega / \omega_o) \simeq 1$ , the ribs substantially subdue the presence of the free waves in the modal drive in lieu of the ribs in the second set of figures, but little in the first set. Indeed, the influence of the resonance in the ribs on  $I_{bn}(k, \omega)$  is substantially greater than on the first order drive  $\bar{P}_{osn}(k, \omega)$ . That the influence of the resonance in the ribs on the peaks in  $I_{bn}(k, \omega)$  is substantial is clearly discernible by judiciously comparing various figures in Figs. 10-8 through 12. A question may arise: Is it merely the high line impedance of the ribs at resonance that is causing this influence or is it the resistance controlled character of the line impedance of the ribs at resonance that is the culprit? In partial answer to this question Figs. 10-21a-c are offered. In these figures  $A'(\omega / \omega_c)$ , stated in Eq. (9-6), replaces  $A(\omega / \omega_o)$  and Figs. 15a-c are then repeated, respectively. Comparing these two sets of figures indicates that the replacement can be hardly discernible, notwithstanding that a slight difference exists between Figs. 10-15c and 21c in the frequency range at and in the vicinity of the normalized resonance frequency, where  $(\omega / \omega_c) \simeq (\omega_o / \omega_c)$ . The overlap between Figs. 10-15a and b and Figs. 10-21a and b is expected and is understood. However, that the

difference between Fig. 10-15c and Fig. 10-21c in the region of resonance is only in details, suggests that the increase in the line impedance, in this frequency region, may be more significant than its character. What are these details and how significant are they, may be explored by extending the sets of figures in both Figs. 10-15 and 10-21. The details under consideration are those associated with the damping that is provided by the resonating ribs in Fig. 10-15c, and the lack of a corresponding damping in the ribs in Fig. 10-21c. To show that at and in the vicinity of the frequency of resonance the damping in Fig. 10-15c is attributable to the damping in the resonating ribs and is not dominated by radiation damping, this figure is repeated in Fig. 10-15d; in Fig. 10-15d the fluid loading parameter is changed from the standard value of  $10^{-2}$  to  $10^{-4}$ . Figures 10-15c and d are substantially identical in this resonance frequency region, indicating that the mechanical damping provided by the resonating ribs is significant. This statement is indirectly confirmed by Fig. 10-21d; this figure repeats Fig. 10-21c except that the fluid loading parameter is changed from the standard value of  $10^{-2}$  to  $10^{-4}$ . In the absence of damping by the resonating ribs, the radiation damping in the resonance frequency region is clearly diminished in Fig. 10-21d from that in Fig. 10-21c. Thus, in the absence of damping by the ribs radiation damping becomes significant in this region even when the fluid loading is at the standard value of  $10^{-2}$ . On the other hand, in Figs. 10-15e and 21e, which repeat Fig. 10-15c and 21c, respectively, except that the fluid loading parameter is changed from the standard value of  $10^{-2}$  to  $10^{-1}$ , the fluid loading mollifies the resonance effects of the ribs so that these two figures are substantially identical; the dominance of fluid loading subdues any phenomenological differences between the two cases. The difference between the two cases, one is reminded, is that in the first the ribs contribute mechanical damping at and in the vicinity of the frequency of resonance, in the second this contribution is artificially removed.

How significant is the damping in the ribs versus the mechanical damping in the shell? Figures 10-15f and g and 21f and g are presented to assist with the answer to this question. These figures repeat Figs. 10-15d and 21d, respectively, except that the loss factor ( $\eta_p$ ) of the flexural free waves is increased from the standard value of  $10^{-3}$  to  $5 \times 10^{-3}$  and  $2.5 \times 10^{-2}$ , respectively. Clearly and obviously, the increased mechanical damping of the flexural free waves subdues the normalized modal drive  $\bar{P}_{sn}(k, \omega)$  in lieu of the ribs; the subduing is most pronounced at the flexural ridges and the associated peaks in the aliased patterns of this drive. Indeed, at and in the vicinity of the frequency of resonance of the ribs, Figs. 10-21f resembles Fig. 10-15d better than does Fig. 10-21d; indicating, thereby, that in this frequency region a loss factor  $\eta_o \simeq 3 \times 10^{-1}$  in the ribs is equivalent to a moderate increase in the loss factor ( $\eta_p$ ) in the shell. Moreover, that a moderate increase in ( $\eta_p$ ) is more extensively useful than is the damping in the ribs, can be readily verified by comparing Fig. 10-15d and Fig. 10-21f. A drastic increase in the loss factor ( $\eta_p$ ) in the shell, as depicted in Figs. 10-15g and 21g, renders these two figures substantially identical; the damping contributed by the ribs at and in the vicinity of the frequency of resonance is substantially overwhelmed by the damping in the shell and whence the identity between these two figures. One remembers that in Fig. 10-21 the damping that is provided by the ribs at resonance is artificially removed, whereas in Fig. 10-15 this type of damping is naturally included.

Fig. 10-1. Normalized modal drive  $\bar{P}_{osn}(k, \omega)$  in lieu of a **first order** model for the ribs on a **hybrid** cylinder as a function of  $(ak)$  in a  $(\omega_o / \omega_c)$  - waterfall format.

- a. Under standard values  $[(\omega_o / \omega_c) = 10]$ .
- b. Stiffness controlled ribs  $[(\omega_o / \omega_c) = 10^{-2}]$ .
- c.  $(\omega_o / \omega_c) = 2.5 \times 10^{-1}$ .

N=0, ETAg=1.E-3, ETAo=.3, Wo\_Wc=10, BETTA=5, ZmnBar=N, EPSc=1.E-2

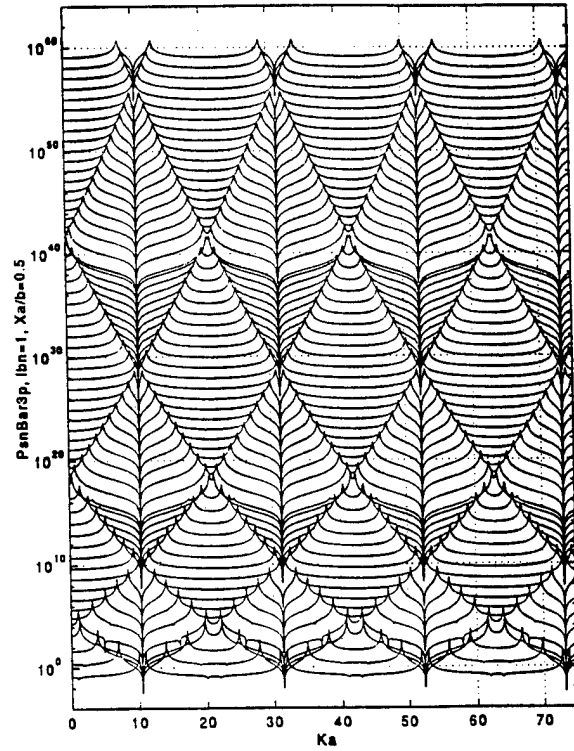


Fig. 10-1a

N=0, ETAg=1.E-3, ETAo=.3, Wo\_Wc=1.E-2, BETTA=5, ZmnBar=N, EPSc=1.E-2

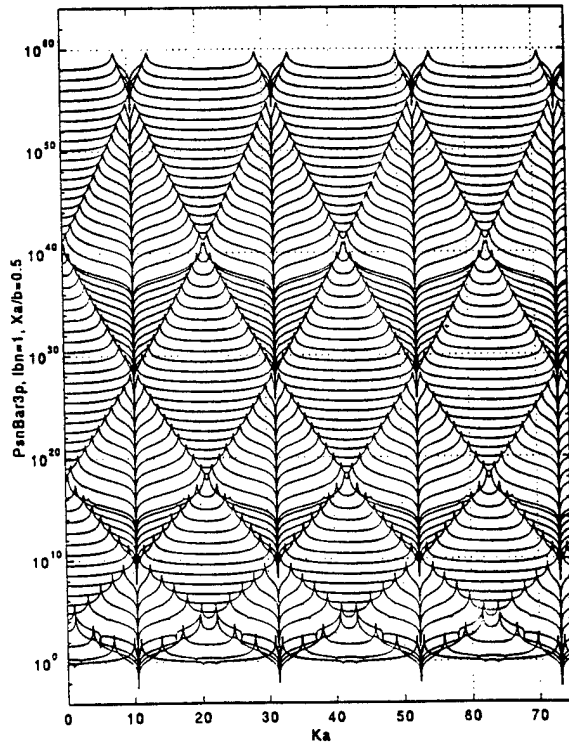


Fig. 10-1b

N=0, ETAg=1.E-3, ETAo=.3, Wo\_Wc=2.5E-1, BETTA=5, ZmnBar=N, EPSc=1.E-2

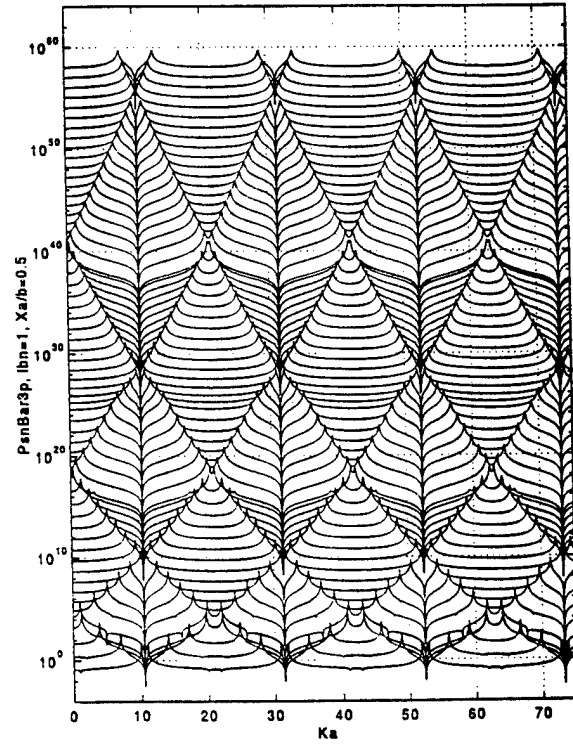


Fig. 10-1c



Fig. 10-2. As in Fig 10-1 except for the change to a natural cylinder.

- Under standard values [ $\omega_o/\omega_c = 10$ ].
- Stiffness controlled ribs [ $(\omega_o/\omega_c) = 10^{-2}$ ].
- $(\omega_o/\omega_c) = 2.5 \times 10^{-1}$

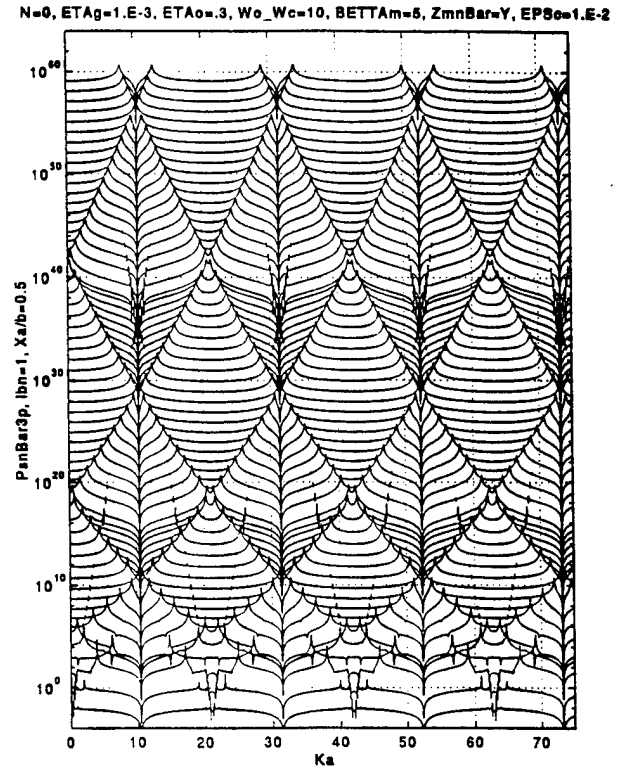


Fig. 10-2a

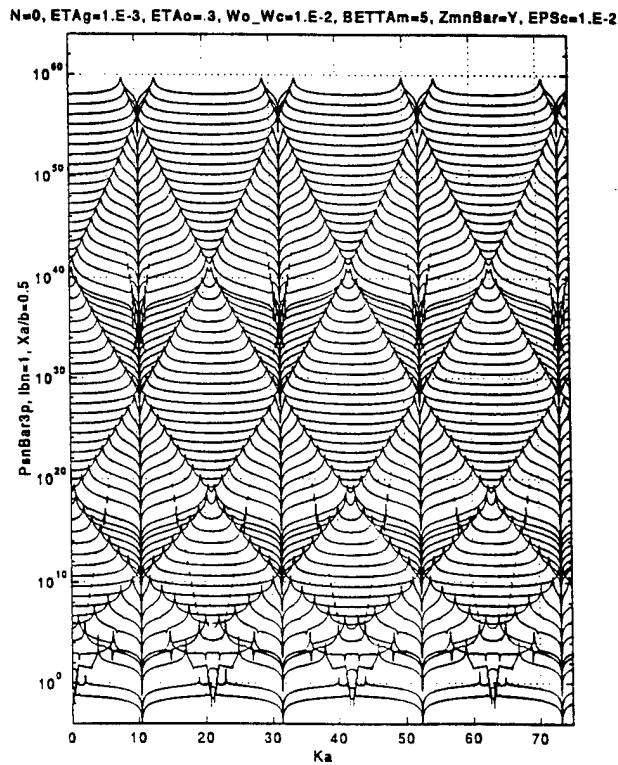


Fig. 10-2b

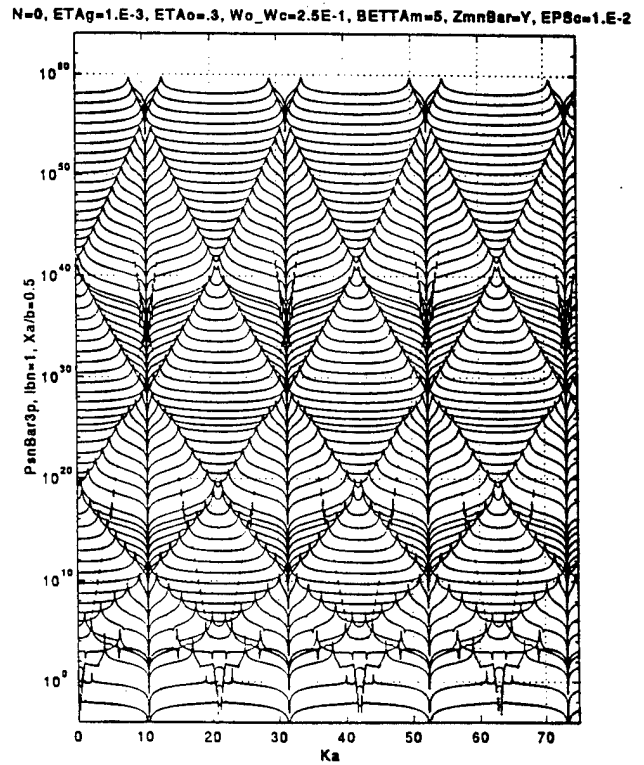


Fig. 10-2c

Fig. 10-3. As in Fig. 10-2 except for the change from the standard mode index ( $n$ ) of zero to unity.

- Mass controlled ribs  $[(\omega_o / \omega_c) = 10]$ .
- Stiffness controlled ribs  $[(\omega_o / \omega_c) = 10^{-2}]$ .
- $(\omega_o / \omega_c) = 2.5 \times 10^{-1}$ .
- Change in the parameter ( $\gamma$ ) [Eq. 9-5] from the standard value of 8 to 0.

N=1, ETAg=1.E-3, ETAo=.3, Wo\_Wc=10, BETTA=6, ZmnBar=Y, EPS=1.E-2

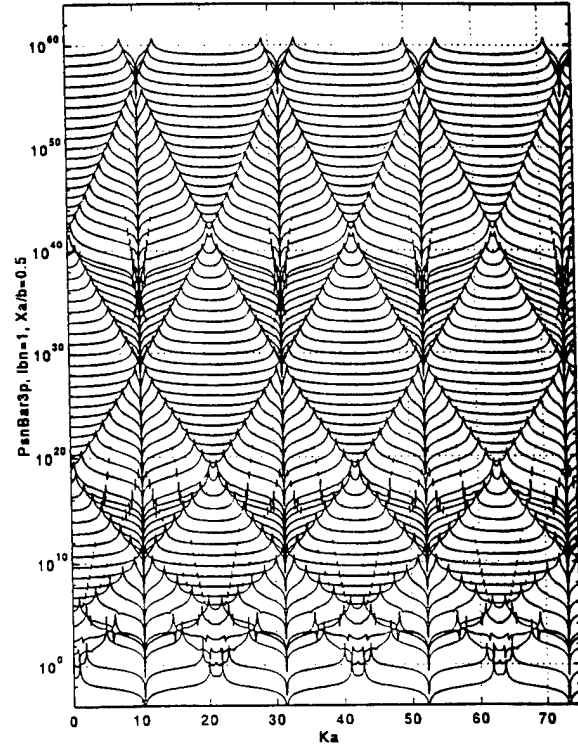


Fig. 10-3a

N=1, Wo/Wc=1E-2, ETAp=1E-3, ZmnBar=Y, EPS=1E-2, b/a=.5

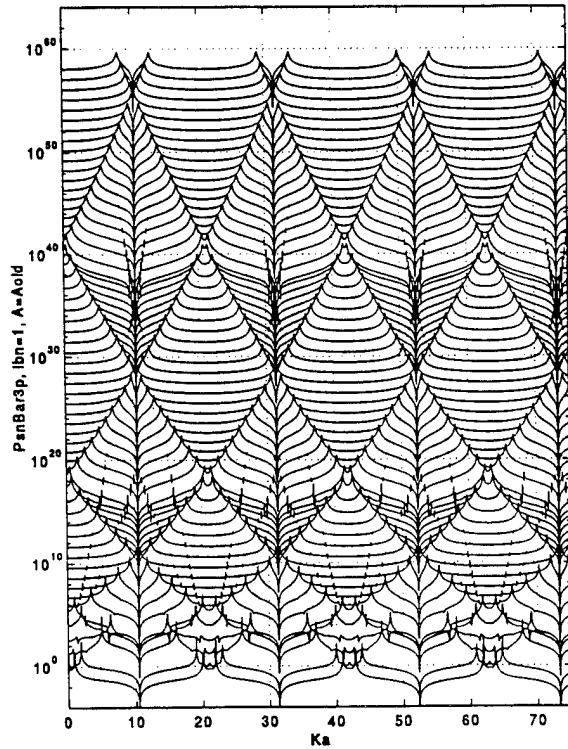


Fig. 10-3b

N=1, ETAg=1.E-3, ETAo=.3, Wo\_Wc=2.5E-1, BETTA=5, ZmnBar=Y, EPS=1.E-2

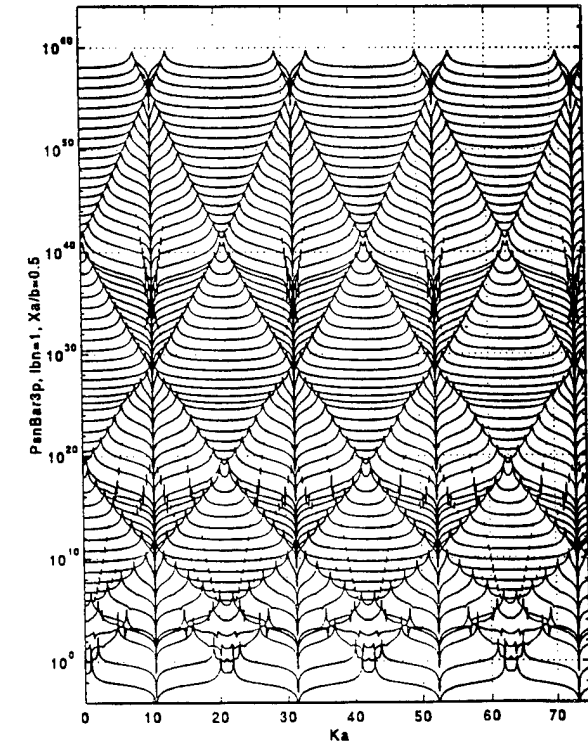


Fig. 10-3c

$N=1$ ,  $ETAo=.3$ ,  $Wo\_Wc=2.5E-1$ ,  $BETTAm=1.E3$ ,  $Gamma=0$ ,  $ZmnBar=Y$ ,  $EPSc=1.E-2$

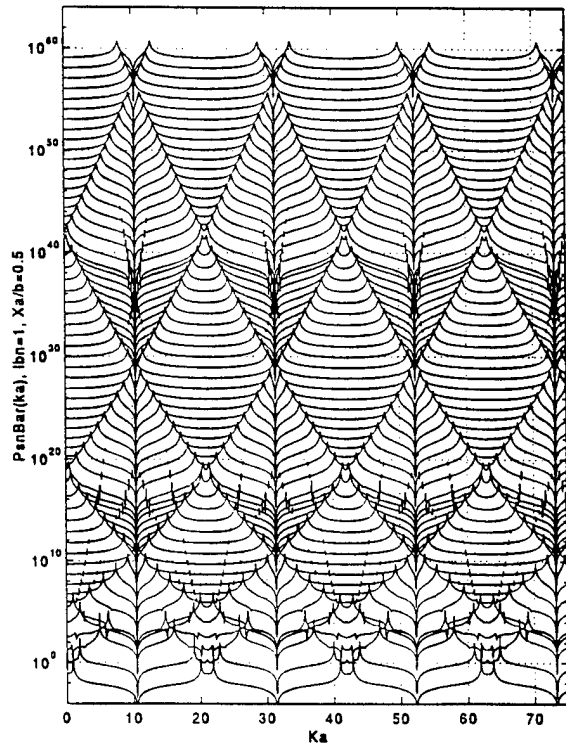


Fig. 10-3d

Fig. 10-4. As in Fig. 10-1 except that the axial positions ( $x_a/b$ ) of application of the external drive is changed from the standard value of 0.5 to 0.3.

- a. Mass controlled ribs [ $(\omega_o/\omega_c) = 10$ ].
- b. Stiffness controlled ribs [ $(\omega_o/\omega_c) = 10^{-2}$ ].
- c.  $(\omega_o/\omega_c) = 2.5 \times 10^{-1}$ .

$N=0$ ,  $ETAg=1.E-3$ ,  $ETAo=.3$ ,  $Wo\_Wc=10$ ,  $BETTAm=5$ ,  $ZmnBar=N$ ,  $EPSc=1.E-2$

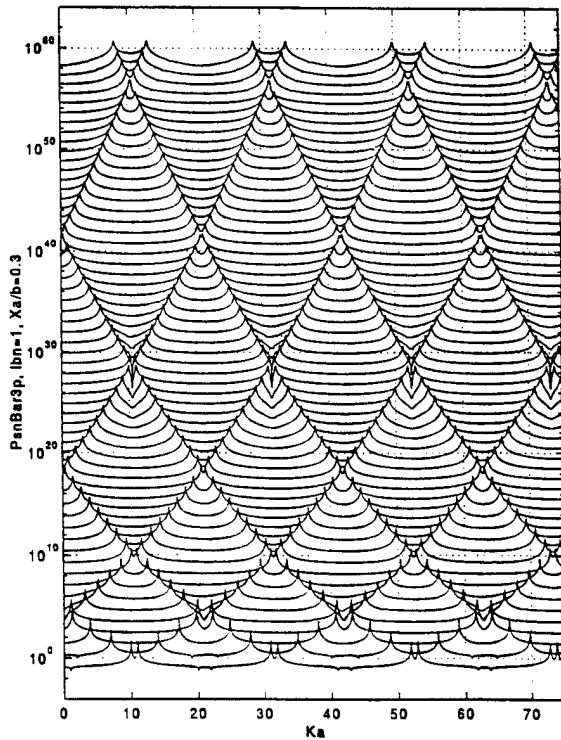


Fig. 10-4a

$N=0$ ,  $ETAg=1.E-3$ ,  $ETAo=.3$ ,  $Wo\_Wc=1.E-2$ ,  $BETTAm=5$ ,  $ZmnBar=N$ ,  $EPSc=1.E-2$

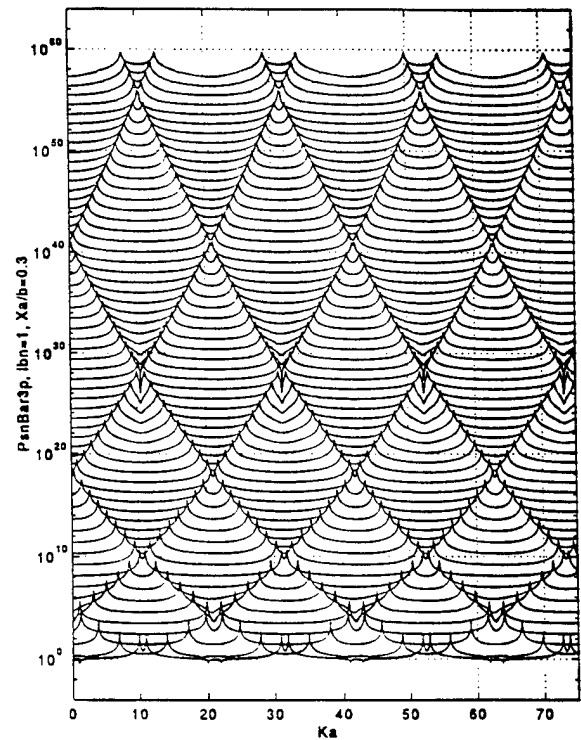


Fig. 10-4b

$N=0$ ,  $ETA_g=1.E-3$ ,  $ETA_o=.3$ ,  $Wo\_Wc=2.5E-1$ ,  $BETTAm=5$ ,  $ZmnBar=N$ ,  $EPSc=1.E-2$

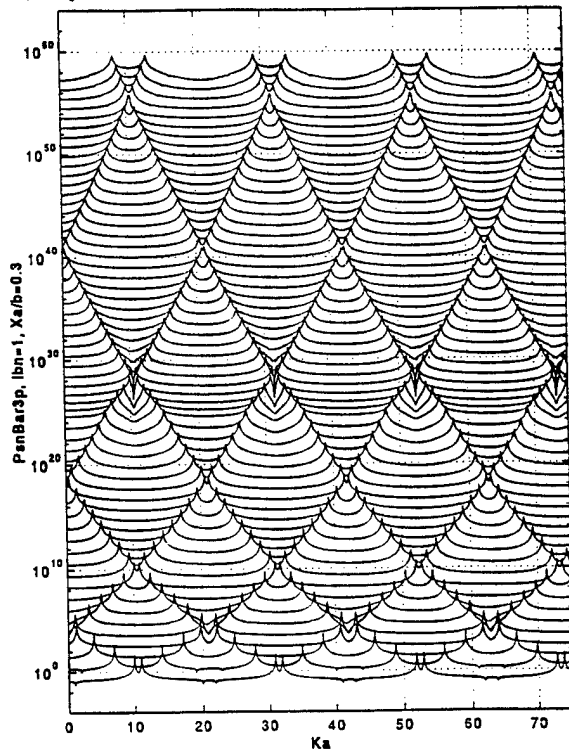


Fig. 10-4c

Fig. 10-5. As in Fig. 10-2 except that the axial position ( $x_a/b$ ) of application of the external drive is changed from the standard value of 0.5 to 0.3.

- a. Mass controlled ribs  $[(\omega_o/\omega_c) = 10]$ .
- b. Stiffness controlled ribs  $[(\omega_o/\omega_c) = 10^{-2}]$ .
- c.  $(\omega_o/\omega_c) = 2.5 \times 10^{-1}$ .

$N=0$ ,  $ETA_g=1.E-3$ ,  $ETA_o=.3$ ,  $Wo\_Wc=10$ ,  $BETTAm=5$ ,  $ZmnBar=Y$ ,  $EPSc=1.E-2$

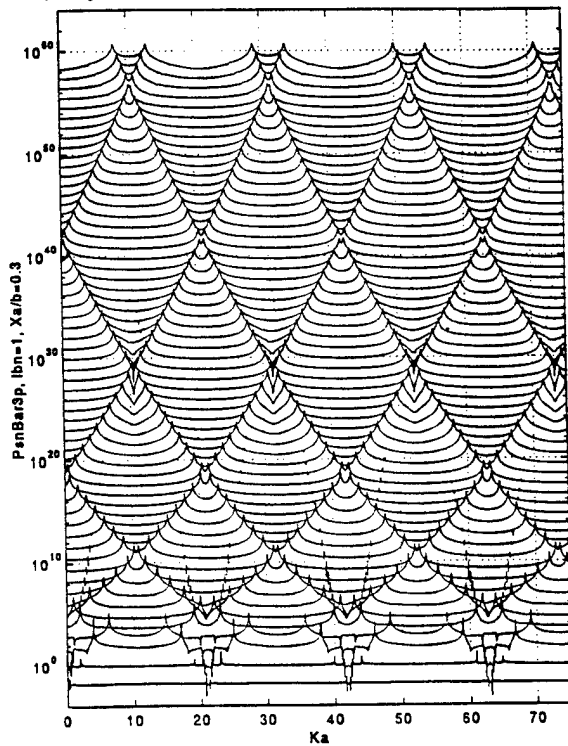


Fig. 10-5a

$N=0$ ,  $ETA_g=1.E-3$ ,  $ETA_o=.3$ ,  $Wo\_Wc=1.E-2$ ,  $BETTAm=5$ ,  $ZmnBar=Y$ ,  $EPSc=1.E-2$

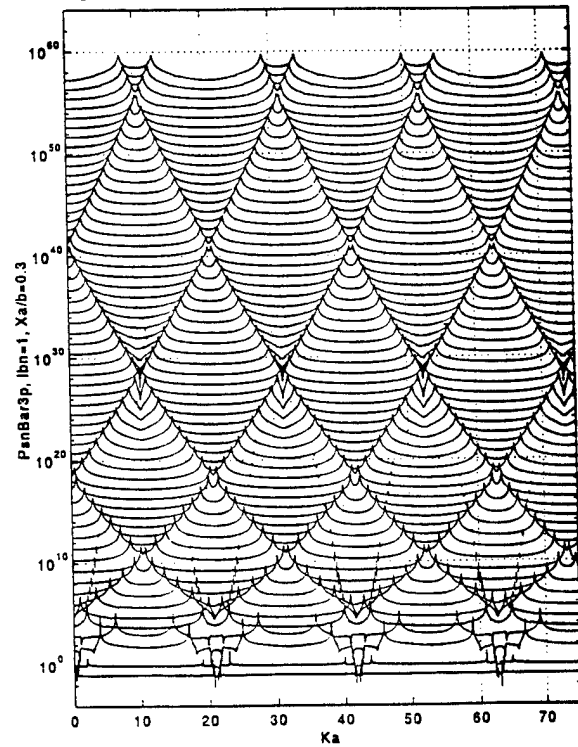


Fig. 10-5b

$N=0$ ,  $ETA_g=1.E-3$ ,  $ETA_o=.3$ ,  $Wo\_Wc=2.5E-1$ ,  $BETTAm=5$ ,  $ZmnBar=Y$ ,  $EPSc=1.E-2$

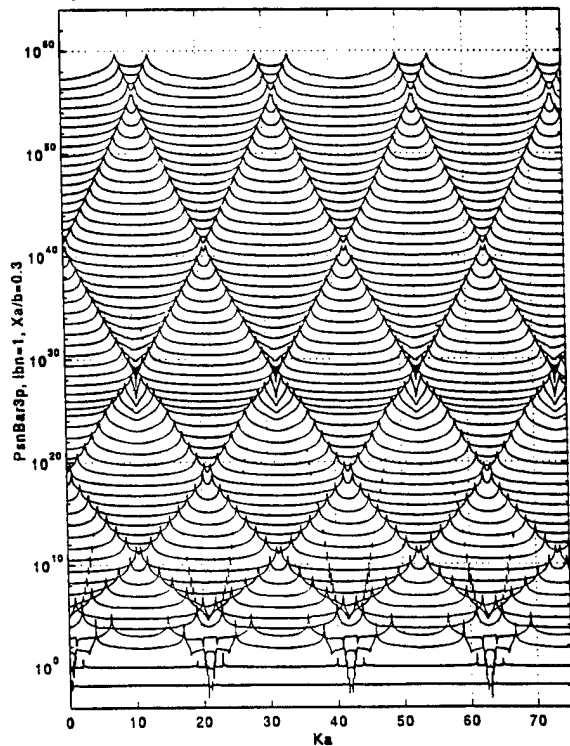


Fig. 10-5c

Fig. 10-6. As in Fig. 10-4a except that the fluid loading parameter ( $\epsilon_c$ ) is changed from the standard value of  $10^{-2}$  to:

- a.  $\epsilon_c = 10^{-4}$ .
- b.  $\epsilon_c = 10^{-1}$ .

$N=0$ ,  $ETA_g=1.E-3$ ,  $ETA_o=.3$ ,  $Wo\_Wc=10$ ,  $BETTAm=5$ ,  $ZmnBar=N$ ,  $EPSc=1.E-4$ ,

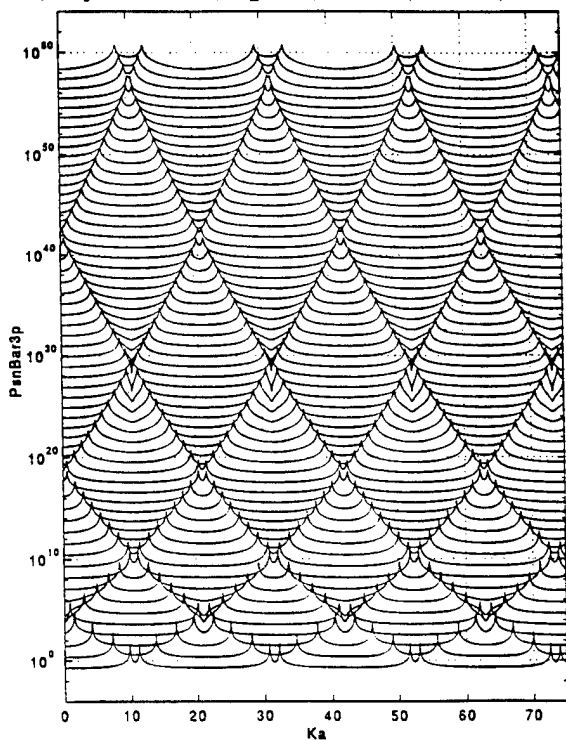


Fig. 10-6a

$N=0$ ,  $ETA_g=1.E-3$ ,  $ETA_o=.3$ ,  $Wo\_Wc=10$ ,  $BETTAm=5$ ,  $ZmnBar=N$ ,  $EPSc=1.E-1$ ,

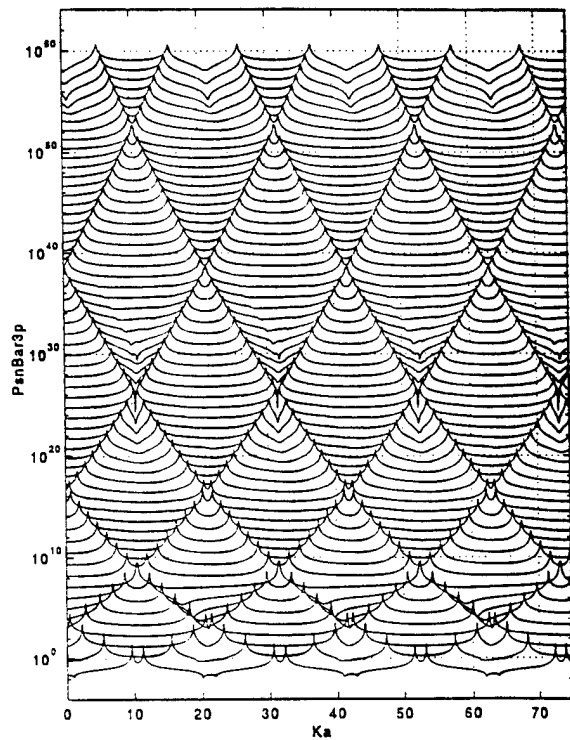


Fig. 10-6b

Fig. 10-7. As in Fig. 10-5a except that the fluid loading parameter ( $\epsilon_c$ ) is changed from the standard value of  $10^{-2}$  to:

- a.  $\epsilon_c = 10^{-4}$ .
- b.  $\epsilon_c = 10^{-1}$ .

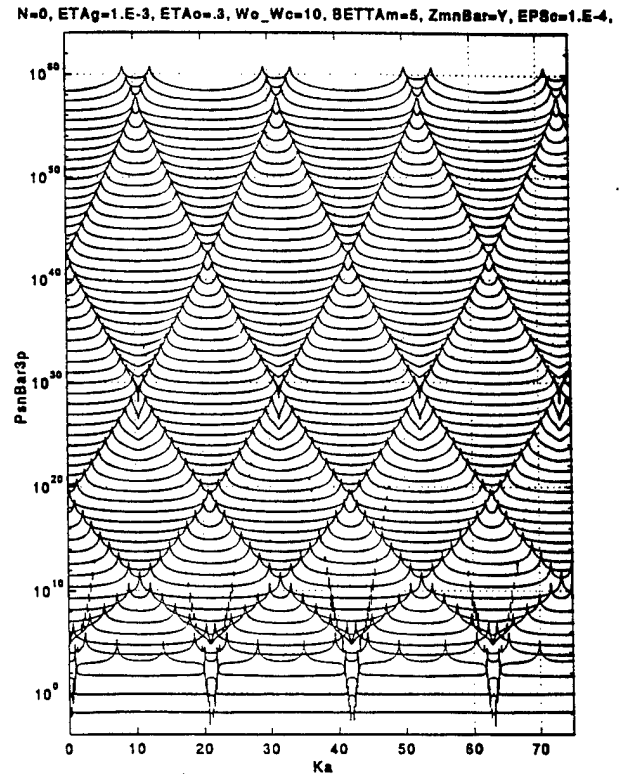


Fig. 10-7a

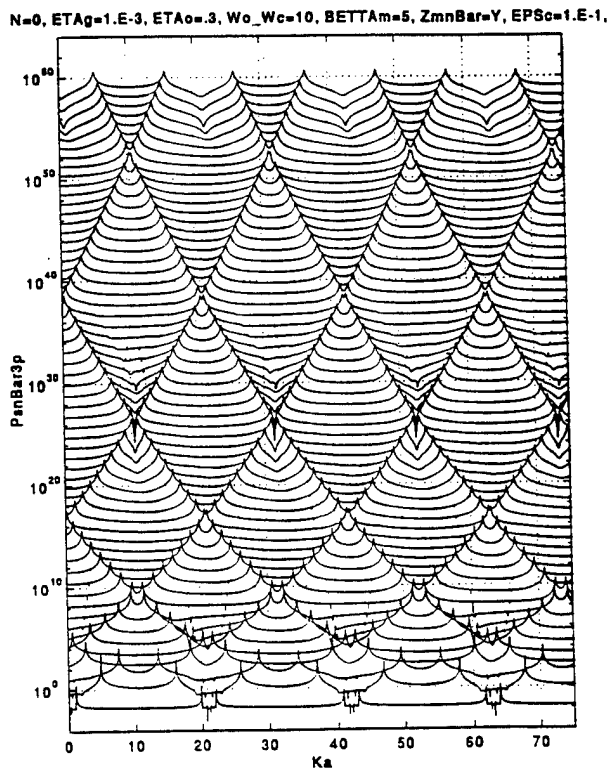


Fig. 10-7b

Fig. 10-8. Modal factor  $I_{bn}(k, \omega)$  [Eq. (10-3b)] for a hybrid cylinder as a function of  $(ak)$  in a  $(\omega/\omega_c)$  - waterfall format.

- a. and d. Mass controlled ribs  $[(\omega_o/\omega_c) = 10]$ .
- a.1 and d.1. Sparsely populated waterfall of a and d.
- b. Stiffness controlled ribs  $[(\omega_o/\omega_c) = 10^{-2}]$ .
- b.1. Sparsely populated waterfall of b.
- c.  $(\omega_o/\omega_c) = 2.5 \times 10^{-1}$ .
- c.1. Sparsely populated waterfall of c.

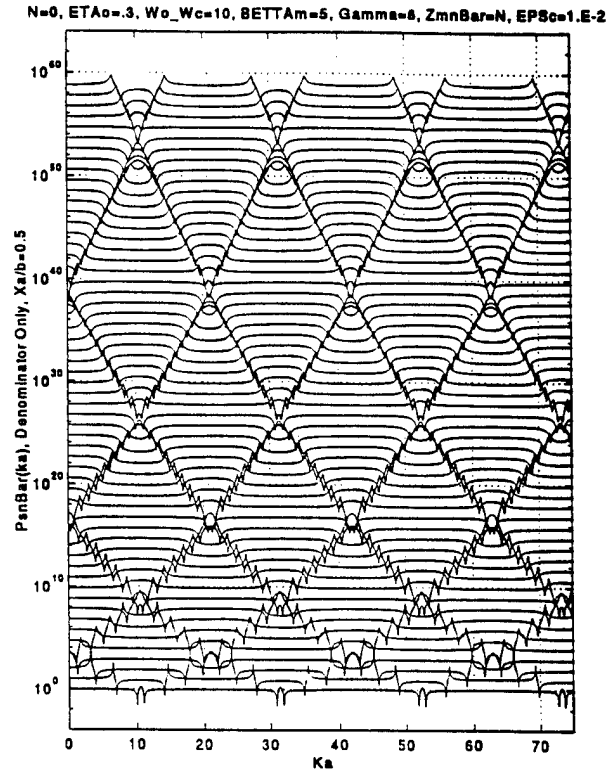


Fig. 10-8a and d

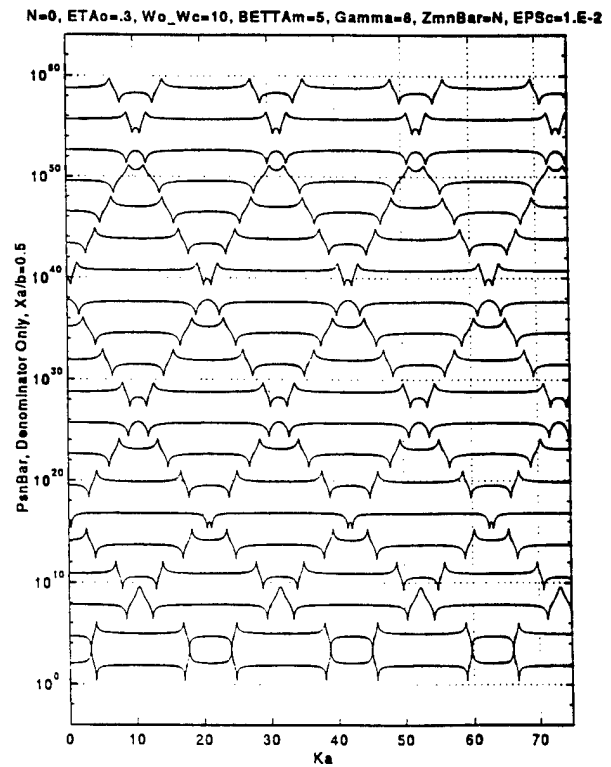


Fig. 10-8a1 and d1

$N=0$ ,  $ETA_0=.3$ ,  $Wo\_Wc=1.E-2$ ,  $BETTAm=5$ ,  $Gamma=8$ ,  $ZmnBar=N$ ,  $EPSc=1.E-2$

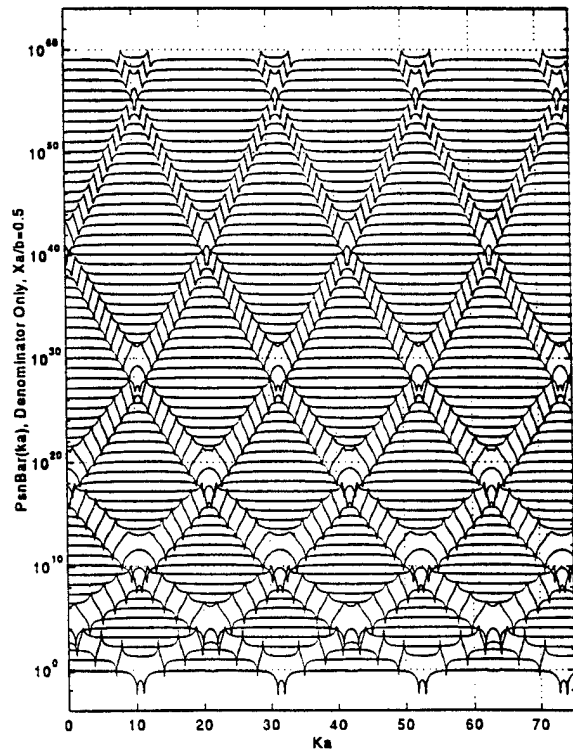


Fig. 10-8b

$N=0$ ,  $ETA_0=.3$ ,  $Wo\_Wc=1.E-2$ ,  $BETTAm=5$ ,  $Gamma=8$ ,  $ZmnBar=N$ ,  $EPSc=1.E-2$

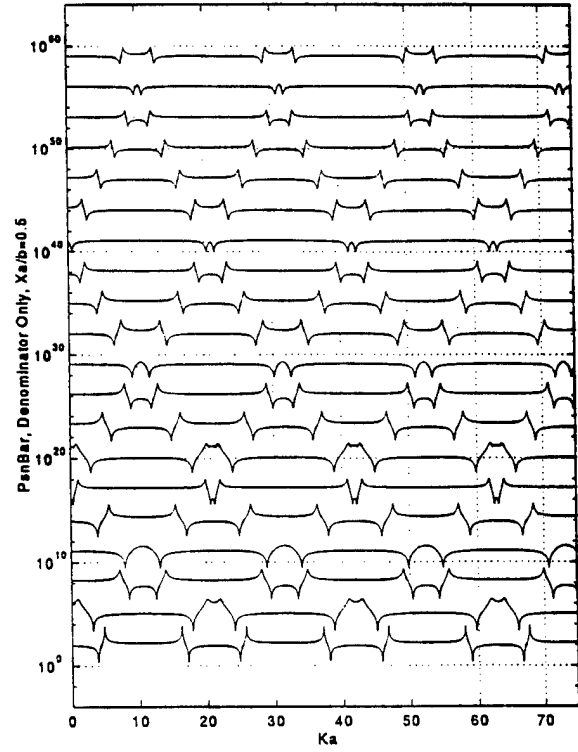


Fig. 10-8b1

$N=0$ ,  $ETA_0=.3$ ,  $Wo\_Wc=2.5E-1$ ,  $BETTAm=5$ ,  $Gamma=8$ ,  $ZmnBar=N$ ,  $EPSc=1.E-2$

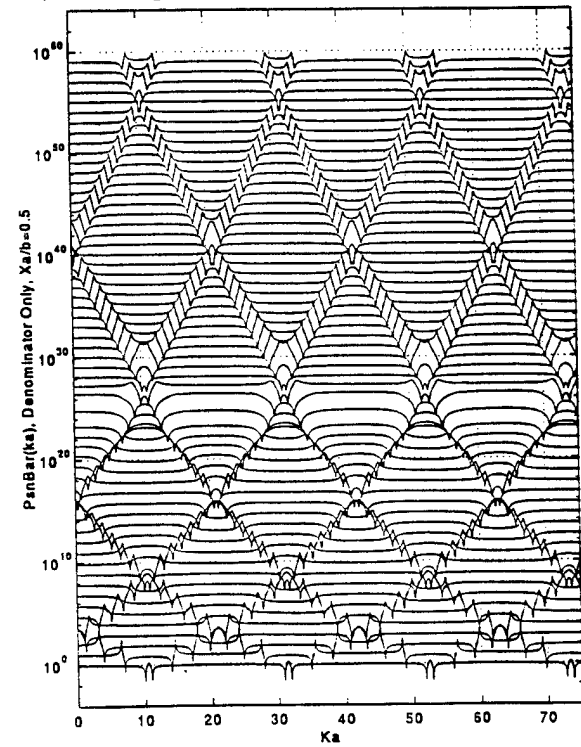


Fig. 10-8c

$N=0$ ,  $ETA_0=.3$ ,  $Wo\_Wc=.25$ ,  $BETTAm=5$ ,  $Gamma=8$ ,  $ZmnBar=N$ ,  $EPSc=1.E-2$

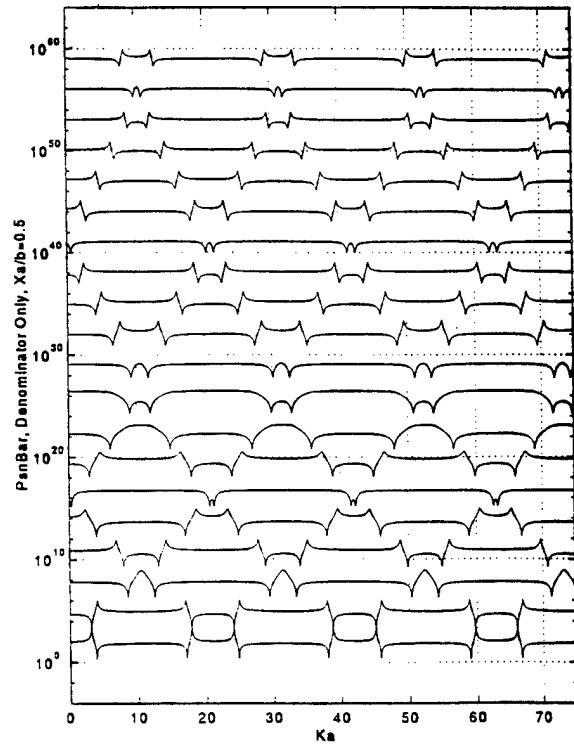


Fig. 10-8c1



Fig. 10-9. As in Fig. 10-8 except for the change to a natural cylinder.

- a. and d. Mass controlled ribs  $[(\omega_o / \omega_c) = 10]$ .
- a.1 and d.1. Sparsely populated waterfall of a and d.
- b. Stiffness controlled ribs  $[(\omega_o / \omega_c) = 10^{-2}]$ .
- b.1. Sparsely populated waterfall of b.
- c.  $(\omega_o / \omega_c) = 2.5 \times 10^{-1}$ .
- c.1. Sparsely populated waterfall of c.

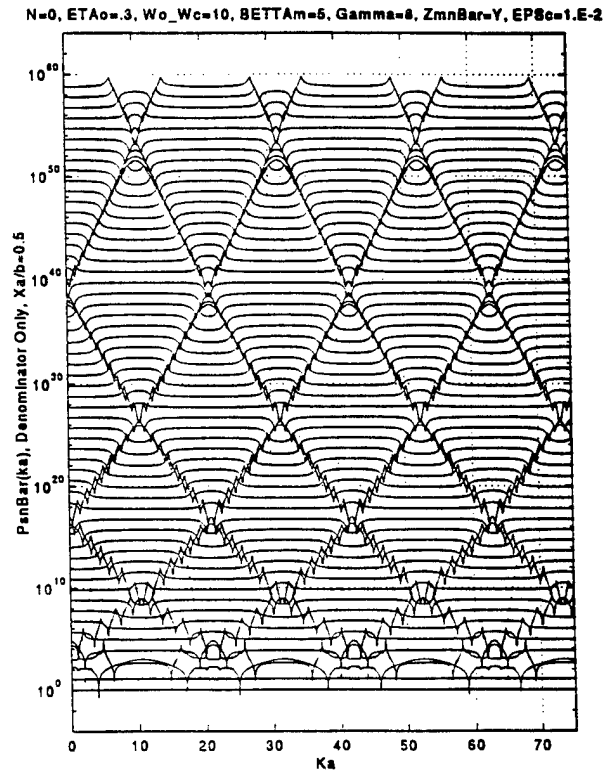


Fig. 10-9a and d

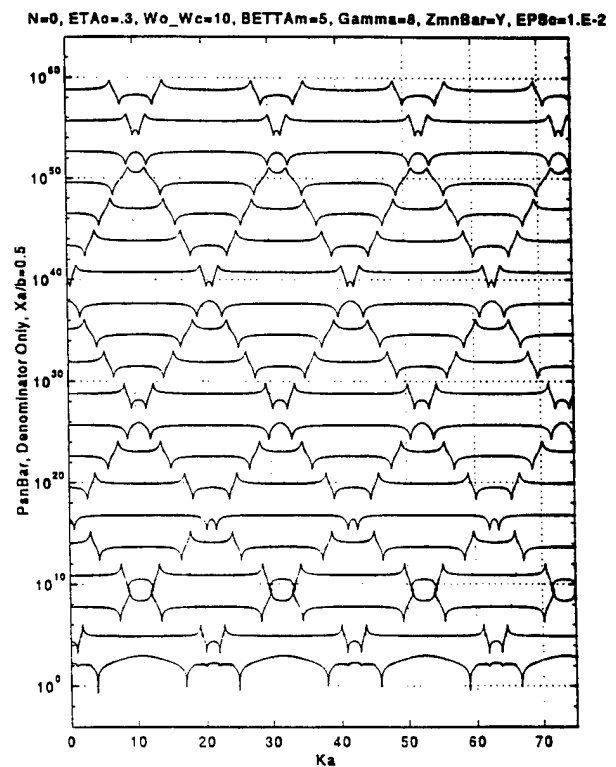


Fig. 10-9a1 and d1

N=0, ETA0=.3, Wo\_Wc=1.E-2, BETTAm=5, Gamma=8, ZmnBar=Y, EPS0=1.E-2

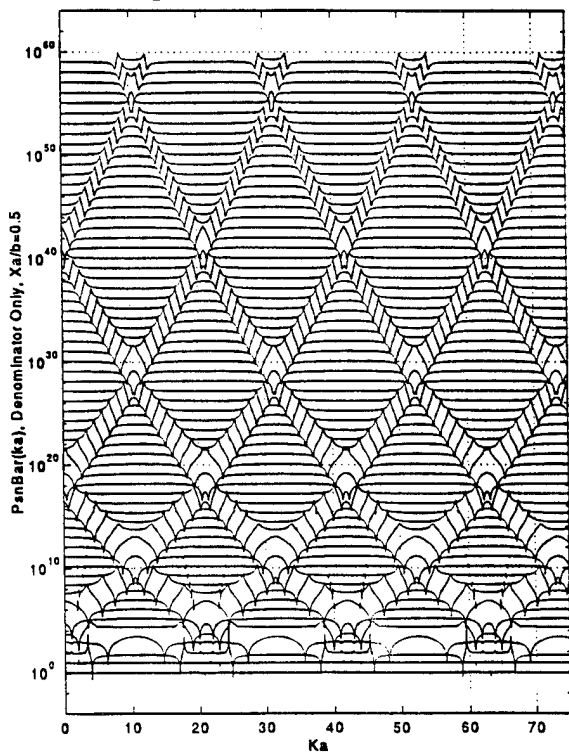


Fig. 10-9b

N=0, ETA0=.3, Wo\_Wc=1.E-2, BETTAm=5, Gamma=8, ZmnBar=Y, EPS0=1.E-2

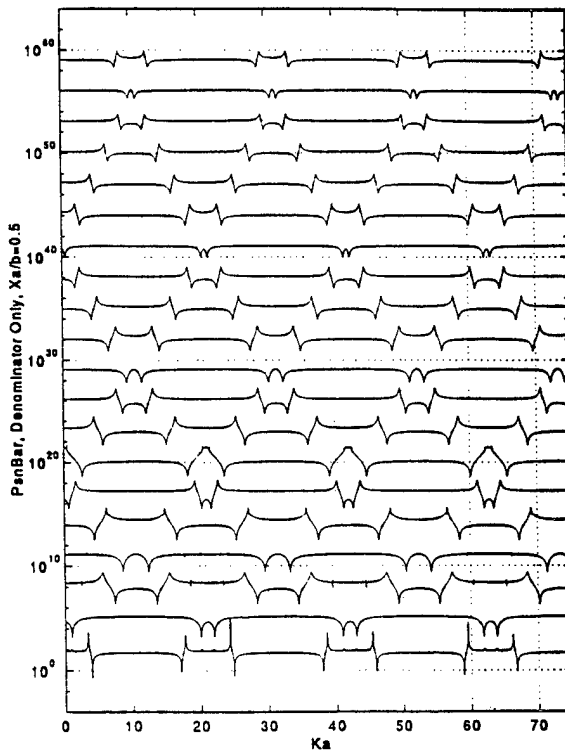


Fig. 10-9b1

N=0, ETA0=.3, Wo\_Wc=2.5E-1, BETTAm=5, Gamma=8, ZmnBar=Y, EPS0=1.E-2

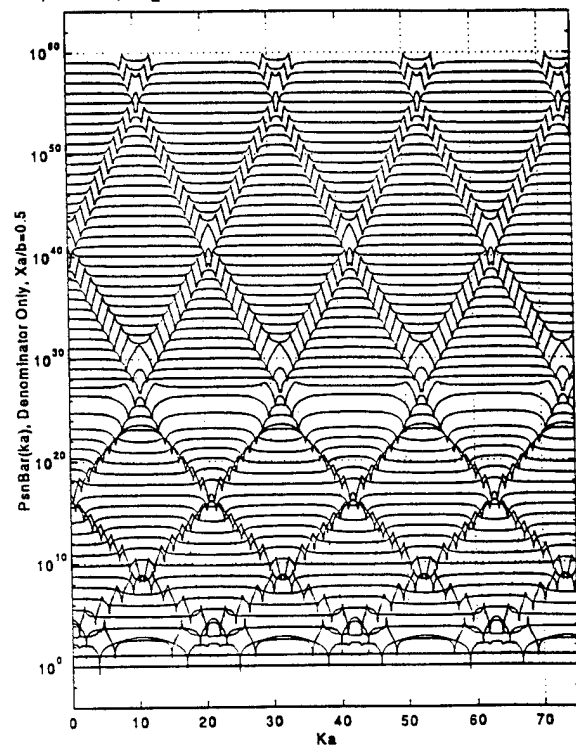


Fig. 10-9c

N=0, ETA0=.3, Wo\_Wc=.25, BETTAm=5, Gamma=8, ZmnBar=Y, EPS0=1.E-2

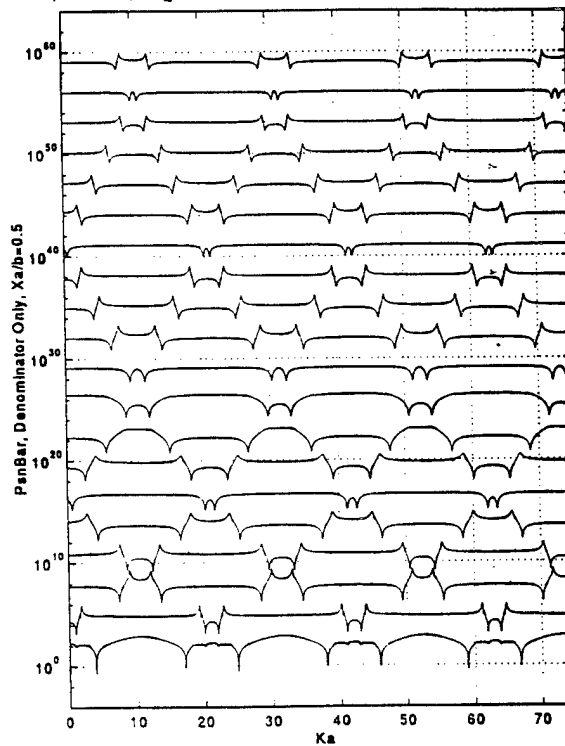


Fig. 10-9c1

Fig. 10-10. As in Fig. 10-9 except for the change from the standard mode index ( $n$ ) of zero to unity.

- a. Mass controlled ribs  $[(\omega_o / \omega_c) = 10]$ .
  - a.1. Sparsely populated waterfall of a.
- b. Stiffness controlled ribs  $[(\omega_o / \omega_c) = 10^{-2}]$ .
  - b.1. Sparsely populated waterfall of b.
- c.  $(\omega_o / \omega_c) = 2.5 \times 10^{-1}$ .
  - c.1. Sparsely populated waterfall of c.
- d. Change in the parameter  $\gamma$  [Eq. (9-5)] from the standard value of 8 to 0.

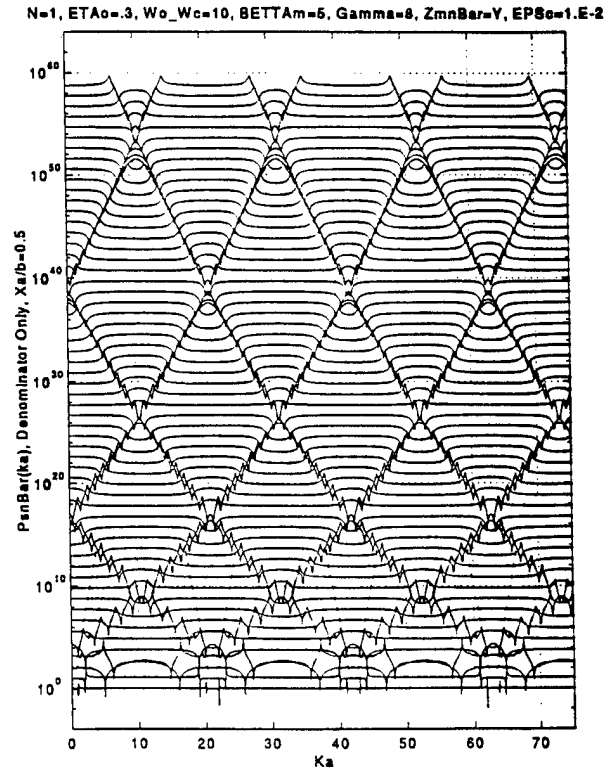


Fig. 10-10a

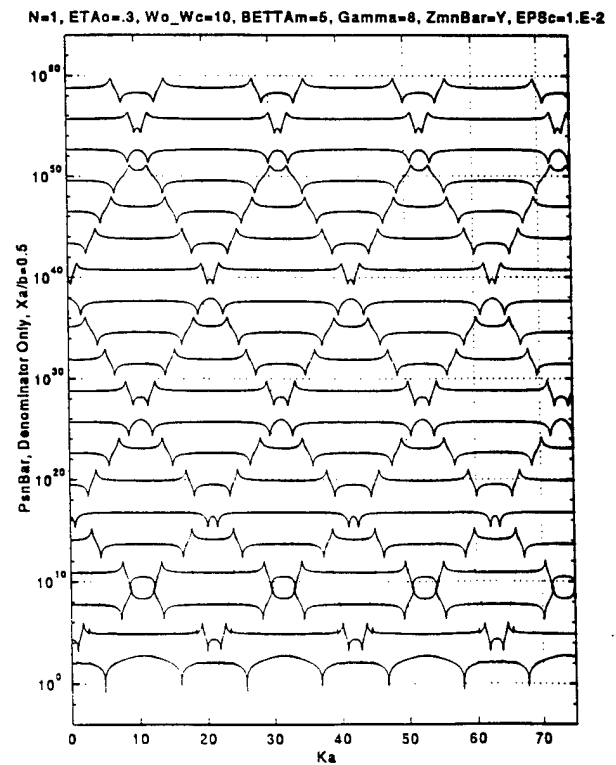


Fig. 10-10a1

$N=1$ ,  $ETA_0=.3$ ,  $Wo\_Wc=1.E-2$ ,  $BETTAm=5$ ,  $Gamma=8$ ,  $ZmnBar=Y$ ,  $EPSc=1.E-2$

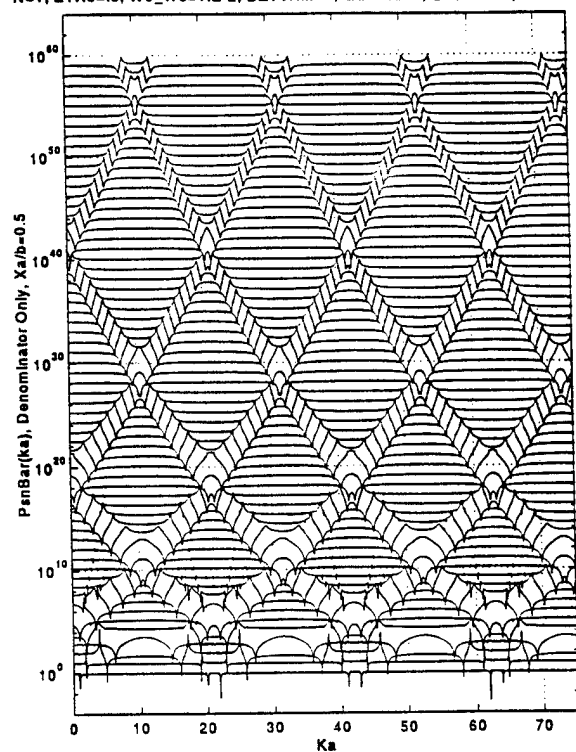


Fig. 10-10b

$N=1$ ,  $ETA_0=.3$ ,  $Wo\_Wc=1.E-2$ ,  $BETTAm=5$ ,  $Gamma=8$ ,  $ZmnBar=Y$ ,  $EPSc=1.E-2$

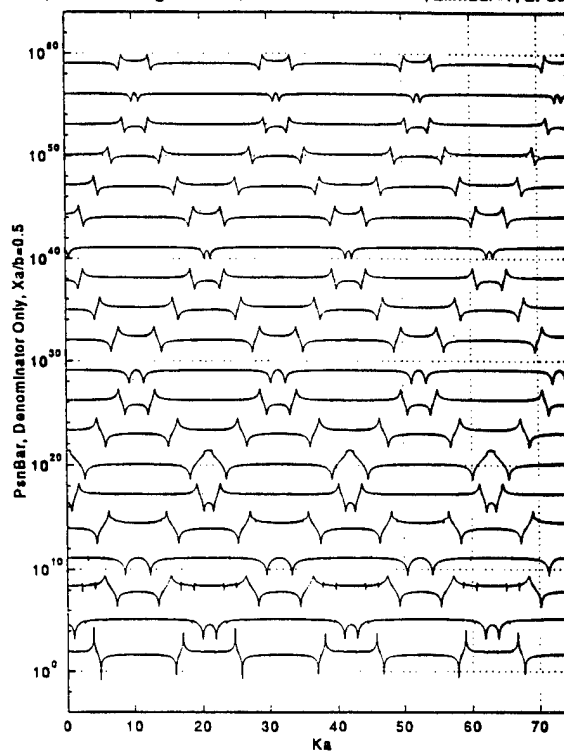


Fig. 10-10b1

$N=1$ ,  $ETA_0=.3$ ,  $Wo\_Wc=2.5E-1$ ,  $BETTAm=5$ ,  $Gamma=8$ ,  $ZmnBar=Y$ ,  $EPSc=1.E-2$

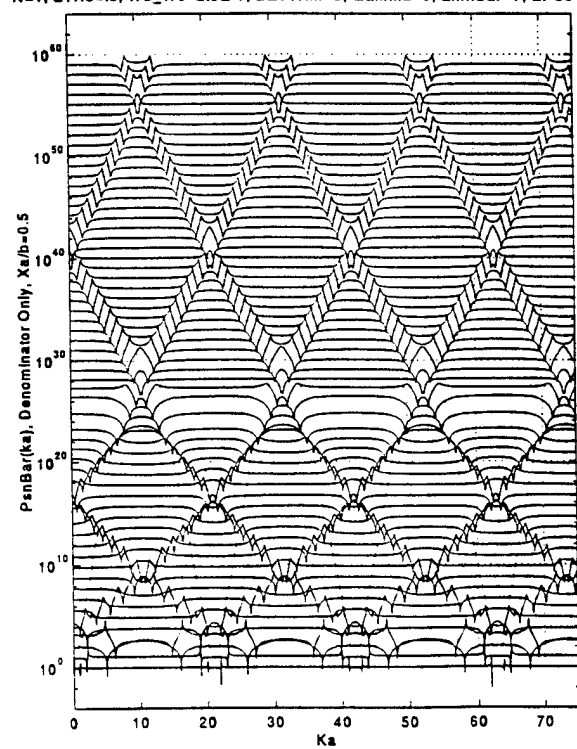


Fig. 10-10c

$N=1$ ,  $ETA_0=.3$ ,  $Wo\_Wc=.25$ ,  $BETTAm=5$ ,  $Gamma=8$ ,  $ZmnBar=Y$ ,  $EPSc=1.E-2$

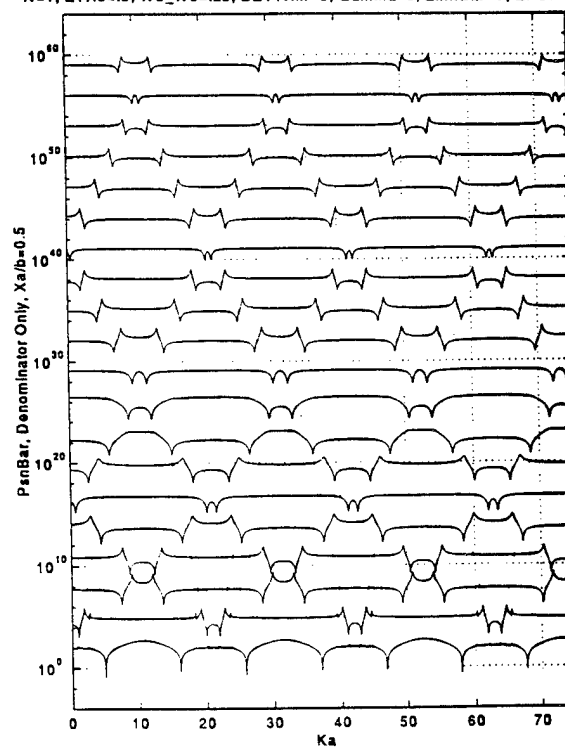


Fig. 10-10c1

N=1, ETAo=.3, Wo\_Wc=2.5E-1, Bettam=1.E3, Gamma=0, ZmnBar=Y, EPSo=1.E-2

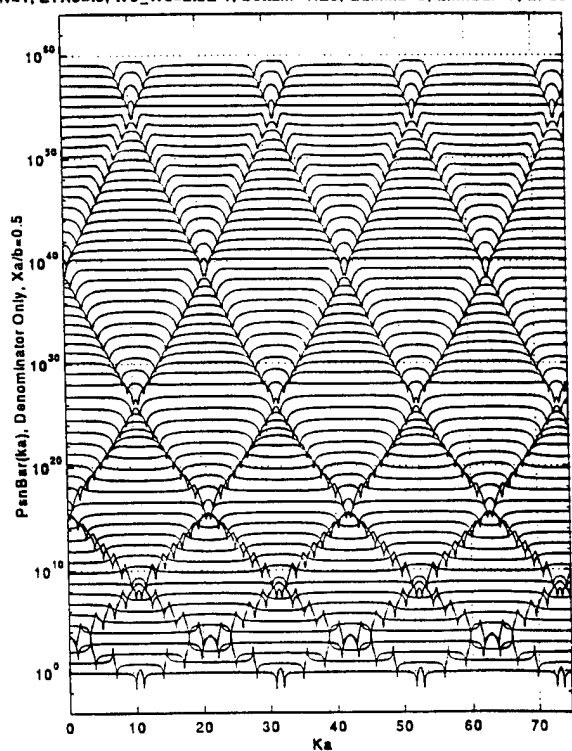


Fig. 10-10d

Fig. 10-11. As in Fig. 10-8a except that the fluid loading parameter ( $\epsilon_c$ ) is changed from the standard value of  $10^{-2}$  to:

- a.  $\epsilon_c = 10^{-4}$ .
- b.  $\epsilon_c = 10^{-1}$ .

N=0, ETAg=1.E-3, Wo\_Wc=10, Bettam=5, ZmnBar=N, EPSo=1.E-4, Xa/b=.5

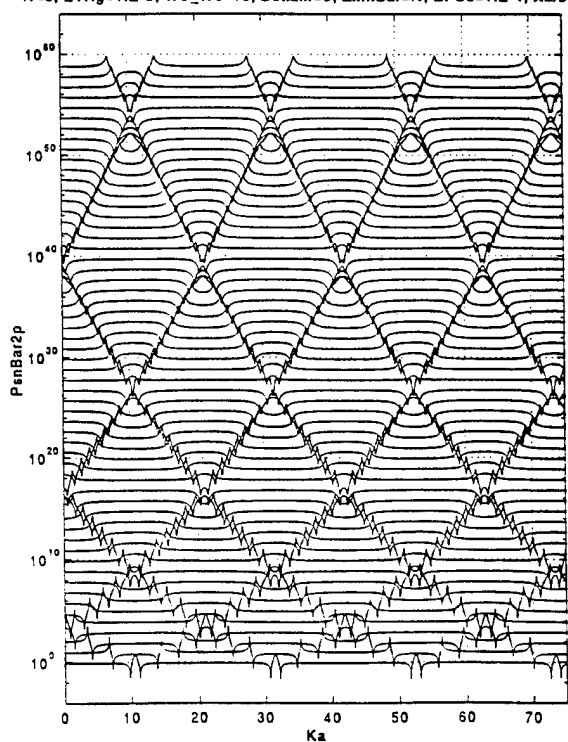


Fig. 10-11a

N=0, ETAg=1.E-3, Wo\_Wc=10, Bettam=5, ZmnBar=N, EPSo=1.E-1, Xa/b=.5

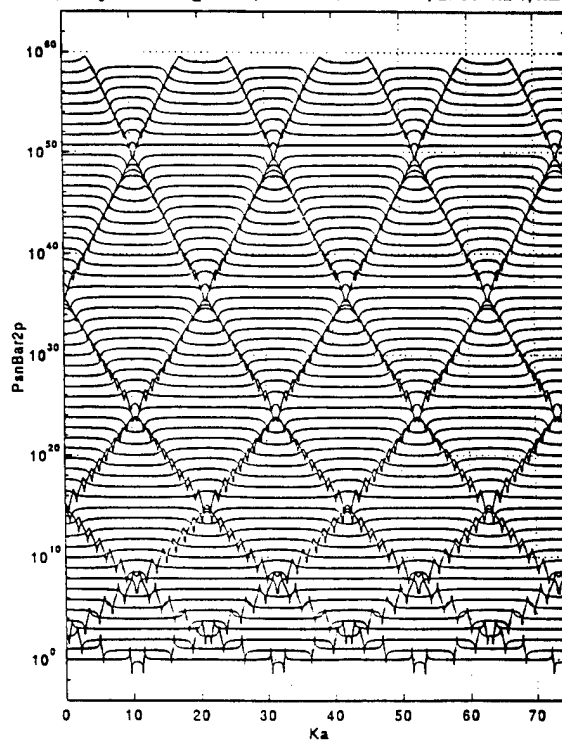


Fig. 10-11b

Fig. 10-12. As in Fig. 10-9a except that the fluid loading parameter ( $\varepsilon_c$ ) is changed from the standard value of  $10^{-2}$  to:

- a.  $\varepsilon_c = 10^{-4}$ .
- b.  $\varepsilon_c = 10^{-1}$ .

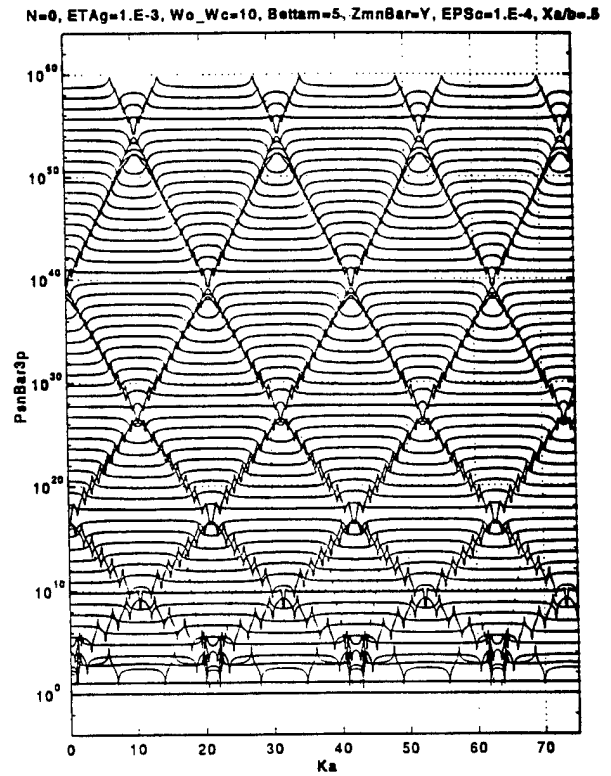


Fig. 10-12a

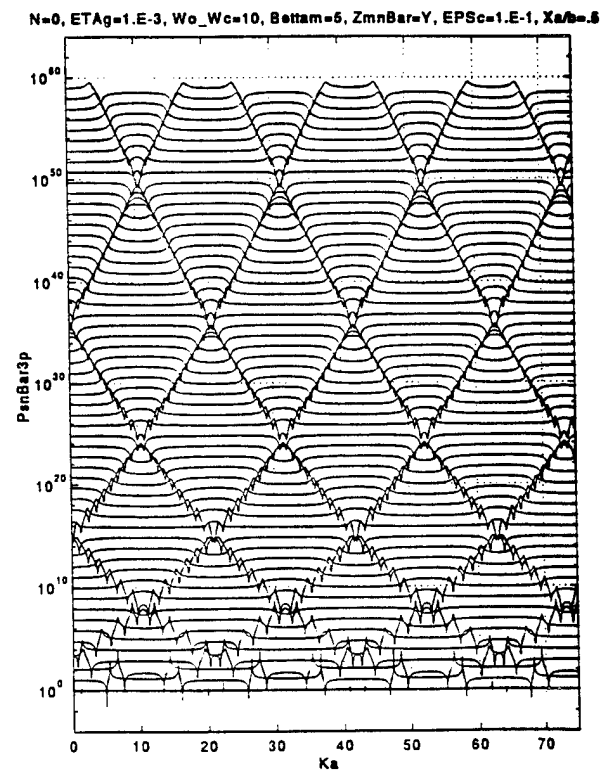


Fig. 10-12b

Fig. 10-13. Normalized modal drive  $\bar{P}_{sn}(k, \omega)$  in lieu of a proper order model for the ribs on a hybrid cylinder as a function of  $(ak)$  in a  $(\omega/\omega_c)$  - waterfall format.

- a. Under standard values  $[(\omega_o/\omega_c) = 10]$ .
- b. Stiffness controlled ribs  $[(\omega_o/\omega_c) = 10^{-2}]$ .
- c.  $(\omega_o/\omega_c) = 2.5 \times 10^{-1}$ .

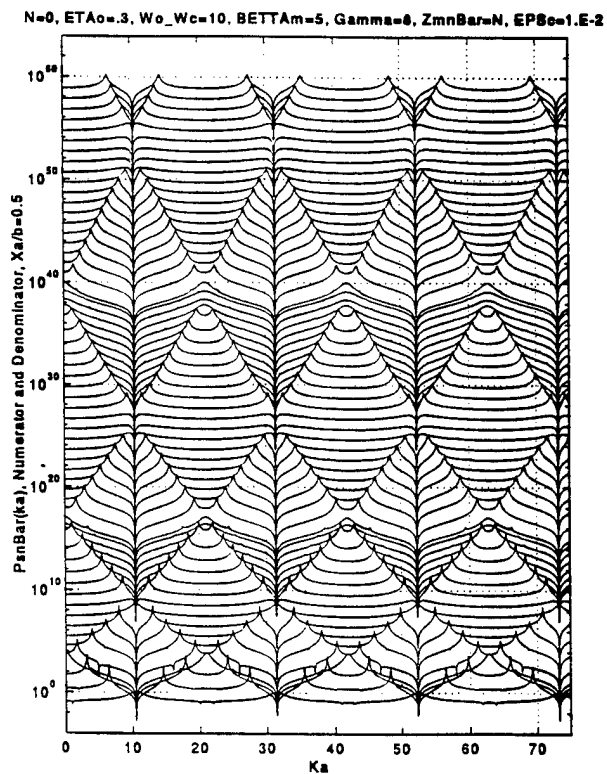


Fig. 10-13a

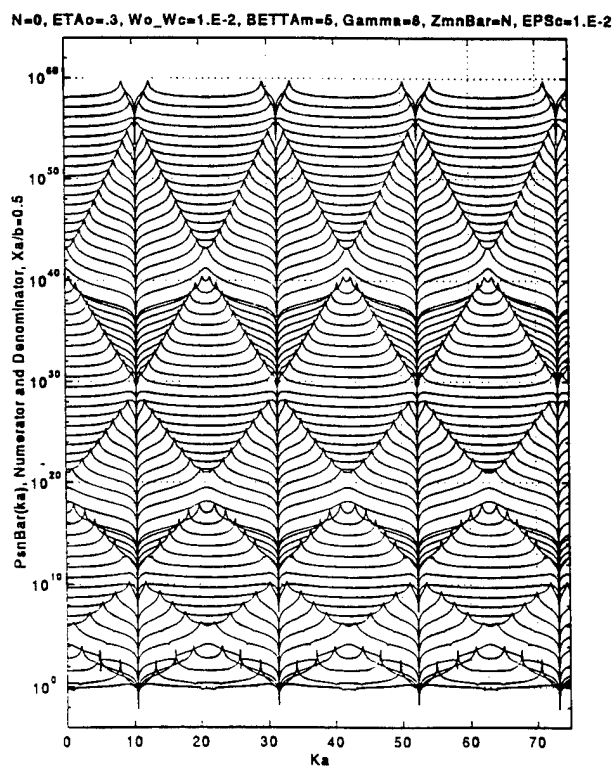


Fig. 10-13b

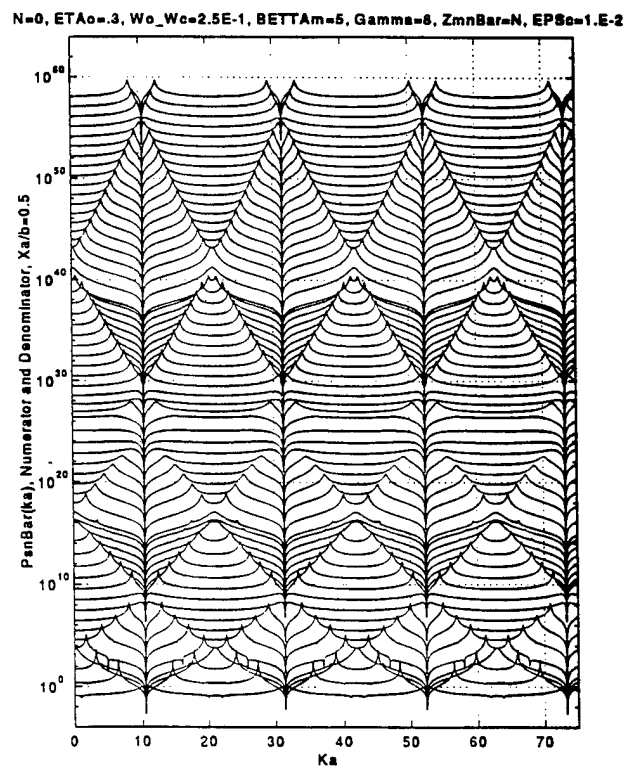


Fig. 10-13c

Fig. 10-14. As in Fig. 10-13 except for the change to a natural cylinder.

- a. Under standard values  $[(\omega_o / \omega_c) = 10]$ .
- b. Stiffness controlled ribs  $[(\omega_o / \omega_c) = 10^{-2}]$ .
- c.  $(\omega_o / \omega_c) = 2.5 \times 10^{-1}$ .

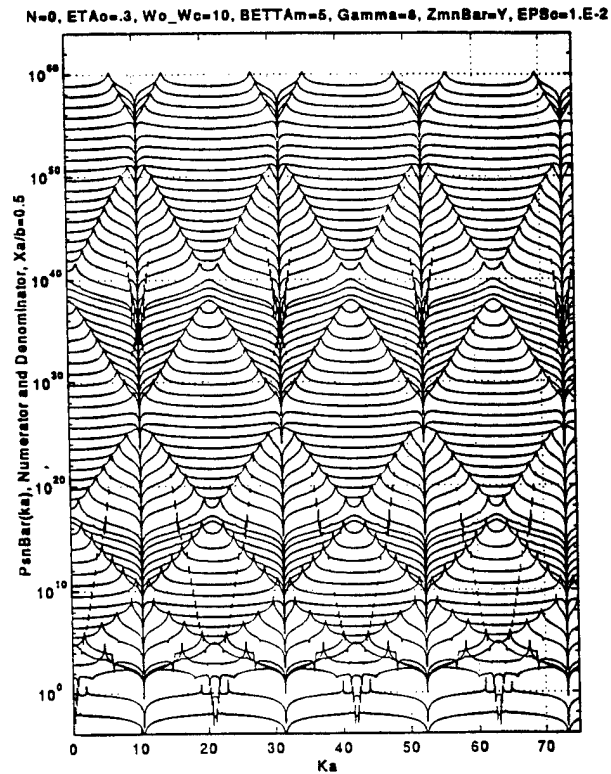


Fig. 10-14a

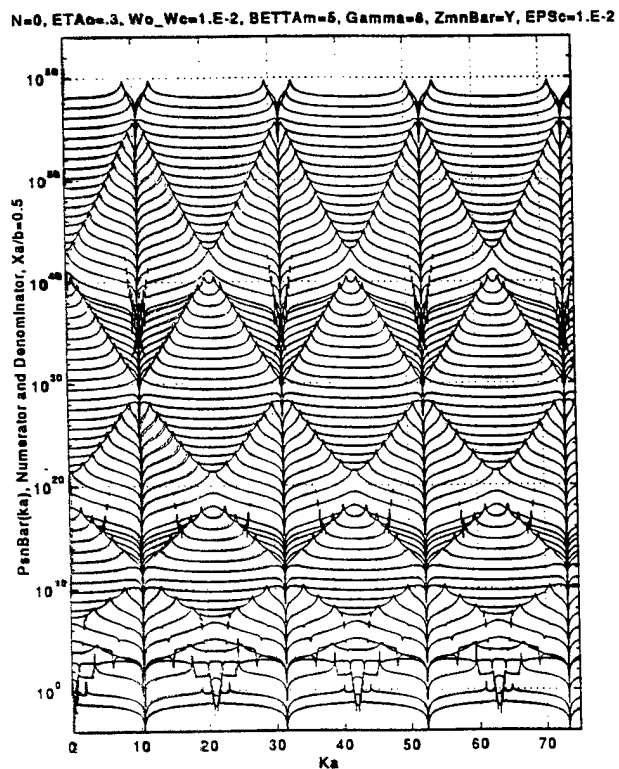


Fig. 10-14b

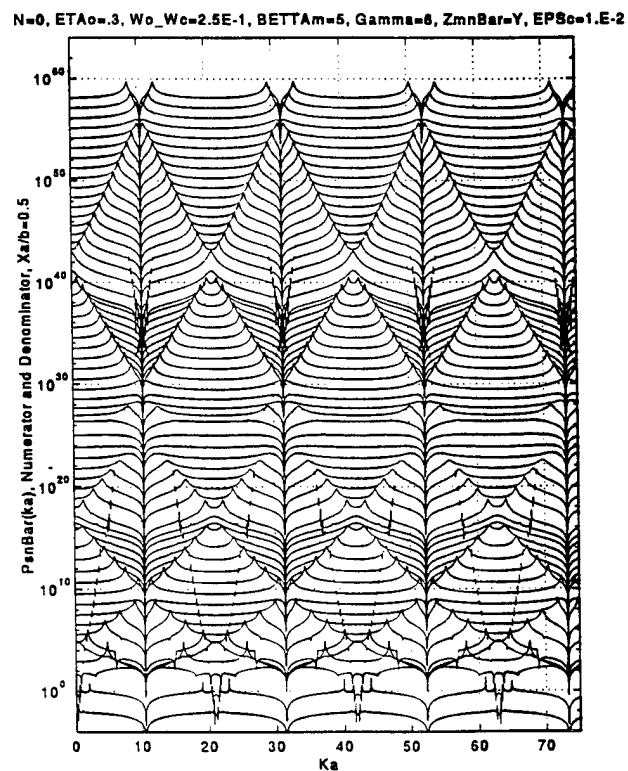


Fig. 10-14c



Fig. 10-15. As in Fig. 10-14 except for the change from the standard mode index ( $n$ ) of zero to unity.

- Mass controlled ribs  $[(\omega_o / \omega_c) = 10]$ .
- Stiffness controlled ribs  $[(\omega_o / \omega_c) = 10^{-2}]$ .
- $(\omega_o / \omega_c) = 2.5 \times 10^{-1}$ .
- As in c. except that  $(\epsilon_c)$  is decreased from  $10^{-2}$  to  $10^{-4}$ .
- As in c. except that  $(\epsilon_c)$  is increased from  $10^{-2}$  to  $10^{-1}$ .
- As in c. except that  $(\epsilon_c)$  and  $(\eta_p)$  are changed from  $10^{-2}$  and  $10^{-3}$  to  $10^{-4}$  and  $5 \times 10^{-3}$ , respectively.
- As in c. except that  $(\epsilon_c)$  and  $(\eta_p)$  are changed from  $10^{-2}$  and  $10^{-3}$  to  $10^{-4}$  and  $2.5 \times 10^{-2}$ , respectively.

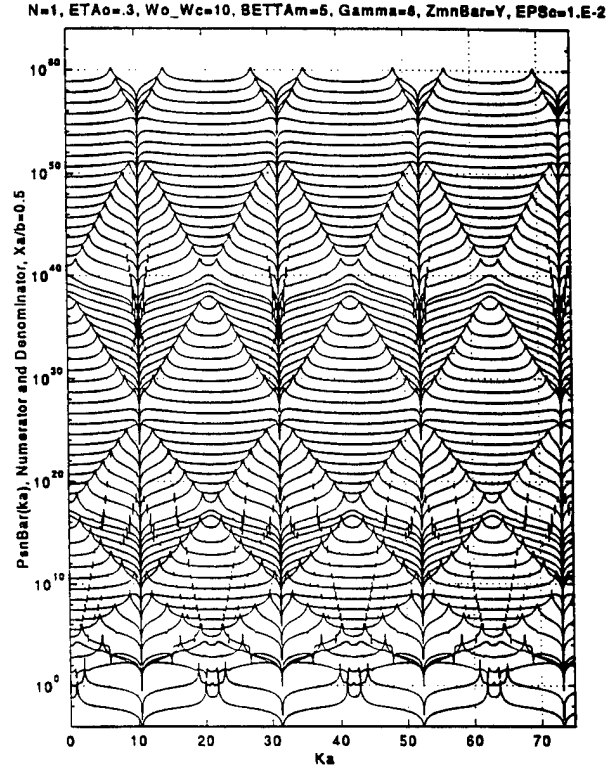


Fig. 10-15a

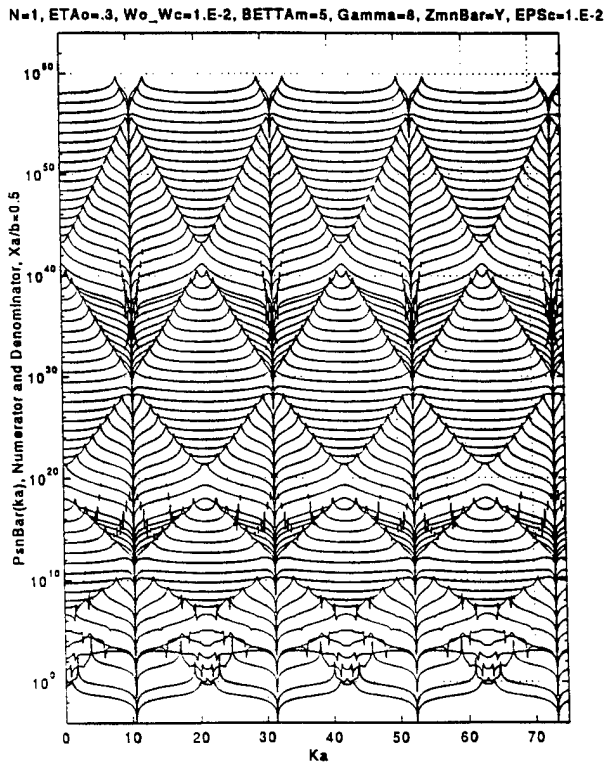


Fig. 10-15b

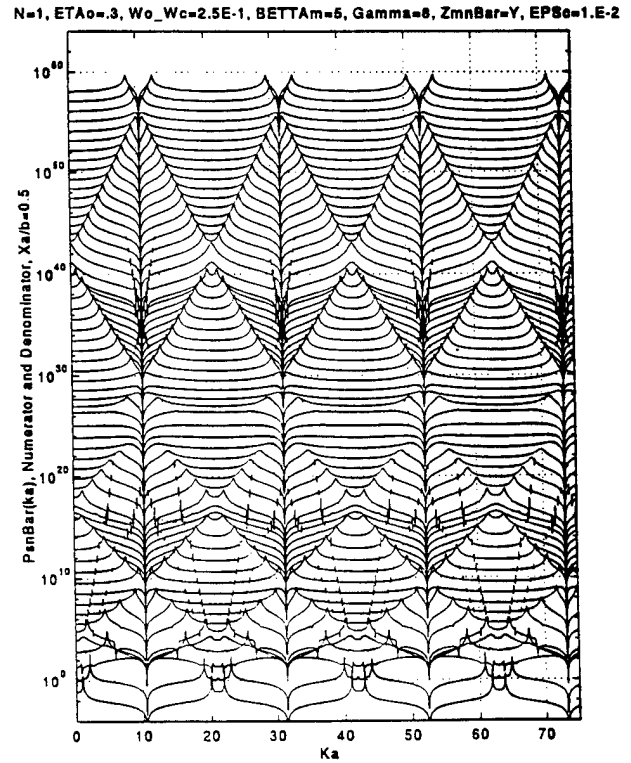


Fig. 10-15c

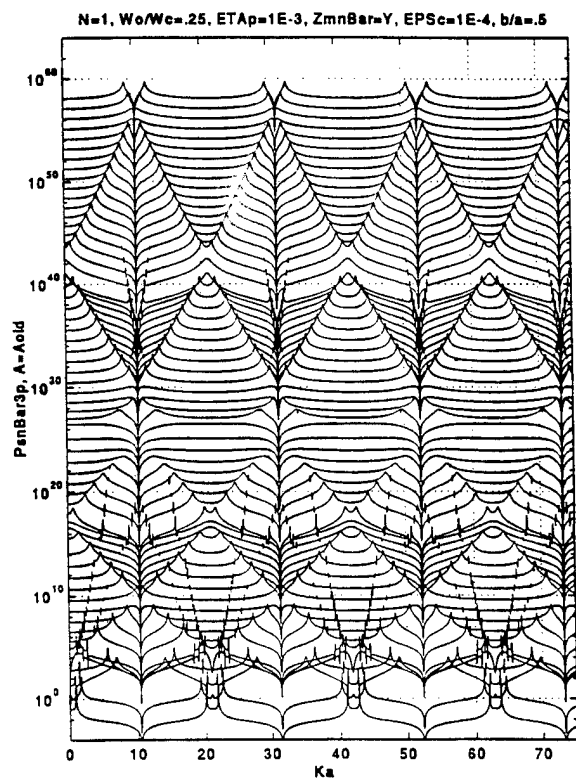


Fig. 10-15d

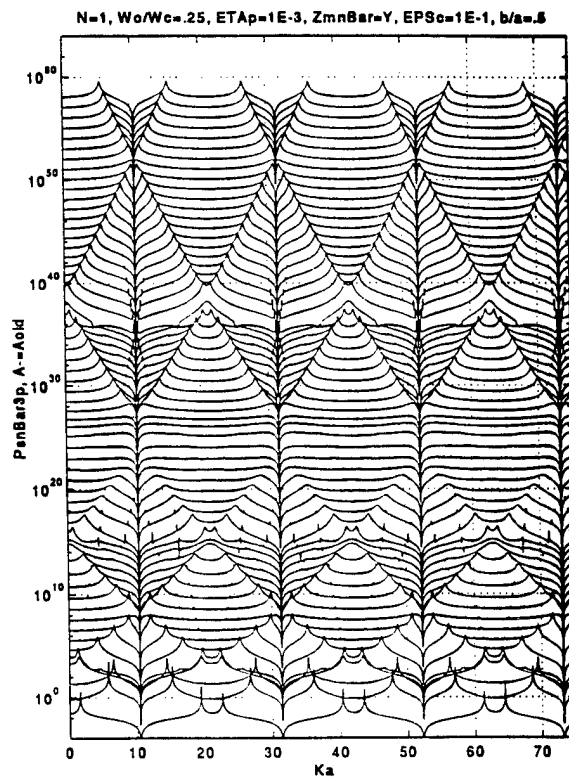


Fig. 10-15e

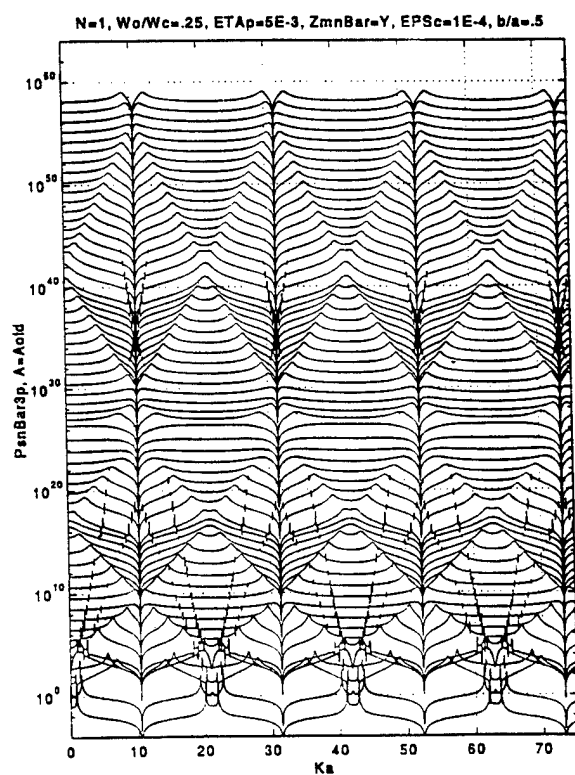


Fig. 10-15f

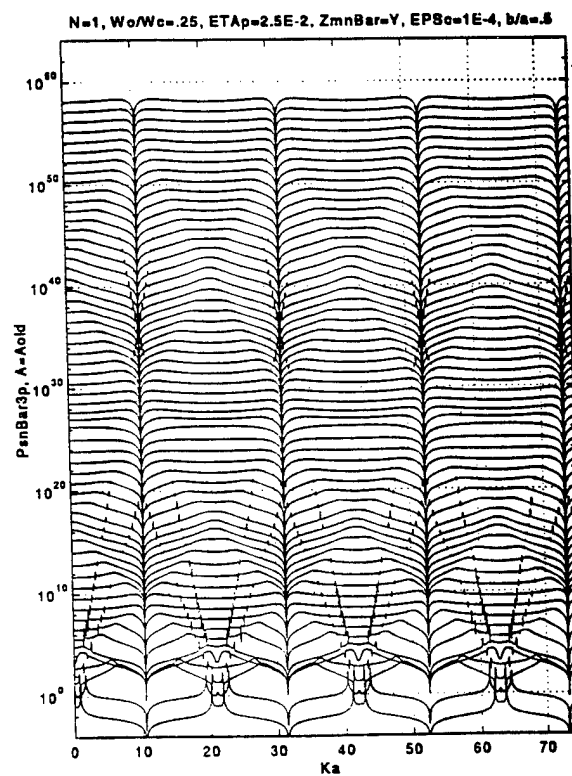


Fig. 10-15g

Fig. 10-16. As in 10-13 except that the axial position ( $x_a/b$ ) of application of the external drive is changed from the standard value of 0.5 to 0.3.

- a. Mass controlled ribs  $[(\omega_o/\omega_c) = 10]$ .
- b. Stiffness controlled ribs  $[(\omega_o/\omega_c) = 10^{-2}]$ .
- c.  $(\omega_o/\omega_c) = 2.5 \times 10^{-1}$ .

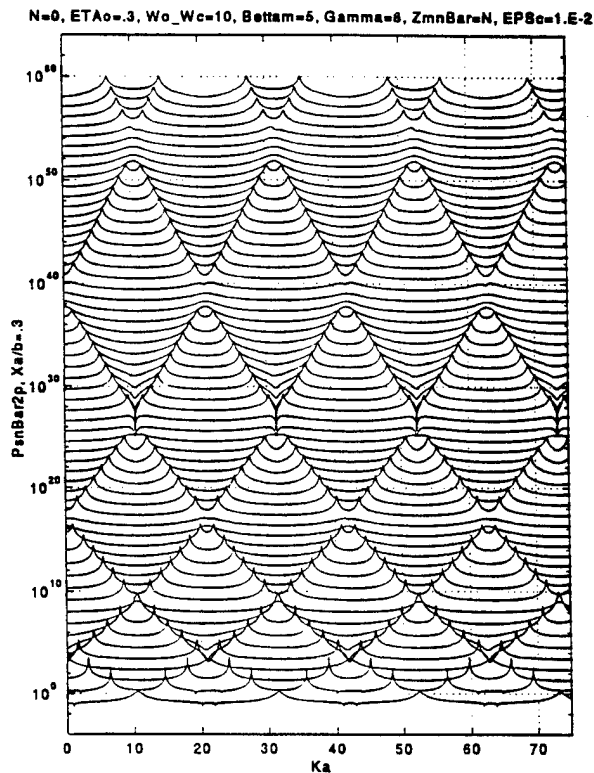


Fig. 10-16a

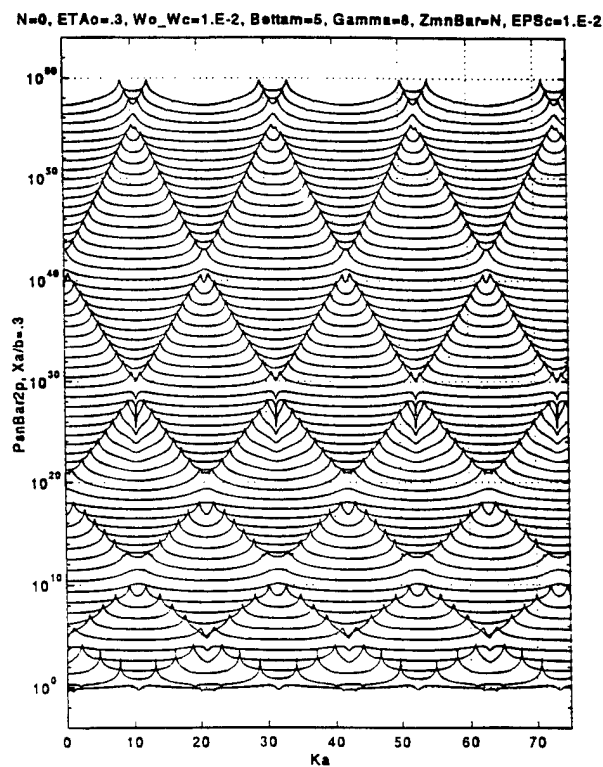


Fig. 10-16b

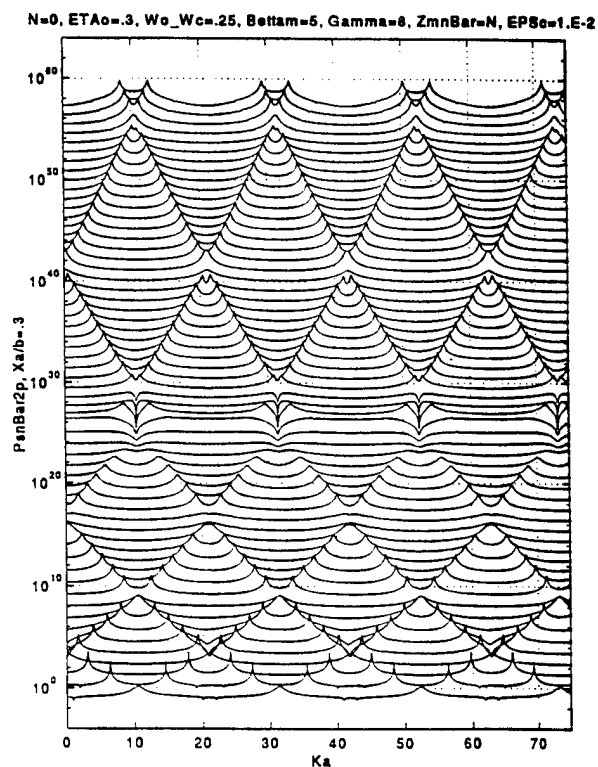


Fig. 10-16c

Fig. 10-17. As Fig. 10-16 except for the change to a **natural** cylinder.

- a. Mass controlled ribs  $[(\omega_o / \omega_c) = 10]$ .
- b. Stiffness controlled ribs  $[(\omega_o / \omega_c) = 10^{-2}]$ .
- c.  $(\omega_o / \omega_c) = 2.5 \times 10^{-1}$ .

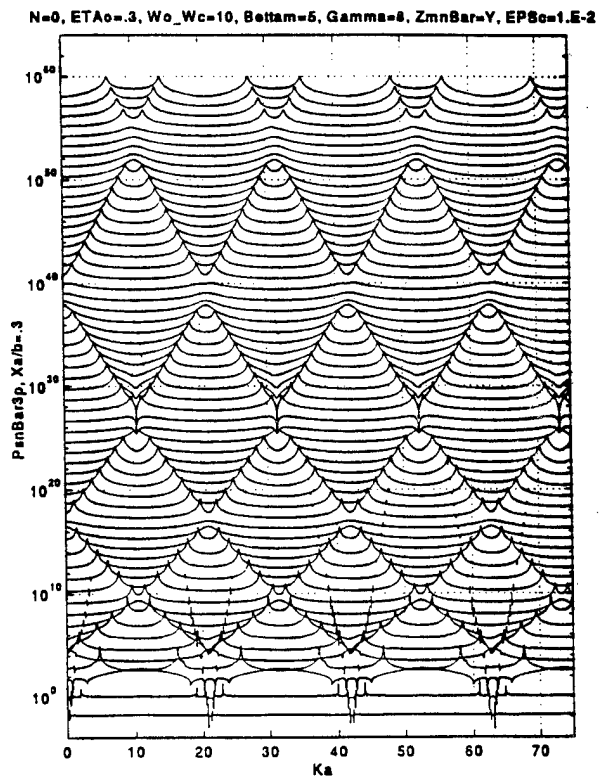


Fig. 10-17a

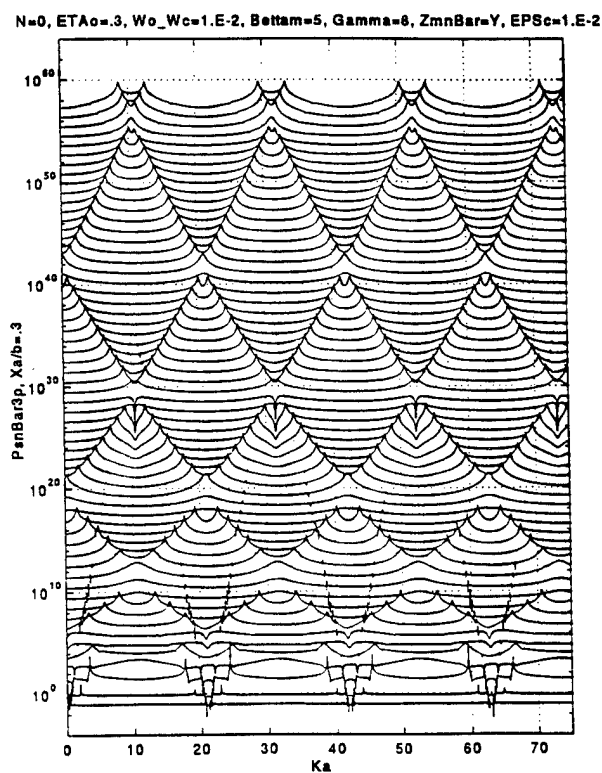


Fig. 10-17b

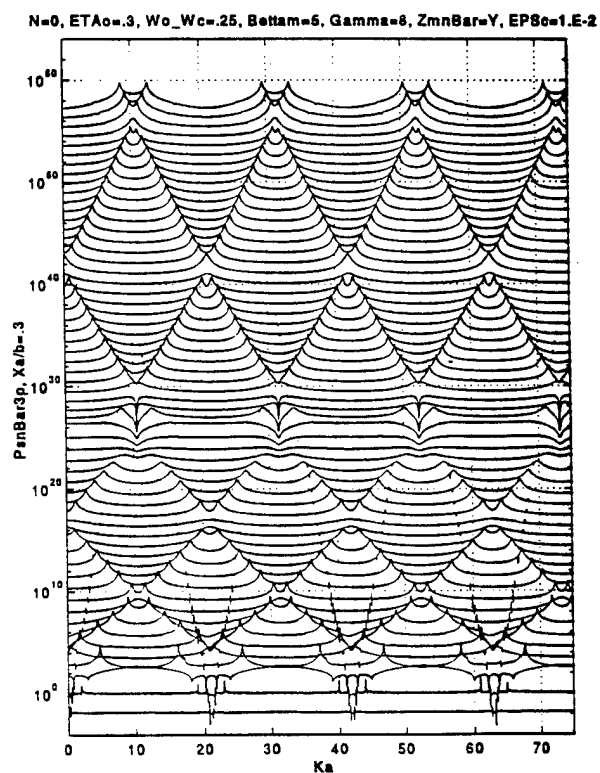


Fig. 10-17c

Fig. 10-18. As in Fig. 10-17 except for the change from the standard mode index ( $n$ ) of zero to unity.

- Mass controlled ribs  $[(\omega_o / \omega_c) = 10]$ .
- Stiffness controlled ribs  $[(\omega_o / \omega_c) = 10^{-2}]$ .
- $(\omega_o / \omega_c) = 2.5 \times 10^{-1}$ .

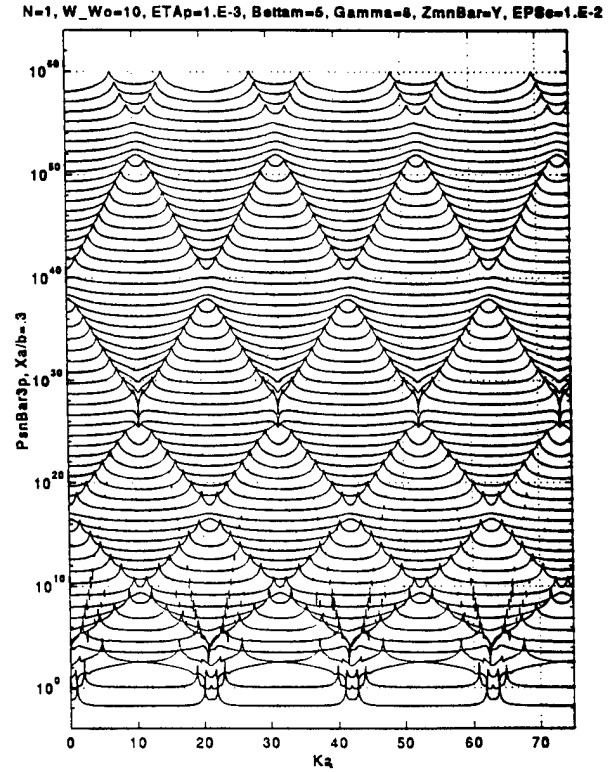


Fig. 10-18a

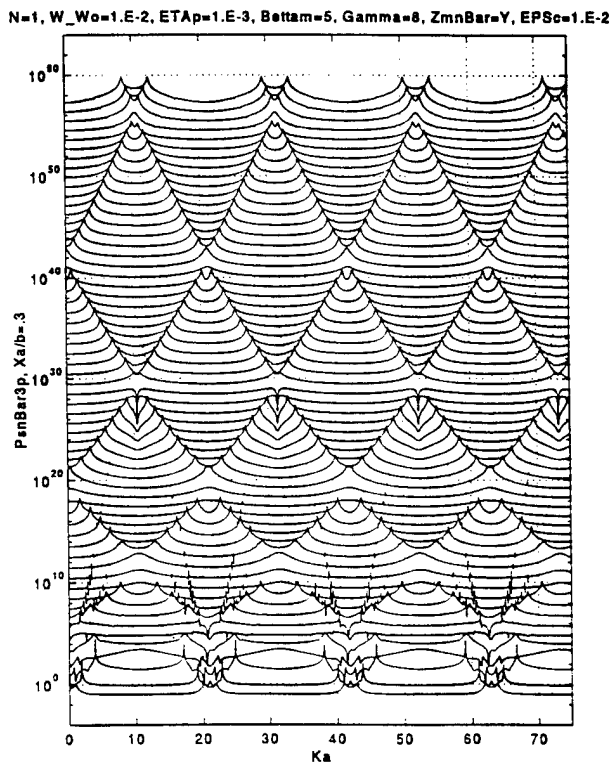


Fig. 10-18b

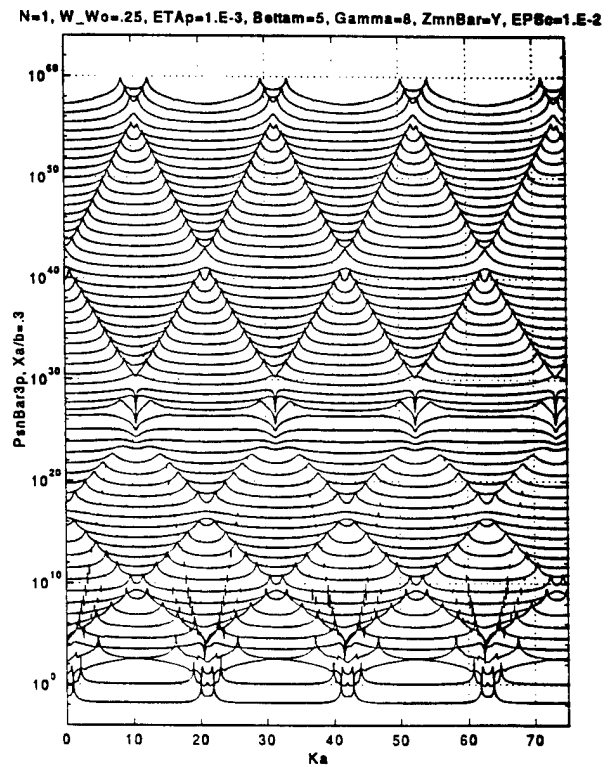


Fig. 10-18c

Fig. 10-19. As in Fig. 10-16 except that the fluid loading parameter ( $\epsilon_c$ ) is changed from the standard value of  $10^{-2}$  to:

- a.  $\epsilon_c = 10^{-4}$ .
- b.  $\epsilon_c = 10^{-1}$ .

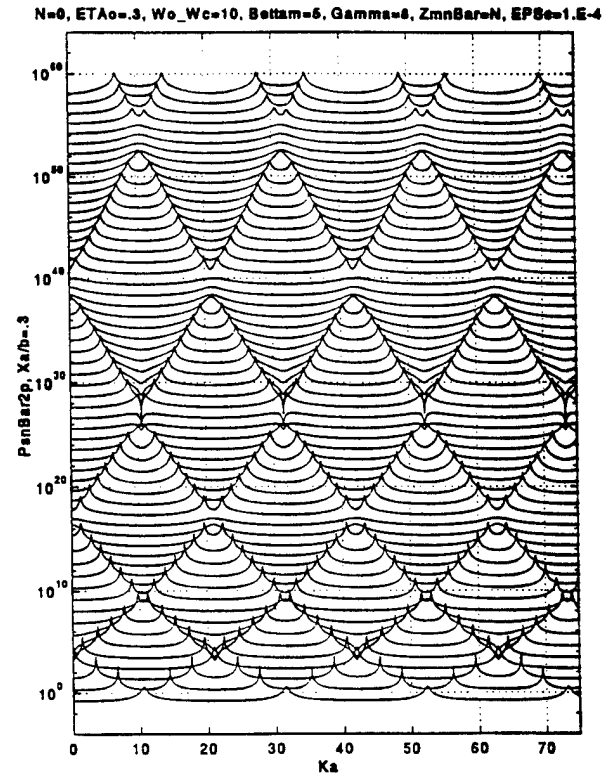


Fig. 10-19a

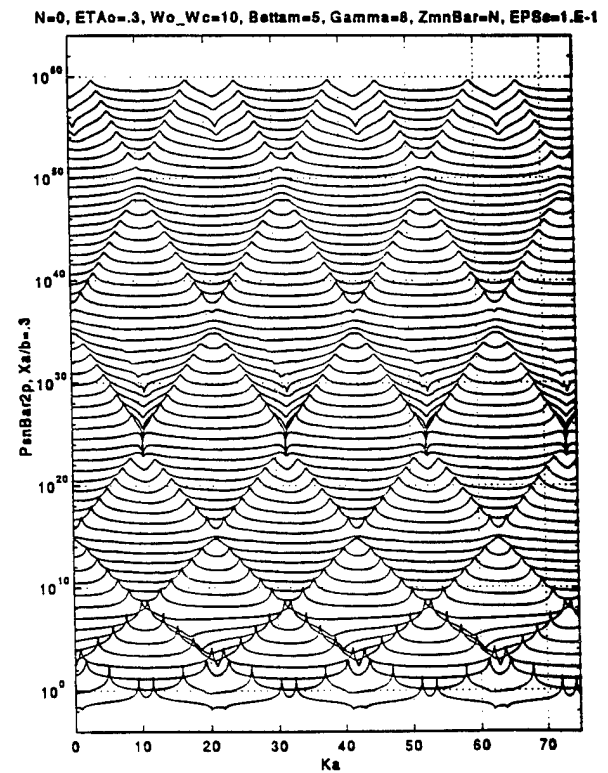


Fig. 10-19b

Fig. 10-20. As in Fig. 10-17 except that the fluid loading parameter ( $\epsilon_c$ ) is changed from the standard value of  $10^{-2}$  to:

- a.  $\epsilon_c = 10^{-4}$ .
- b.  $\epsilon_c = 10^{-1}$ .

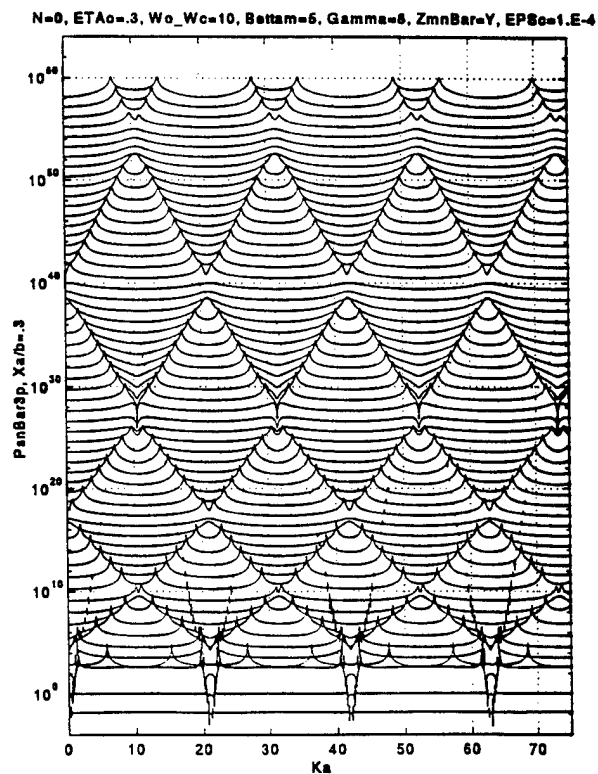


Fig. 10-20a

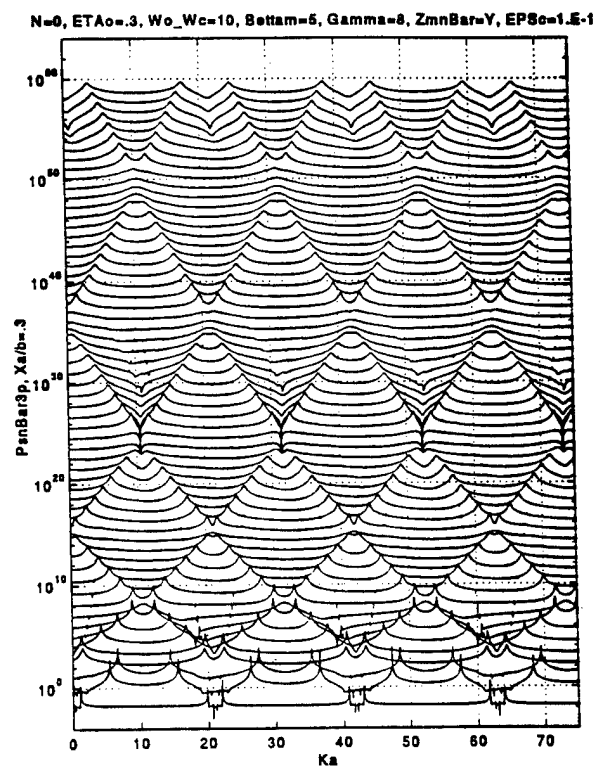


Fig. 10-20b

Fig. 10-21. As in Fig. 10-15 except that  $A(\omega/\omega_o)$  [Eq. (9-3)] is replaced by  $A'(\omega/\omega_o)$  [Eq. (9-6)].

- Mass controlled ribs  $[(\omega_o/\omega_c) = 10]$ .
- Stiffness controlled ribs  $[(\omega_o/\omega_c) = 10^{-2}]$ .
- $(\omega_o/\omega_c) = 2.5 \times 10^{-1}$ .
- As in c. except that  $(\epsilon_c)$  is decreased from  $10^{-2}$  to  $10^{-4}$ .
- As in c. except that  $(\epsilon_c)$  is increased from  $10^{-2}$  to  $10^{-1}$ .
- As in c. except that  $(\epsilon_c)$  and  $(\eta_p)$  are changed from  $10^{-2}$  and  $10^{-3}$  to  $10^{-4}$  and  $5 \times 10^{-3}$ , respectively.
- As in c. except that  $(\epsilon_c)$  and  $(\eta_p)$  are changed from  $10^{-2}$  and  $10^{-3}$  to  $10^{-4}$  and  $2.5 \times 10^{-2}$ , respectively.

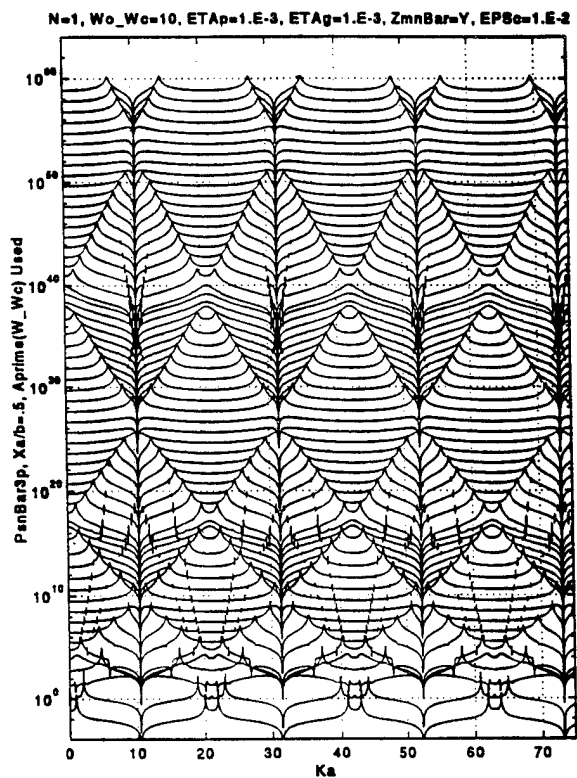


Fig. 10-21a

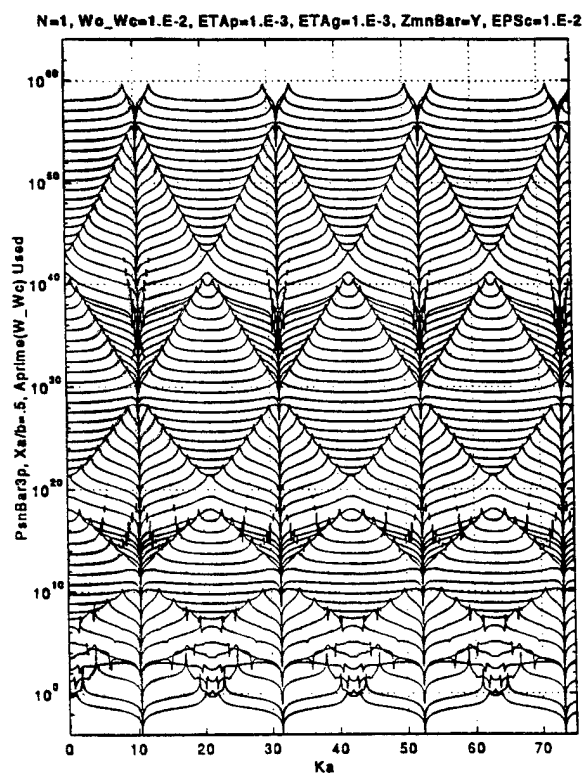


Fig. 10-21b

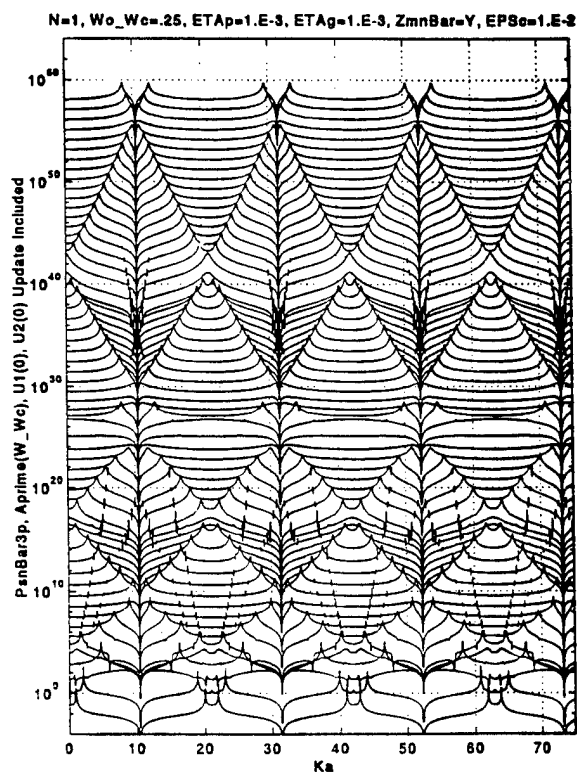


Fig. 10-21c



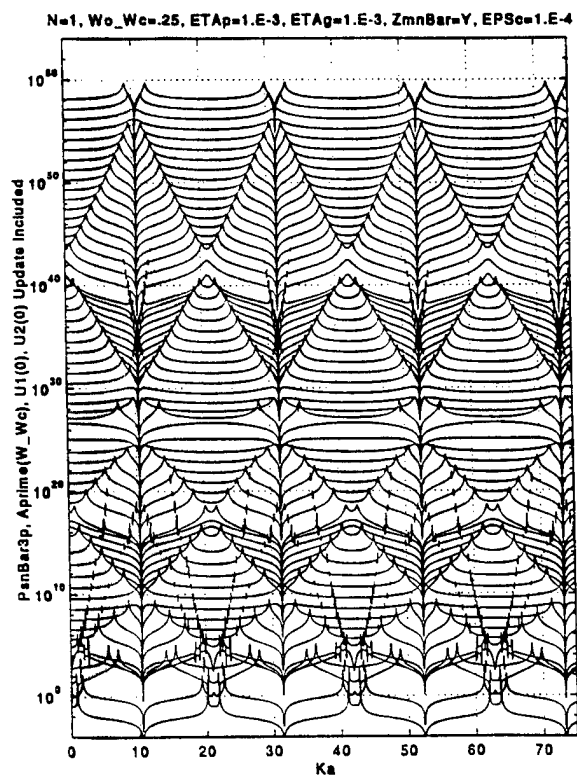


Fig. 10-21d

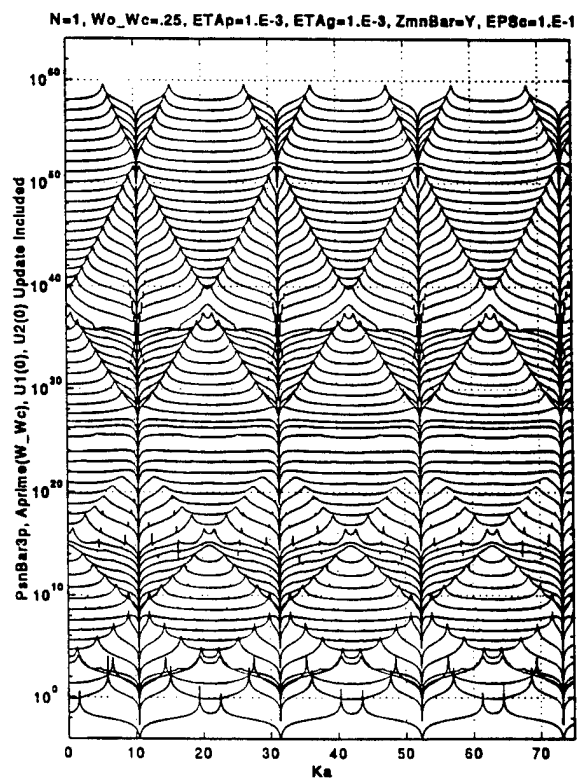


Fig. 10-21e

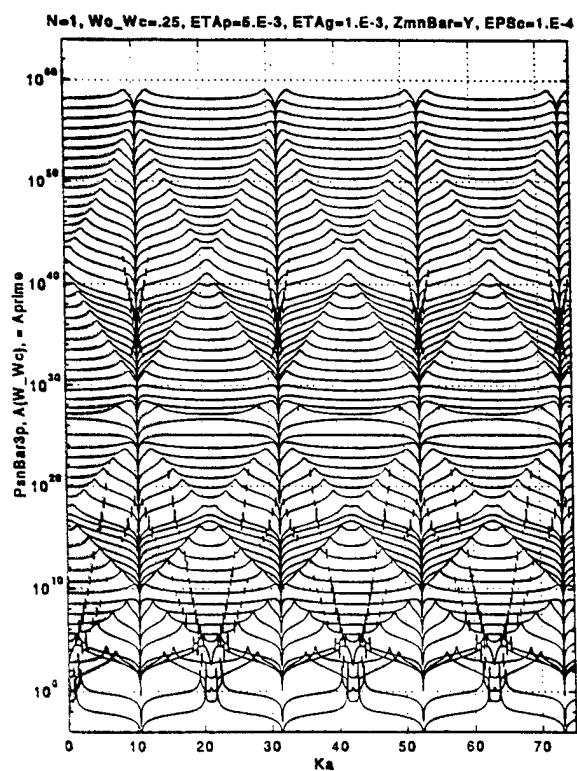


Fig. 10-21f

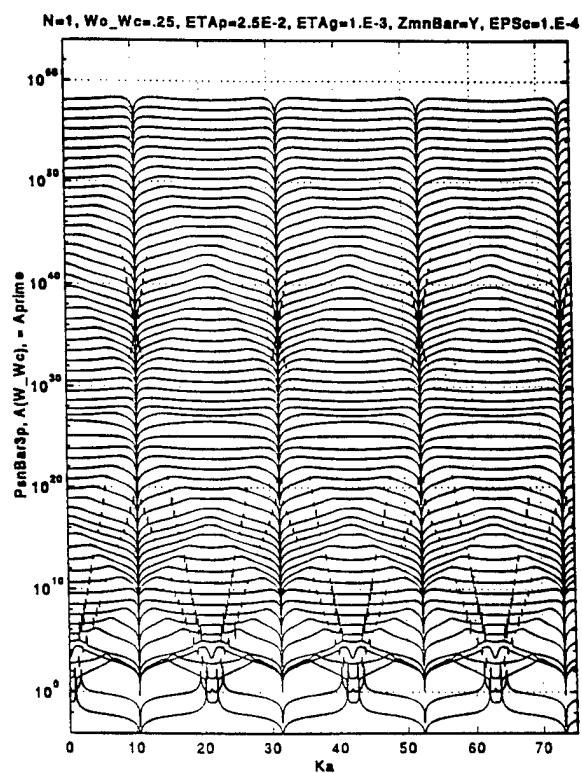


Fig. 10-21g

# XI. PASS AND STOP BANDS IN THE DRIVE $P_{sn}(k, \omega)$ IN LIEU OF THE RIBS

It may be useful to recount some aspects of the material covered in Section X. The quantity  $\bar{P}_{osn}(k, \omega)$ , which describes the normalized modal drive in lieu of the ribs in the first order model of a regularly ribbed cylinder, is depicted in Figs. 10-1 through 7. The phenomenon of aliasing is clearly visible in the patterns of these figures. The patterns are largely governed by the dispersive ridges and associated peaks and their duplications by the action of the self-aliased wavenumber operator  $S_b(k)$ . At aliasing knots, which are regions in which pairs of aliasing orders cross, the contribution of each order at the knot substantially add. There is hardly a phase matching or mismatching of the contributions at a knot. In a first order model the interactions among the ribs via the shell are neglected. [A first order Born approximation of a sort?] Significantly, in the regularly ribbed shell the interactions among the ribs are accounted for by a factor. This factor is designated  $I_{bn}(k, \omega)$ ; the drive  $\bar{P}_{sn}(k, \omega)$ , which describes the normalized modal drive in lieu of the ribs in a proper order model of a regularly ribbed shell, accommodates this factor in the form

$$\bar{P}_{sn}(k, \omega) = I_{bn}(k, \omega) \bar{P}_{osn}(k, \omega) . \quad (11-1)$$

[cf. Eq. (10-3b).] For ribs of some influence; e.g.,  $(M / mb) \simeq 0.2$ , the influence of  $I_{bn}(k, \omega)$  on the behavior of  $\bar{P}_{sn}(k, \omega)$  is a major one. [So much so that any notion to use a Born approximation of higher orders to account for  $I_{bn}(k, \omega)$  need not be contemplated!] The behavior of  $I_{bn}(k, \omega)$  is depicted in Figs. 10-8 through 12. These figures show that  $I_{bn}(k, \omega)$  is aliased in  $(k)$  with respect to  $(\kappa_1)$ , as is  $\bar{P}_{osn}(k, \omega)$ . The ridges and associated peaks in Figs. 10-8 through 12

are, however, displaced from those of the dispersive loci; these new loci are designated false to distinguish them from the bonafide dispersive loci which dominate the scenes in Figs. 10-1 through 7. Whether the displacement is on one side of the dispersive loci or the other depends on whether the line impedance of the ribs is mass or stiffness controlled. This characteristic in the line impedance of the ribs is assigned to the province of the factor  $A(\omega / \omega_o)$ . This factor is defined in Eqs. (9-2) and (9-3). Moreover, pairs of crossing aliasing orders possess opposite signs and, therefore, when they cross at an aliasing knot, they cancel each other out. Those curves in the waterfall displays of  $I_{bn}(k, \omega)$  that string aliasing knots are devoid of ridges and associated peaks; these ridges and peaks are suppressed by cancellations. These features are more easily read in Figs. 10-8.1 through 12.1 than in Figs. 10-8 and 12. The behavior of the modal drive  $\bar{P}_{sn}(k, \omega)$  in lieu of the ribs is shown in Eq. (11-1) to be composed of both factors  $\bar{P}_{osn}(k, \omega)$  and  $I_{bn}(k, \omega)$ ; its behavior is depicted in Figs. 10-13 through 20. From the foregoing descriptions, it is clear that the factor  $I_{bn}(k, \omega)$  systematically suppresses the ridges and associated peaks that characterize the prominences in the factor  $\bar{P}_{osn}(k, \omega)$ . Thus, in  $\bar{P}_{sn}(k, \omega)$  the dispersive patterns that dominate the patterns in  $\bar{P}_{osn}(k, \omega)$  are absent. On the other hand, the factor  $I_{bn}(k, \omega)$  systematically introduces ridges and associated peaks that prominently show in the patterns of  $\bar{P}_{sn}(k, \omega)$ ; these new loci are false dispersive loci and are displaced on one side or the other of the dispersive loci. The side is determined by the sign of the real part of  $A(\omega / \omega_o)$ . Significantly, the false dispersive loci do not possess ridges and peaks at the aliasing knots where pairs of aliasing orders of false dispersive loci cross. Since the contributions of the crossing aliasing orders, of false dispersive loci, at the aliasing knots possess equal magnitudes but opposite phases, they cancel out. A string of knots at the same frequency band, establish a stop band; the absence of ridges and associated peaks renders, in this

frequency band, a fairly uniform set of components with respect to the wavenumber ( $k$ ), implying thereby a lack of propagating free waves and a confinement in the spatial  $x$ -domain in that frequency band. The false dispersive loci and the cancellations at the aliasing knots are in direct consequence of the interactions among the ribs via the shell. In the first order model, in contrast, the aliasing is governed by the dispersive loci and the cancellations are absent. The stop bands are, therefore, a phenomenon that manifest these interactions. On the other hand, away from an aliasing knot, reinforcement may take place between aliasing orders as the opposite phases change when the false dispersive loci approach or recede an aliasing knot. These reinforcements give rise to pass bands in which propagation of free waves run substantially unimpeded, if not aided, by the presence of the ribs. Again, the pass and stop bands are, therefore, a phenomenon that manifest the interactions among the ribs via the shell; the pass and stop bands are a phenomenon that is absent in this first order model. Again, the first order model is used in this report to emphasize the role played by the interactions among the ribs via the shell. The notion of the false dispersive loci and the phenomenon of pass and stop bands are facilitated by the first order model in that this very notion and phenomenon are absent in this model. However, since the first order model is merely a device in this service, and the service is rendered; its use is terminated at this stage.

The pass and the stop bands constitute respectively, frequency ranges (bands) of prominent and subdued wavenumber activities in the drive in lieu of the ribs. These are clearly discernible in Figs. 10-13 through 21. [The dominance of the flexural free waves in the spectral range of concern in this report is such that only flexural pass and stop bands are of real investigative relevance.] To accentuate the vision of the pass and stop bands, a clipped version of a few of

these figures is presented. The clipping is here achieved by suppressing the presence of information that lies below a specific value; only prominences are then shown in these figures [15]. In this manner Figs. 10-15a-c, 17a, and 20 are clipped and shown as such in Figs. 11-1a-f and 2a-f; the clipping in the second set is higher. The pass bands are clearly defined by the ridges and associated peaks that the clipping accentuates in both sets of figures. An appropriately selected clipping features the stop bands as components that are substantially flat or even arid in the clipped figures.

Another investigation of worth is the influence of damping on ribbed shells. In the uniform shell it is found that a selected mechanical damping subdues a type of free waves according to its assigned loss factor; this feature is depicted in Figs. 6-4a-c for the three types of free waves; flexural, longitudinal, and shear, respectively. These figures make clear that increasing the damping of one type of free waves does not substantially influence the response in the others. When ribs are attached, scatterings of free waves take place; the aliasing patterns in Figs. 10-15a-c are reliable indicators that scattering of free waves indeed take place under the parametric values that pertain to these figures. Apparently, all three types of free waves undergo scattering and, therefore, "reverberant fields" are established by all three types of free waves. A question arises: Do the three types of free waves interact with each other; in particular, do the membrane free waves interact with the flexural free waves and vice versa? If they do, one may speculate that increasing the loss factor of the flexural free waves will subdue, not only the flexural free waves in  $\bar{P}_{sn}(k, \omega)$ , but also the membrane free waves and vice versa. The answer to this question is illustrated in Figs. 11-3 through 5 in which Figs. 10-15a-c are repeated with changes in the standard loss factors  $\{\eta_p, \eta_\gamma\}$  of  $\{10^{-3}, 10^{-3}\}$  to  $\{3 \times 10^{-3}, 10^{-3}\}$ ,

$\{10^{-2}, 10^{-3}\}$  and  $\{10^{-3}, 10^{-2}\}$ , respectively. These figures; Figs. 11-3a-c, 4a-c and 5a-c, indicate that the "cross-over" interactions induced by the ribs are weak among the flexural and membrane free waves; notwithstanding that there is a substantial subduing of the normalized modal drive  $\bar{P}_{sn}(k, \omega)$  in each type of free waves when the loss factor of this type is substantially increased. Noting that fluid loading is a mollifier of phenomena, Figs. 11-6 through 8 repeat Figs. 10-15a-c and 11-4 and 5, except that the fluid loading parameter ( $\epsilon_c$ ) is decreased by four orders of magnitude from the standard value; from  $10^{-2}$  to  $10^{-6}$ . Figures 11-6 through 8 indicate that the statement just made needs no modification because of fluid loading influences; the standard fluid loading does not appear to seriously inhibit the interactions induced by the ribs among these three types of free waves.

Fig. 11-1. A clipped [clipping index 0.7] version of:

- a. Fig. 10-15a.
- b. Fig. 10-15b.
- c. Fig. 10-15c.
- d. Fig. 10-17a.
- e. Fig. 10-20a.
- f. Fig. 10-20b.

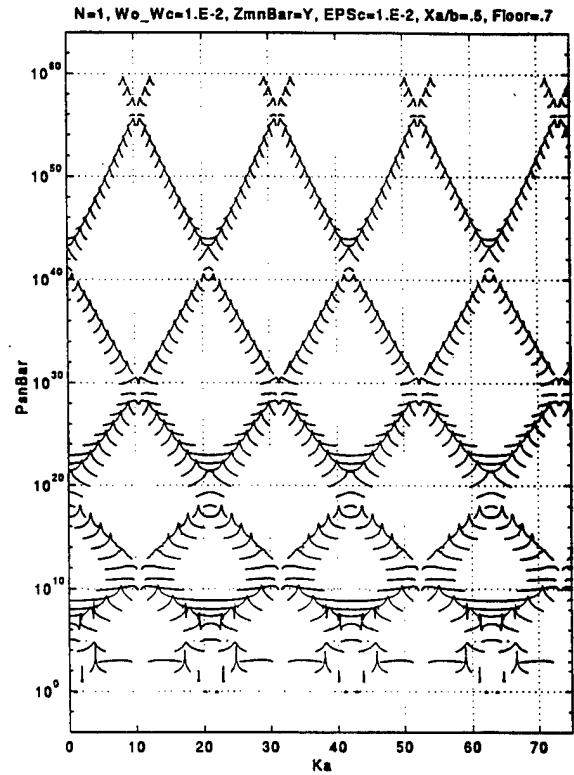


Fig. 11-1a

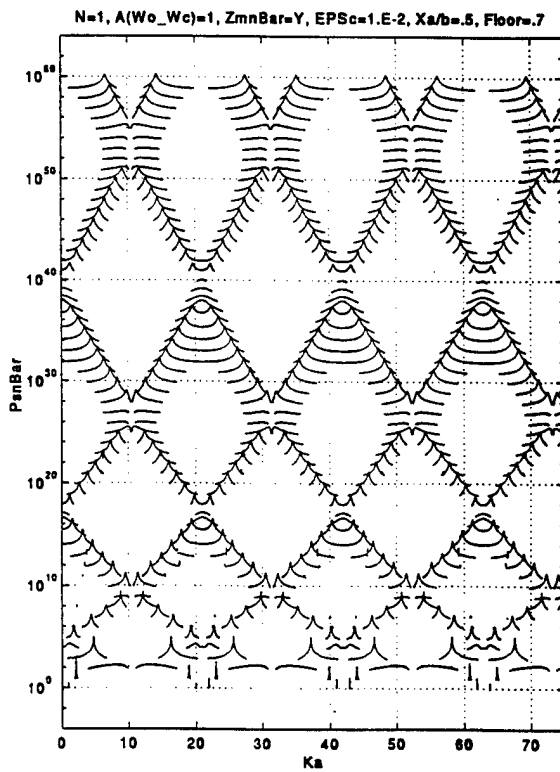


Fig. 11-1b

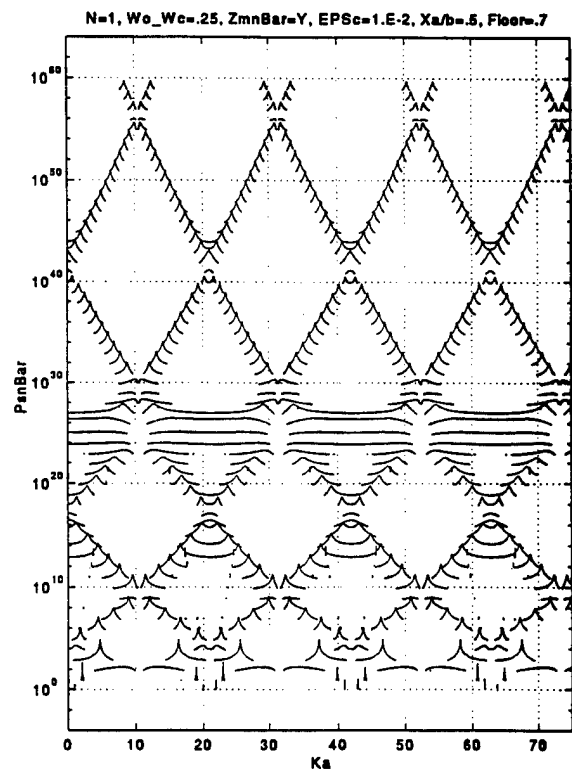


Fig. 11-1c

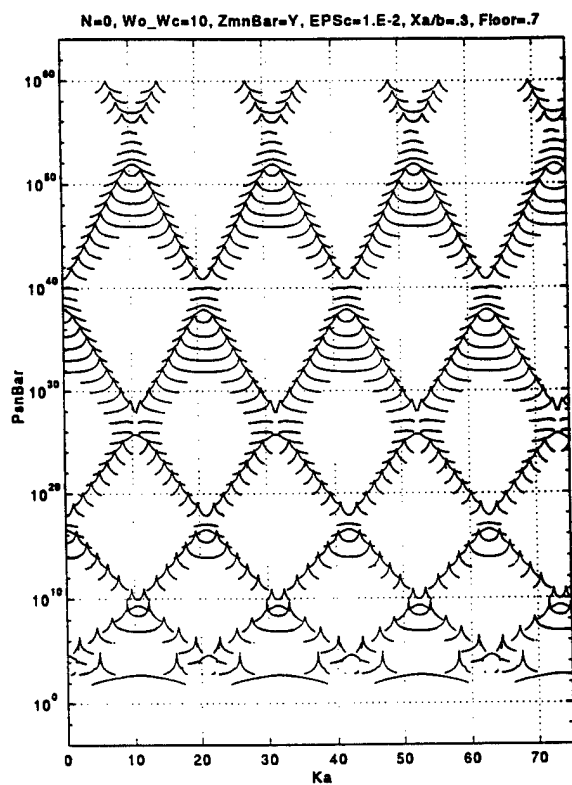


Fig. 11-1d

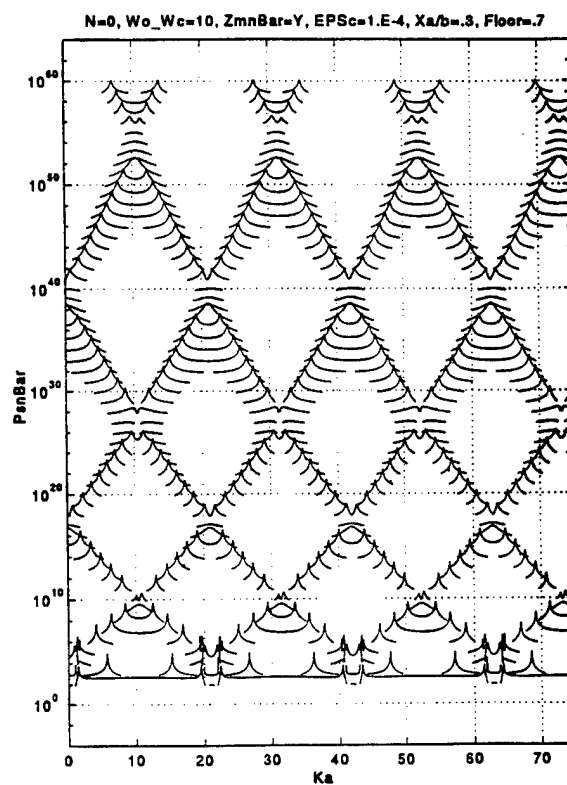


Fig. 11-1e

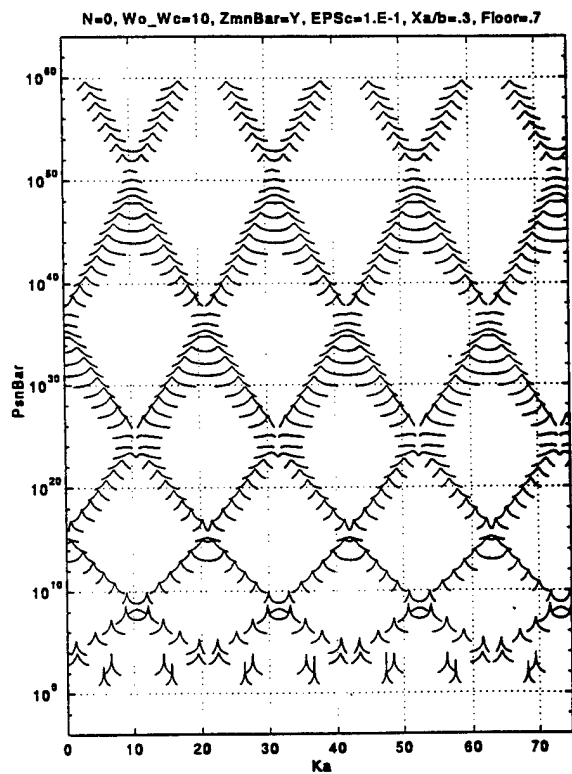


Fig. 11-1f



Fig. 11-2. A clipped [clipping index 1.4] version of:

- a. Fig. 10-15a.
- b. Fig. 10-15b.
- c. Fig. 10-15c.
- d. Fig. 10-17a.
- e. Fig. 10-20a.
- f. Fig. 10-20b.

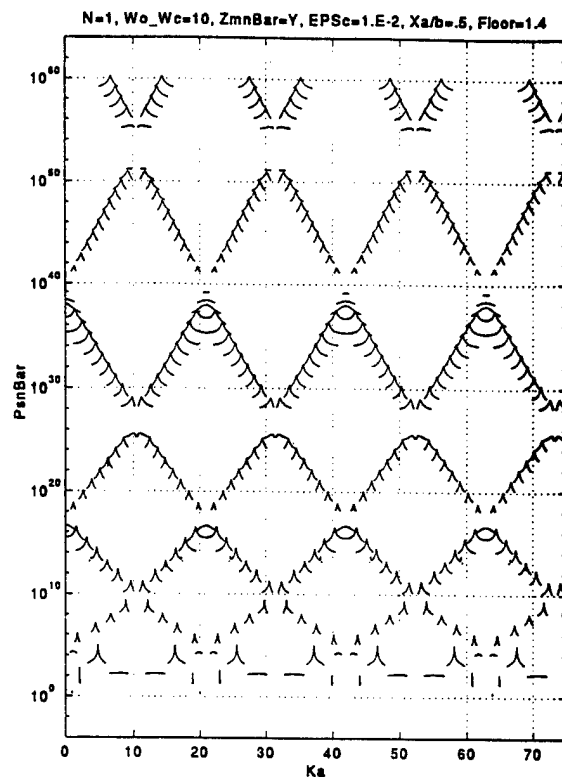


Fig. 11-2a

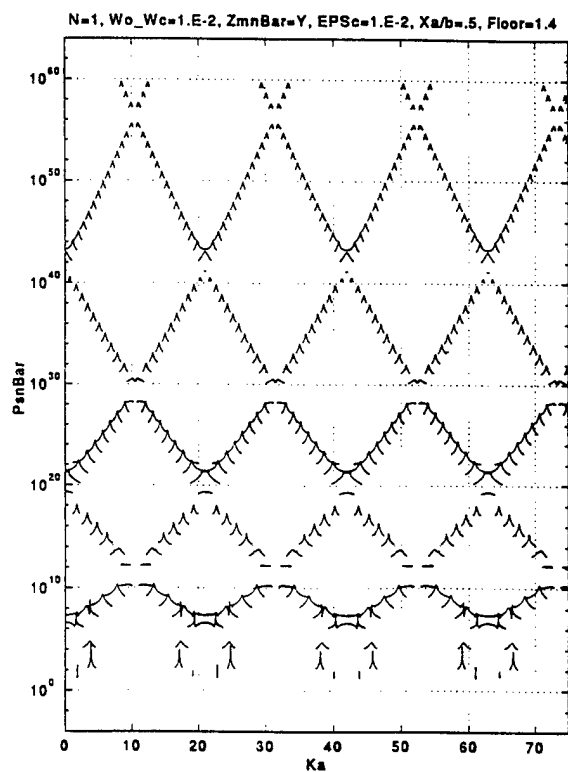


Fig. 11-2b

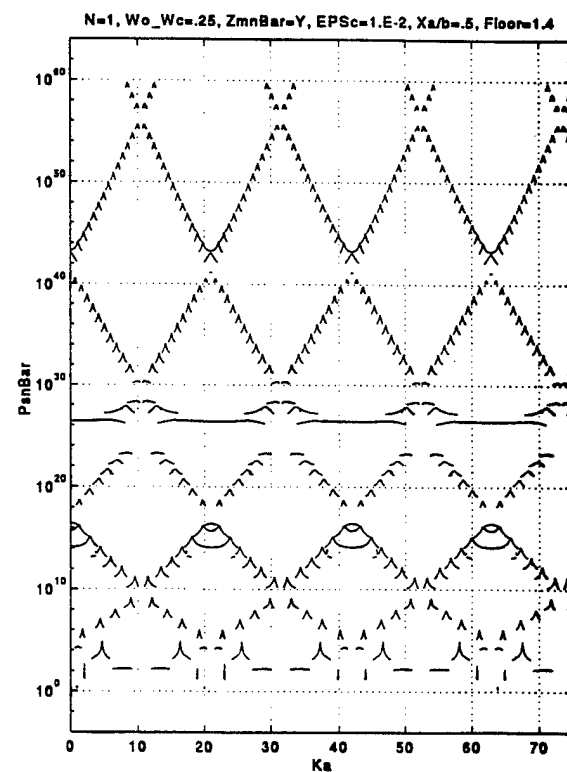


Fig. 11-2c

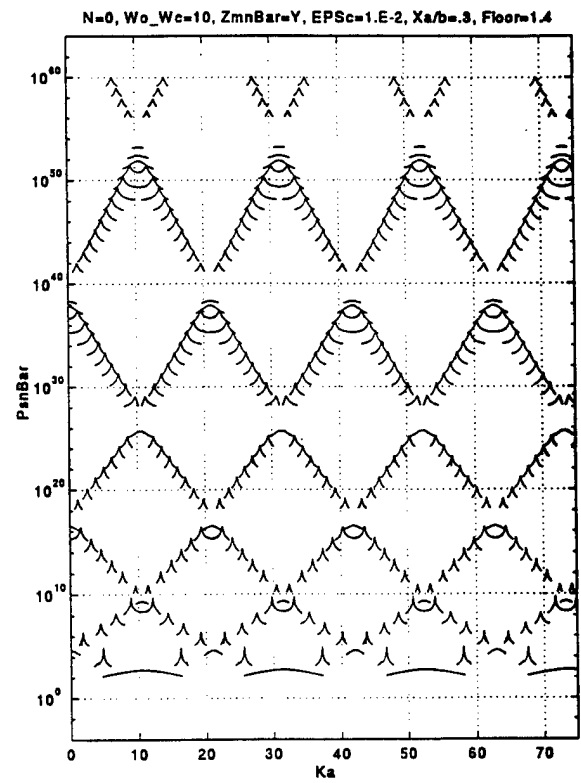


Fig. 11-2d

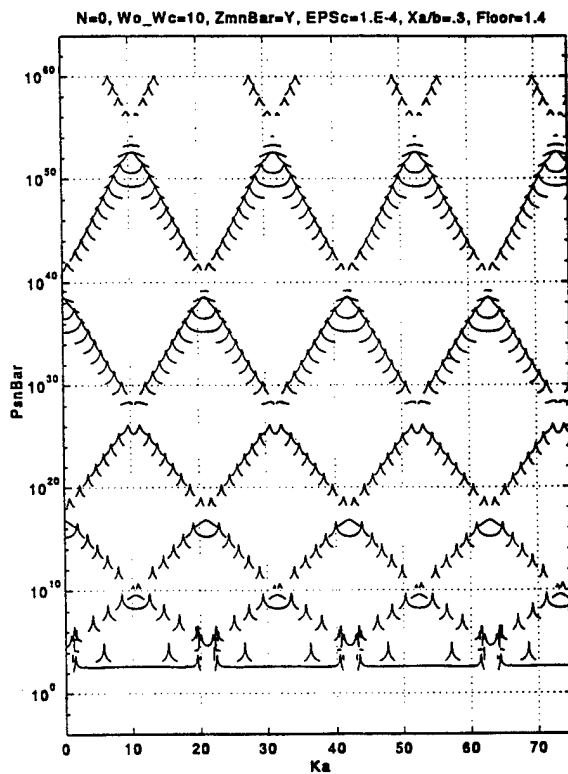


Fig. 11-2e

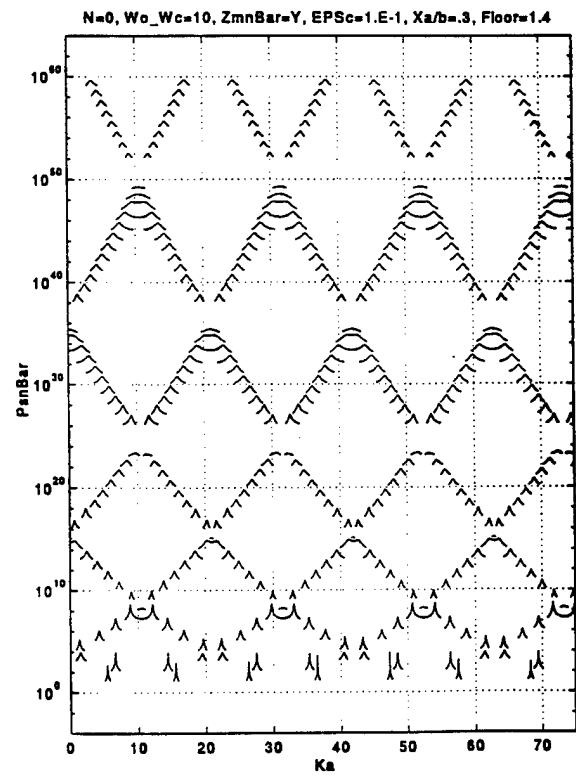


Fig. 11-2f

Fig. 11-3. Figures 10-15a-c are repeated with changes in the standard loss factors  $\{\eta_p, \eta_\gamma\}$  of  $\{10^{-3}, 10^{-3}\}$  to  $\{3 \times 10^{-3}, 10^{-3}\}$ .

- a. Fig. 10-15a.
- b. Fig. 10-15b.
- c. Fig. 10-15c.

N=1, Wo\_Wc=10, ETAp=3.E-3, Bettam=5, Gamma=8, ZmnBar=Y, EPSc=1.E-2

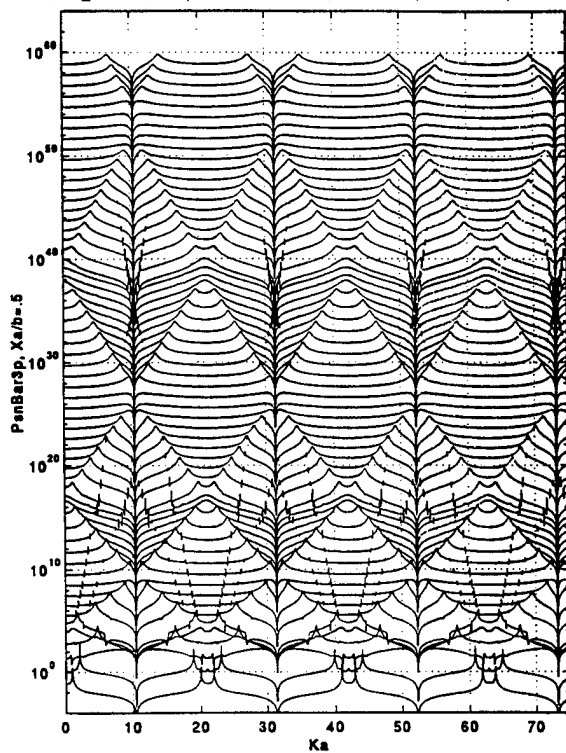


Fig. 11-3a

N=1, Wo\_Wc=1.E-2, ETAp=3.E-3, Bettam=5, Gamma=8, ZmnBar=Y, EPSc=1.E-2

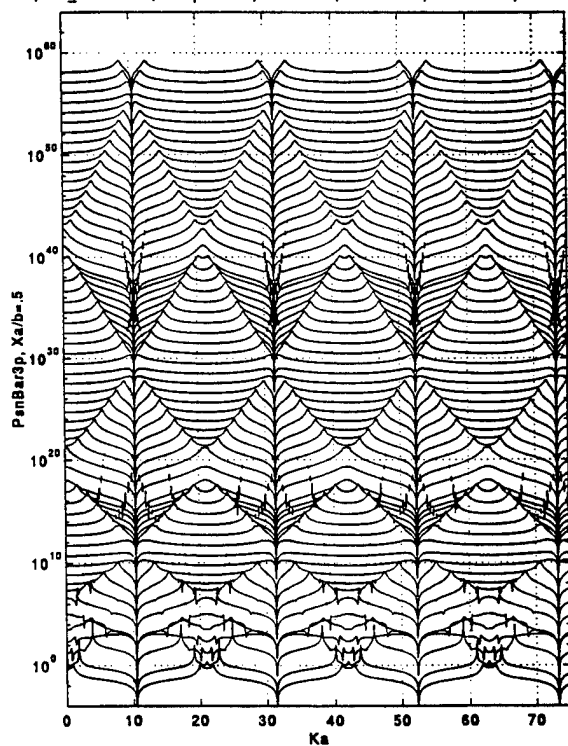


Fig. 11-3b

N=1, Wo\_Wc=.25, ETAp=3.E-3, Bettam=5, Gamma=8, ZmnBar=Y, EPSc=1.E-2

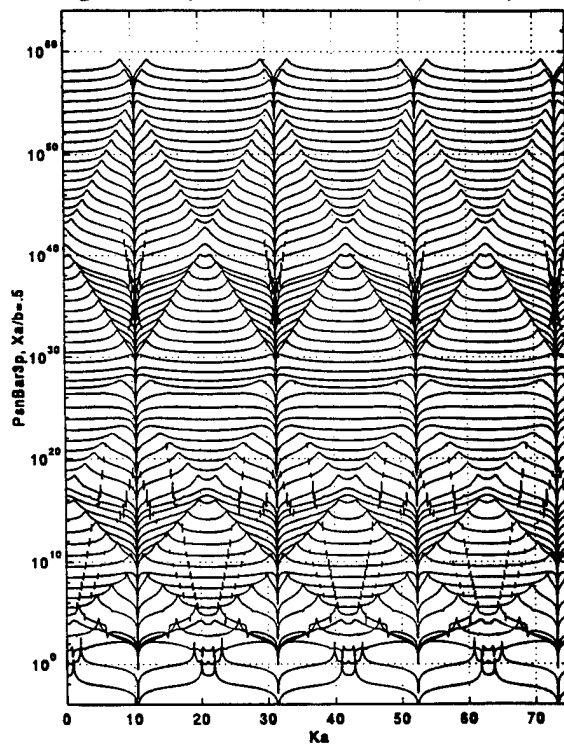


Fig. 11-3c

Fig. 11-4. Figures 10-15a-c are repeated with changes in the standard loss factors  $\{\eta_p, \eta_\gamma\}$  of  $\{10^{-3}, 10^{-3}\}$  to  $\{10^{-2}, 10^{-3}\}$ .

- a. Fig. 10-15a.
- b. Fig. 10-15b.
- c. Fig. 10-15c.

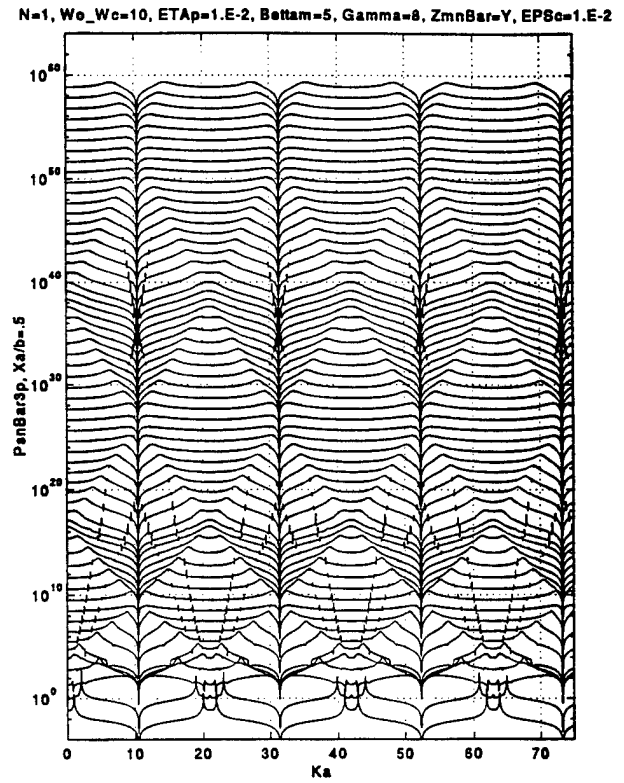


Fig. 11-4a

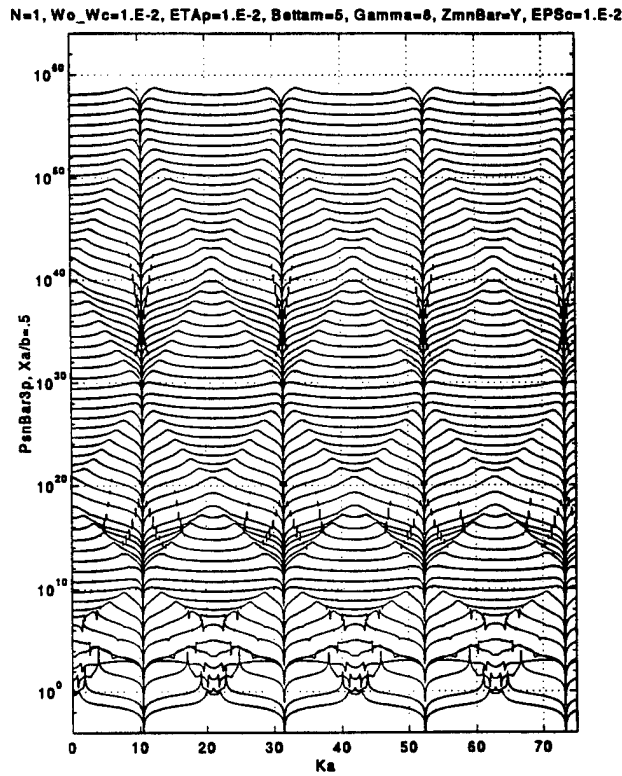


Fig. 11-4b

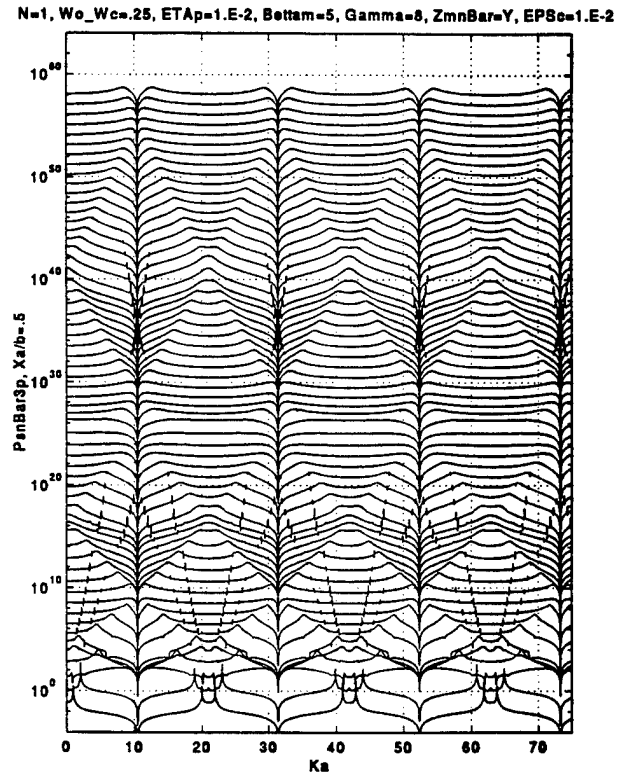


Fig. 11-4c

Fig. 11-5. Figures 10-15a-c are repeated with changes in the standard loss factors  $\{\eta_p, \eta_\gamma\}$  of  $\{10^{-3}, 10^{-3}\}$  to  $\{10^{-2}, 10^{-3}\}$ .

- a. Fig. 10-15a.
- b. Fig. 10-15b.
- c. Fig. 10-15c.

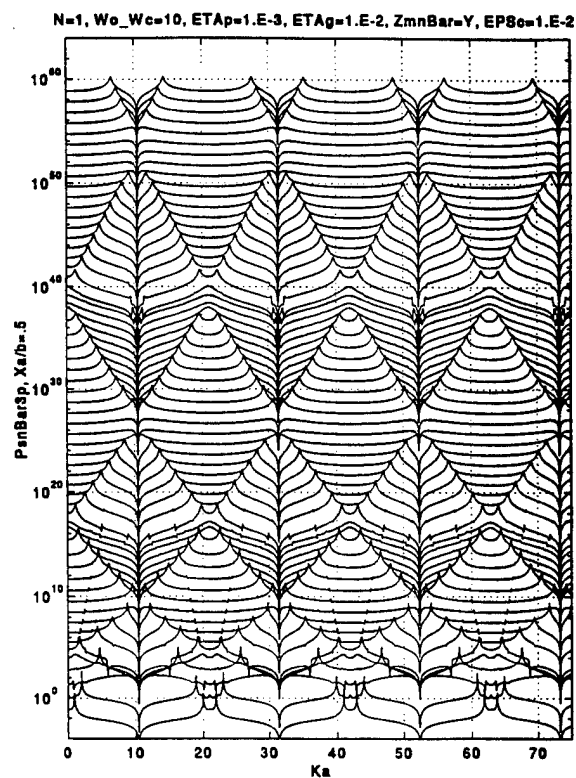


Fig. 11-5a

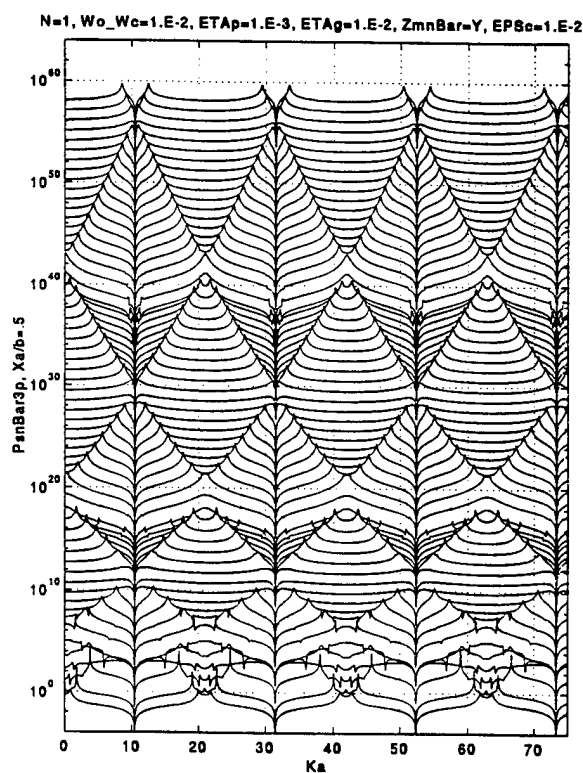


Fig. 11-5b

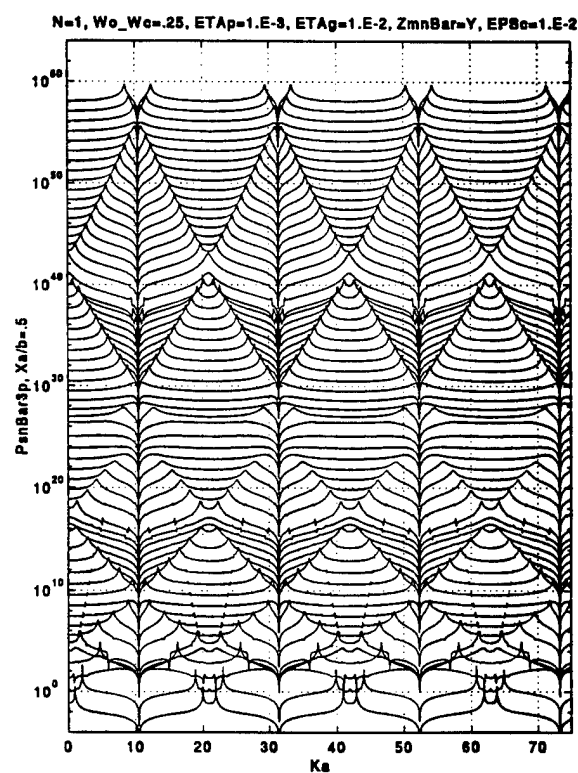


Fig. 11-5c

Fig. 11-6. Figures 10-15a-c are repeated except that the standard fluid loading parameter ( $\epsilon_c$ ) is changed from the standard value of  $10^{-2}$  to  $10^{-6}$ .

- a. Fig. 10-15a.
- b. Fig. 10-15b.
- c. Fig. 10-15c.

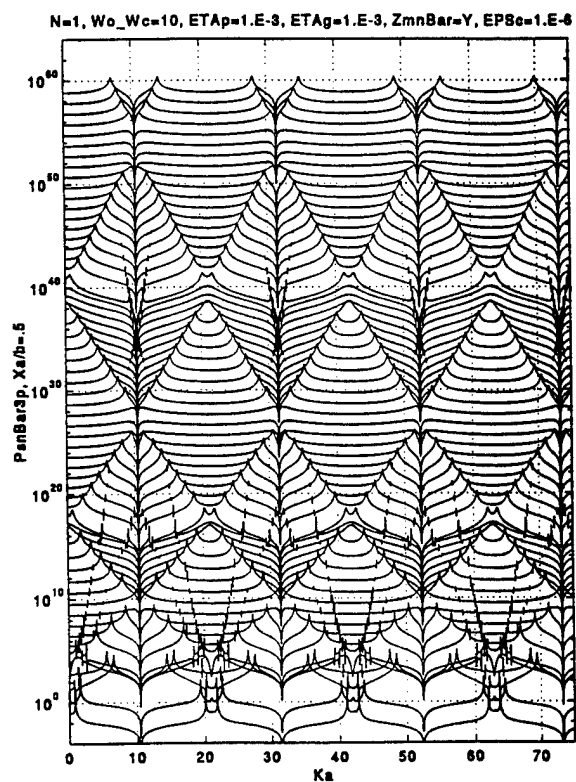


Fig. 11-6a

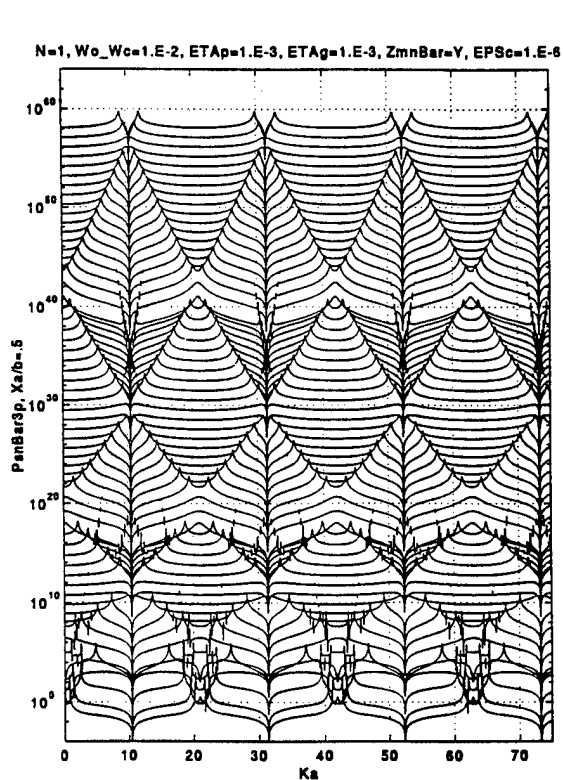


Fig. 11-6b

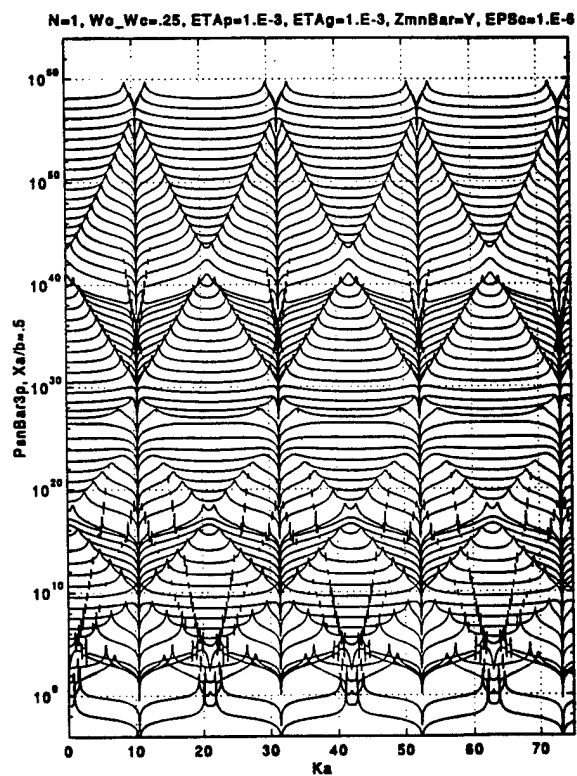
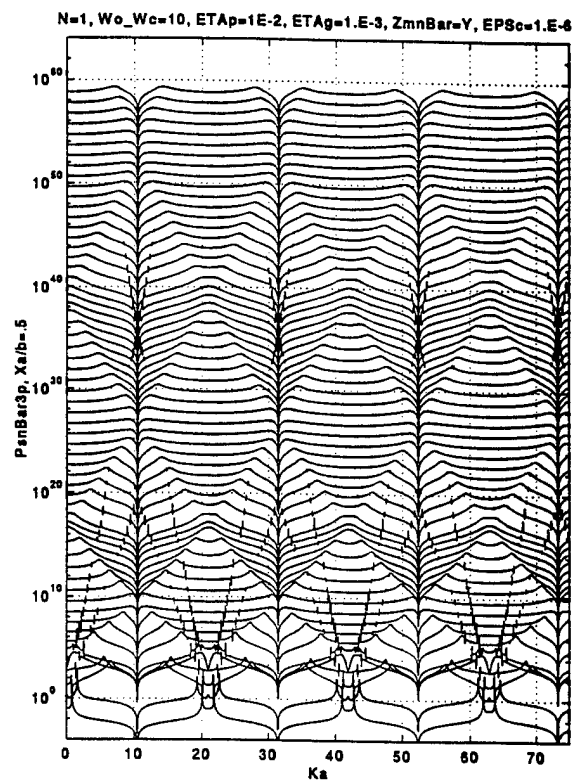


Fig. 11-6c

Fig. 11-7. Figures 11-4a-c are repeated except that the standard fluid loading parameter ( $\epsilon_c$ ) is changed from the standard value of  $10^{-2}$  to  $10^{-6}$ .

- a. Fig. 11-4a.
- b. Fig. 11-4b.
- c. Fig. 11-4c.



11-7a

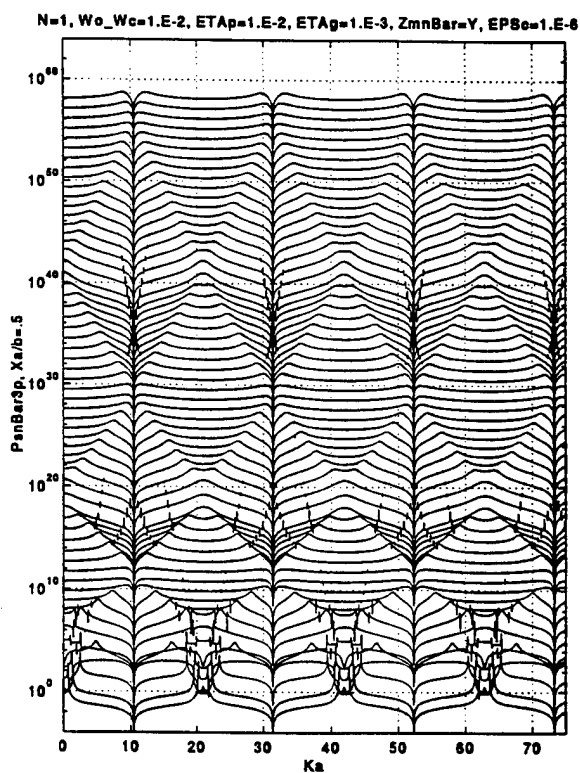


Fig. 11-7b

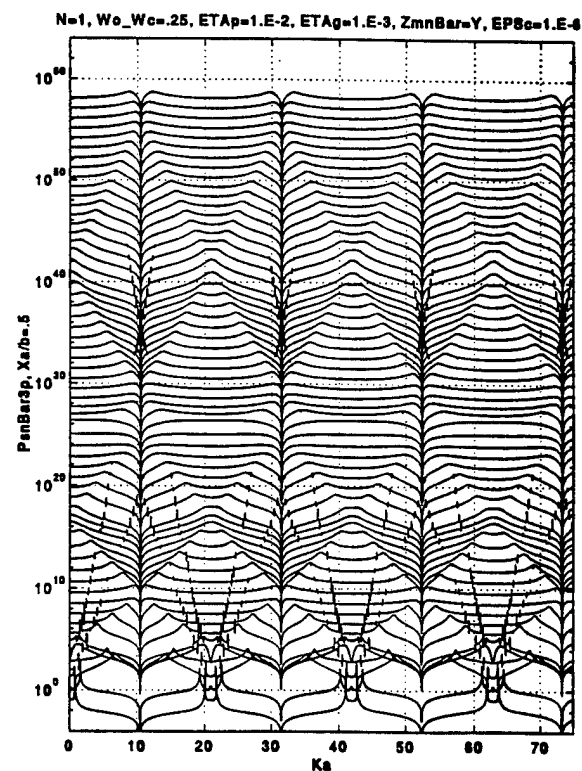
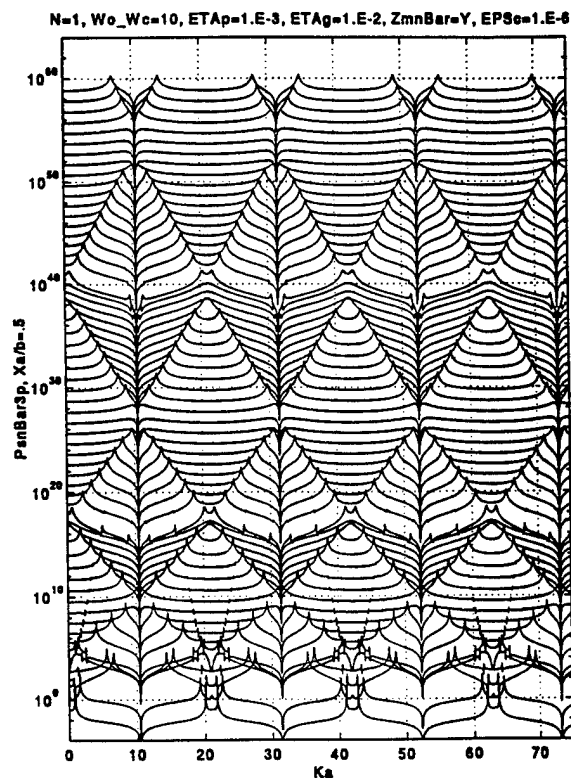


Fig. 11-7c

Fig. 11-8. Figures 11-5a-c are repeated except that the standard fluid loading parameter ( $\epsilon_c$ ) is changed from the standard value of  $10^{-2}$  to  $10^{-6}$ .

- a. Fig. 11-5a.
- b. Fig. 11-5b.
- c. Fig. 11-5c.



11-8a

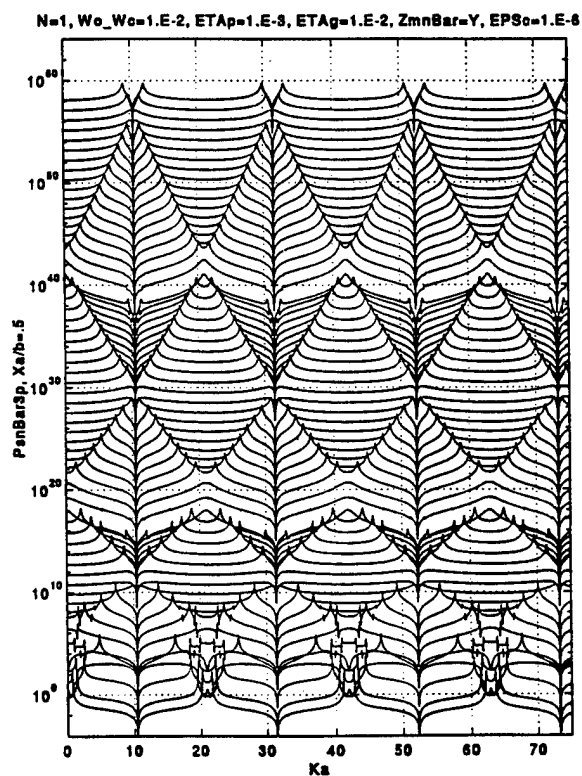


Fig. 11-8b

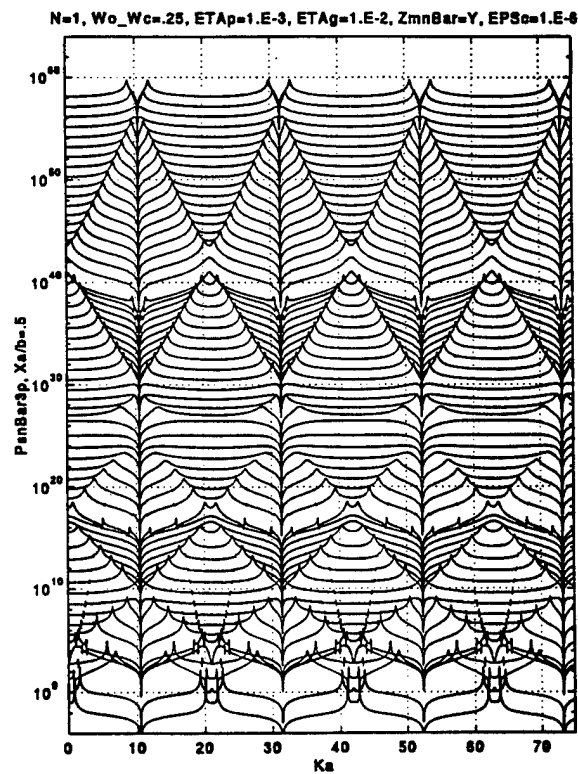


Fig. 11-8c



## XII. PASS AND STOP BANDS IN THE DRIVE $\tilde{P}_{sn}(x, \omega)$ IN LIEU OF THE RIBS

One familiar with spectral and modal descriptions may now rest and feel that the promise of this report is fulfilled. Many of the phenomena in the response of panels, hybrid cylinders and natural cylinders are investigated, in conjunction and separately, in the spectral and modal domains. This spectral and modal investigative agenda is itemized below:

1. The surface admittances of uniform shells are formulated and numerically investigated.
2. The role of fluid loading on these admittances are also formulated and numerically investigated.
3. The relationship between the three forms of a shell are discussed and commonalities and differences are emphasized.
4. The dispersive loci are exhibited and investigated. The membrane free waves in the natural cylinders are defined and their characteristics are contrasted with those of the flexural free waves which exist in all three forms of a shell here considered.
5. The influence of damping, mechanical and indirectly radiative damping, is investigated.
6. The ribs are defined in simple terms. However, in this definition ribs that are mass, stiffness, and resistance controlled are available. The transitions with frequency between these controlled stages are also considered.
7. The phenomena of aliasing and pass and stop bands are formulated, discussed and displayed. It is argued that these phenomena are manifest in the drive in lieu of the ribs. The first phenomenon, that of aliasing, resides

completely in the modal drive in lieu of the ribs. This phenomenon is directly related to the equi-separations between adjacent ribs and is not predicated on the interactions among the ribs via the shell. On the other hand, the second phenomenon, that of pass and stop bands, arises in direct consequence of the interactions among the ribs via the shell; in the absence of these interactions this phenomenon is absent. When the aliasing phenomenon resides in the modal drive in lieu of the ribs and the interactions among the ribs via the shell are accounted for, the phenomenon of pass and stop bands is present in this drive. There are those among the readers of this report who may, at this stage, prefer displays and discussions that pertain, in part or in whole, to the Fourier and modal conjugate domains. To satisfy the least of this preference, the complementarity with respect to the Fourier conjugate axial domains is attempted to this report. These Fourier conjugate axial domains comprise the  $k$ -domain and the  $x$ -domain. Indeed, displays and discussions that pertain to the complementarities with respect to the other Fourier and modal conjugate domains, are deferred to subsequent presentations. Were the complementarity in the Fourier conjugate axial domains to prove advantageous, the incentive, to subsequently duplicate it in the other Fourier and modal conjugate domains, may be strengthened.

The computations and displays to this point are performed and depicted on the spectral domain; the  $\{(ak), (\omega/\omega_c)\}$ -domain. None of these computations and displays pertain to the  $\{(x/a), (\omega/\omega_c)\}$ -domain, where  $(x/a)$  is the Fourier conjugate domain to  $(ak)$ , notwithstanding that there are situations in which the interpretation of data is more readily conducted in one domain than in another even though the two domains may be Fourier conjugate domains. This is

particularly relevant to the interpretation of pass and stop bands. In the  $x$ -domain a pass band is merely a frequency band in which the transmission of vibration from a localized external drive position to a localized observation position that is removed a few bays away, hardly encounters more attenuation than is indicated by the distributed damping on an unribbed shell. On the other hand, a stop band in a similar geometrical situation, will indicate a more severe attenuation. A Fourier transformation of  $P_{sn}(k, \omega)$  into  $\tilde{P}_{sn}(x, \omega)$  may thus be efficacious. There are a number of approximate techniques designed to perform this transformation. A first order Born approximation model and other similar approximation models are devoid of the phenomenon of pass and stop bands. In these models the interactions among the ribs via the shell are discounted. It is shown in Section XI that the pass and stop bands occur in direct consequence of these interactions among the ribs. Therefore, it becomes necessary to perform a Fourier transformation that is sophisticated enough so that the phenomenon is not suppressed by the technique that handles the approximation; either a first order Born approximation or a similar approximation that reduces the modeling to a first order model is not acceptable. There are nonetheless several techniques that are adequate to the task, e.g., the Fast Fourier Transformation (FFT). However, in this report a somewhat new technique is used. The technique is particularly, but not exclusively, useful with respect to the phenomenon of pass and stop bands of regularly ribbed panels and/or cylinders. The exclusivity is with respect to the regularity of the spacings between adjacent ribs. The spectral formalism of this phenomenon in a regularly ribbed shell is expressed for a proper order model in the form

$$\bar{P}_{sn}(k, \omega) = I_{bn}(k, \omega) \bar{P}_{osn}(k, \omega) , \quad (12-1a)$$

$$\bar{P}_{osn}(k, \omega) = S_b(k) [Q_{\infty n}(k, \omega) (2\pi)^{-1/2} \exp(ikx_a)] , \quad (12-1b)$$

$$I_{bn}(k, \omega) = \{1 + S_b(k) [Q_{\infty n}(k, \omega)]\}^{-1} , \quad (12-1c)$$

where  $\bar{P}_{osn}(k, \omega)$  is defined in Eq. (10-3) and  $I_{bn}(k, \omega)$  is defined in Eqs. (10-41b) and (10-3). From Eq. (3-26a) the Fourier transform of  $\bar{P}_{sn}(k, \omega)$  with respect to  $(k)$  is defined

$$\bar{\bar{P}}_{sn}(x, \omega) = (2\pi)^{-1/2} \int dk \bar{P}_{sn}(k, \omega) \exp(-ikx) , \quad (12-2)$$

where  $\bar{\bar{P}}_{sn}(x, \omega)$  is the normalized drive in lieu of the ribs. [cf. Eq. (3-17b).]

Equation (12-2) may be cast in the form

$$\bar{\bar{P}}_{sn}(x, \omega) = (2\pi)^{-1/2} \int_0^{k_1} dk S_b(k) [\bar{P}_{sn}(k, \omega) \exp(-ikx)] . \quad (12-3)$$

Since  $\bar{P}_{sn}(k, \omega)$  is an aliased quantity it follows that Eq. (12-3) can be simplified to read

$$\bar{\bar{P}}_{sn}(x, \omega) = (2\pi)^{-1/2} \int_0^{k_1} dk \bar{P}_{sn}(k, \omega) S_b(k) [\exp(-ikx)] , \quad (12-4a)$$

and hence

$$\bar{P}_{sn}(x, \omega) = s_b(x) [\delta(x) (\kappa_1)^{-1} \int_0^{\kappa_1} dk \exp(-ikx) \bar{P}_{sn}(k, \omega)] , \quad (12-4b)$$

where

$$\begin{aligned} S_b(k) [\exp(-ikx)] &= (2\pi)^{-1/2} \exp(-ikx) \sum_j \delta(x - jb) \\ &\equiv (2\pi)^{-1/2} \exp(-ikx) \sum_j s_b(x) [\delta(x)] ; \end{aligned}$$

$$s_b(x) [n(x)] = \sum_j n(x - jb). \quad (12-5)$$

Approximating the integral by a summation in the form

$$\int_0^{\kappa_1} dk M(k) \Rightarrow \kappa_1 (1+R)^{-1} \sum_{r=0}^R M(k_r) ;$$

$$k_r = (1+R)^{-1} \kappa_r ; \quad \kappa_r = r \kappa_1 , \quad (12-6)$$

one derives from Eq. (12-4b)

$$\bar{P}_{sn}(x, \omega) = s_b(x) [\delta(x) \bar{P}_{Rn}(x, \omega)] , \quad (12-7)$$

where

$$\bar{P}_{Rn}(x, \omega) = (1 + R)^{-1} \sum_{r=0}^R \bar{P}_{sn}(k_r, \omega) \exp(-ik_r x). \quad (12-8)$$

The validation of Eq. (12-8) for a particular form of  $\bar{P}_{sn}(k, \omega)$ , as stated in Eq. (12-1), requires that

$$\{\eta_\gamma(1 + R)\}^{-1} \ll (k_\gamma / \kappa_1) \ll (k_m / \kappa_1) \ll J = J_o(1 + R)^{-1}, \quad (12-9)$$

where  $(J)$  is the span of  $(j)$  in the summation that is dictated by the aliasing operator  $S_b(k)$  in the expression for  $\bar{P}_{sn}(k, \omega)$ ,  $(k_M)$  is the wavenumber that renders  $G_{\infty n}(k, \omega)$  small enough compared to unity so that the subsequent values of  $|G_{\infty n}(k, \omega)|$  for  $k > k_M$  can be neglected in the summations,  $(k_\gamma)$  and  $(\eta_\gamma)$  are the free wavenumber and the loss factor for the free waves of concern. The value of  $(R)$  is clearly dependent on  $(\kappa_1)$  and the appropriate values of  $(k_\gamma)$  and  $(\eta_\gamma)$ . Indeed, the advantage of this technique of performing a Fourier transform is that it is geared to accommodate the particular separation wavenumber  $(\kappa_1)$  that is basic to the aliasing and the pass and stop bands phenomena in regularly ribbed panels and/or cylinders. It is, therefore, adopted in the computations performed in this report. Returning to Eq. (12-7), it is clear that  $\bar{P}_{Rn}(x, \omega)$  is evaluated at the locations of the ribs only and that  $|\bar{P}_{Rn}(x_j, \omega)|$  is the normalized strength of the drive in lieu of the rib at the position  $(x_j)$  of the  $(j)th$  rib. In this drive the interactions among the ribs via the shell are accounted for. Clearly, in the pass bands the spatial decay in this normalized strength, away from the drive point at the normalized position  $(x_a / b)$ , is light. On the other hand, in the stop bands the spatial decay in this normalized strength, away from the external drive point at

the normalized position  $(x_a/b)$ , is heavy. One is reminded that the bands are in reference to the frequency  $\omega$ -domain. The presence of pass and stop bands is illustrated in Fig. 12-1a. The strength  $\bar{P}_{Rn}(x_j, \omega)$  is depicted as a function of the normalized frequency  $(\omega/\omega_c)$  for three values of the rib-positions;  $(x_j/b) = 5, 10$  and  $15$ , and the application of the external drive is at the standard position of  $(x_a/b) = 0.5$ . The kind of decays just discussed are clearly demonstrated in Fig. 12-1a in which the standard parametric values are employed on a hybrid cylinder. The pass and stop bands in Fig. 12-1a cannot be missed. In Fig. 12-2a the corresponding situation with respect to a natural cylinder is depicted. Except for a major difference at the frequency below an octave or so above the ring frequency and a kink or two at the higher frequency range, the two figures, Figs. 12-1a and 2a, show substantial identity, notwithstanding that a few of the kinks are common to both figures. Thus, in the range of frequency of interest and in the format in which the displays are cast in this report, the differences are minor. In Figs. 12-1b and c and 12-2b and c, Figs. 12-1a and 12-2a are repeated except that the fluid loading parameter  $(\epsilon_c)$  is changed from the standard value of  $10^{-2}$  to  $10^{-4}$  and  $10^{-1}$ , respectively. The influence of fluid loading is clearly discernible in these figures. In order to bring out this influence Figs. 12-1a-c and 12-2a-c are placed side by side; (a) in the middle, (b) above and (c) below. A major influence is the frequency shift in the prevailing flexural stop bands with increase in the fluid loading; the shift between Figs. 12-1a and 2a and Figs. 12-1b and 2b, respectively, is minor, but between these two sets of figures and Figs. 12-1c and 2c, respectively, the shift is substantial. Also the shift is to lower frequency, which is commensurate with increase of surface mass. This surface mass is contributed by the fluid loading as explained in Section VII. On the one hand, kinks in the curves that disappear with decrease in fluid loading are fluid bearing. On the other hand, those kinks in Fig. 12-2 that persist with such a

decrease are, by definition, associated with the membrane free waves. These figures further show that when fluid loading is high;  $\epsilon_c > 10^{-2}$ , the extremes between stop bands and pass bands is mollified. Is this mollification attributable to the radiation damping? This damping is increased by the presence of the ribs, in particular in the frequency range that lies below the critical frequency, but above the first flexural resonance frequency of a bay. [A bay is the strip of the shell between two adjacent ribs.] Figure 12-3a depict the drive  $\bar{P}_{Rn}(x, \omega)$  on a regularly ribbed hybrid cylinder in which the flexural loss factor ( $\eta_p$ ) is increased from the standard value of  $10^{-3}$  to  $10^{-2}$ . Figures 12-3b and c repeat Fig. 12-3a except that the fluid loading parameter ( $\epsilon_c$ ) is changed from the standard value of  $10^{-2}$  to  $10^{-4}$  and  $10^{-1}$ , respectively. The increase in damping indeed mollifies the extremes between the stop bands and pass bands. [cf. Fig. 12-1c.] It is noted that the way the mechanical damping is introduced in this report, it diminishes with a decrease in frequency; the mechanical damping is proportional to the wavenumber of the free waves of the wave type of concern and this wavenumber diminishes with frequency. This explains the decrease in the influence of a frequency independent loss factor ( $\eta_p$ ) at the lower frequency range. Figures 12-4a-c and 5a-c repeat Figs. 12-1a-c and 2a-c, respectively, except that the position ( $x_a/b$ ) of application of the external drive is changed from the standard value of 0.5 to 0.3. A comparison between these two sets of figures reveals the influence of a geometrical asymmetry in the external driving; the influence can be sparsely substantial. Again, Figs. 12-1a-c and 2a-c are repeated in Figs. 12-6a-c and 7a-c, respectively, and in Figs. 12-8a-c and 12-9a-c, respectively, except that in the first repeated set the mode index ( $n$ ) is changed from the standard value of zero to unity and in the second to nine (9). In the second set, in addition, a change in ( $x_a/b$ ) from the standard value of 0.5 to 0.3 is instituted. Expectedly, at the very low frequency range in Figs. 12-8 and 9, a



gap is discernible in the data; this frequency range, however, lies outside the scope of this report. Note a prominent kink at  $(\omega / \omega_c) \simeq 0.36$  in Fig. 12-9 and note the absence of this kink in Fig. 12-8; and, therefore one may conclude that this kink is a manifestation of membrane free waves. Finally in this series of figures, Figs. 12-10a-c repeat Figs. 12-1a-c, respectively, except that the surface mass impedance ratio ( $M / mb$ ) of a rib is increased from the standard value of 0.2 to 1.0. A comparison between Figs. 12-1a and 10a reveals that the stop bands are wider and they are more inclined to bottom with distance away from the external drive position at  $(x_a / b)$ . A stop band bottoming manifests in that the disparity, in a stop band, between the curves at  $(x_{15} / b)$  and  $(x_{10} / b)$  is less pronounced than between the curves at  $(x_{10} / b)$  and  $(x_5 / b)$ . A comparison between Figs. 12-10a and b indicates that the stop bands bottoming is substantially induced by the higher fluid loading in the former figure. Indeed, a glance at Fig. 12-10c confirms this indication. Moreover, this figure lends further support to the common rule that claims that fluid loading tends to mollify extremes in the response behavior of structures; Fig. 12-10 is an uncommon example of this rule. The bottoming phenomenon in these figures is associated with the flexural stop bands which dominate the pass and stop bands phenomenon in these figures. In Fig. 12-11 this bottoming phenomenon is examined more directly; this figure repeats Fig. 12-6 for a hybrid cylinder, except that the spatial positions  $(x_j / b)$  at which the drive  $\bar{P}_{Rn}(x_j, \omega)$  is assessed is at 7, 14, 21 and 35 instead of 5, 10 and 15 which are the adopted positions in Figs. 12-1 through 10. Comparing Figs. 12-6a-c with Figs. 12-11a-c, respectively, the bottoming phenomenon in the flexural stop bands is more clearly discernible in the latter set than in the former set, especially at the higher values of the fluid loading parameter. In a similar manner, Figs. 12-12a-c repeat Figs. 12-7a-c, respectively, for the natural cylinder. Comparing these two sets of figures clearly demonstrates the phenomenon of

bottoming in the (flexural) stop bands. Figures 12-1 through 12 pertain to ribs which have line (ring) impedances that are identical and are mass controlled. How are these figures modified by changes in the character of these impedances?

To answer this question Figs. 12-13a-c and 14a-c are offered in which the normalized drive  $\bar{P}_{sn}(x, \omega)$  for a hybrid and a natural cylinder, respectively, is displayed as a function of  $(\omega / \omega_c)$  for the four values of  $(x_j / b)$ . In these figures the line impedance of the ribs is changed from that of mass controlled to stiffness controlled and on to a resonating rib with a resonance frequency at  $(\omega_o / \omega_c) = 0.25$ , respectively. In Figs. 12-13c and 12-14c the line impedance is mass controlled in the frequency range  $(\omega / \omega_o) \leq 1$ , resistance controlled in the frequency range  $(\omega / \omega_o) \simeq 1$  and stiffness controlled in the frequency range  $(\omega / \omega_o) \geq 1$ . [cf. Section IX.] In Fig. 12-13 and 14, as in the preceding figures, the three cases are cast side by side in a single figure. The bottoming feature in the (flexural) stop bands is clearly discernible in all three components of Figs. 12-13 and 14. Some exceptions are found in the higher frequency range when the line impedance of the ribs is stiffness controlled and its strength is subdued, which is, in that respect, the antonym of the situation depicted in Fig. 12-10. Also of note is the "additional stop band" established at  $(\omega / \omega_c) \simeq (\omega_o / \omega_c) = 0.25$  in Figs. 12-13c and 14c. This additional stop band is generated by the accentuated strength in the line impedance of the ribs and it is noted that this impedance is resistance controlled at the resonance frequency where this additional stop band is located. Further, Figs. 12-13 and 14 indicate that the flexural stop bands are shifted to the higher frequency ranges when the line impedance of the ribs is changed from mass to stiffness controlled. This feature is, in part, discussed in Section X with respect to the false dispersive loci, their aliasing orders and the cancellations that occur at knots at which pairs

of these aliasing orders cross. Figures 12-14a-c are augmented by Figs. 12-15a-c, respectively, in which the only change is in the mode index ( $n$ ) from zero to unity. The two sets of figures are substantially similar, notwithstanding that for example, a kink at  $(\omega / \omega_c) \simeq 0.125$  is apparently a membrane stop band for a mass controlled line impedance for the ribs. This is emphasized by the differences that contrast Fig. 12-13 from Figs. 12-14 and 15; the former figure pertaining to a hybrid cylinder and the latter figures to a natural cylinder. Other differences can be similarly interpreted in this comparison.

Returning to the resistance controlled region of frequency, in which the ribs resonate and create an additional stop band in consequence, one may inquire as to whether it is either the high magnitude of the ring (line) impedance, the resistance controlled characteristics of that ring impedance or both that contribute to this phenomenon; the phenomenon being the additional stop band. To examine this phenomenon more intimately Figs. 12-15d and e repeat Figs. 12-15c except that in these figures the fluid loading parameter ( $\epsilon_c$ ) is changed from the standard value of  $10^{-2}$  to  $10^{-4}$  and  $10^{-1}$ , respectively. The removal of fluid loading in Fig. 12-15d renders the additional stop band narrower and sharper as is rendered onto all the other stop bands. On the other hand, the increase of fluid loading in Fig. 12-15e tends to mollify the additional stop band. Nonetheless, even with this high fluid loading;  $\epsilon_c = 10^{-1}$ , the additional stop band is clearly discernible in this figure. Figure 12-15f repeats Fig. 12-15d except that the loss factor ( $\eta_p$ ) of the flexural free waves is increased from the standard value of  $10^{-3}$  to  $5 \times 10^{-3}$ . The increase in damping tends to subdue the stop bands and simultaneously increase the decay in the pass bands. At and in the vicinity of the additional stop band, the influence of this increase in damping is similar to that of other stop bands. Indeed, when the damping is increased further,

as depicted in Figs. 12-15g, in which  $\eta_p = 2.5 \times 10^{-2}$ , the stop bands are substantially subdued. Indeed, except for the saturation at the higher distances away from the position of application of the external drive, there is a simultaneous increase in the decay in the pass bands. Noticeably, the additional stop band is the only one that remains substantial before saturation is attained. As in Section X one may be asked: How significant to the existence and behavior of the additional stop band is the resistance controlled character of the ribs at resonance, or is this existence and behavior merely controlled by the high magnitude of the line (ring) impedance of the ribs at resonance? To answer the question Figs. 12-16a-g are offered. These figures repeat Figs. 12-15a-g except that the standard quantity  $A(\omega/\omega_o)$  is changed to  $A'(\omega/\omega_o)$ . The former quantity is defined in Eq. (9-3), the latter, in Eq. (9-6). This change removes the resistance character of the ribs at resonance while retaining the high line (ring) impedance of the ribs at resonance. [cf. Fig. 10-15 versus Fig. 10-21, respectively.] Again, as in Section X the overlap between Figs. 12-15 and 12-16 in the region of resonance is only in details, suggesting, thereby, that the increase in the line impedance may be more significant than its character. Nonetheless, the resistance character of the ribs at resonance, except at the highest of fluid loading;  $\epsilon_c = 10^{-1}$  and the highest of damping;  $\eta_p = 2.5 \times 10^{-2}$ , the differences between the two sets of figures are diminished, even in details. It is clear from Figs 10-15 and 21 and Figs. 12-15 and 16, respectively, that these two sets of figures address similar commonalities and differences, except that the first set depicts the computational data in the  $k$ -domain and the second in the  $x$ -domain. It emerges that some details are more prominently displayed in the

first domain and others in the second domain. Can the two domains be jointly displayed to advantageously decipher and interpret phenomena of interest?

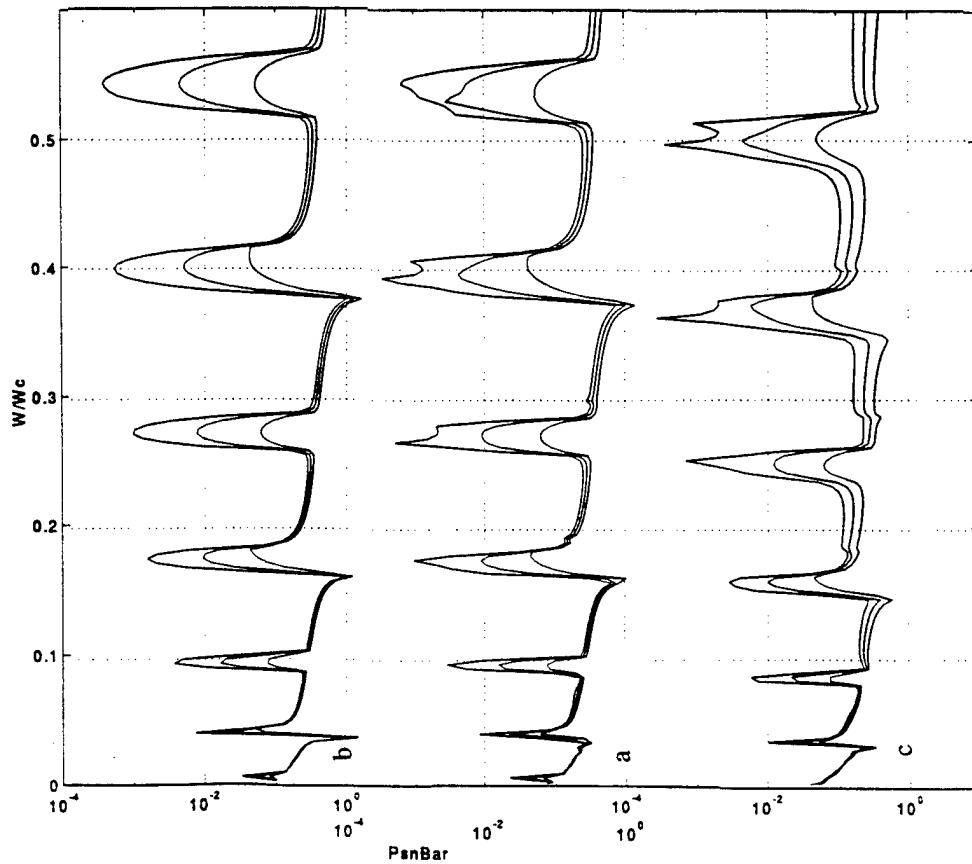


Fig. 12-1. Normalized modal drive  $\bar{P}_{Rn}(x_j, \omega)$  in lieu of the  $(j)th$  rib on a hybrid cylinder as function of  $(\omega / \omega_c)$  at the positions  $(x_j / b) = 5, 10$  and  $15$ .

- a.  $\epsilon_c = 10^{-2}$  (standard value).
- b.  $\epsilon_c = 10^{-4}$ .
- c.  $\epsilon_c = 10^{-1}$ .

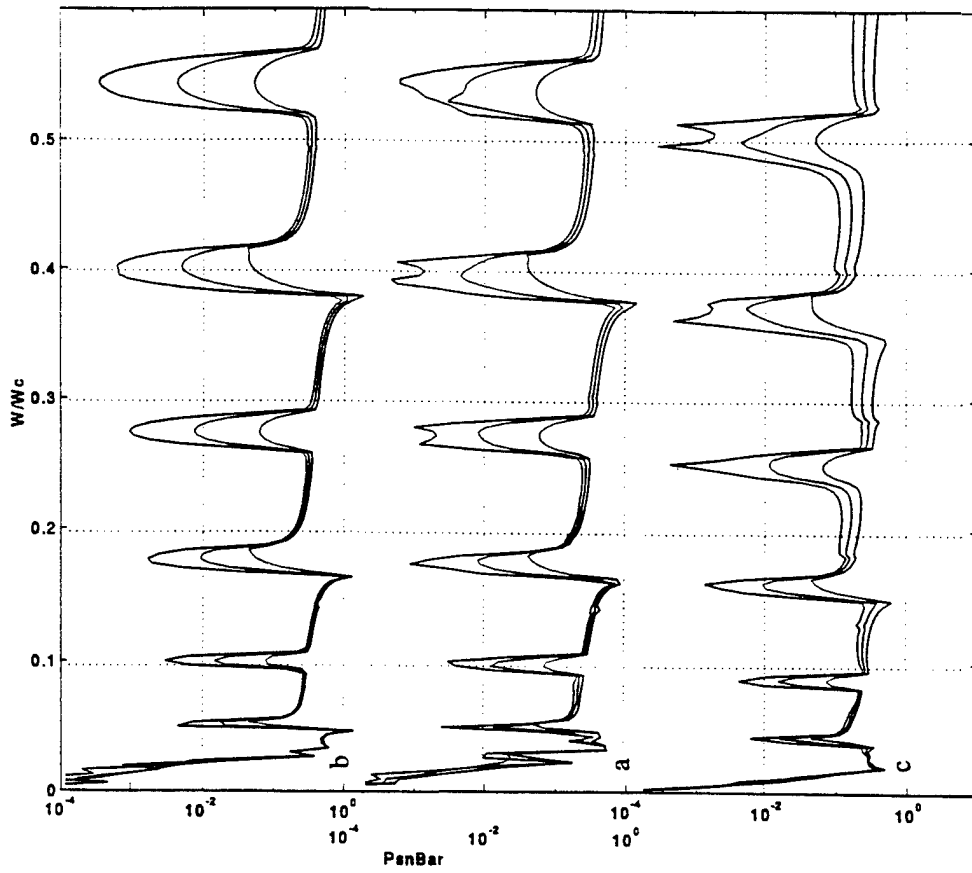


Fig. 12-2. As in Fig. 12-1 except for the change to a natural cylinder.

- a.  $\epsilon_c = 10^{-2}$  (standard value).
- b.  $\epsilon_c = 10^{-4}$ .
- c.  $\epsilon_c = 10^{-1}$ .

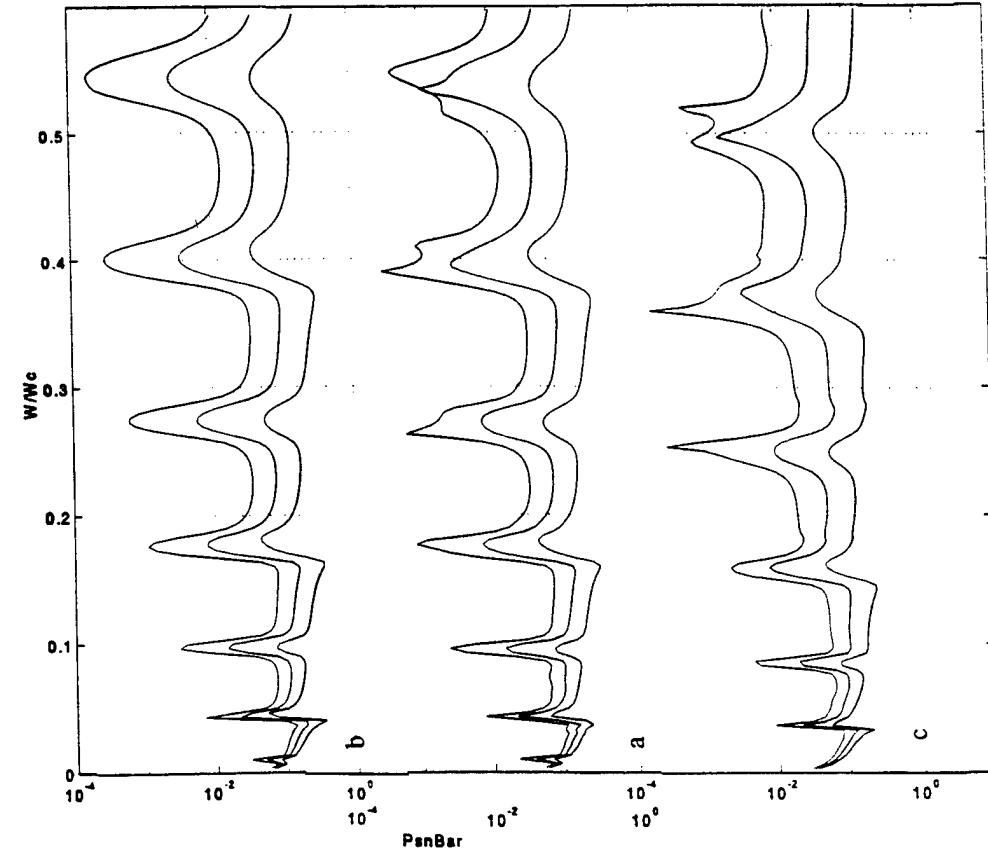


Fig. 12-3. As in Fig. 12-1 except for the increase in the loss factor of  $\eta_p$  the flexural free waves from the standard value of  $10^{-3}$  to  $10^{-2}$ .

- a.  $\epsilon_c = 10^{-2}$  (standard value).
- b.  $\epsilon_c = 10^{-4}$ .
- c.  $\epsilon_c = 10^{-1}$ .

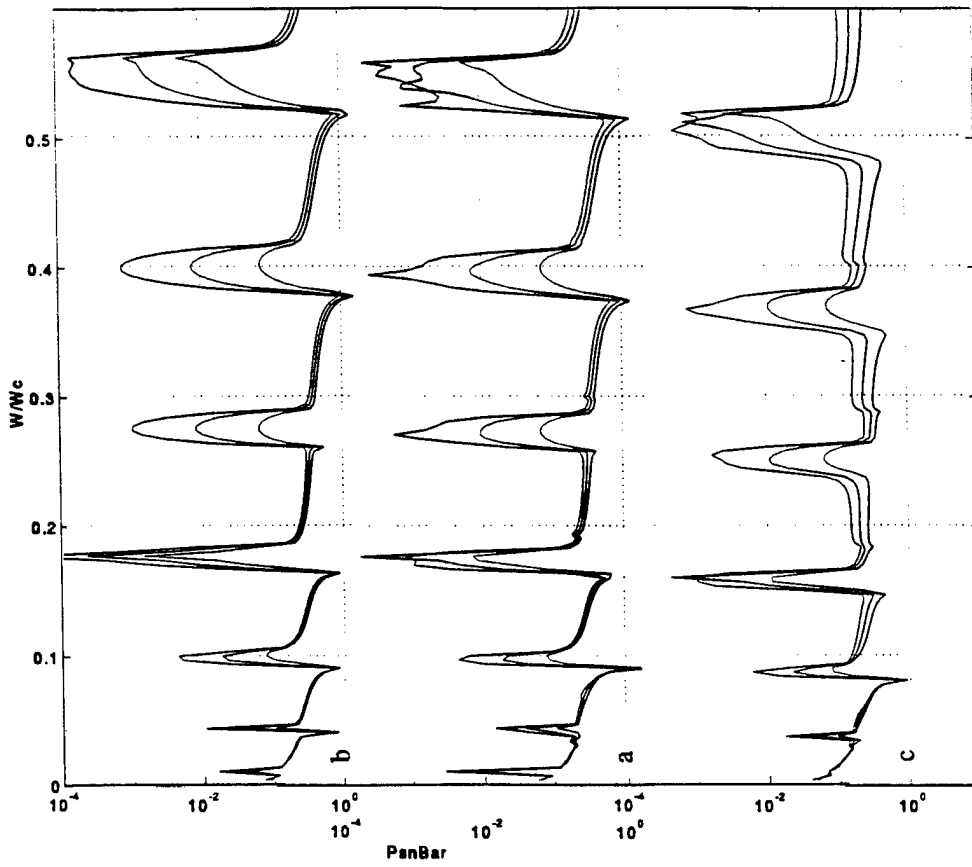


Fig. 12-4. As in Fig. 12-1 except that the axial position ( $x_a/b$ ) of application of the external drive is changed from the standard value of 0.5 to 0.3.

- a.  $\epsilon_c = 10^{-2}$  (standard value).
- b.  $\epsilon_c = 10^{-4}$ .
- c.  $\epsilon_c = 10^{-1}$ .

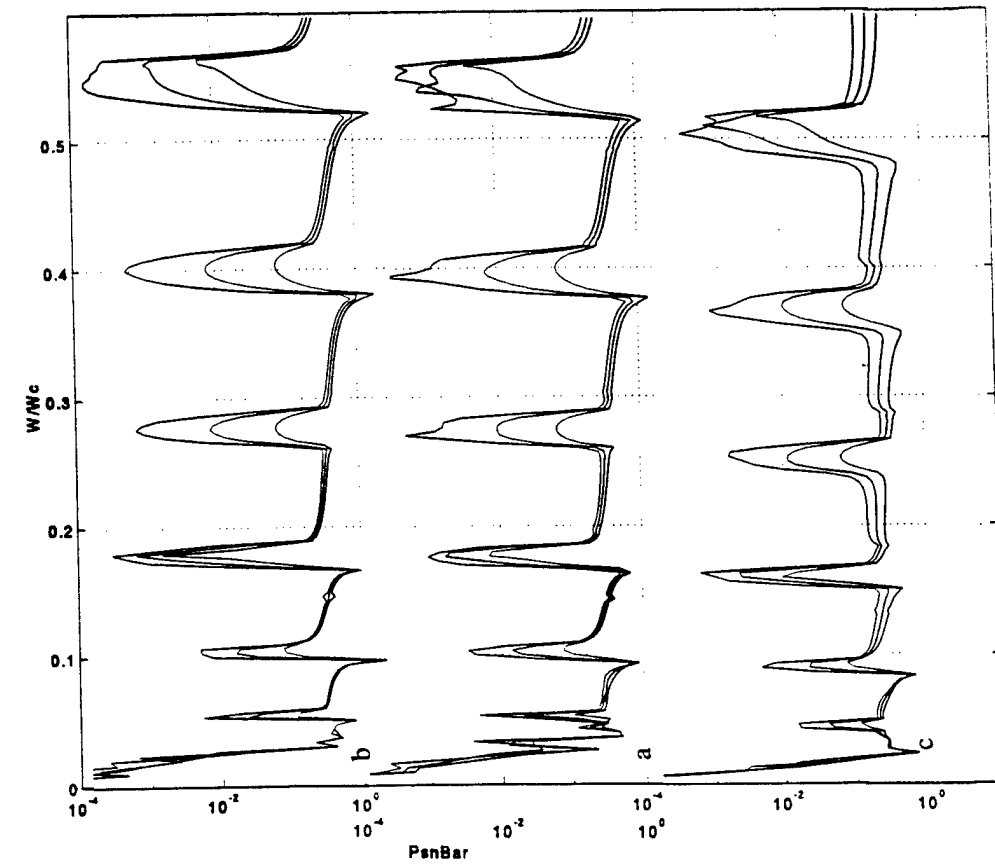


Fig. 12-5. As in Fig. 12-2 except that the axial position ( $x_a$  /  $b$ ) of application of the external drive is changed from the standard value of 0.5 to 0.3.

- a.  $\epsilon_c = 10^{-2}$  (standard value).
- b.  $\epsilon_c = 10^{-4}$ .
- c.  $\epsilon_c = 10^{-1}$ .

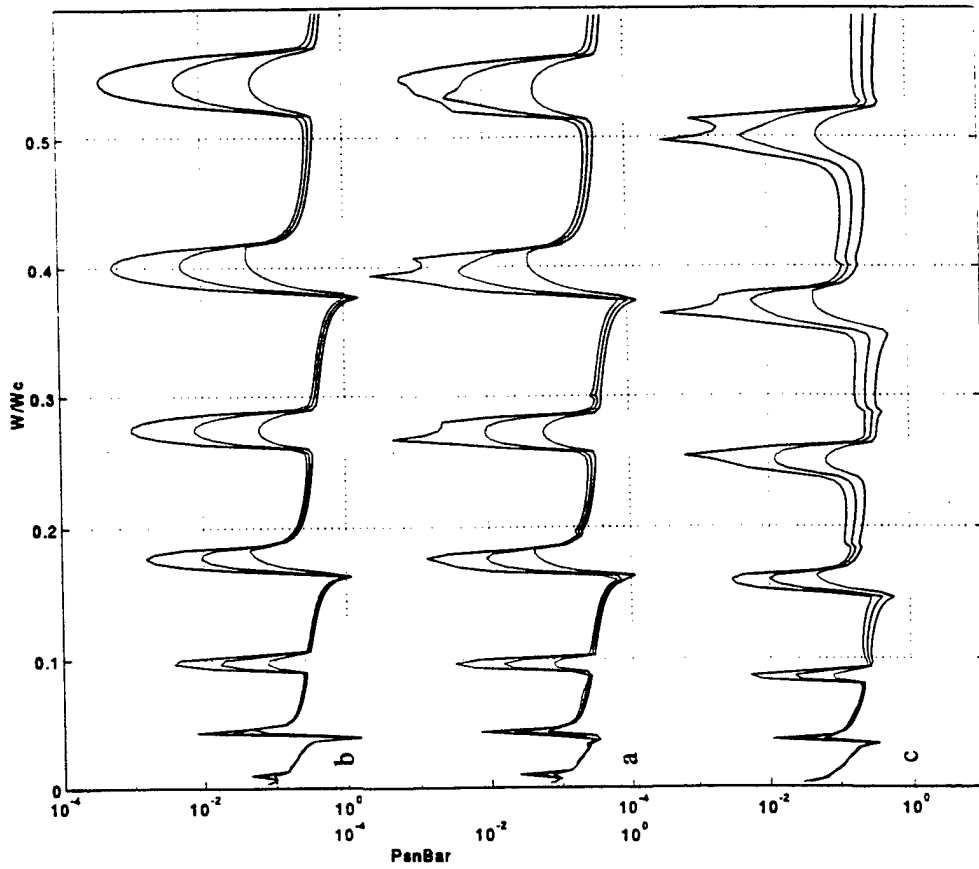


Fig. 12-6. As in Fig. 12-1 except for the change from the standard mode index ( $n$ ) of zero to unity.

- a.  $\epsilon_c = 10^{-2}$  (standard value).
- b.  $\epsilon_c = 10^{-4}$ .
- c.  $\epsilon_c = 10^{-1}$ .



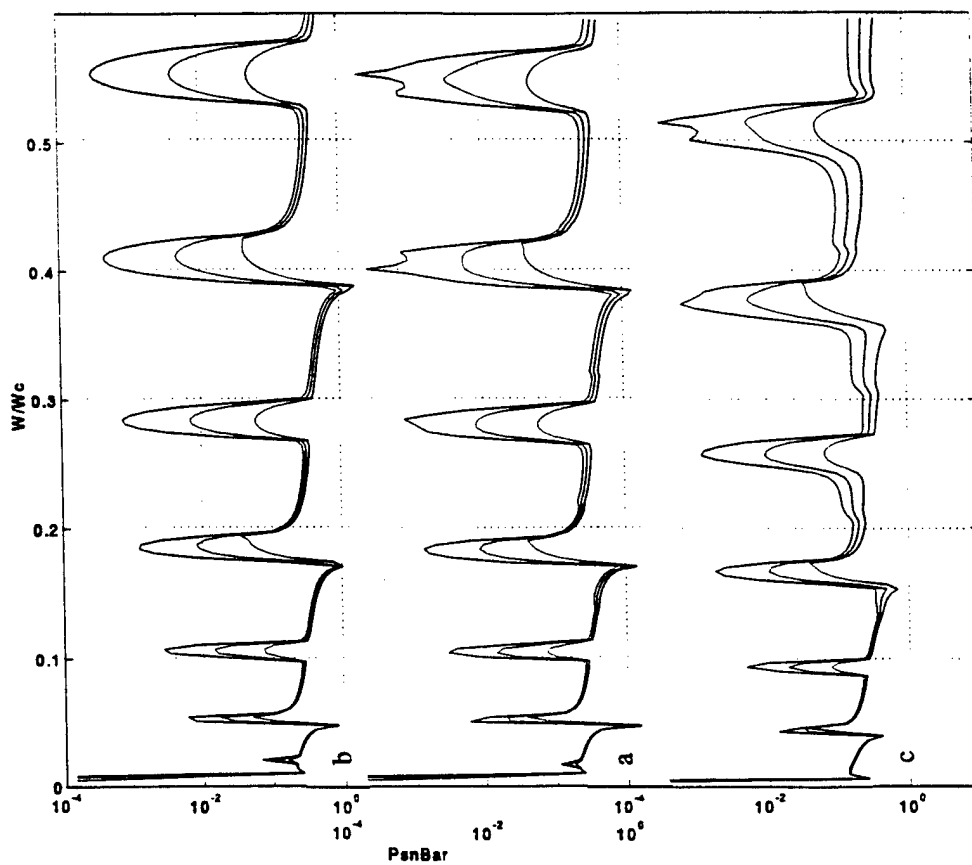


Fig. 12-8. As in Fig. 12-4 except for the change from the standard mode index ( $n$ ) of zero to nine (9).

- a.  $\epsilon_c = 10^{-2}$  (standard value).
- b.  $\epsilon_c = 10^{-4}$ .
- c.  $\epsilon_c = 10^{-1}$ .

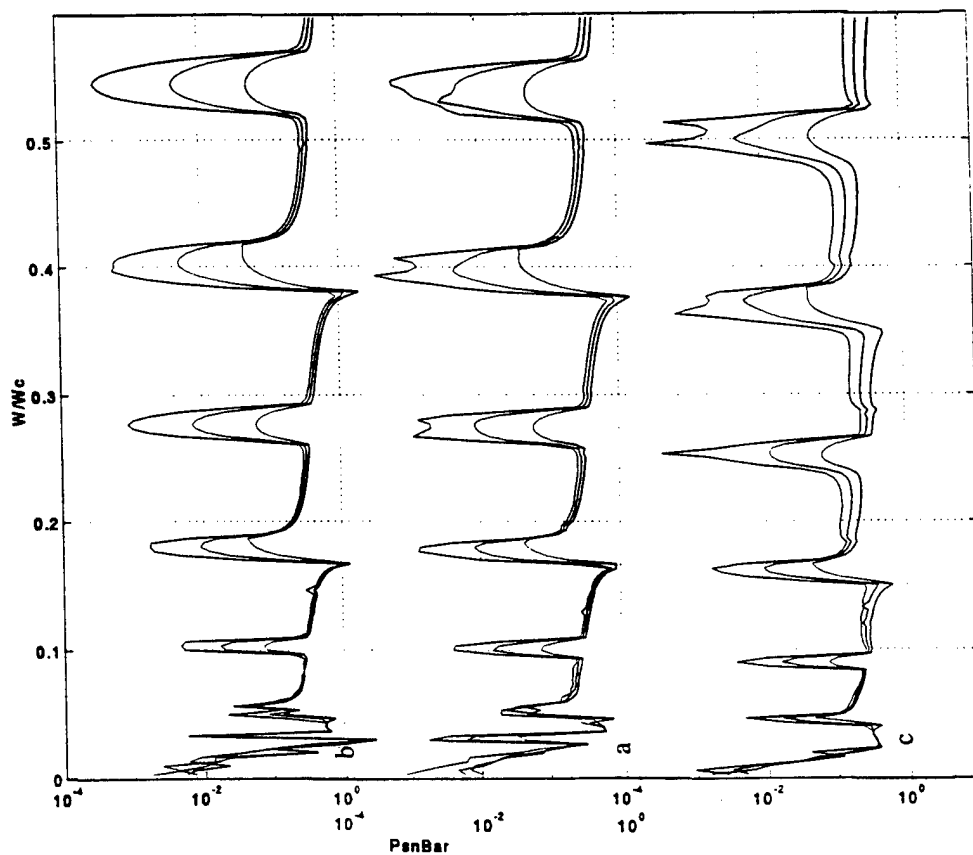


Fig. 12-7. As in Fig. 12-2 except for the change from the standard mode index ( $n$ ) of zero to unity.

- a.  $\epsilon_c = 10^{-2}$  (standard value).
- b.  $\epsilon_c = 10^{-4}$ .
- c.  $\epsilon_c = 10^{-1}$ .

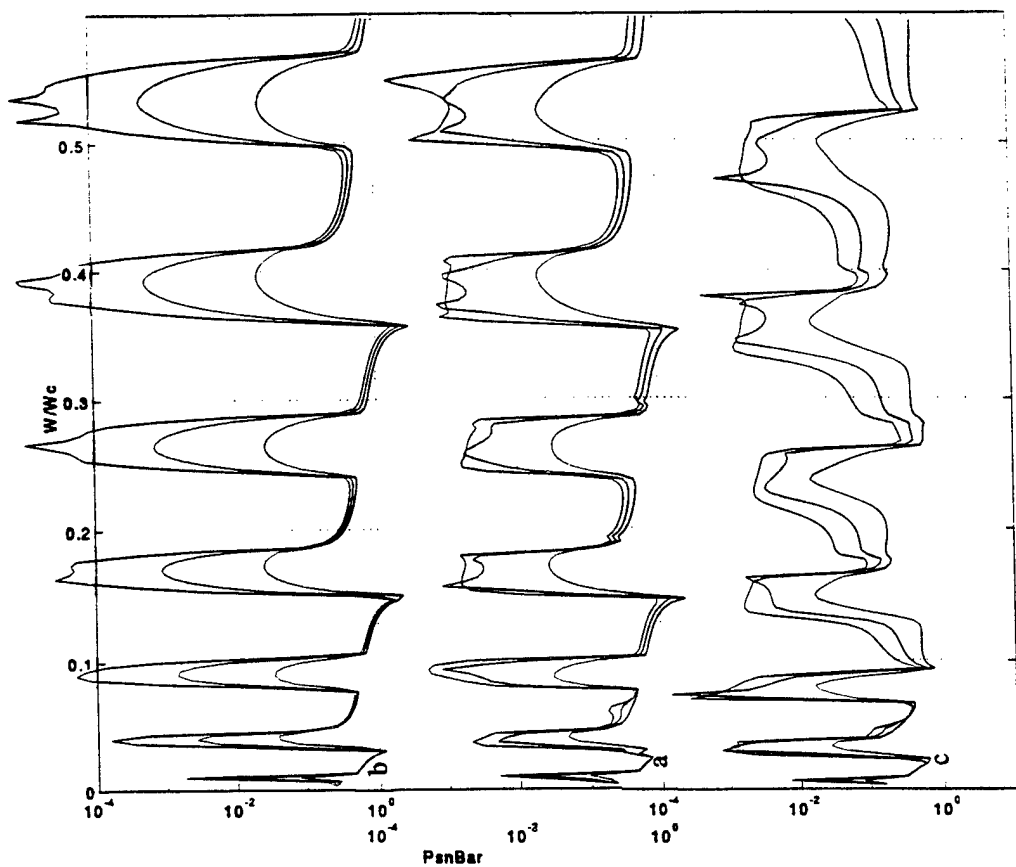


Fig. 12-9. As in Fig. 12-5 except for the change from the standard mode index ( $n$ ) of zero to nine (9).

- a.  $\epsilon_c = 10^{-2}$  (standard value).
- b.  $\epsilon_c = 10^{-4}$ .
- c.  $\epsilon_c = 10^{-1}$ .

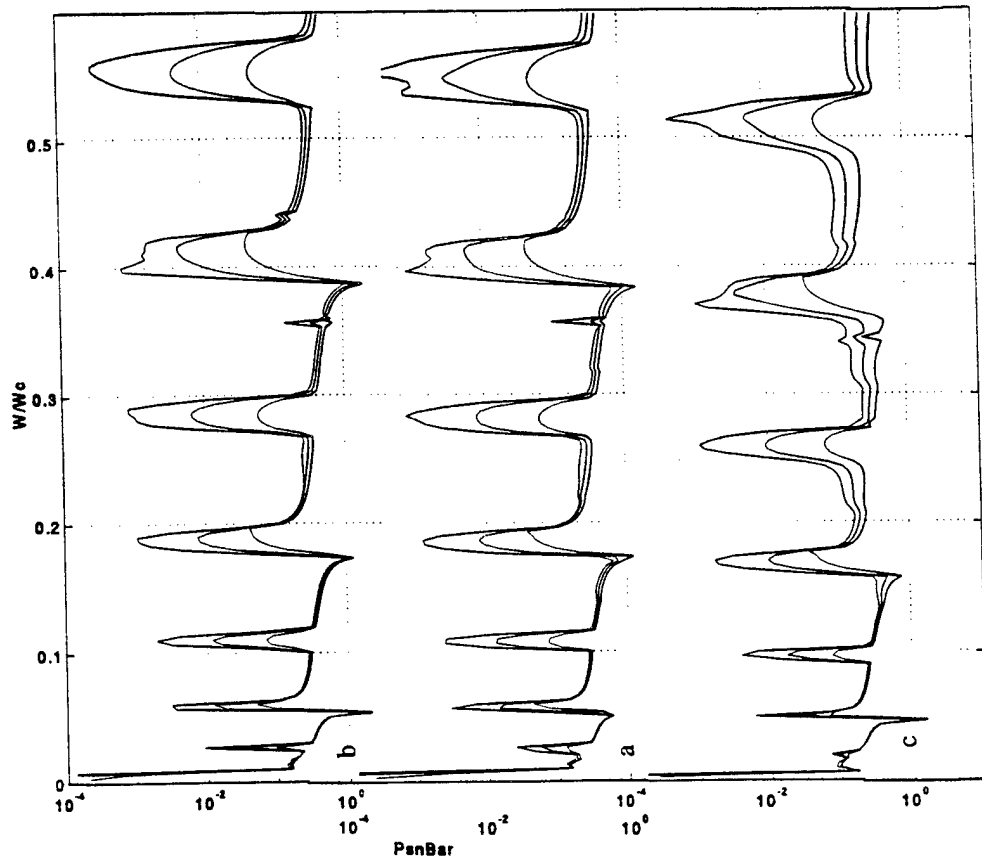


Fig. 12-10. As in Fig. 12-1 except for the change from the standard value for ( $M/mb$ ) of 0.2 to 1.0.

- a.  $\epsilon_c = 10^{-2}$  (standard value).
- b.  $\epsilon_c = 10^{-4}$ .
- c.  $\epsilon_c = 10^{-1}$ .

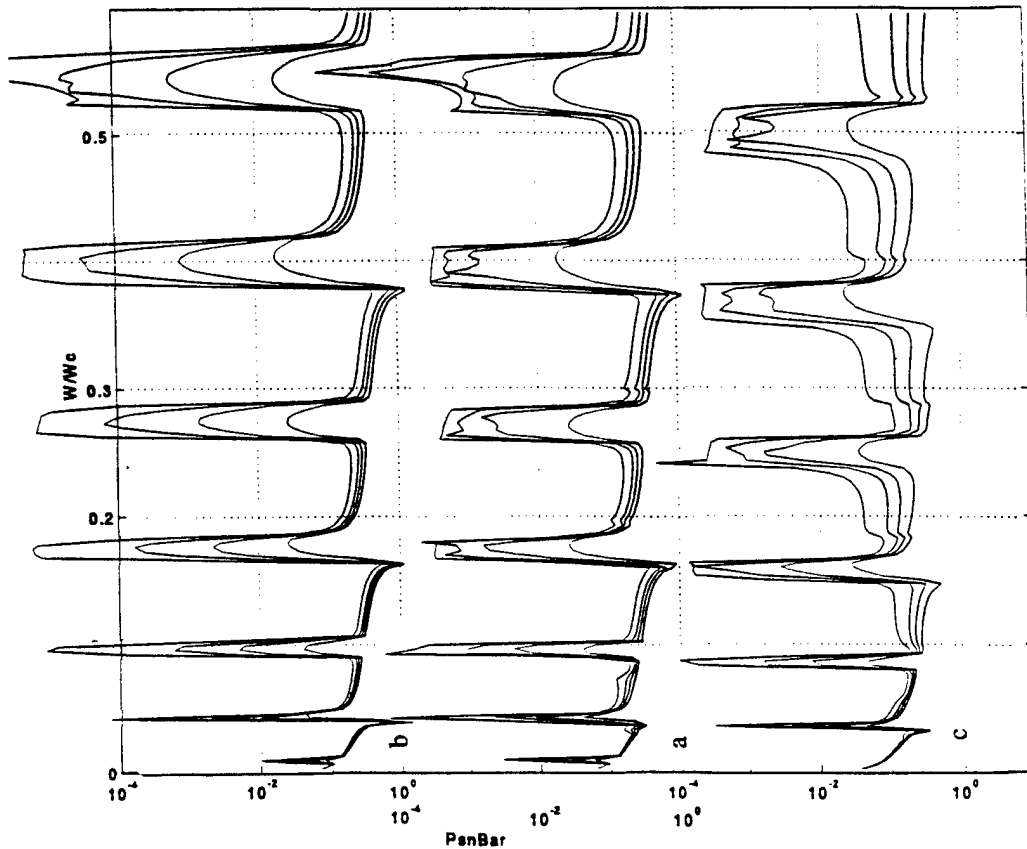


Fig. 12-11. Normalized modal drive  $\bar{P}_{Rn}(x_j, \omega)$  in lieu of the  $(j)$ th rib on a hybrid cylinder as function of  $(\omega / \omega_c)$  at the positions  $(x_j / b) = 7, 14, 21$  and 35 for a mode index  $(n)$  of unity.

- a.  $\epsilon_c = 10^{-2}$  (standard value).
- b.  $\epsilon_c = 10^{-4}$ .
- c.  $\epsilon_c = 10^{-1}$ .

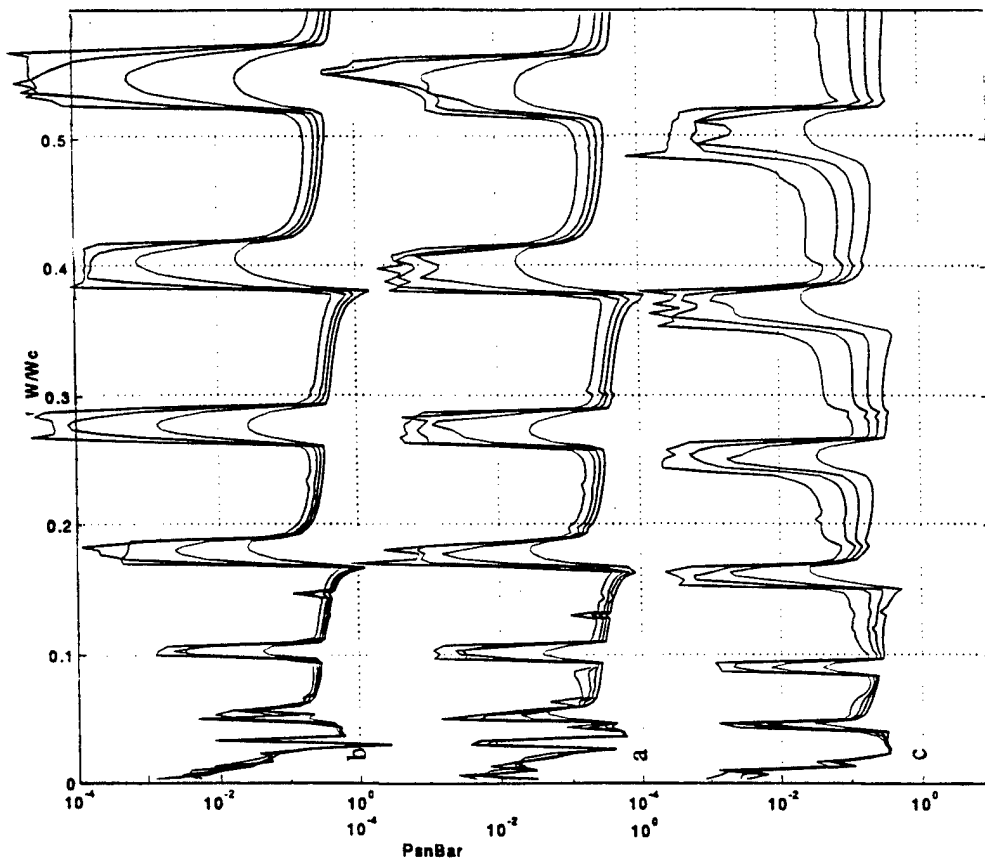


Fig. 12-12. As in Fig. 12-11 except for the change to a natural cylinder.

- a.  $\epsilon_c = 10^{-2}$  (standard value).
- b.  $\epsilon_c = 10^{-4}$ .
- c.  $\epsilon_c = 10^{-1}$ .

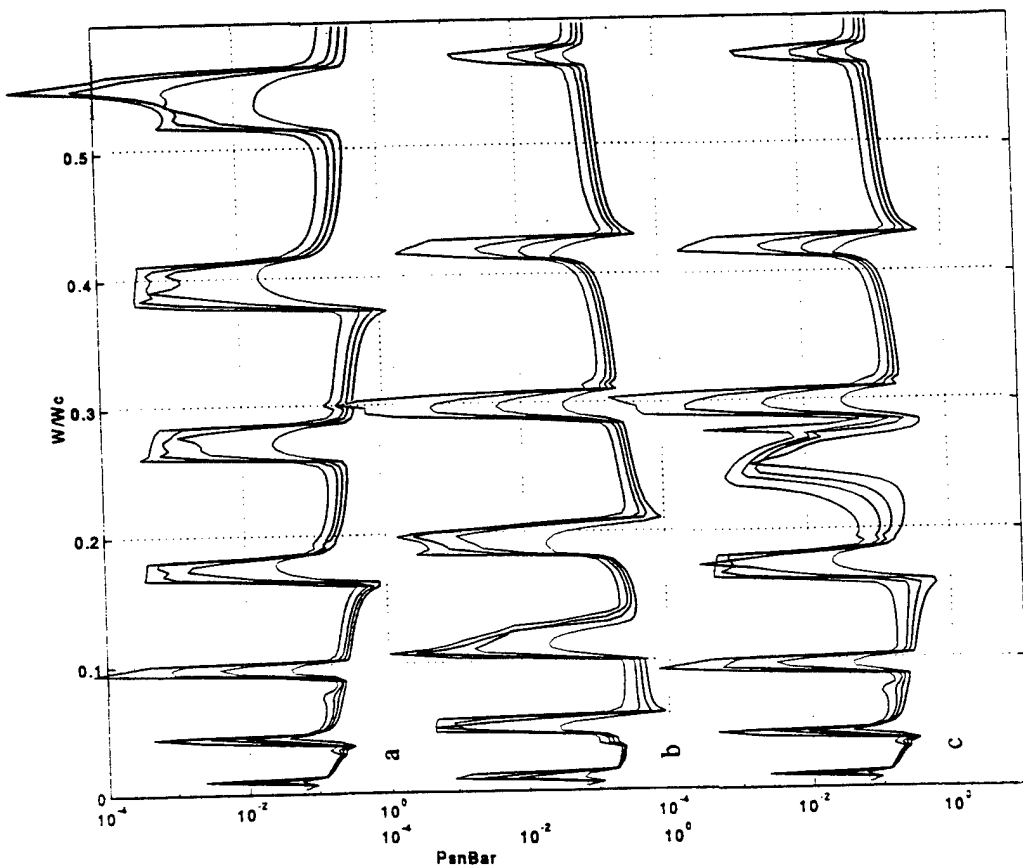


Fig. 12-13. Normalized modal drive  $\bar{P}_{Rn}(x_j, \omega)$  in lieu of the  $(j)th$  rib on a hybrid cylinder as a function of  $(\omega/\omega_c)$  at the positions  $(x_j/b) = 7, 14, 21$  and  $35$ .

- a. Mass controlled ribs  $[(\omega_o/\omega_c) = 10]$ .
- b. Stiffness controlled ribs  $[(\omega_o/\omega_c) = 10^{-2}]$ .
- c.  $(\omega_o/\omega_c) = 2.5 \times 10^{-1}$ .

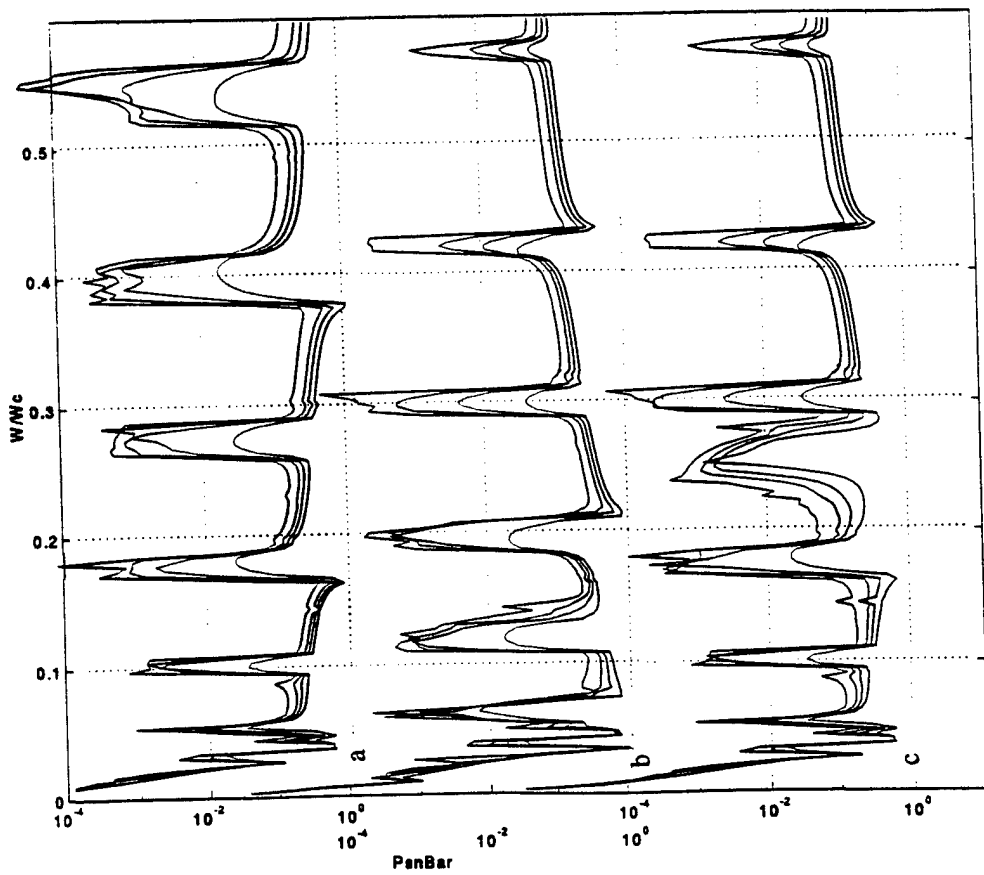


Fig. 12-14. As in Fig. 12-13 except for the change to a natural cylinder.

- a. Mass controlled ribs  $[(\omega_o/\omega_c) = 10]$ .
- b. Stiffness controlled ribs  $[(\omega_o/\omega_c) = 10^{-2}]$ .
- c.  $(\omega_o/\omega_c) = 2.5 \times 10^{-1}$ .

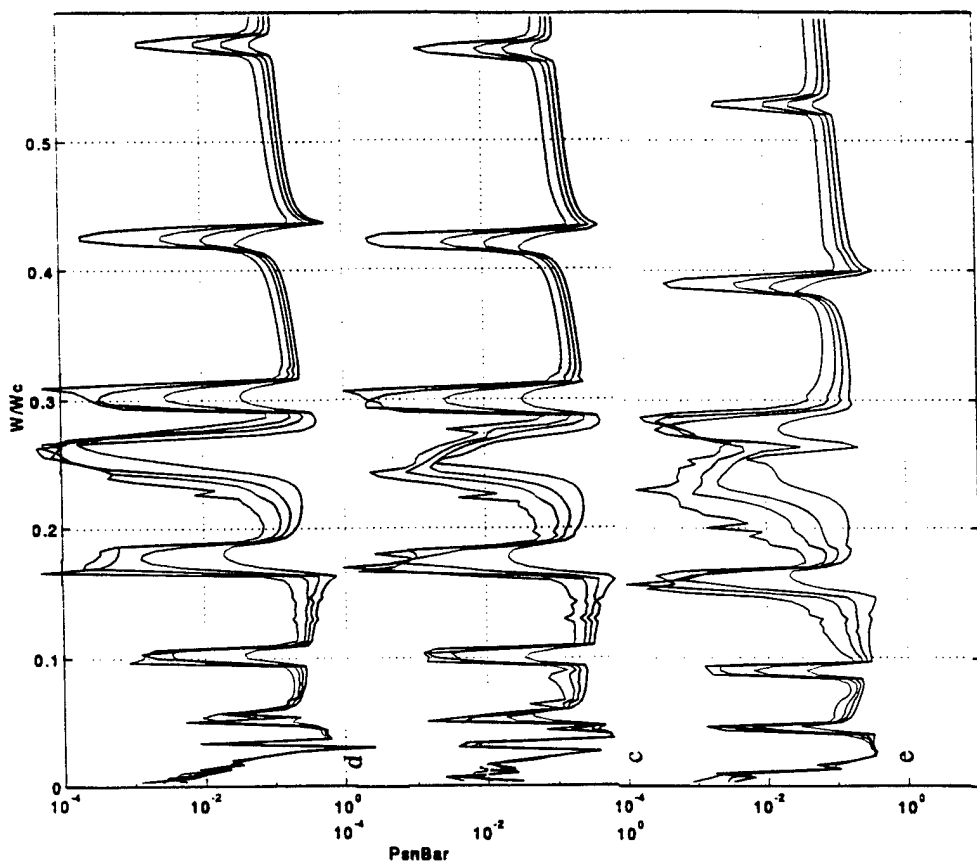


Fig. 12-15 (Cont.)

- d. As in c. except that  $(\epsilon_c)$  is decreased from  $10^{-2}$  to  $10^{-4}$ .
- e. As in c. except that  $(\epsilon_c)$  is increased from  $10^{-2}$  to  $10^{-1}$ .

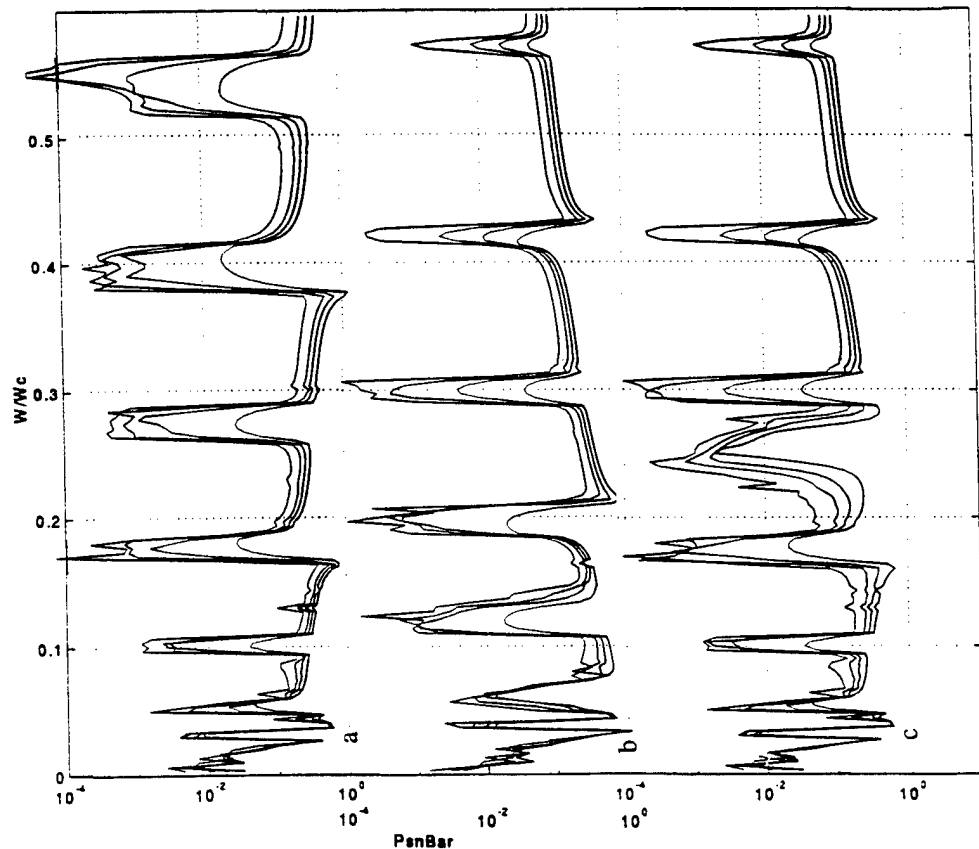


Fig. 12-15. As in Fig. 12-14 except for the change from the standard mode index ( $n$ ) of zero to unity.

- a. Mass controlled ribs  $[(\omega_o / \omega_c) = 10]$ .
- b. Stiffness controlled ribs  $[(\omega_o / \omega_c) = 10^{-2}]$ .
- c.  $(\omega_o / \omega_c) = 2.5 \times 10^{-1}$ .

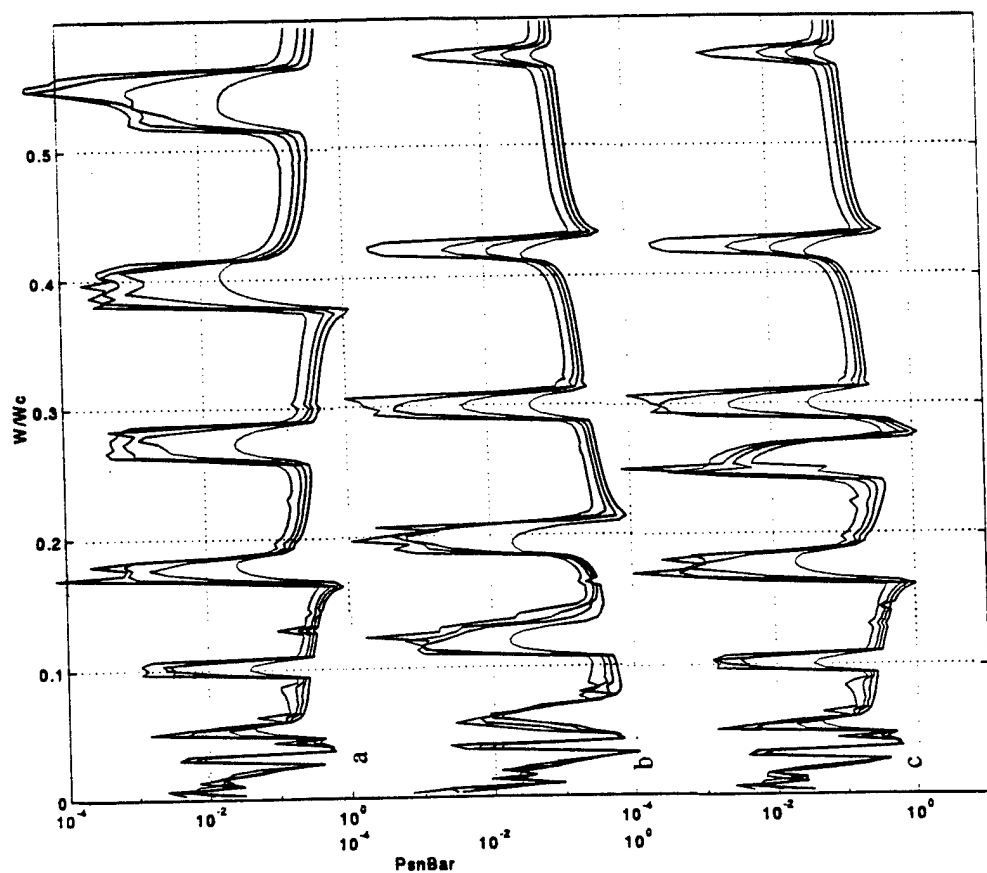


Fig. 12-16. As in Fig. 12-15 except that  $A(\omega/\omega_o)$  [Eq. (9-3)] is replaced by  $A'(\omega/\omega_o)$  [Eq. (9-6)].

- a. Mass controlled ribs  $[(\omega_o/\omega_c) = 10]$ .
- b. Stiffness controlled ribs  $[(\omega_o/\omega_c) = 10^{-2}]$ .
- c.  $(\omega_o/\omega_c) = 2.5 \times 10^{-1}$ .

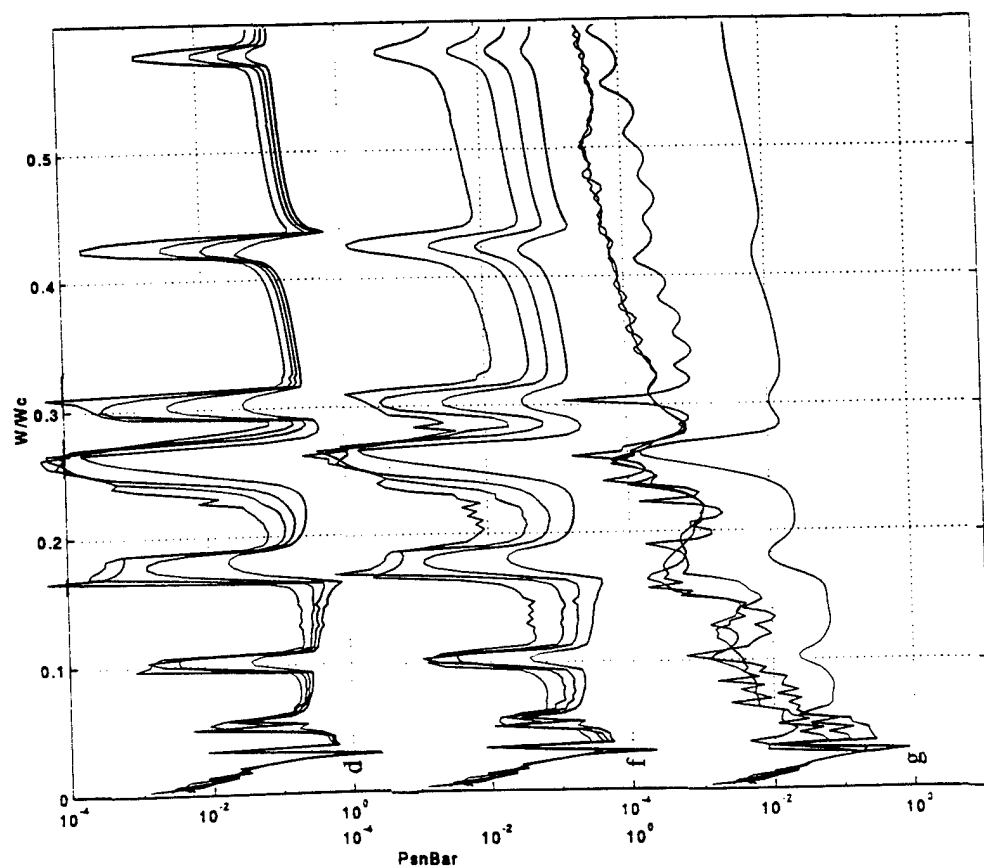


Fig. 12-15 (Cont.)

- f. As in c. except that  $(\epsilon_c)$  and  $(\eta_p)$  are changed from  $10^{-2}$  and  $10^{-3}$  to  $10^{-4}$  and  $5 \times 10^{-3}$ , respectively.
- g. As in c. except that  $(\epsilon_c)$  and  $(\eta_p)$  are changed from  $10^{-2}$  and  $10^{-3}$  to  $10^{-4}$  and  $2.5 \times 10^{-2}$ , respectively.

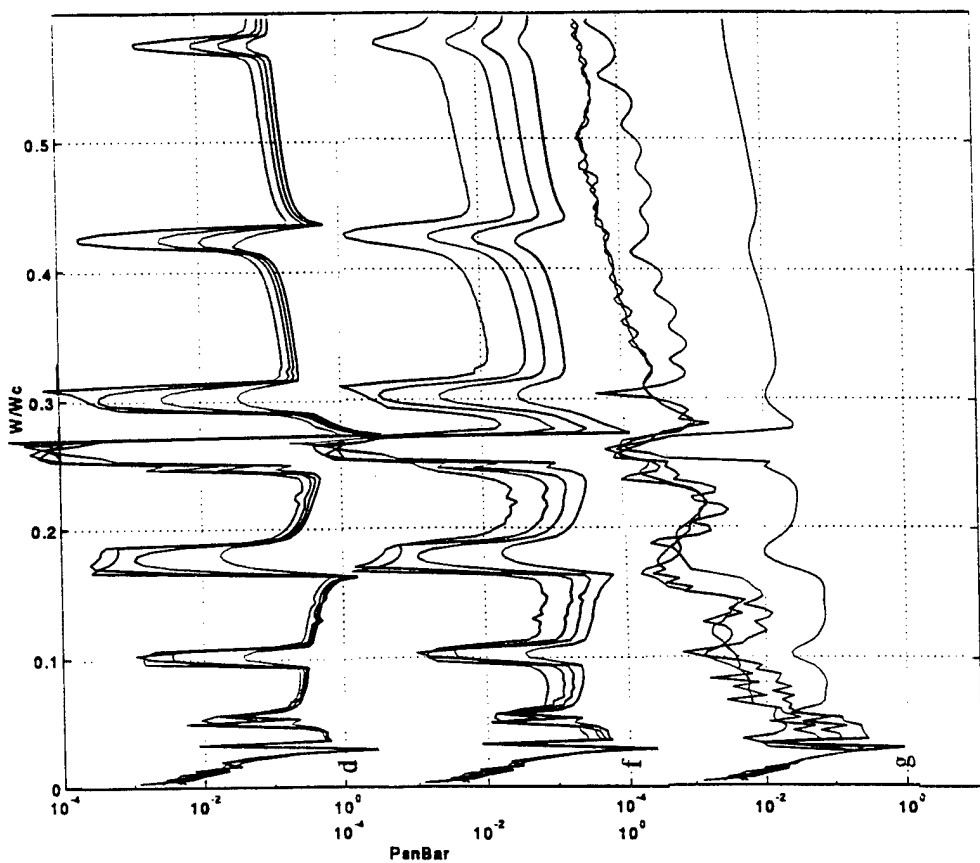


Fig. 12-16 (Cont.)

- d. As in c. except that  $(\epsilon_c)$  is decreased from  $10^{-2}$  to  $10^{-4}$ .
- e. As in c. except that  $(\epsilon_c)$  is increased from  $10^{-2}$  to  $10^{-1}$ .

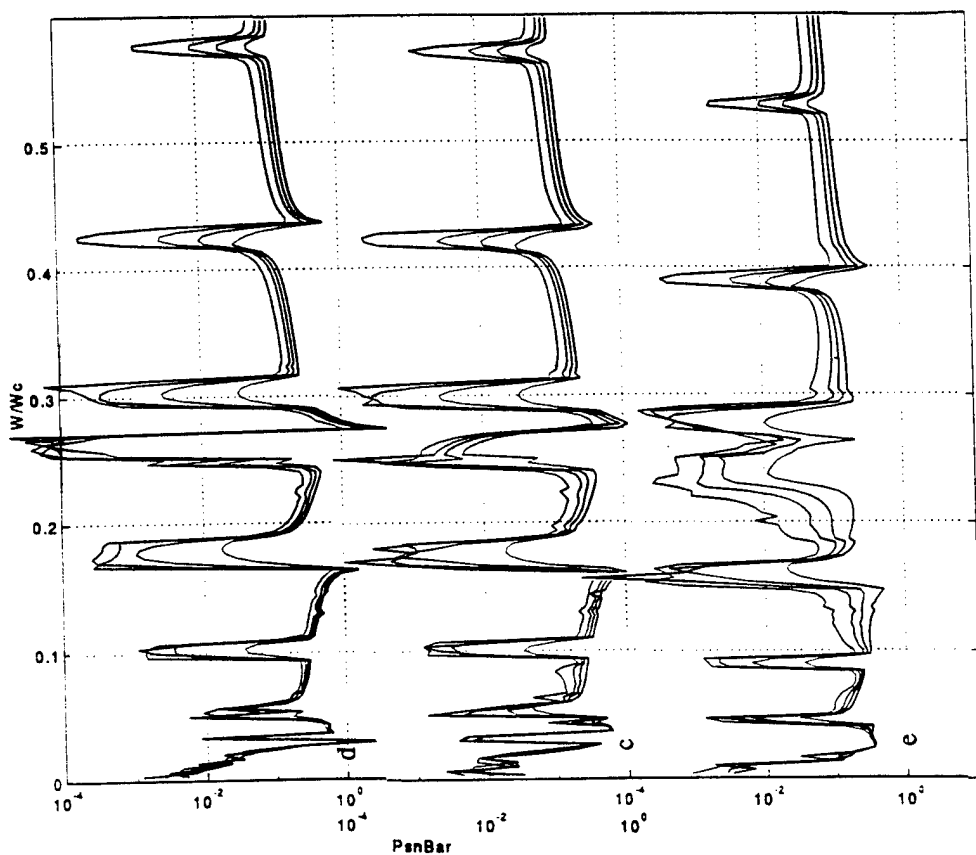


Fig. 12-16 (Cont.)

### XIII. COMPLEMENTAL DISPLAYS OF THE DRIVE IN LIEU OF THE RIBS

From Sections X and XI and from Section XII it emerges that a phenomenon described in the two Fourier conjugate domains, the (axial)  $k$ -domain and the (axial)  $x$ -domain, exhibit common characteristics with possibly different emphasis. In these sections the drive in lieu of the ribs is computed complementally in this pair of Fourier conjugate domains. Is it advantageous, to the discovering and interpreting of phenomena, to cast the pair of conjugate descriptions of this drive under a single cover? To facilitate this casting it is necessary to render compatible the displays in Section X and Section XII. The displays in Figs. 12-13 through 16 are accordingly replotted with a normalized frequency  $(\omega/\omega_c)$  axis that appropriately befits the  $(\omega/\omega_c)$  - waterfall format employed in Figs. 10-13 through 15 and 21. With this replotting scheme, corresponding figures in these two sets are paired and cast under single covers. These single covers are presented in Figs. 13-1 through 4. The phenomena of aliasing and pass and stop bands in the modal drive in lieu of the ribs are of particular manifestation in these figures. It is clear that the complementary displays in the figures of this section are useful analytical tools in the investigation of these phenomena.



Fig. 13-1. Complementary of Figs. 10-13 and 12-13 (frequency adjusted).

- a. Mass controlled ribs  $[(\omega_o / \omega_c) = 10]$ .
- b. Stiffness controlled ribs  $[(\omega_o / \omega_c) = 10^{-2}]$ .
- c.  $(\omega_o / \omega_c) = 2.5 \times 10^{-1}$ .

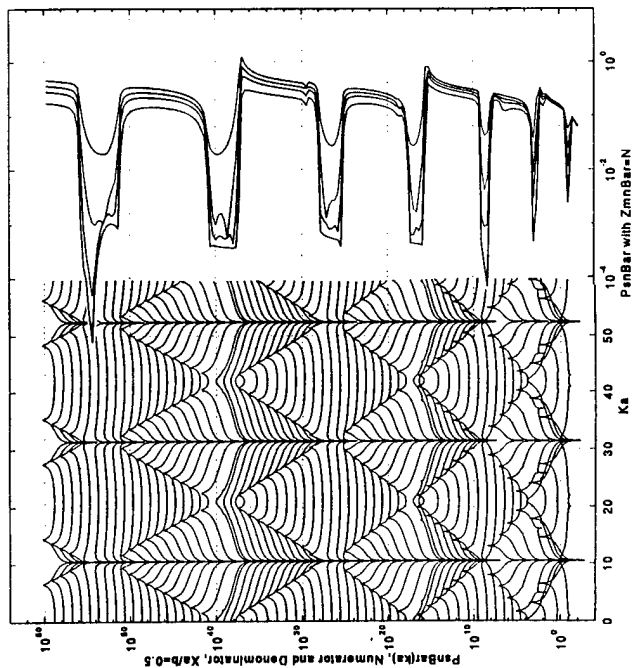


Fig. 13-1a

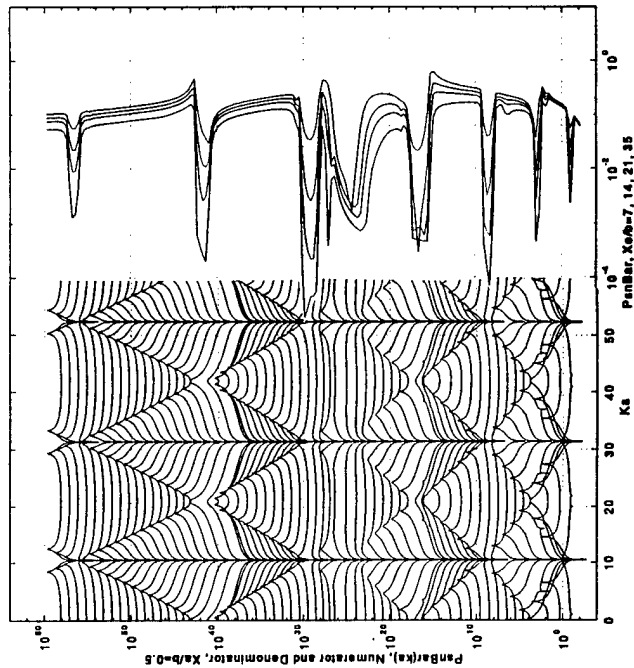


Fig. 13-1c

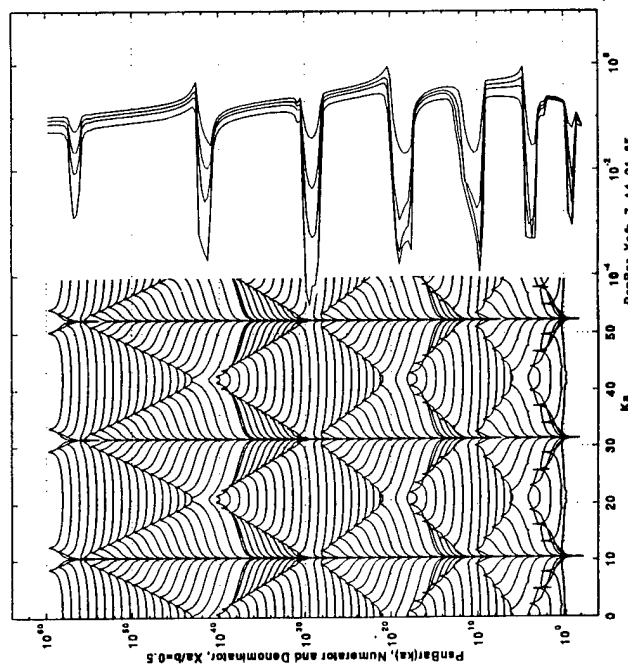


Fig. 13-1b

Fig. 13-2. Complementary of Figs. 10-14 and 12-14 (frequency adjusted).

- Mass controlled ribs  $[(\omega_o / \omega_c) = 10]$ .
- Stiffness controlled ribs  $[(\omega_o / \omega_c) = 10^{-2}]$ .
- $(\omega_o / \omega_c) = 2.5 \times 10^{-1}$

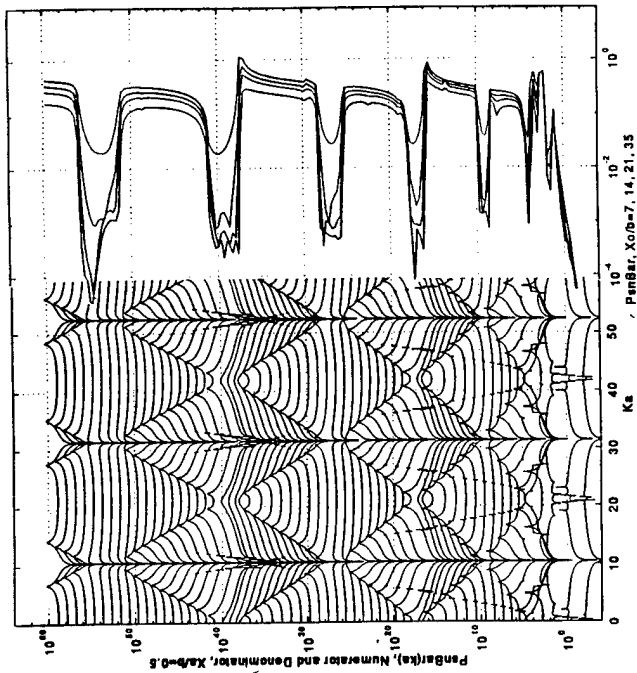


Fig. 13-2a

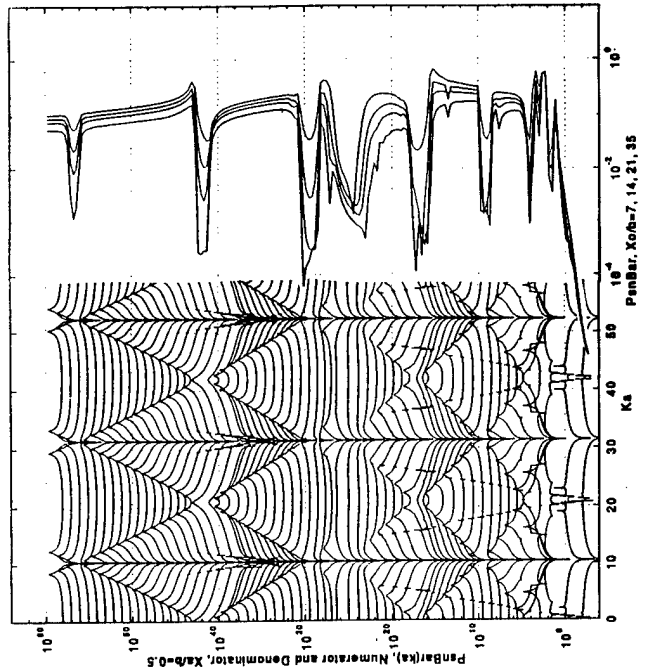


Fig. 13-2c

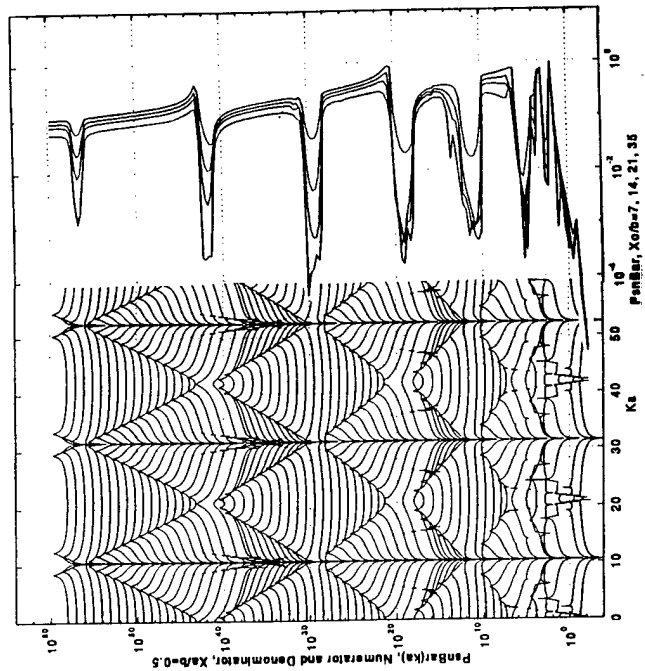


Fig. 13-2b

Fig. 13-3. Complementary of Fig. 10-15 and 12-15 (frequency adjusted).

- Mass controlled ribs  $[(\omega_o / \omega_c) = 10]$ .
- Stiffness controlled ribs  $[(\omega_o / \omega_c) = 10^{-2}]$ .
- $(\omega_o / \omega_c) = 2.5 \times 10^{-1}$ .
- As in c. except that  $(\epsilon_c)$  is decreased from  $10^{-2}$  to  $10^{-4}$ .
- As in c. except that  $(\epsilon_c)$  is increased from  $10^{-2}$  to  $10^{-1}$ .
- As in c. except that  $(\epsilon_c)$  and  $(\eta_p)$  are changed from  $10^{-2}$  and  $10^{-3}$  to  $10^{-4}$  and  $5 \times 10^{-3}$ , respectively.
- As in c. except that  $(\epsilon_c)$  and  $(\eta_p)$  are changed from  $10^{-2}$  and  $10^{-3}$  to  $10^{-4}$  and  $2.5 \times 10^{-2}$ .

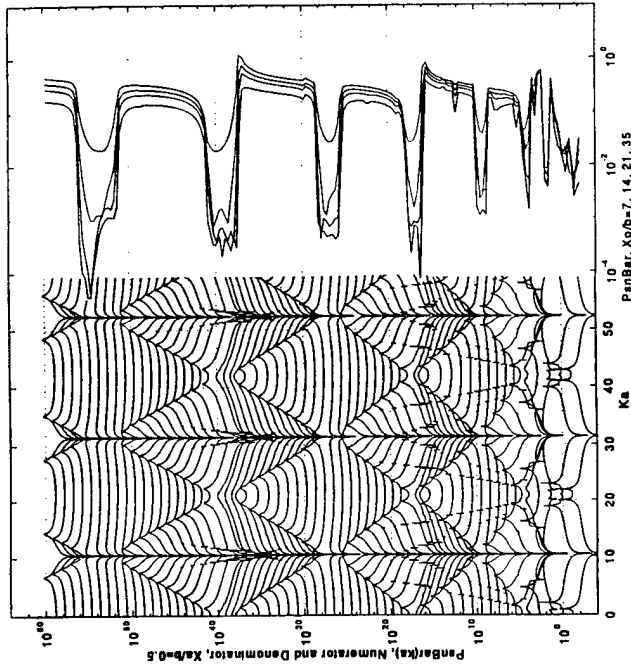


Fig. 13-3a

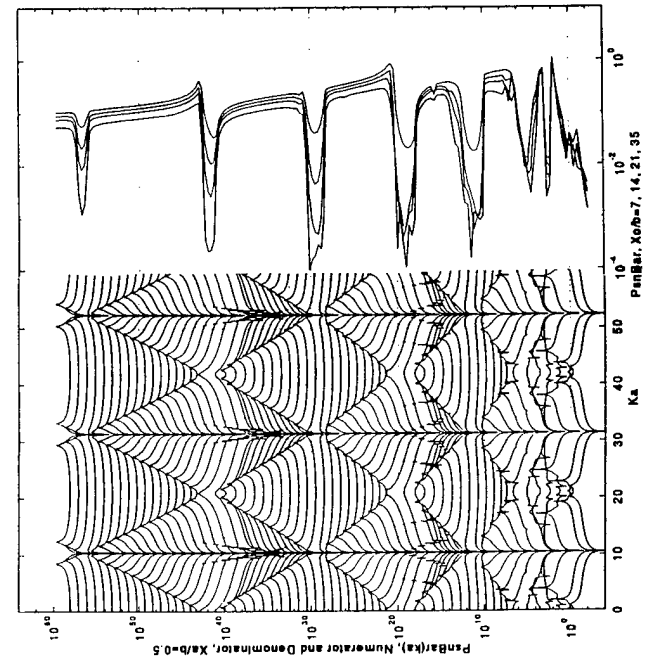


Fig. 13-3b

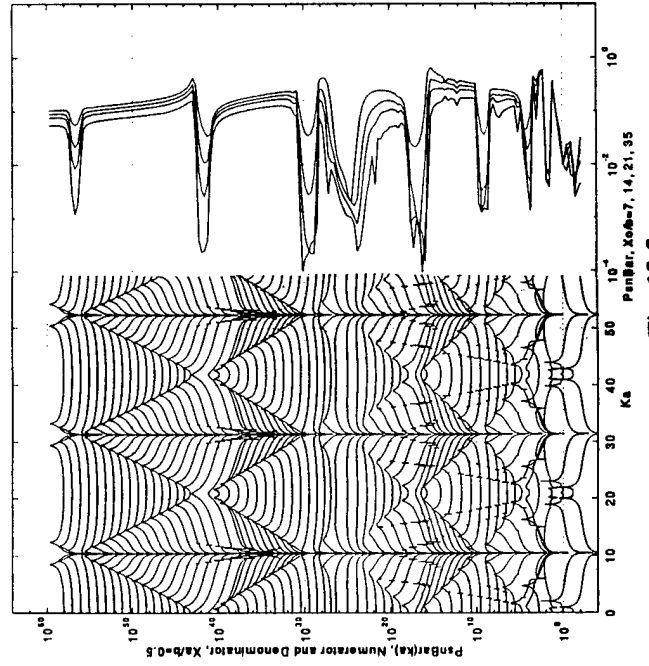


Fig. 13-3c

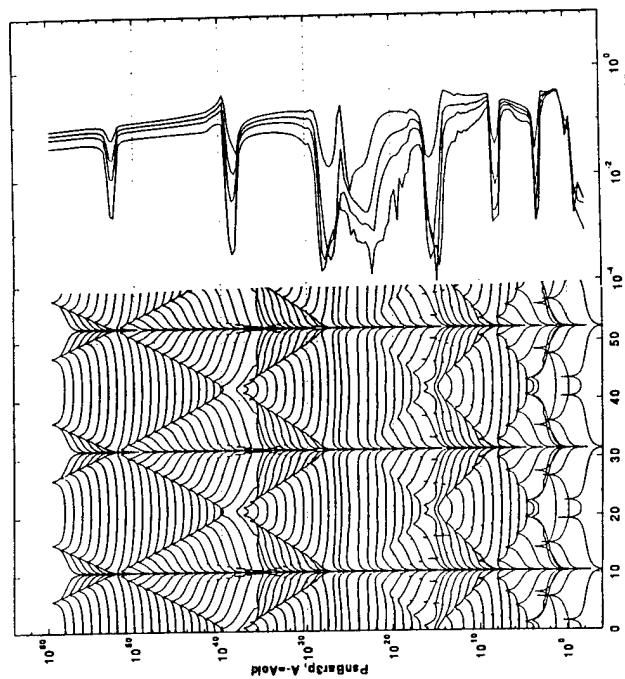


Fig. 13-3e

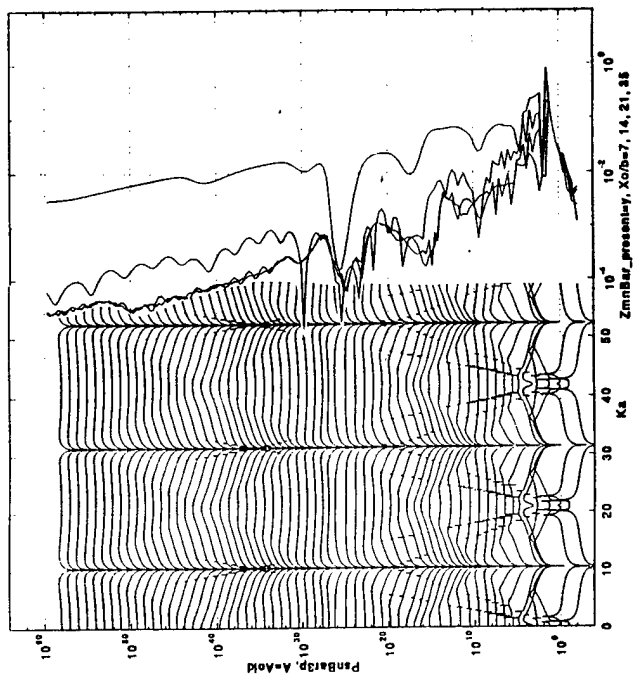


Fig. 13-3g

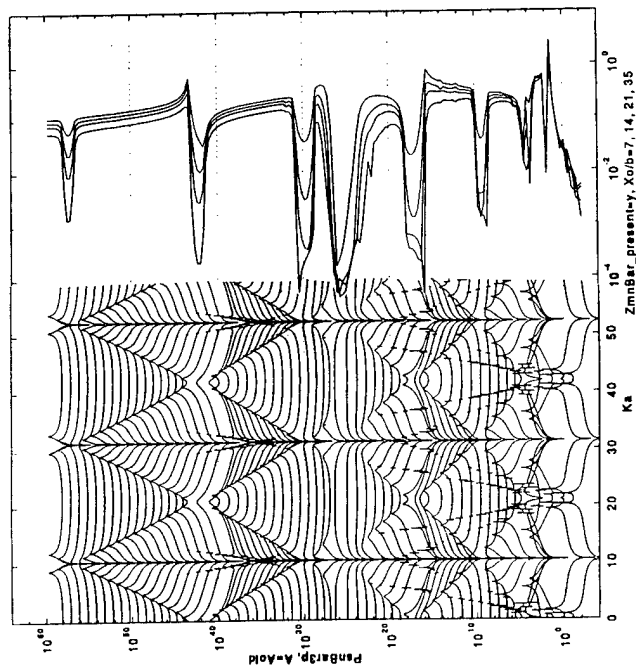


Fig. 13-3d

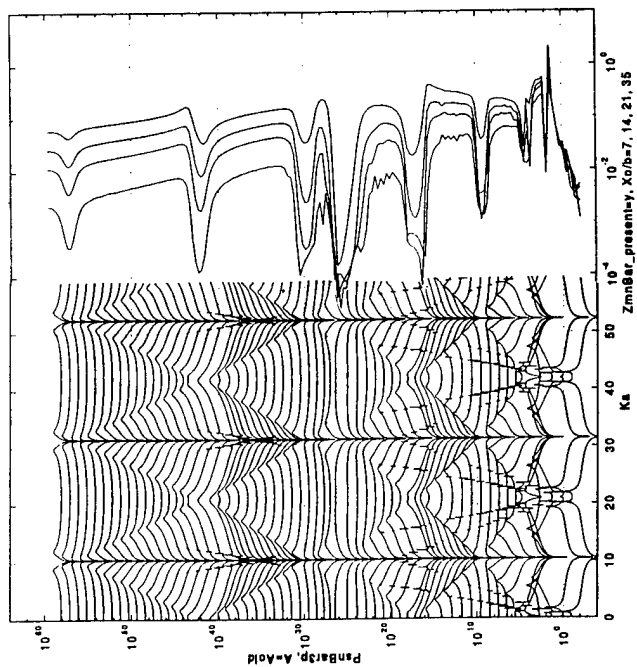


Fig. 13-3f

Fig. 13-4. Complementary of Fig. 10-21 and 12-16 (frequency adjusted).

- Mass controlled ribs  $[(\omega_o / \omega_c) = 10]$ .
- Stiffness controlled ribs  $[(\omega_o / \omega_c) = 10^{-2}]$ .
- $(\omega_o / \omega_c) = 2.5 \times 10^{-1}$ .
- As in c. except that  $(\epsilon_c)$  is decreased from  $10^{-2}$  to  $10^{-4}$ .
- As in c. except that  $(\epsilon_c)$  is increased from  $10^{-2}$  to  $10^{-1}$ .
- As in c. except that  $(\epsilon_c)$  and  $(\eta_p)$  are changed from  $10^{-2}$  and  $10^{-3}$  to  $10^{-4}$  and  $5 \times 10^{-3}$ , respectively.
- As in c. except that  $(\epsilon_c)$  and  $(\eta_p)$  are changed from  $10^{-2}$  and  $10^{-3}$  to  $10^{-4}$  and  $2.5 \times 10^{-2}$ .

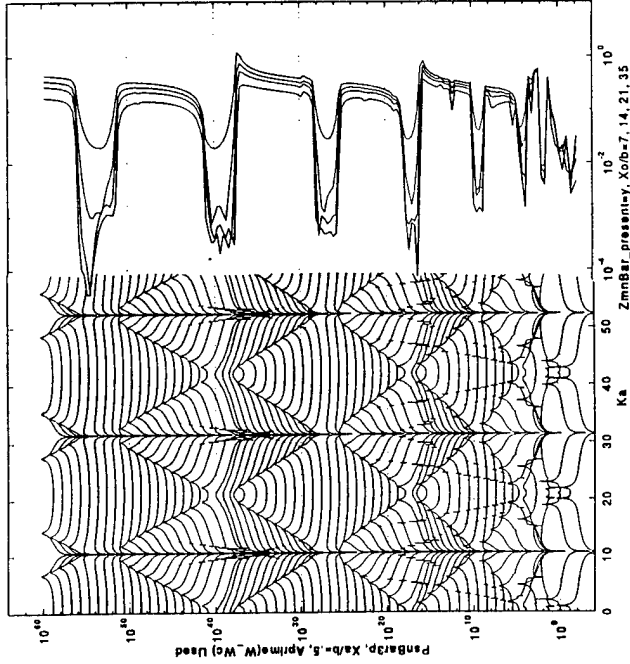


Fig. 13-4a

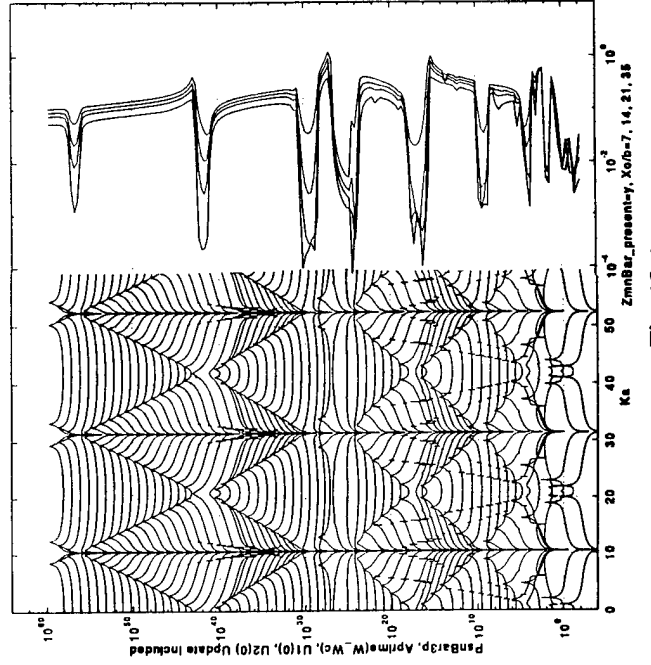


Fig. 13-4c

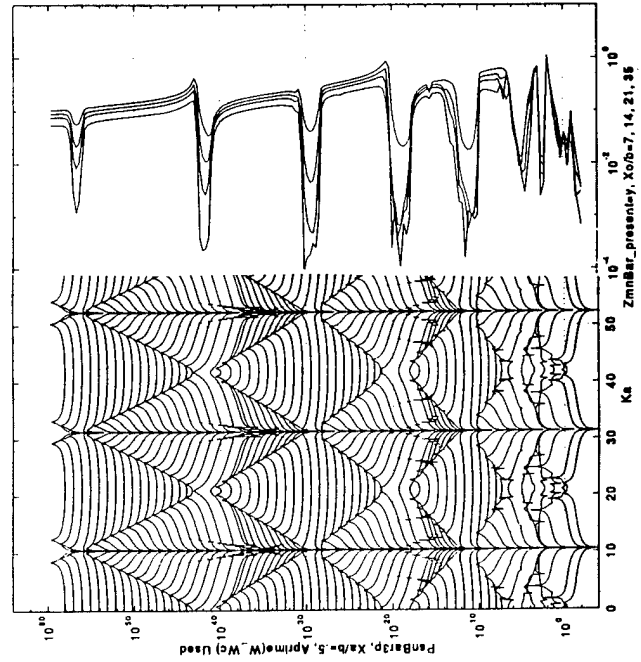


Fig. 13-4b

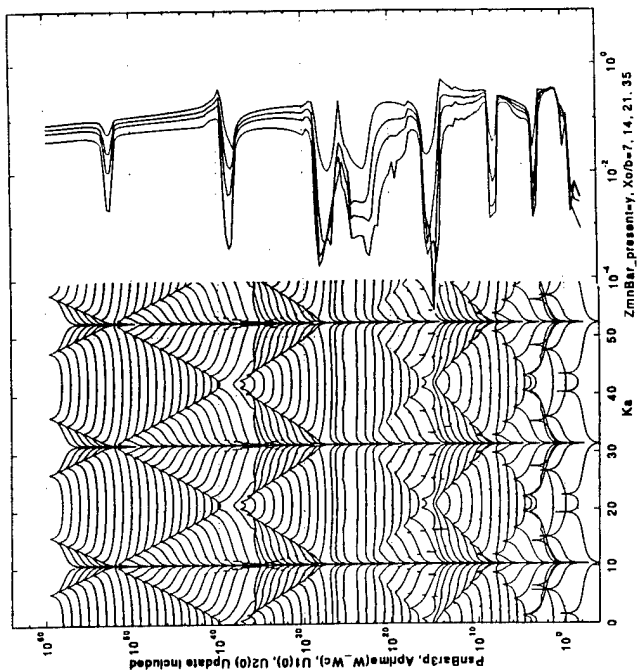


Fig. 13-4e

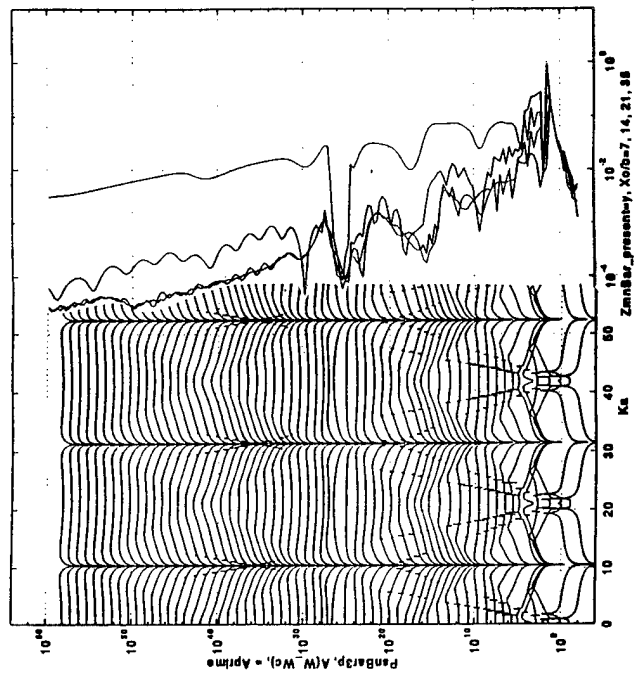


Fig. 13-4g

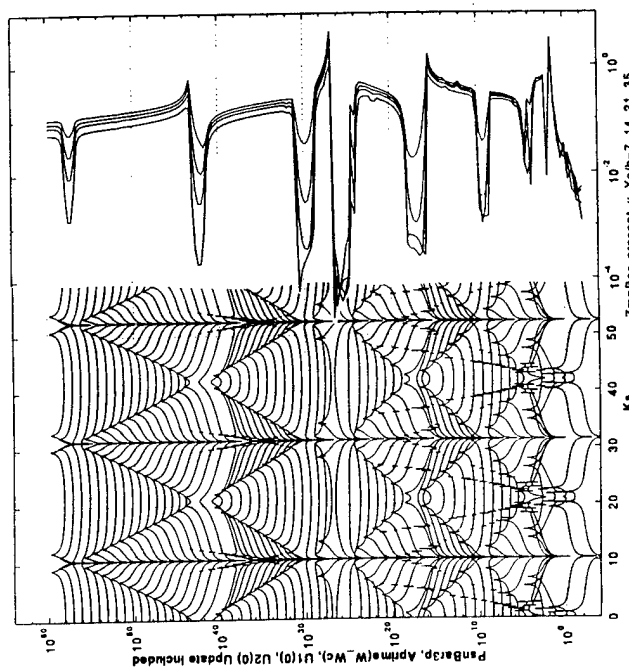


Fig. 13-4d

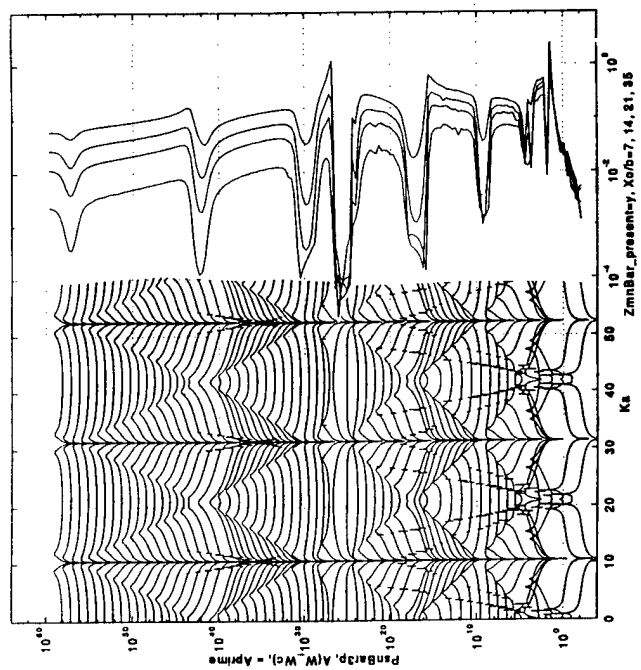


Fig. 13-4f

## APPENDIX A: THE EQUIVALENCE OF AN EIGENOPERATOR AND A STATIONARY IMPULSE RESPONSE FUNCTION

The equation of motion in terms of the impedance operator is

$$\tilde{z}(x, y, t) \tilde{v}(x, y, t) = \tilde{p}_e(x, y, t), \quad (\text{A1})$$

where  $\tilde{z}(x, y, t)$  is the impedance operator,  $\tilde{v}(x, y, t)$  is the response, and  $\tilde{p}_e(x, y, t)$  is the external drive. [cf. Eq. (3-2).] An assumption is made that  $\tilde{z}(x, y, t)$  is an eigenoperator with respect to the temporal variable ( $t$ ): namely,

$$\tilde{z}(x, y, t) (2\pi)^{-1/2} \exp(i\omega t) = z(x, y, \omega) (2\pi)^{-1/2} \exp(i\omega t), \quad (\text{A2a})$$

or more concisely, but equivalently,

$$\{\tilde{z}(x, y, t) = z(x, y, \omega)\} (2\pi)^{-1/2} \exp(i\omega t), \quad (\text{A2b})$$

where typically

$$v(x, y, \omega) = (2\pi)^{-1/2} \int dt \tilde{v}(x, y, t) \exp(i\omega t). \quad (\text{A3})$$

From Eqs. (A1) through (A3) one obtains

$$z(x, y, \omega) v(x, y, \omega) = p_e(x, y, \omega). \quad (\text{A4})$$

[cf. Eq. (3-2).] The response in terms of the impulse response function is by definition

$$\tilde{v}(x, y, t) = \int \tilde{g}(x|x', y|y', t|t') dx' dy' dt' \tilde{p}_e(x', y', t') . \quad (A5)$$

An assumption is now made that  $\tilde{g}(x|x', y|y', t|t')$  is stationary with respect to the temporal variable; namely,

$$\tilde{g}(x|x', y|y', t|t') , \rightarrow (2\pi)^{-1/2} \tilde{g}(x|x', y|y', t-t') , \quad (A6)$$

where typically and by convention

$$\begin{aligned} g(x|x', y|y', \omega|\omega') \\ = (2\pi)^{-1/2} \int dt \int dt' \tilde{g}(x|x', y|y', t-t') \exp[i(\omega t - \omega' t')] . \end{aligned} \quad (A7)$$

From Eqs. (A6) and (A7) one obtains

$$g(x|x', y|y', \omega) = (2\pi)^{-1/2} \int ds \tilde{g}(x|x', y|y', s) \exp(i\omega s) . \quad (A8)$$

From Eqs. (A6) through (A8) one obtains

$$g(x|x', y|y', \omega|\omega') \equiv g(x|x', y|y', \omega) \delta(\omega - \omega') , \quad (A9)$$



and whence from Eq. (A5) one derives

$$v(x, y, \omega) = \int g(x | x', y | y', \omega) dx' dy' p_e(x', y', \omega), \quad (\text{A10})$$

which is the impulse response form of Eq. (A4).

## APPENDIX B: COMPUTATIONAL DISPLAYS

A large number of quantities, typified by  $X$ , that are investigated in this report are dependent on the two-vector variable  $\{k, \omega\}$  and usually on another or other dependent variables: e.g.,  $X(k, k_y, \omega)$ ;  $X(k, n, \omega) \equiv X_n(k, \omega)$ ;  $X(k, \omega, \phi | \phi_a)$  etc. and also on a number of parameters; e.g., the fluid loading parameter ( $\varepsilon_c$ ), the critical frequency ( $\omega_c$ ), etc. A convenient and yet a rich way of illustrating the computations performed on these quantities is to determine them in a normalized form;  $X \rightarrow \bar{X} \{k, \omega\}$ , and to display them on the normalized  $\{(ak), (\omega/\omega_c)\}$  - plane, with other dependent variables, if present, and parameters that are properly normalized and then assigned fixed values; e.g.,  $(ak_y) = 6$ ,  $(\phi - \phi_a) = 0$ ,  $(ak_c) = (a\omega_c/c) = 26.8$ ,  $\varepsilon_c = 10^{-2}$  etc., where  $(a)$  and  $(\omega_c)$  are given normalizing length and frequency, respectively, and  $(c)$  is a speed. The quantity  $\log_{10}(\bar{X})$  is displayed as function of the normalized wavenumber  $(ak)$ , usually in  $(\omega/\omega_c)$  frequency waterfall format. In this format the origins of plots of  $\log_{10}[\bar{X}(k, \omega)]$  for specific normalized frequency  $(\omega/\omega_c)$  are discretely and successively shifted by equal increments in the normalized frequency  $(\omega/\omega_c)$ . The density of the increments and/or the levels in the plots are chosen and adjusted to suit particular needs and conveniences. The display of the computed and normalized quantities is cast conveniently by specifying standard values for the other normalized variables and normalized parameters. This procedure does not only help in the comparison between various displays but it also helps with the figure captions. Only changes from the standard fixed values of the other normalized variables and normalized parameters need to be specifically reported.

Often the normalized quantity, as typified by  $\bar{X}$ , exhibits patterns when displayed in the manner just discussed. Significant contributions to the patterns are provided by the prominences and anti-prominence in the values of  $\log_{10}(\bar{X})$ . Situations arise in which it is advantageous to accentuate the prominences in the displays. This may be accomplished by clipping out the values of  $\log_{10}(\bar{X})$  that are below an assigned threshold. The assigned threshold is designated by  $\log_{10}(\bar{X}^0)$ . The clipping is achieved then by displaying  $\{\log_{10}(\bar{X}) U[(\bar{X} / \bar{X}^0) - 1]\}$ , where  $U$  is the unit step function. Also, often the normalized quantity, as typified by  $\bar{X}$ , exhibits patterns in certain regions on the  $\{(ak), (\omega / \omega_c)\}$  - plane, the details of which hold particular interest. One may then satisfy this interest by zooming onto the region so that details can be more readily examined by direct observation of the displays. Moreover, the zoomed on details in the region can be scaled to suite a particular requirement. Additionally, curves in different waterfall displays may be advantageously compared side by side. In such situations single curves at the same frequency, from each of the  $(\omega / \omega_c)$  - waterfall displays, can be compared. In this display the origins of the single curves are discretely and successively shifted. Again, the scales of the curves may be amplified to suite a particular requirement. Some of these aids to displaying the computed quantities are employed in this report.

THIS PAGE INTENTIONALLY LEFT BLANK

## REFERENCES

1. L. Cremer, M. Heckl, and E. Ungar, Structure-Borne Sound, Structural Vibrations and Sound Radiation at Audio Frequencies, (Springer-Verlag, 2nd Ed., 1988).
2. M.C. Junger and D. Feit, Sound Structures, and Their Interaction, (MIT Press, 1986).
3. F. Fahy, Sound and Structural Vibration (Radiation, Transmission and Response), (Academic Press, 1985).
4. G. Maidanik and J. Dickey, "Flexural response matrix for ribbed panels," J. Acoust. Soc. Am., 95, 1245-1255 (1944) and "Significance of modification in the expression for the mechanical surface impedance of panels at high wavenumbers," J. Sound Vib., 134, 369-379 (1989).
5. M. Heckl, "Vibration of point-driven cylindrical shells," J. Acoust. Soc. Am., 34, 1553-1557 (1962).
6. G. Maidanik and E. Kerwin, "Influence of fluid loading on the radiation from infinite panels below the critical frequency," J. Acoust. Soc. Am., 40, 1034-1038 (1966).
7. D. Feit, "Pressure radiated by a point-excited panel," J. Acoust. Soc. Am., 40 1489-1494 (1966).
8. W. Vogel and D. Feit, "Response of a point excited infinitely long cylindrical shell immersed in an acoustic medium," DTNSRDC report no. 80/061 (1980).
9. Y. Liu and A. Tucker, "The distribution of radiated and vibratory powers of a point-driven infinite cylindrical shell, Part I-Uncoated structure," DTNSRDC report no. 84/043 (1984) and "Part II-Structures with a compliant coating," DTNSRDC report no. 84/044 (1984).

10. C.B. Burroughs, "Acoustic radiation from fluid-loaded infinite circular cylinders with doubly periodic ring supports," J. Acoust. Soc. Am., 75, 715-722 (1984).
11. P. Morse and K.U. Ingard, Theoretical Acoustics, (McGraw-Hill Book Company, 1968).
12. M.P. Norton, Fundamentals of Noise and Vibration Analysis for Engineers, (Cambridge University Press, 1989).
13. G. Maidanik and A.J. Tucker, "Proper and first order solutions of regularly ribbed panels," J. Sound and Vib., 44, 267-274 (1976).
14. G. Maidanik and J. Dickey, "Acoustic behavior of ribbed panels," J. of Sound and Vib., 123, 293-307 (1988).
15. G. Maidanik and J. Dickey, "Velocity distributions on unloaded finitely and regularly ribbed membranes," J. Acoust. Soc. Am., 149, 43-70 (1991) and "Response of regularly ribbed fluid loaded panels," J. Acoust. Soc. Am., 155, 481-495 (1992).
16. G. Maidanik and K.J. Becker, "Use of a double-sum technique for computing the modal response of a regularly ribbed cylinder," NSWCCD-SIG-96/061-7030 (1996).
17. D.M. Photiadis, "Fluid loaded structures with one dimensional disorder," App. Mech. Rev., 49, 100-125 (1996).
18. G. Maidanik and K.J. Becker, "A double-sum technique for performing a Fourier transformation on an integrand composed of aliased factors," NSWCCD-SIG-96/060-7030 (1996).

# INITIAL DISTRIBUTION

## Copies

3	NAVSEA 03T2
2	Taddeo
1	Becker
4	ONR/ONT
1	334 Vogelsong
1	334 Tucker
1	334 Main
1	Library
4	NRL
1	5130 Bucaro
1	5130 Williams
1	5130 Photiadis
1	Library
4	NUWC/New London
1	Sandman
1	Harari
1	3332 Lee
1	Library
1	NUWC/NPT
	Library
2	DTIC
1	Johns Hopkins University
	Green
1	Applied Physics Lab
	Johns Hopkins University
	Library
4	ARL/Penn State University
1	Biancardi
3	Burroughs
1	Cambridge Collaborative
	Manning
1	Georgia Tech/M.E. Dept.
	Ginsberg
1	MIT
	Dyer

## Copies

1	Penn State University
1	Koopman
2	Virginia Tech
1	Knight
1	Fuller

## CENTER DISTRIBUTION

Copies	Code	Name
1	011	
1	0112	Douglas
1	0112	Halsall
1	20	
1	204	
1	2040	Everstine
1	2042	
1	2042	Hambric
1	70	
1	7030	
1	7200	Hwang
1	7250	
1	7250	Maga
1	7250	Vasudevan
1	726	Szilagyi
1	804.1	Dickey
2	3421	(TIC-Carderock)